

Atmospheric Chemistry

István Lagzi
Róbert Mészáros
Györgyi Gelybó
Ádám Leelőssy

Atmospheric Chemistry

by István Lagzi, Róbert Mészáros, Györgyi Gelybó, and Ádám Leelőssy
Copyright © 2013 Eötvös Loránd University

This book is freely available for research and educational purposes. Reproduction in any form is prohibited without written permission of the owner.

Made in the project entitled "E-learning scientific content development in ELTE TTK" with number TAMOP-4.1.2.A/1-11/1-2011-0073. Consortium leader: Eötvös Loránd University, Consortium Members: ELTE Faculties of Science Student Foundation, ITStudy Hungary Ltd.

National Development Agency
www.ujszechenyiterv.gov.hu
06 40 638 638



The project is supported by the European Union
and co-financed by the European Social Fund.

Table of Contents

Preface	vi
1. The structure and composition of the atmosphere	1
1.1. Formation of the Earth atmosphere	1
1.2. A short history of the atmospheric chemistry	3
1.3. Atmospheric composition	4
1.4. Vertical structure of the atmosphere	8
1.4.1. Vertical change of composition	8
1.4.2. Vertical temperature changes	9
1.5. The planetary boundary layer	12
2. Emission of air pollutants	14
2.1. Source types of air pollutants	15
2.2. Natural emission sources	16
2.2.1. Terrestrial ecosystems	16
2.2.2. Aquatic Ecosystems	17
2.2.3. Forest fires	17
2.2.4. Volcanic and tectonic activities	17
2.2.5. Lightning	17
2.3. Anthropogenic emission sources	18
2.3.1. Industrial energy production and use	18
2.3.2. Transport	19
2.3.3. Agriculture	19
2.3.4. Waste management	20
2.3.5. Biomass burning	20
2.3.6. Anthropogenic sources of air pollutants by different sectors	20
3. Basics of the reaction kinetics	26
3.1. Differential rate law	26
3.2. Integrated rate law	27
3.3. Three-body reaction	28
3.4. Photochemical reaction (Photolysis)	28
3.5. Radicals in the atmosphere	29
3.6. Arrhenius Equation	30
3.7. Half-life	31
3.8. Reaction mechanism	31
3.9. The quasi steady-state approximation (QSSA)	32
3.10. Application of a reaction mechanism	33
4. Reactions of air pollutants in the atmosphere	41
4.1. General notes	41
4.2. Reactions of atmospheric oxygen	41
4.3. General reactions in the troposphere and stratosphere	44
5. Biogeochemical cycle of carbon	46
5.1. The natural carbon cycle	47
5.1.1. Terrestrial processes	48
5.1.2. Oceanic processes	49
5.1.3. Geological processes	52
5.2. Methane	53
5.2.1. Sources and sinks of atmospheric methane	53
5.3. Human disruption of carbon cycle	54
5.4. Carbon cycle research in Hungary	58
6. Nitrogen compounds	60
6.1. Nitrogen fixation	61
6.2. Nitrification	62
6.3. Denitrification	63
6.4. Nitrogen deposition	63
6.5. Anthropogenic sources of nitrogen compounds	64
6.6. Atmospheric reactions of nitrogen species	65

7. Sulphur compounds	67
7.1. Sulphur oxides (SO _x)	70
7.1.1. Reaction sulphur dioxide in the atmosphere	70
7.2. Hydrogen sulphide (H ₂ S)	71
7.3. Carbonyl sulphide (COS)	72
7.4 Carbon disulfide (CS ₂)	72
8. Ozone	73
8.1. Stratospheric ozone	73
8.1.1. A short history	73
8.1.2. Natural balance of stratospheric ozone	73
8.1.3. Circulation patterns in the stratosphere	77
8.1.4. Gas-phase chemistry in the stratosphere	77
8.1.5. Polar ozone chemistry	79
8.2 Tropospheric ozone	81
8.2.1. Global tropospheric ozone budget	82
8.2.2. Ozone production in the troposphere	83
8.2.3. Sinks of the tropospheric ozone	84
8.2.4. Spatial and temporal variability of ozone in the near surface layer	84
9. Aerosol particles	89
9.1. Sources and sinks of atmospheric aerosols	89
9.1.1. Sources of aerosol particles	89
9.1.2. Sink processes	91
9.2 Physical and chemical characteristics of aerosols	92
9.2.1. Concentrations:	93
9.2.2. Size distribution:	93
9.2.3. Chemical composition	96
9.2.4. Water solubility	98
9.2.5. Atmospheric lifetime	98
9.3. Effects of atmospheric aerosols	99
9.3.1. Direct effects: direct radiative forcing due the scattering radiation.	100
9.3.2. Indirect effects: indirect radiative forcing through cloud formation effects	100
10. Dispersion of air pollutants	102
10.1. Introduction	102
10.2. Overview of air dispersion modelling	102
10.2.1. The transport equation	102
10.2.2. Turbulence parameterization	104
10.2.3. Chemical reactions and radioactive decay	109
10.3. Gaussian dispersion models	110
10.3.1. Theory and limitations of Gaussian models	110
10.3.2. History of development	111
10.3.3. Advanced Gaussian models	112
10.4. Lagrangian models	112
10.4.1. Calculation of trajectories	113
10.4.2. Puff models	113
10.4.3. Trajectory models	115
10.5. Eulerian models	119
10.5.1. Solving atmospheric transport equations	119
10.5.2. Operator splitting	120
10.6. Computational Fluid Dynamics models	122
11. Air pollution modelling	127
11.1. Adaptive gridding	127
11.1.1. Introduction	127
11.1.2. Adaptive gridding for simulating photochemical air pollution	128
11.1.3. Adaptive gridding for simulating accidental release	135
11.2. Parallelization	144
11.2.1. Introduction	144
11.2.2. Supercomputers, clusters, and Grids	144
11.2.3. GPU – Graphical Processing Unit	145

12. Deposition of air pollutants	153
12.1. Dry deposition of trace gases	154
12.1.1. Field measurements	154
12.1.2. Deposition/exchange models	155
12.1.3. Some results	157
12.2. Dry deposition of aerosol particles	161
12.2.1. Field measurements	161
12.2.2. Modelling the dry deposition of particles	161
12.3. Modelling of wet deposition	162
12.3.1. Wet deposition in Europe	163
13. Environmental effects of air pollution	165
13.1. The role of each pollutant	165
13.1.1. Carbon monoxide (CO)	167
13.1.2. Sulphur dioxide (SO ₂)	167
13.1.3. Nitrogen dioxide (NO ₂)	168
13.1.4. Ozone (O ₃)	169
13.1.5. Particulate matter	170
13.2. Some effects on the environment	171
13.2.1. Smog	171
13.2.2. Acid rain	171
13.3.3. Crop and forest damage by ozone	172
14. The role of air pollution in the global climate change	175
14.1. Effects of atmospheric composition on the radiation budget	175
14.2. Anthropogenic perturbation of the greenhouse gases	176
14.3. Radiative forcing of atmospheric components	178
14.4. Future scenarios	180
14.4.1. SRES scenarios	180
14.4.2. Representative Concentration Pathways (RCPs)	183
15. Monitoring of Air Pollution	187
15.1. Measurement locations	187
15.1.1. Classification of measurement sites	187
15.1.2. Measurement network in Europe and Hungary	189
15.2. Measurement techniques	191
15.2.1. Sampling methods	191
15.2.2. Measurement of gas concentrations	192
15.2.3. Measurement of aerosol concentrations	194
15.2.4. Remote sensing	195
15.2.5. Rainwater analysis	198
15.3. Conclusion	198
16. Questions:	200

Preface

Atmospheric chemistry is a multidisciplinary research field with respect to emissions, interactions and physical and chemical transformation of chemical compounds in the atmosphere. It also investigates the key physical processes occurring in the atmosphere. This eBook provides a comprehensive review of this topic showing recent advances in this field e.g., parallelization of mathematical models with CUDA, effect of air pollutants on global climate change. The authors of this book hope that material presented will be useful and essential for bachelor and master students as well as graduate students, and they can use it as a basic source for their studies.

Chapter 1. The structure and composition of the atmosphere

The total mass of the atmosphere is approximately $5.3 \cdot 10^{18}$ kg, against the $1.4 \cdot 10^{21}$ kg mass of the hydrosphere (oceans, seas, lakes, rivers, groundwater, snow and ice) and $5.98 \cdot 10^{24}$ kg mass of the Earth. The upper border of the atmosphere is not a well-defined altitude. The atmospheric material steadily decreases with height, until it gradually reaches interplanetary space. The atmosphere is an envelope of gases and particles surrounding the Earth. This amount of materials remains around our planet during the rotation around its axis and orbit around the Sun.

The relatively dense area of the Earth's atmosphere is an extremely thin layer compared to the whole atmosphere. Half of the atmosphere's mass can be found below 5.5 km and around 99% of the air is located in the lower 30 km's layer. The whole atmosphere actually the same as the range of the magnetosphere (Figure 1.1), which is the result of the interaction between Earth's natural magnetic field and solar wind¹.

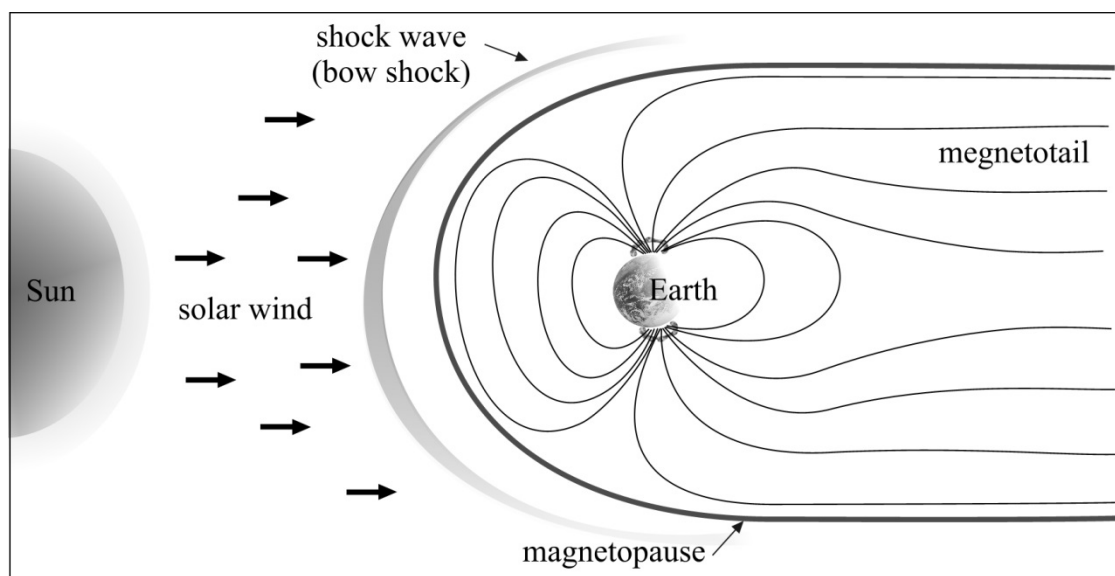


Figure 1.1: The magnetosphere around the Earth is formed by the interaction between Earth's natural magnetic field and solar wind

1.1. Formation of the Earth atmosphere

The Earth formed about 4.5 billion years ago, as hot molten rock. It's first atmosphere probably contained hydrogen and helium and some simple compounds of hydrogen, like ammonia (NH_3) or methane (CH_4). This first atmosphere of the Earth could be similar to the atmosphere of Jupiter and Saturn today. Because our planet didn't have a magnetic field to protect it yet, the intense solar wind from the Sun blew this early atmosphere away. In essence, the Earth lost its early atmosphere. Meanwhile, as the Earth cooled enough, a solid crust with several active volcanoes was developed about 4.4 billion years ago. By the strong volcanic activity, gases from the hot interior of our planet reached the surface. These gases – basically water vapour, carbon dioxide and ammonia – created the secondary atmosphere of the Earth. The atmospheres of Mars and Venus today – which contain mainly carbon-dioxide – are similar to this early atmosphere of the Earth.

Over hundred millions of years the atmosphere cooled down gradually, therefore most of water vapour condensed and formed the clouds. Precipitation from these clouds created the oceans. Simultaneously, most of atmospheric carbon-dioxide was absorbed by the oceans. At the same time, light from the Sun broke down the ammonia molecules releasing the chemically inactive nitrogen into the atmosphere (Figure 1.2).

¹ Solar wind: a stream of charged particles (electrons and protons) ejected from the upper atmosphere of the Sun.

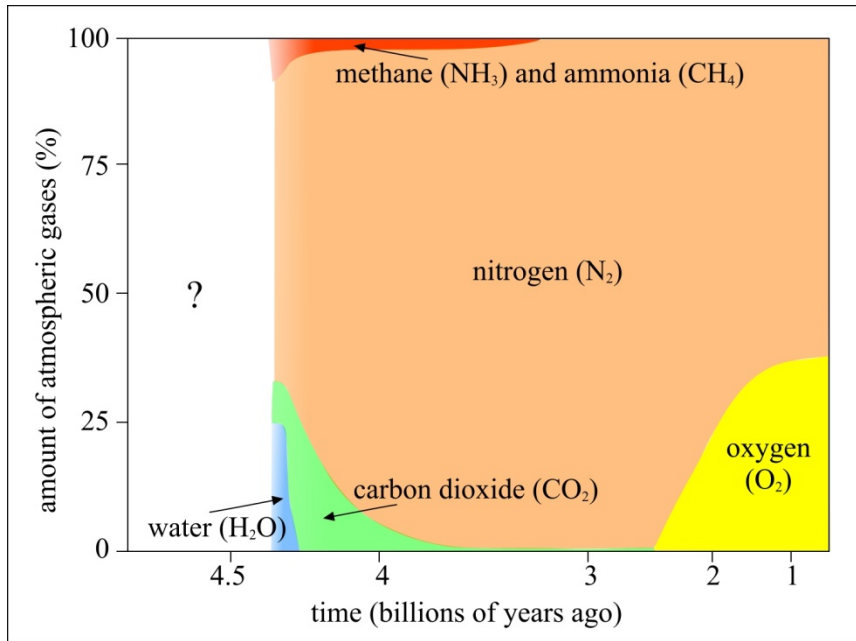
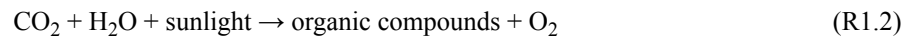


Figure 1.2: Probable composition of the atmosphere during the history of the Earth

Based on some theory, the oxygen was first produced in the atmosphere by photochemical dissociation of water vapour by intense ultraviolet radiation:



However this amount was negligible and free oxygen was probably produced as a by-product of photosynthesis² by tiny organisms known as cyanobacteria (or blue-green algae) from around 2.500 millions years ago. Photosynthesis uses carbon dioxide, water, and light energy releasing organic compounds (carbohydrates) and oxygen:



Initially, the small amount of atmospheric oxygen consumed for oxidation of rocks at the surface (weathering process). Complete oxidation of the surface rocks, oxygen levels in the atmosphere began to grow more intensively. As the atmospheric oxygen reached 1–2% of present oxygen level, ozone (O₃) could form to shield Earth's surface from intense ultraviolet radiation:



and



At this time, primitive plants formed which facilitated the photosynthesis process. Land plants developed a few million (based on new studies around 700 million) years ago and would have removed carbon dioxide (from around 1–5% down to 0.04%) at the same time steadily increased the amount of oxygen in the atmosphere. Oxygen levels fluctuated in the last few million years during various time periods regulated by climate, volcanism and plate tectonics (Holland, 2006). Finally, the atmospheric oxygen level stabilized at around 21% (Figure 1.3).

² Photosynthesis: during this process, plants and other organisms convert light energy from the Sun to chemical energy. Photosynthesis requires sunlight, carbon-dioxide and water. In plants, photosynthesis occurs mainly within the leaves.

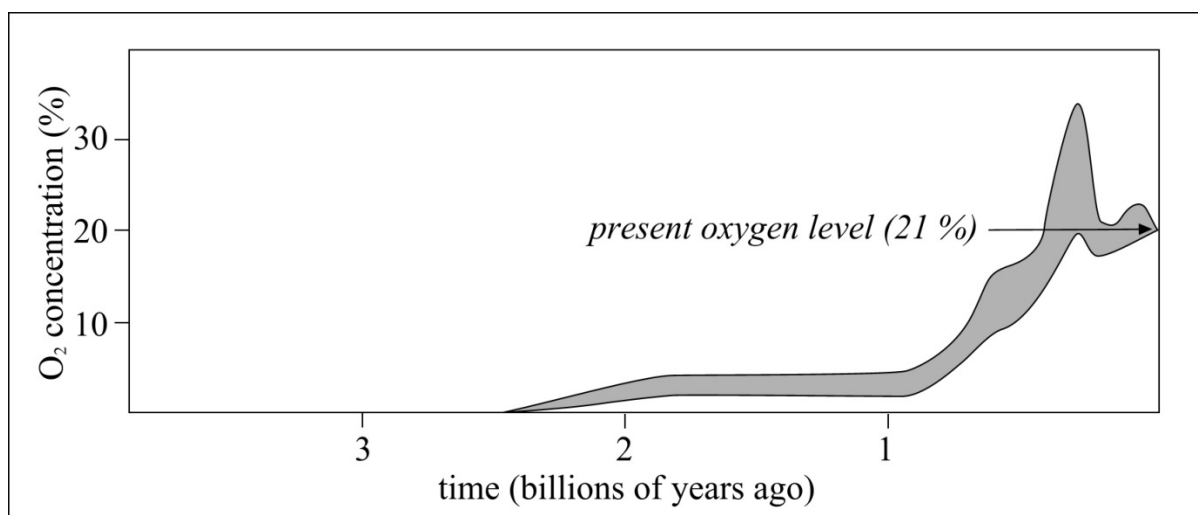


Figure 1.3: The probable variation of oxygen level in the atmosphere during the history of the Earth

1.2. A short history of the atmospheric chemistry

Greek philosopher, Anaximenes (585–528 BC) declared that air was the primary substance and the source of all other things. Later, Empedocles (ca. 490–430 BC) described the air as one of the four elements (see e.g. May, 2010). This conception was accepted until 18th century. At this time, a question was arisen: whether air is a compound, or a mixture of individual gases. First scientific studies about atmospheric composition were published in the 1700s. Chemical compounds in the atmosphere were discovered one after the other (Table 1.1) to confirm that air is a mixture of gases (see e.g. Anfossi and Sandroni, 1993).

Table 1.1: Important discoveries of atmospheric elements

Date	Compound	Explorer(s)
1750s	carbon dioxide	Joseph Black
1766	hydrogen	Henry Cavendish
1772	nitrogen	Daniel Rutherford
1774	oxygen	Joseph Priestley and
1772 (published in 1777)		Carl Wilhelm Scheele
1840	ozone	Christian Friedrich Schönbein
1894	argon	Lord Rayleigh and William Ramsay

Table 1.2: Some important milestones of atmospheric chemistry in the 20th century

Date	Explorer(s)	Discovery
1924	Gordon Dobson	developed a spectrophotometer and started the regular measurements of total-column ozone
1930	Sydney Chapman	described theory that explains existence of ozone „layer“
1960	Arie Jan Haagen-Smit	described the emergence of the photochemical smog
1973	James Lovelock	first detected CFC's (Chlorofluorocarbons) in the atmosphere

1995	Paul Crutzen, Mario Molina and Frank Sherwood Rowland	the Nobel Prize in Chemistry was awarded jointly "for their work in atmospheric chemistry, particularly concerning the formation and decomposition of ozone".
------	-------------------------------------------------------------	---------------------------------------------------------------------------------------------------------------------------------------------------------------

After the clarification of fundamental composition of the atmosphere till the late 19th century, the attention was focused on the atmospheric trace gases with very small concentrations. In the 20th century new research directions were appeared, namely the analysis of temporal variation of trace gas concentrations and investigations of chemical reactions in the atmosphere (Table 1.2).

Today, major challenges of atmospheric chemistry are to describe the relationships and feedbacks between chemistry and climate, as well as the exchange processes between the surface and the atmosphere.

1.3. Atmospheric composition

Earth's atmosphere contains mainly several different gases and additionally aerosol particles. Atmospheric gases are generally classified by their amount and residence time. The residence time (or removal time or lifetime) is an average amount of time that a particle or substance spends in a particular system (as the atmosphere). The residence time can be defined as the amount of the compound in the atmosphere divided by the rate at which this compound removed from the atmosphere. Based on the quantity, major components and trace gases, while according to residence time, constant and variable (and sometimes highly variable) gases can be distinguished (Table 1.3).

The amount of atmospheric gases can be expressed by different measures. Generally used terms are the concentration (kg m^{-3}), the volume ratio (m^3 gas per m^3 air) and mole fraction (mol mol^{-1}). For trace gases, this mixing ratio are commonly given in units of parts per million volume (ppmv or simply ppm), parts per billion volume (ppbv or ppb), or parts per trillion volume (pptv or ppt); $1 \text{ ppmv} = 10^{-6} \text{ mol mol}^{-1}$, $1 \text{ ppbv} = 10^{-9} \text{ mol mol}^{-1}$ and $1 \text{ pptv} = 10^{-12} \text{ mol mol}^{-1}$.

The abundances of constant gases has remained the same over geological timescales, while residence time generally means years in case of variable gases and days in case of highly variable gases (Table 1.4).

The main constituents of the dry atmosphere are nitrogen (78.084% by volume), oxygen (20.946% by volume) and argon (0.934% by volume), but much lower concentrations other noble gases can also be found (Table 1.4). Concentrations of these gases do not vary substantially in time and space (in the lower 80 km layer of the atmosphere) and therefore they are called permanent gases.

Table 1.3: Classification of atmospheric gases

Amount	Main components	Trace gases
Residence time		
Constant gases	nitrogen, oxygen and argon (major components of the atmosphere)	other noble gases
Variable gases	carbon dioxide	other long-lived tracers
Highly variable gases	water vapour	other short-lived tracers

Table 1.4: Composition of the Earth's atmosphere

Chemical species		Concentration	Residence time	Sources					
Name	Formula			Biogenic	Anthropogenic	Photochemical	Volcanic	Radiogenic	Other
Nitrogen	N ₂	78.084%	1.6×10 ⁷ years	✓			✓		
Oxygen	O ₂	20.946%	3×10 ³ –10 ⁴ years	✓					
Argon	Ar	0.934%						✓	
Water vapour*	H ₂ O	0–4% (0–40 000 ppm)	10 days	✓	✓		✓		(1)
Carbon dioxide	CO ₂	3.94×10 ⁻² % (394 ppm)	20–150 years	✓	✓		✓		
Neon	Ne	1.818×10 ⁻³ % (18.18 ppm)					✓?		
Helium	He	5.24×10 ⁻⁴ % (5.24 ppm)	10 ⁷ years					✓	
Methane	CH ₄	1.79×10 ⁻⁴ % (1.79 ppm)	10 years	✓	✓				
Krypton	Kr	1.14×10 ⁻⁴ % (1.14 ppm)						✓	
Hydrogen	H ₂	5.3×10 ⁻⁵ % (0.53 ppm)	2 years	✓	✓				(2)
Nitrous oxide	N ₂ O	3.25×10 ⁻⁵ % (0.325 ppm)	150 years	✓	✓				
Carbon-monoxide	CO	5–25×10 ⁻⁶ % (0.05–0.25 ppm)	0.2–0.5 year	✓	✓				
Xenon	Xe	8.7×10 ⁻⁶ % (0.087 ppm)							
Ozone	O ₃	1–5×10 ⁻⁶ % (0.01–0.05 ppm)	weeks - months			✓			
Nitrogen-dioxide	NO ₂	0.1–5×10 ⁻⁷ % (0.001–0.05 ppm)	8–10 days	✓	✓	✓			
Ammonia	NH ₃	0.01–1×10 ⁻⁷ % (0.0001–0.01 ppm)	~5 days	✓	✓				
Sulphur-dioxide	SO ₂	0.003–3×10 ⁻⁷ % (0.03–30×10 ⁻³ ppm)	~2 days		✓	✓	✓		
Hydrogen-sulphide	H ₂ S	0.01–6×10 ⁻⁶ % (0.01–0.6×10 ⁻³ ppm)	~0.5 day	✓	✓		✓		



constant gases



variable gases



highly variable gases

* Concentration of water vapour is not included in dry atmosphere; (1) evaporation and transpiration; (2) oxidation of methane and non-methane hydrocarbons

Nitrogen (N₂) is a relatively inert gas³ and fundamental to all living systems. Through the nitrogen cycle nitrogen is removed from the atmosphere and becomes part of living organisms. This process is realized by nitrogen fixation⁴ by soil bacteria, and by way of lightning through precipitation. Nitrogen returns to the atmosphere mainly by biomass combustion and denitrification⁵.

As nitrogen, oxygen (O₂) has also very important relations with life. Oxygen exchange between the atmosphere and biosphere is realized by photosynthesis and respiration⁶.

Argon (Ar) in the atmosphere is the third most abundant gas. Among noble gases, argon was first detected in the atmosphere in 1894 by Lord Rayleigh and William Ramsay. Almost 100% of atmospheric argon is the radiogenic ⁴⁰Ar isotope derived from decay in ⁴⁰K (potassium) in the Earth's crust.

Water vapour (H₂O) is a significant component of the atmosphere. Its concentration varies over a wide range both spatially and temporally. Most of water vapour concentrated in the lower atmosphere (about 90% of total atmospheric water vapour is found in the lower 5 km atmospheric layer, and more than 99% of it can be found in the troposphere⁷). The capacity of air to hold water vapour (called saturation level) is a function only of the air temper-

³ Inert gas: Unreactive gas, which does not react with other chemicals to form new compounds under a set of given conditions. Inert gases are noble gases and relatively inert gas for example the nitrogen.

⁴ Nitrogen fixation: a process by which atmospheric nitrogen is reduced to form ammonia.

⁵ Denitrification: Reduction of nitrates to gaseous nitrogen by microorganisms in a series of biochemical reactions.

⁶ Respiration: an oxidative process by which the chemical energy of organic molecules is released in a series of metabolic steps involving the consumption of oxygen and the release of carbon dioxide and water.

⁷ Troposphere: a layer of the atmosphere from the surface to about 7–20 km (depending on latitude). In this layer temperature decreases with increasing altitude in the function of the distance from warming surface.

ature. The higher the temperature the greater amount of water vapour can be held without condensation (Figure 1.4).

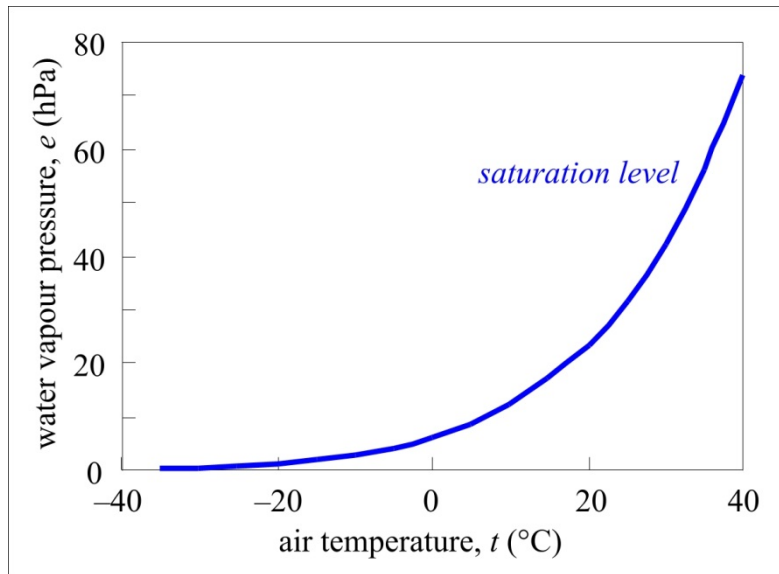
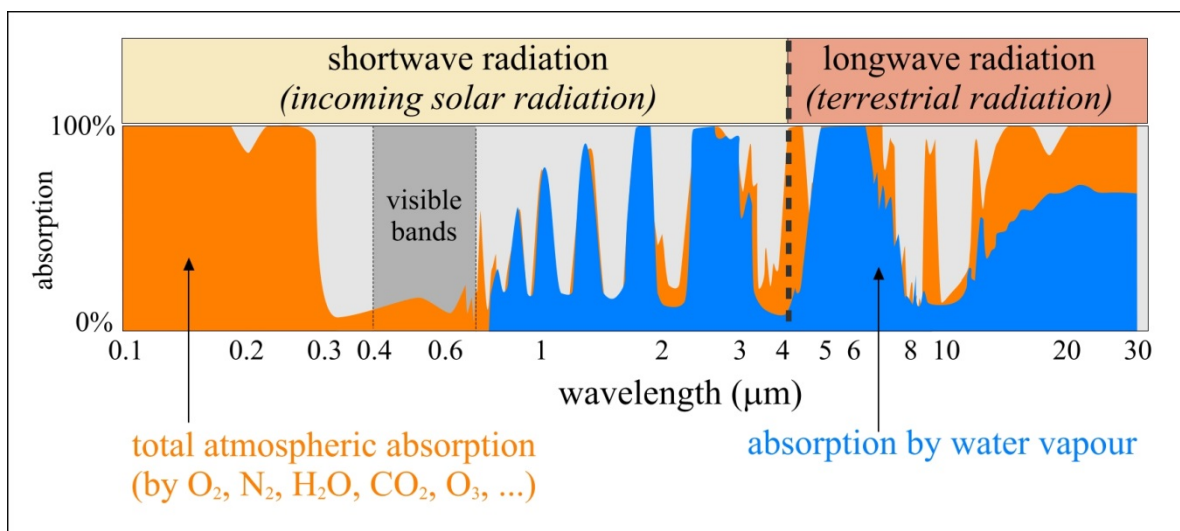


Figure 1.4: Dependence of saturated water vapour pressure from air temperature. The higher the temperature, the greater water vapour can be held by the air.

The highest atmospheric moisture content is observable over equatorial ocean area and tropical rain forests, while the lowest water vapour concentrations can be measured over cold, polar regions, and subtropical deserts. Atmospheric water vapour has several significant direct and indirect effects on both weather and climate. It plays important roles in the radiation and the energy budgets of the atmosphere, and also in the formations of clouds and precipitations. About 70% of total absorption of the incoming shortwave solar radiation, particularly in the infrared region, and about 60% of total absorption of long-wave radiation by the Earth are realized by water vapour (Figure 1.5) thereby it is the most significant greenhouse gas⁸. Water vapour also influences heat energy transfer on the surface-atmosphere system through the latent heat flux. The latent heat flux is a component of surface energy budget. It plays an important role in the heat transfer from Earth's surface into the atmosphere. During this process heat from evaporation and transpiration of water at the surface is transferred to the troposphere by water vapour and it is released there by condensation. Latent heat of evaporation of water at the surface is released to the atmosphere when condensation occurs. Due to the condensation, cloud, fog and precipitation can be produced.



⁸ Greenhouse gas (GHG): gases in the atmosphere, which cause greenhouse effect. Most abundant greenhouse gases are water vapour (H₂O), carbon-dioxide (CO₂), methane (CH₄), nitrous-oxide (N₂O), tropospheric ozone (O₃) and chlorofluorocarbons (CFCs).

Figure 1.5: Absorption of solar and terrestrial radiation by all atmospheric components and by water vapour. Water vapour has significant absorption bands both in shortwave (incoming solar radiation) and longwave (outgoing terrestrial radiation) spectra.

Carbon dioxide (CO₂) is an important greenhouse gas as it has a strong absorption capacity in the infrared and near-infrared bands. It has a natural exchange between the atmosphere and biosphere through the photosynthesis and respiration. A part of atmospheric CO₂ is dissolved by the seas and oceans. Atmospheric concentration of carbon-dioxide has increased steadily worldwide by over 35% since the beginning of 1800's. Before the Industrial Era, atmospheric carbon dioxide concentration was 280 ± 10 ppm for several thousand years. The present atmospheric CO₂ concentration has not been exceeded during the past 420,000 years, and likely not during the past 20 million years. The rate of increase over the past century is unprecedented, at least during the past 20,000 years (IPCC, 2001). The increase has speeded up in the last few decades. In the beginning of the measurements of background concentration⁹ of CO₂ on Mauna Loa observatory in 1958, CO₂ level was less than 320 ppm, while in 2010 it has reached and exceeds 390 ppm (Figure 1.6). This rapid growth is primarily due to growing anthropogenic activities, like burning of fossil fuels, deforestation, and other forms of land-use change. This man-made increase of atmospheric concentration of carbon-dioxide has definitely contributed to global warming over the last decades with the increase of greenhouse effect. Carbon-dioxide concentration shows characteristic seasonal cycle, which is related mainly to Northern Hemisphere growing season.

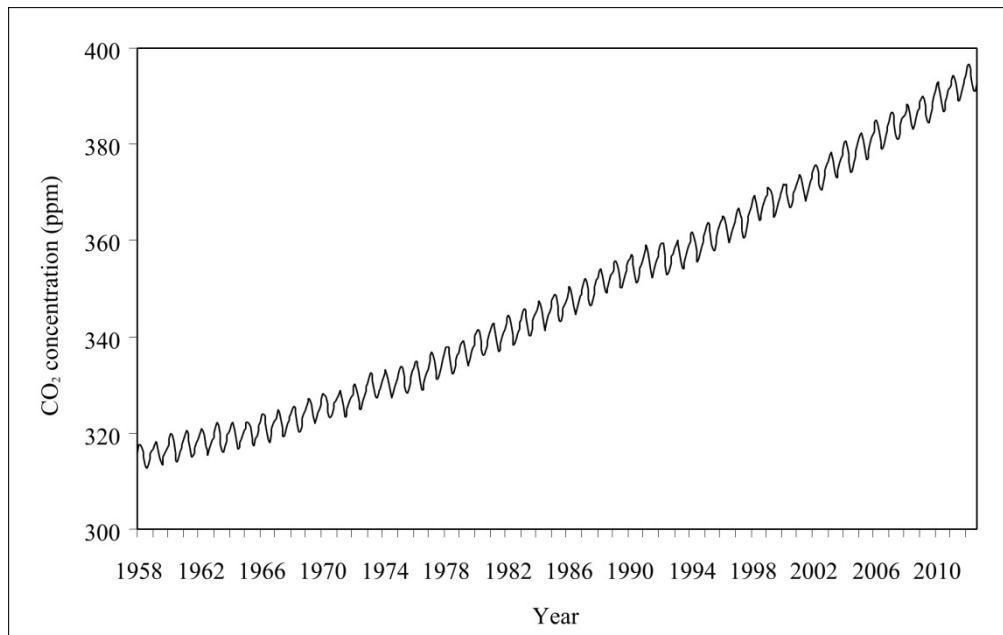


Figure 1.6: Monthly mean background concentration of atmospheric carbon dioxide (CO₂) from 1958 to 2012, measured at the Mauna Loa Observatory. Source of data: <http://www.esrl.noaa.gov/gmd/ccgg/trends/>

The volume of other gases compared to the main components, are very low, and therefore they are called trace gases. Despite their low concentrations, these tracers (e.g. ozone both in troposphere and stratosphere, carbon, nitrogen, sulphur compounds etc.) can be of critical importance for several environmental issues (for example: greenhouse effect¹⁰, atmospheric pollution etc.).

Next to the different gases, Earth's atmosphere contains a huge number of aerosol particles. Aerosols are generally defined as suspension of solid particles or liquid droplets in a gas. Their size are very small, the particle diameters in the range of 10⁻⁹–10⁻⁴ m. Aerosol particles originate in large part from different natural sources, and in lesser extent, from anthropogenic sources. Main emission sources of primary particles – which are emitted directly to

⁹ Background concentration (or baseline concentration): a concentration of a gives species that are normally found in the atmosphere without consideration of local sources. Background concentration measurements are performed away from emission sources.

¹⁰ Greenhouse effect: a natural process in the atmosphere, by which a part of long wave radiation from Earth's surface is absorbed by atmospheric greenhouse gases, and is re-emitted in all directions, thereby heating the atmosphere. Due to this process, the Earth's atmosphere is more than 33 °C warmer than it would be without it. Human activities can modify this greenhouse effect, which is the most important factor in recent climate change.

the atmosphere – are soil and mineral dusts, sea salts, volcanic eruptions, biomass burning, biological materials (e.g. pollen, plant fragments, microorganisms), incomplete combustion of fossil fuels, industrial particulates and traffic. Secondary particles are formed when gas-to-particle conversion occurs by nucleation and condensation of gaseous precursors.

The concentration, size distribution and composition of atmospheric aerosol particles vary significantly with time and space. In the lower troposphere, the aerosol mass concentration varies in a range of 1–100 $\mu\text{g m}^{-3}$, and particle number is typically varies from 10^2 to 10^5 cm^{-3} (Pöschl, U., 2005). Most particles can be found over deserts and urban area, while polar atmosphere and alpine air contains fewer aerosols. Generally, aerosol concentration decreases with altitude.

Atmospheric aerosols have significant effects on different atmospheric processes, climate and human health. Aerosol particles modify the radiation balance of the Earth through scattering and absorbing incoming solar and terrestrial radiation. They are essential in the formation of clouds and precipitations, as they provide condensation nuclei. They have influence on oxidation processes, and affect the cycles of nitrogen, sulphur and atmospheric oxidants (see more information about aerosol particles in Chapter 9).

1.4. Vertical structure of the atmosphere

1.4.1. Vertical change of composition

According to the homogeneity of atmospheric composition, two layers can be defined in the atmosphere. The lower layer, up to an altitude of about 80 km above sea level is the homosphere, where due to the continuous turbulent mixing the composition of the atmosphere is relatively constant for chemical species which have long mean residence times. This region is closed by a thin transition layer, called turbopause. Above the turbopause, in the heterosphere, the molecular diffusion dominates and the chemical composition of the atmosphere becomes stratified and varies according to the molecular mass of chemical species (Figure 1.7). The lower heterosphere are dominated by nitrogen and oxygen molecules and the lighter gases being concentrated in the higher layers. Up to 1,000 km the oxygen atoms and above this height the helium and hydrogen are the dominant species.

In the upper part of the atmosphere – from about 60 km to 2000 km above the Earth's surface – ionic species or free radicals (O^+ , O_2^+ , NO^+ , N_2^+ , free electrons) can also be found, and high number of ionized particles affect the propagation of radio waves. This region of the atmosphere is called ionosphere. There are three important layers in the lower part of the ionosphere (at altitudes between about 60 km and 600 km), where the absorption of solar extreme ultraviolet radiation and x-rays ionize the neutral atmosphere. These are the D (60–90 km), E (90–150 km) and F regions (150–500 km) with F1 and F2 sub-layers. The ion density of each layer depends on the solar activity and time of day (Figure 1.8).

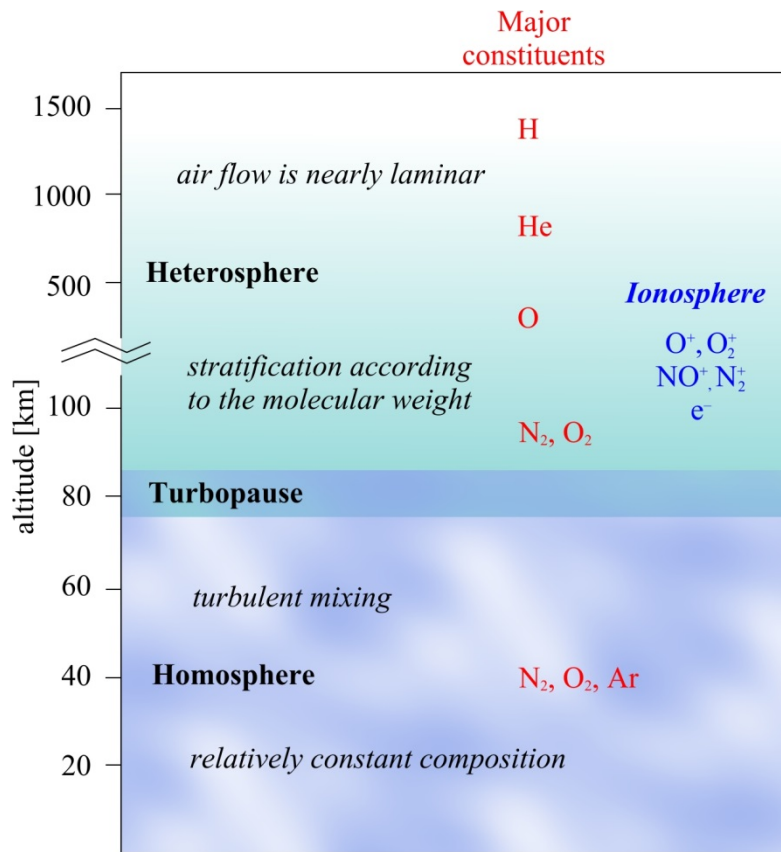


Figure 1.7: Vertical structure of the atmosphere according to chemical composition

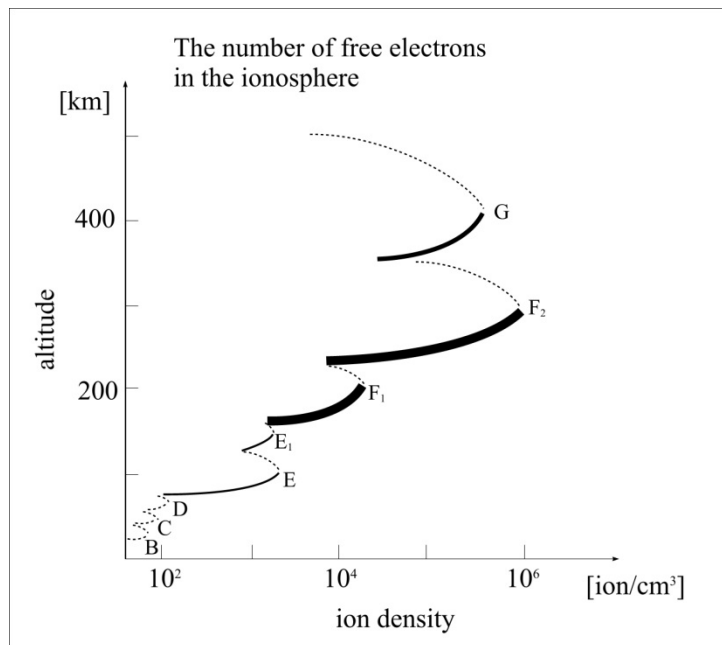


Figure 1.8: The layers of the ionosphere

1.4.2. Vertical temperature changes

Based on the variation of temperature with height, the atmosphere can be divided to different layers (Figure 1.9).

Troposphere:

The lowest major atmospheric layer is the *troposphere*, extending from the Earth's surface to the tropopause (Figure 1.9). The thickness of the troposphere varies with latitude: it is about 7 km in polar region, generally 11–12 km in the mid-latitudes and even 18 km over the Equator. The height of the tropopause is also depends on season, weather condition and time of day.

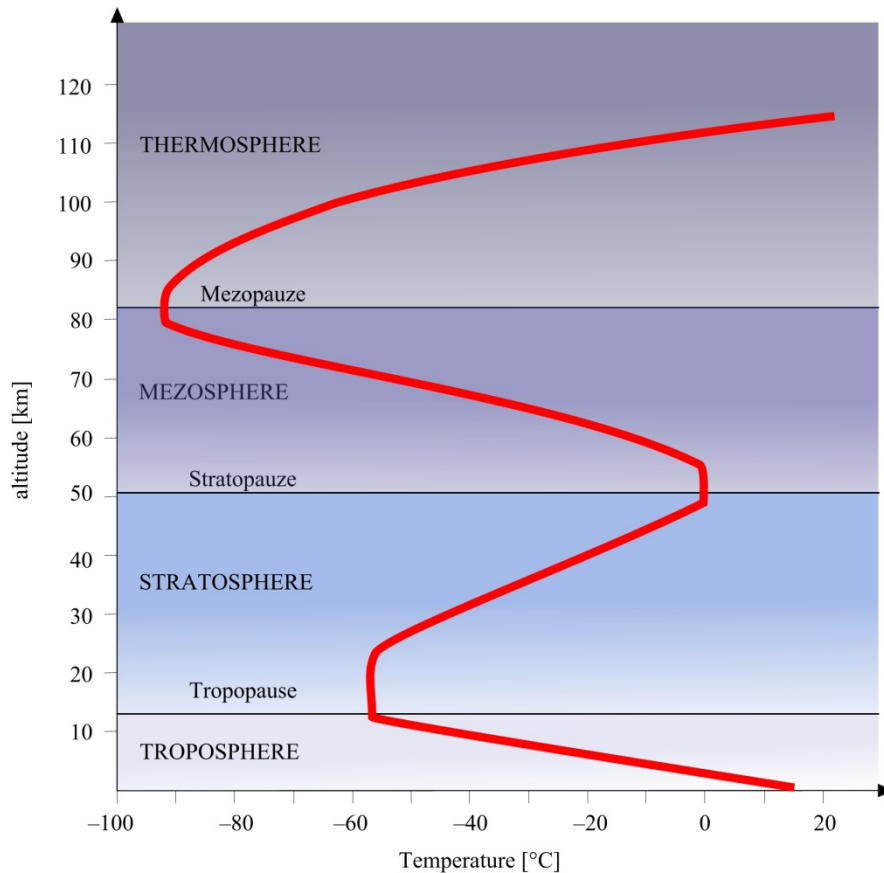


Figure 1.9: The vertical structure of the atmosphere according to the vertical temperature changes

Troposphere contains about 80% of total mass of the atmosphere, nearly all water vapour and dust particles can be found here. Almost all weather phenomena and cloud formation take place in this layer. The troposphere is heated from below by the Earth's surface. Incoming solar radiation first warms the surface, which radiates heat into the atmosphere. The warmer air in the near surface layer generates turbulent vertical motions, which transfer water vapour and other tracers to higher altitudes.

Temperature decreases with increasing height in the troposphere to away from the warming surface. The changing rate of temperature with height is called "lapse rate"¹¹. Tropospheric air temperature is generally proportional with distance from surface and lapse rate is fairly uniform, it is about 6,5 °C / 1000 m, but this rate is affected by water vapour content. Temperature is generally lower than -50 °C at the top of the troposphere (in mid-latitude, temperature is -56.5 °C at 11 km based on ICAO standard atmosphere¹²).

However, in the lower troposphere, the atmospheric stratification can differ from normal, and temperature can increase with height in the function of time of day and weather condition. This situation is called inversion¹³, which generally occurs at night. When temperature remains the same with height, the stratification is isothermal. The atmospheric stratification and thereby the stability conditions play important role in dispersion of tracers.

¹¹ Lapse rate: a rate of change in temperature observed while moving upward through the Earth's atmosphere. The lapse rate is positive when temperature increasing with altitude, zero in case of isothermal stratification and negative when temperature decreasing with height.

¹² ICAO standard atmosphere: a hypothetical model atmosphere created by ICAO (International Civil Aviation Organization) to describe the vertical distribution of atmospheric temperature, pressure, and density.

¹³ Temperature inversion: an atmospheric condition, in which the temperature increases with increasing altitude.

The troposphere can be divided into two main parts. The lower part is the planetary boundary layer (PBL) or atmospheric boundary layer, extending upward from the surface to a height that ranges from about 100 to 3000 m in the function of season, weather condition and time of day. Above this layer, the free troposphere can be found.

Stratosphere:

At the tropopause, the decrease of temperature halts and to about 50 km above ground level, an inversion layer can be found, when temperature increases with height. This layer is the stratosphere. Temperature increase in the stratosphere (Figure 1.9) is due to the relatively high concentration of ozone. Ozone strongly absorbs uv radiation¹⁴ from the Sun in the bands between 210 and 290 nm (more information about ozone see Chapter 8). This absorption by the ozone is the primary cause of temperature increase in the stratosphere. Without ozone layer, a further decrease of temperature with increasing height would be observable in the stratosphere (Figure 1.10).

Stratosphere holds about 19% of total mass of the atmosphere, and it contains only a very small amount of water vapour. Due to the vertical stratification, stratosphere is a stable layer and the mixing is weak. Particles that reach the stratosphere from the troposphere (e.g. from a large volcanic eruption) can stay a long time (many years) in the stratosphere without removing from it. Polar stratospheric clouds¹⁵ (PSCs) can be observed in winter polar stratosphere between 15 and 25 km height. They form at only very low temperature (below $-78\text{ }^{\circ}\text{C}$). Different types of PSCs contain water, and different particles (e.g. nitric acids) or only water ice (see more information about polar stratospheric clouds in Chapter 8).

The stratosphere is bounded above by the stratopause at about 50 km height, where the average temperature is generally just below $0\text{ }^{\circ}\text{C}$.

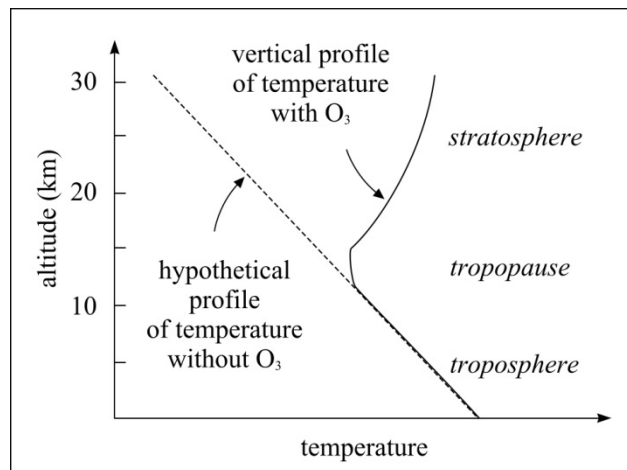


Figure 1.10: Real and hypothetical vertical profile of temperature with and without ozone in the stratosphere, respectively.

Mesosphere:

Over the stratopause, the next layer is the mesosphere from about 50 km to 85–100 km above the Earth’s surface (Figure 1.9). Air density is too low to absorb solar radiation, thus the mesosphere is warmed from below by the stratosphere and hence the temperature decreases with increasing height. However the atmosphere is still thick enough to slow down meteoroids enter to the atmosphere. The upper boundary of mesosphere is the mesopause, which is the coldest region of Earth’s atmosphere, where the temperature is around $-100\text{ }^{\circ}\text{C}$.

¹⁴ uv radiation: (ultraviolet radiation) a high energy part of electromagnetic spectrum emitted by the Sun. Wavelength of uv radiation varies between 100 and 400 nm: (UVC: 100–280 nm, UVB: 280–315 nm, UVA: 315–400 nm). Harmful UVC rays are blocked by atmospheric components, while both UVB and UVA rays are of major importance to human health.

¹⁵ Polar stratospheric clouds: stratospheric clouds between 15 and 25 km above Earth’s surface over polar region.

Within the mesosphere, noctilucent clouds¹⁶ can be appeared, when Sun is below the horizon and the lower layers of the atmosphere are in the Earth's shadow. These thin clouds are composed from tiny ice crystals, but their emergences, properties and relationships with global climate change are still not fully understood.

Upper atmospheric electrical discharges (like red sprites or blue jets) over tropospheric thunderstorms also occur in the mesosphere.

However, in the absence of frequent direct measurements (only by occasionally sounding rockets), mesosphere is a less known layer of the atmosphere.

Thermosphere:

In the thermosphere, over the mesopause, temperature rise continually with increasing height due to the direct absorption of high energy solar radiation by atmospheric gases. Temperatures are highly dependent on solar activity, and can rise well beyond to 1000 °C. However, this value is not comparable to those of the lower part of the atmosphere, as the air density is extremely low in this layer.

Considering the composition, this layer is a part of the heterosphere, where the atmospheric compounds stratified by their molecular mass. Major layers of the ionosphere (see above) are situated in the thermosphere. Auroras, form by collisions of energetic charged particles with atoms, occur also in the thermosphere.

Over about 500–1000 km above the Earth's surface (depending on solar activity), the collisions between atmospheric constituent become negligible. This layer is often called as exosphere, which gradually merge into interplanetary space.

1.5. The planetary boundary layer

The lowest level of the atmosphere – the bottom layer of the troposphere – called planetary boundary layer (PBL) is directly and strongly influenced by the underlying surface (Stull, 1988). Within the PBL the convective air motions generate intense turbulent mixing. The upper boundary of PBL is a statically stable layer (temperature inversion). Interactions between the atmosphere and the surface take place in the PBL. Timescale of atmospheric response to surface forcing is an hour or less. Atmospheric variables (wind speed, temperature, water vapour content etc.) show great variability and fluctuation and the vertical mixing is strong.

The structure of PBL varies with season, weather condition and time of day. The depth of the PBL ranges from tens of meters in case of strongly stable stratification, to a few thousand meters in very unstable condition; it is lower at night and winter and higher in day-time and summer.

¹⁶ Noctilucent cloud: thin cloud in the mesosphere which are composed of tiny crystals of water ice. They can be observed at latitudes between 50° and 70°, when Sun is below the horizon.

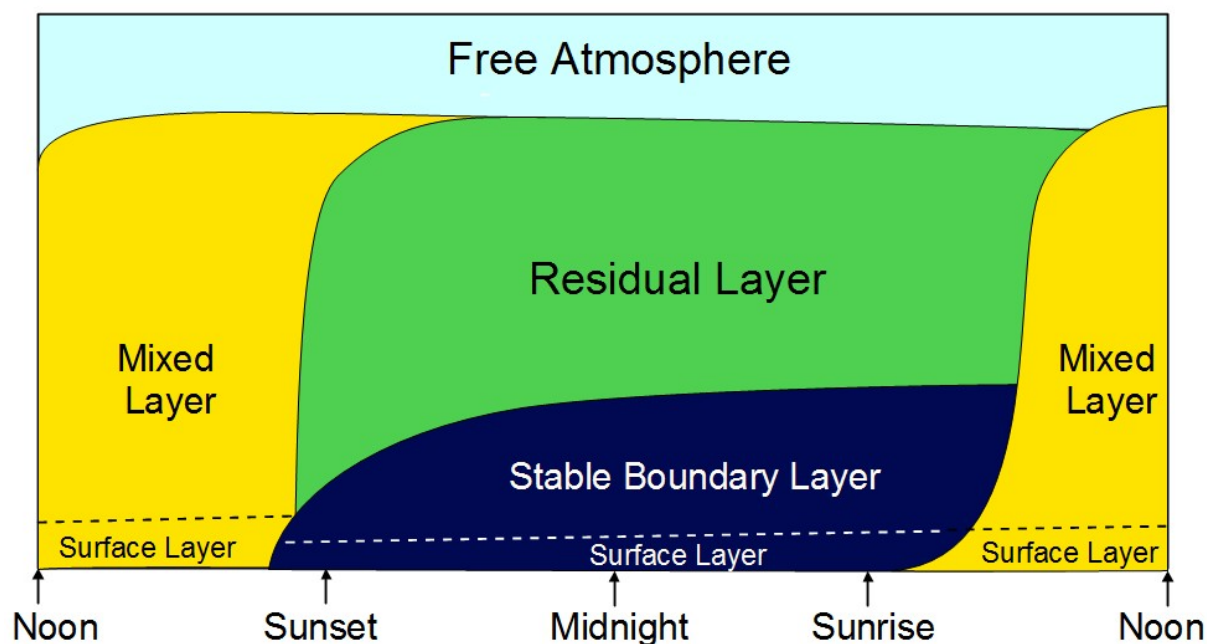


Figure 1.11: The structure of the planetary boundary layer

Daily variation of PBL shows a typical pattern during pleasant weather condition (Fig 1.11.) The lowest (about 10%) part of PBL is called surface layer. The thickness of this layer is typically 10–30 m at night, and 50–100 m in day-time. Exchange processes between the atmosphere and the surface (vegetation) are realized here by the turbulent fluxes¹⁷ of heat, momentum, water and air pollutants. After sunrise, a convective mixed layer growing rapidly due to the intensive turbulence. This layer is capped by a stable entrainment zone. Near sunset, the mixed layer collapses and in its place a nocturnal boundary layer is formed. The bottom part of this layer is stabilized by the night time radiative cooling of the surface. Above this stable zone a residual layer can be found.

Planetary boundary layer has great importance in dispersion, dilution and deposition of air pollutants.

References

- Anfossi D. and Sandroni S.. 1993. *Surface Ozone at Mid Latitudes in the Past Century In: Il Nuovo Cimento*. No. 17. Vo 2. 199-207.
- Holland H.D.. 2006. *The oxygenation of the atmosphere and oceans*. Phil. Trans. R. Soc. B.. Vo. 361. 903-915.
- IPCC, 2001: Climate Change 2001: The Scientific Basis. Contribution of Working Group I to the Third Assessment Report of the Intergovernmental Panel on Climate Change*. Houghton J.T., Ding Y., Griggs D.J., Noguer M., van der Linden P.J., Dai X., Maskell K., and Johnson C.A.. (eds.). Cambridge University Press, Cambridge, United Kingdom and New York, NY, USA. 881 pp. ISBN 0521 80767 0.
- May L.. 2010. *Atomism before Dalton. In: Atoms in chemistry: from Dalton's predecessors to complex atoms and beyond. Book Series: ACS Symposium Series*. Vo. 1044. 21-33.
- Pöschl U.. 2005. *Atmospheric Aerosols: Composition, Transformation, Climate and Health Effects In: Angewandte Chemie International Edition*. Vo. 44. 7520-7540.
- Stull R.B.. 1988. *An Introduction to Boundary Layer Meteorology (Atmospheric Sciences Library)*. Kluwer Academic Publishers, Dordrecht. 669 pp. ISBN 90-277-2768-6.

<http://www.esrl.noaa.gov/gmd/ccgg/trends/>.

¹⁷ Turbulent flux: transport of a quantity by quasi-random eddies. Turbulent fluxes play important role in the surface layer.

Chapter 2. Emission of air pollutants

Earth's atmosphere contains various gases and aerosol particles (see Chapter 1). Detailed description about the cycles of some important components can be found in other chapters (carbon compound: Chapter 5, nitrogen compounds: Chapter 6, sulphur compounds: Chapter 7, ozone: chapter 8, aerosol particles: Chapter 9). The atmospheric transport processes of air pollutants (Chapter 10), as well as chemical reactions (Chapter 4) and deposition processes (Chapter 12) are also described in detail hereinafter. This chapter present the main source types of air pollutants and their key features.

During air pollution, different gases, particulates or biological materials get to the atmosphere from various natural and anthropogenic sources and modify its natural composition. Emissions influenced by weather conditions, a number of physical and chemical properties and, in case of anthropogenic sources also by technological parameters. The emitted amounts vary with respect to the location and time. Pollutants emitted to the atmosphere can be transported from emission sources to even a long distance (transmission) in the function of their properties and weather conditions. In the atmosphere, complex chemical reaction processes can be realized which can produce secondary air pollutants. After these processes, air pollutants can be removed from the atmosphere by chemical reactions, dry or wet deposition (Figure 2.1).

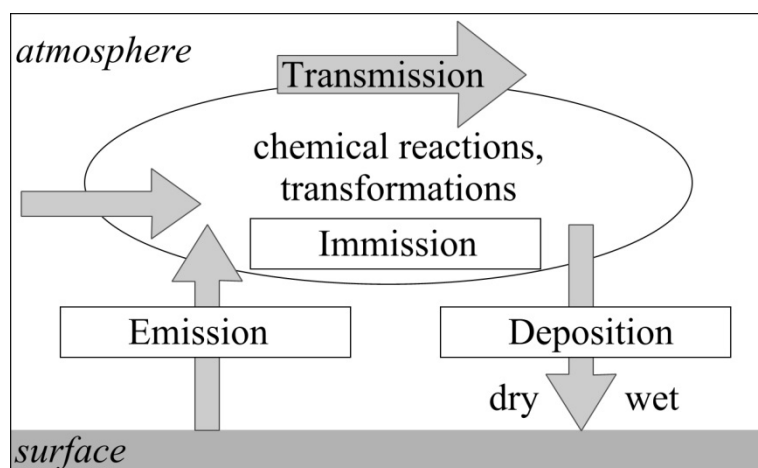


Figure 2.1: A schematic picture about life cycle of air pollutants

Atmospheric air pollutants have several effects on the environment in the atmosphere and after they remove into the different surfaces. The chemical composition of the atmosphere can influence both the weather condition and the climate (e.g. cloud formation, visibility, radiation budget). Various air pollutants emitted into the atmosphere by both natural and human activities are the cause of many current and potential environmental problems, such as acidification, air quality degradation (Figure 2.2), global warming/climate change, stratospheric ozone depletion, harmful effects on vegetation, soils, ground water, aquatic ecosystems, human health and also on built environment (further information about the effects of air pollutants can be seen in Chapter 13 and Chapter 14).



Figure 2.2: Severe air pollution in an industrial area

2.1. Source types of air pollutants

There are many different types of sources of atmospheric emissions, for example industry, energy supply (power plants, refineries, incinerators, factories, fossil fuel extraction and production sites, etc.) transport, animals and humans, agricultural activities, natural and managed vegetations, soil etc (EEA Technical report, 2009).

Due to the high variability and complexity of emission sources, it is not possible to measure emissions from all the different source types. In practice, atmospheric emissions are generally estimate based on measurements made at selected or representative samples of the (main) sources and source types. These estimated emissions are collected into emission inventories. Emissions inventories may contain three main types of sources, namely point, area and line sources. However, in some cases the emission inventories refer to a specific area (e.g. to a country or a region).

Three main types of emission sources are the following:

Point source: a single, fixed point, from were air pollutants can be emitted into the atmosphere continuously or instantaneously (for example during an accidental release). Typical example for point source is a smokestack.

Area source: emission of air pollutants from a specific area (e.g. from a city, or from a forest fire). In emission inventories, area sources can refer to an administrative area, such as a country, or region, or for a regular grid, (e.g. 50 km × 50 km grid in EMEP emission inventories: <http://www.ceip.at/ceip/>, or other derived grid: see Figure 2.3).

Line source: generally refers to emissions from transport (vehicle emissions from road transport, railways, shipping or aviation) along a line of the road, railway-track, sea-lane etc.

The primary sources of atmospheric pollutants could be classified as natural or anthropogenic sources. During natural processes the atmosphere interacts continuously with other spheres (e.g. biosphere, lithosphere, hydrosphere), and these spheres can be both sources and sinks of atmospheric components. This quasi steady state is disrupted by human activities. Anthropogenic emissions are mainly related to energy and food supply of world population.

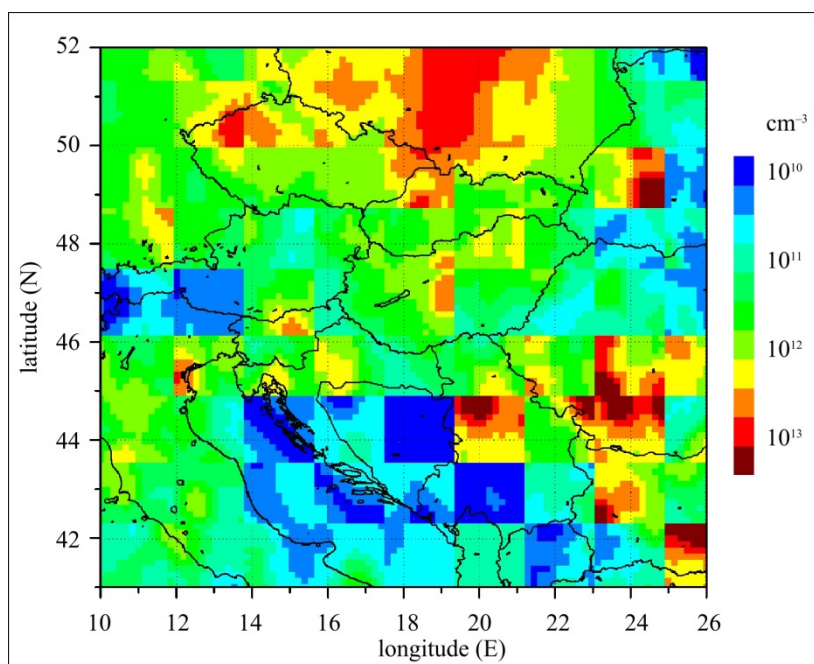


Figure 2.3.: An example of emission inventory: Derived sulphur dioxide emission field on a regular grid over Central Europe used in a dispersion model simulation. In some cases, emission data has large uncertainties. Source of data: <http://www.ceip.at/ceip/>

2.2. Natural emission sources

Natural emission sources are not influenced by human activities. A variety of air pollutants is generated during a range of processes taking place in terrestrial and aquatic ecosystems or in Earth's crust.

2.2.1. Terrestrial ecosystems

Various carbon and nitrogen species are emitted to the atmosphere during microbiological and plant physiological processes. Natural sources of carbon compounds, such as carbon dioxide (CO_2) and methane (CH_4) can be aerobic and anaerobic respiration. Nitrogen species such as nitrogen (N_2), nitrous oxide (N_2O) and nitric oxide (NO) are produced by biological oxidations and reductions of inorganic nitrogen in soils and waters. The most important factor controlling the rate of the nitrogen emission is the soil temperature.

The soil fluxes of N_2O in a Norway spruce forest in Mátra Mountain were determined by small static chambers. Accumulation of nitrous oxide was measured by a gas chromatography-mass spectrometry system. N_2O emission fluxes were calculated from the accumulation of nitrous oxide gas in the chamber (Figure 2.4).

Due to metabolic processes in forest trees, grasslands or scrublands several types of hydrocarbons are also emitted to the atmosphere.

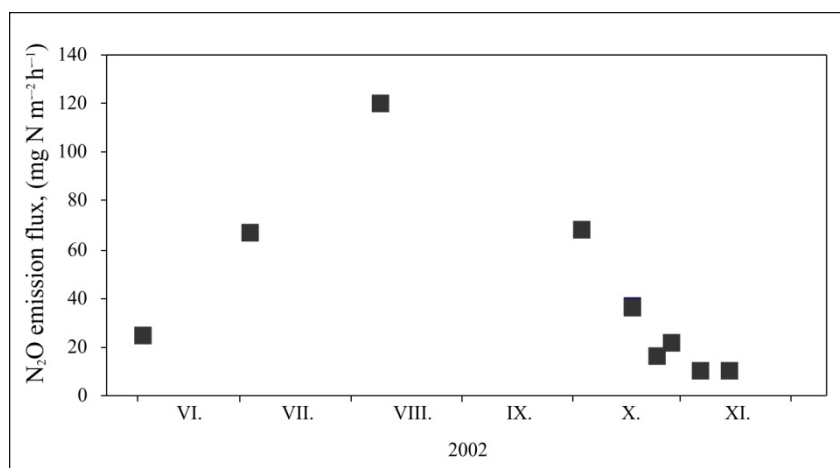


Figure 2.4: N₂O emission flux from forest soil measured by static chamber in 2002, in Mátra Mountain.

2.2.2 Aquatic Ecosystems

Several physical, chemical and biological processes occur at surface of wetlands and oceans, which influence the global cycles on a number of species, e.g. carbon, nitrogen, sulphur and trace metals. The most important emission process in wetlands and anaerobic waterlogged soils is the bacterial production of methane. Oceans play an important role in the global biochemical sulphur cycle. Dimethyl sulphide (DMS) is produced during biological activity of phytoplankton then enters the atmosphere by the exchange between sea and the atmosphere. Dimethyl sulphide is the major precursor of sulphate particles (SO₄²⁻). Large amount of water droplets and sea salts are emitted into the maritime atmosphere. After the evaporation of water aerosol particles, such as sodium chloride (NaCl), magnesium sulphate (MgSO₄) are formed. Various halogenated organic compounds are also emitted to the atmosphere from the oceans. Among them, methyl chloride (CH₃Cl) is the major natural source of atmospheric chlorine.

2.2.3 Forest fires

Almost all forest fires are human induced. Naturally occurring biomass burnings are usually the consequence of lightning. The major products of biomass burning are carbon dioxide (CO₂) and water vapour. However, a large number of particulates and trace gases are produced, including the products of incomplete combustion of CO, NMVOCs, nitrogen and sulphur species.

2.2.4 Volcanic and tectonic activities

Volcanoes release significant amount of gases and ash particles into the atmosphere. Volcanic emissions occur both during occasionally eruption and long term non-eruptive activities. Most prevailing volcanic gas is water vapour, which can reach 50–90% of total volcanic emission. However, this amount of water vapour is negligible in comparison to its atmospheric concentration. Other important gases emitted from volcanic activities are carbon dioxide (CO₂), sulphur dioxide (SO₂), hydrogen sulphur (H₂S) and some other sulphur species, hydrogen chloride (HCl) and other halogen compounds. Besides the gases, considerable emissions of aerosols are present in most volcanic plumes.

2.2.5 Lightning

Lightning during thunderstorm events creates plasma channels in the atmosphere characterized by the high fraction of ionic loads and high temperatures. High temperature cause chemical reactions. Major compounds of the atmosphere (nitrogen, oxygen, and water vapour) are undergoing chemical transformation and various species containing nitrogen, oxygen and hydrogen atoms are formed. A major species produced during lightning is nitric oxide (NO).

2.3 Anthropogenic emission sources

Anthropogenic emissions of air pollutants into the atmosphere depend on the population and various human activities to improve the quality of life. These activities are mainly related to supply of energy and food. Human-made emissions are very diverse. In the following, some major source types are presented.

2.3.1 Industrial energy production and use

Combustion processes are the major anthropogenic sources of air pollutants during the production and use of energy. Combustion process produces carbon dioxide (CO₂) and water (H₂O) as the main products. Additionally, combustion also produces several by-products, which originate either from incomplete fuel oxidation (e.g. CO, hydrocarbons, aerosol particles etc.) or from the oxidation of non-combustible species present in the combustion chamber (e.g. NO_x, SO_x etc.).

During combustion processes in energy and transformation industries, or in manufacturing industries, the emissions depend on the fuel and process activity. Relevant pollutants are generally CO₂, H₂O, SO₂, NO_x, CO, NMVOC, aerosol particles, heavy metals (HM), polycyclic aromatic hydrocarbons (PAH), polychlorinated dibenzo-dioxin and polychlorinated dibenzo-furans (PCDD/F) and, for some activities, polychlorinated biphenyls (PCB) and hexachlorobenzene (HCB).

Current anthropogenic emissions of CO₂ are primarily the result of the consumption of energy from fossil fuels (IPCC, 2001). About 20–33% of total anthropogenic sources of methane (CH₄) is also originated from combustion.

In the absence of flue gas desulphurisation (FGD) technology, the emissions of sulphur oxides (SO_x) are directly related to the sulphur content of the fuel. The sulphur content of refined natural gas is negligible. The majority of SO_x is sulphur dioxide (SO₂) although small proportions of sulphur trioxide (SO₃) can arise. For cement manufacture, some of the SO₂ (and other acid gases) is absorbed through contact with alkaline media in the cement kiln and, in the dry process, the raw meal.

The emission of NO_x is generally in the form of nitric oxide (NO) with a small proportion present as nitrogen dioxide (NO₂). Nitric acid manufacture includes catalytic combustion of ammonia to provide NO₂ for subsequent absorption. Emissions of nitrogen oxides arise from nitrogen in the fuel (mainly relevant to solid and liquid fuels) and from reaction of atmospheric nitrogen. Combustion control can provide a high degree of NO_x emission control (low NO_x burner technology) and this may be supplemented by use of selective catalytic reduction (SCR) or selective non-catalytic reduction techniques (SNCR).

Particulate matter (PM) emissions from large combustion plants (> 50 MW) burning solid fuels are often lower than emissions from smaller plants (per unit of energy input); the physical and chemical characteristics of the particulate matter also differ. This is because different combustion and abatement techniques are applied. Combustion of fuels can generate solid residues, which may be deposited within combustion chambers (furnace bottom ash) within the furnace, boiler surfaces or ducting (fly ash) or on heat exchanger surfaces (soot and fly ash). Coal and other fuels with significant ash content have the highest potential to emit particulate matter. Suspended ash material in exhaust gases may be retained by particulate abatement or other emission abatement equipment (abatement residues). Materials, which remain in the flue gases beyond the abatement equipment and pass to the atmosphere, are primary particles.

The emission of heavy metals (arsenic (As), cadmium (Cd), chromium (Cr), copper (Cu), mercury (Hg), nickel (Ni), lead (Pb), Selenium (Se), Zinc (Zn) and Vanadium (V)) during combustion processes strongly depends on their contents in the fuels and process feedstock. Most of the heavy metals considered are normally released as compounds (e.g. oxides, chlorides) in association with particulates. Only Hg and Se are at least partly present in the vapour phase. The content of heavy metals in coal is normally several orders of magnitude higher than in oil (except occasionally for Ni and V in heavy fuel oil) and in natural gas. For natural gas, only emissions of mercury are relevant. During the combustion of coal, particles undergo complex changes, which lead to vaporisation of volatile elements. The rate of volatilisation of heavy metal compounds depends on fuel characteristics (e.g. concentrations in coal, fraction of inorganic components, such as calcium) and on characteristics of technology (e.g. type of boiler, operation mode).

The emissions of dioxins and furans are highly dependent on the conditions under which combustion and subsequent treatment of exhaust gases is carried out. The sintering process in iron and steel manufacture has been identified as a significant source of dioxins.

The emissions of polycyclic aromatic hydrocarbons (PAH) results from incomplete (intermediate) conversion of fuels. Emissions of PAH depend on the combustion process, particularly on the temperature (too low temperature favourably increases their emission), the residence time in the reaction zone and the availability of oxygen.

Carbon monoxide is found in gas combustion products of all carbonaceous fuels, as an intermediate product of the combustion process and in particular for under-stoichiometric conditions. CO is the most important intermediate product of fuel conversion to CO₂; it is oxidized to CO₂ under appropriate temperature and oxygen availability. Thus, CO can be considered as a good indicator of the combustion quality. Substantial emissions of CO can occur if combustion conditions are poor.

Emissions of non-methane volatile organic compounds (NMVOC), e.g. olefins, ketones, aldehydes, result from incomplete combustion. Furthermore, unreacted fuel compounds such as ethane (C₂H₆) can be emitted. The relevance of NMVOC and CH₄ emissions from boilers, which are often reported together as VOC, is very low for large-sized combustion plants.

2.3.2. Transport

Transport is another major source of air pollutants. Terrestrial, naval and aerial transportation use a huge amount of energy and during the combustion processes, various components are emitted into the atmosphere. In order to comply with emission legislation, vehicle manufacturers have installed various after-treatment devices, such as catalytic converters and diesel particle filters (DPFs) to reduce pollutant emissions. However, such devices may, as a result of their action, also produce small quantities of pollutants such as NH₃ and N₂O.

During terrestrial transport, the most important pollutants emitted by road vehicles are ozone precursor compounds, (CO, NO_x, NMVOCs), greenhouse gases (CO₂, CH₄, N₂O), acidifying substances (NH₃, SO₂), aerosol particles, carcinogenic species, such as polycyclic aromatic hydrocarbons (PAHs) and persistent organic pollutants (POPs), heavy metals and other toxic substances (dioxins and furans).

The emissions produced by railways arise from combusting the fuel in an internal combustion engine. Consequently, the principal pollutants are those from diesel engines, i.e. similar to those used in road transport. These are principally CO₂, PM and NO_x, plus to a lesser extent CO and hydrocarbons, together with SO_x and heavy metals originating from the content of fuel in sulphur and metals, respectively.

The emissions produced by aviation come from the use of jet fuel (jet kerosene and jet gasoline) and aviation gasoline (used to fuel small piston engine aircraft only) that are used as fuel for the aircraft. Consequently, the principal pollutants are those common to other combustion activities, i.e. CO₂, CO, hydrocarbons and oxides of nitrogen, with SO₂ emissions being dependent of the level of sulphur in the fuel. Other important species (like PM, N₂O, CH₄) are emitted at relatively low concentrations. Air pollutants emitted by aircrafts can affects the atmospheric processes in the free troposphere and in the lower stratosphere too.

Water-borne navigation causes emissions of carbon dioxide (CO₂), methane (CH₄) and nitrous oxide (N₂O), as well as carbon monoxide (CO), non-methane volatile organic compounds (NMVOCs), sulphur dioxide (SO₂), particulate matter (PM) and oxides of nitrogen (NO_x).

2.3.3 Agriculture

Agricultural activities can also result human-made emission of air pollutants into the atmosphere. Main sources of emission from animal husbandry and manure management are livestock housing and holding areas, manure storage, field-applied manure and manure deposited during grazing. During these activities NH₃, NO and NMVOCs are emitted to the atmosphere. Additionally, livestock feeding is another source of particles.

Main sources of crop production and agricultural soils are fertiliser application (NH₃), soil microbial processes (NO) crop processes (NH₃ and NMVOCs) soil cultivation and crop harvesting (PM).

An additional, less important agricultural source of air pollutants is crop burning. During these processes ammonia (NH_3), nitrogen oxides (NO_x), non-methane volatile organic compounds (NMVOCs), sulphur dioxide (SO_2), carbon monoxide (CO), particulate matter (PM), heavy metals (HM) and dioxin are released to the atmosphere.

2.3.4 Waste management

Major emissions from waste disposal are emissions of greenhouse gases. Small quantities of NMVOCs, CO, NH_3 and NO_x may be released as well. Particulate matter (PM) emissions are also emitted from waste handling, but no emission factors are available.

2.3.5 Biomass burning

The relative contribution of (open and domestic) biomass burning emissions to the global annual emission for CO is ~ 25 %, for NO_x ~ 18 % and for non-methane volatile organic compounds (NMVOC) and CH_4 ~ 6 % (Intergovernmental Panel on Climate Change (IPCC), 2001). In Europe however, the contribution to total emissions is much lower, since the vast majority of fires occur in tropical regions.

2.3.6. Anthropogenic sources of air pollutants by different sectors

The air pollutants emissions vary greatly with time and space. The distribution among each sectors are also highly variable depending to the development level of each country. Here we focus only on the emission inventories of the European Union based on the Technical Reports of European Environment Agency (EEA, Technical Report, 2008, 2009, 2012). Further data can be available for example at <http://www.epa.gov/air/emissions/>.

Greenhouse gases:

The total greenhouse gas (GHG) emission in the European Union was 4720.9 Mt CO_2 equivalent in 2010. The most significant sectors that release GHGs into the atmosphere are energy supply and use as well as transport, both in the whole European Union (Figure 2.5) and in Hungary (Figure 2.6).

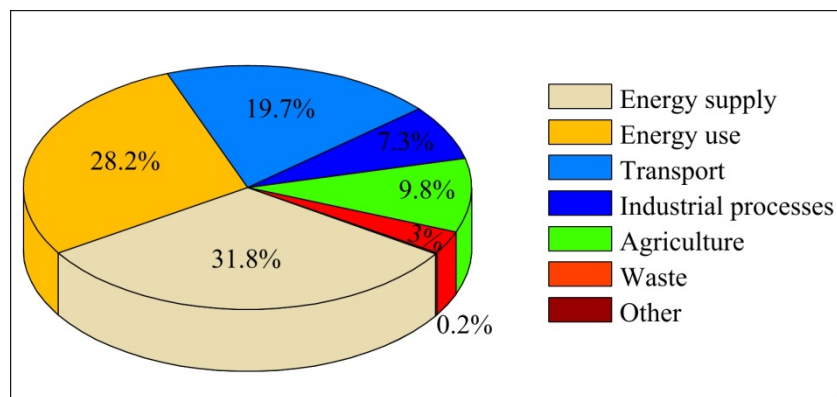


Figure 2.5: Share of greenhouse gas (GHG) emissions by main source types in EU countries in 2010

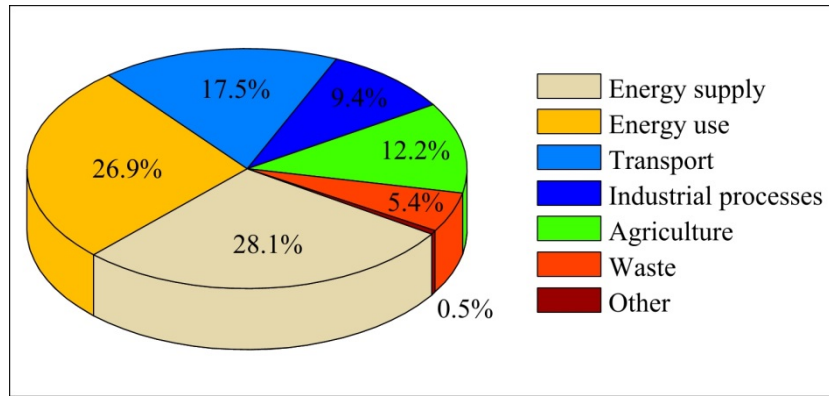


Figure 2.6: Share of greenhouse gas (GHG) emissions by main source types in Hungary in 2010

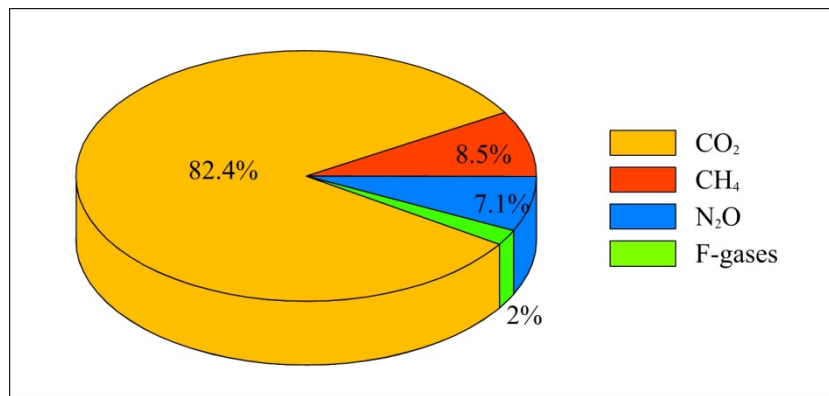


Figure 2.7: Share of greenhouse gas (GHG) emissions by species in EU countries in 2010

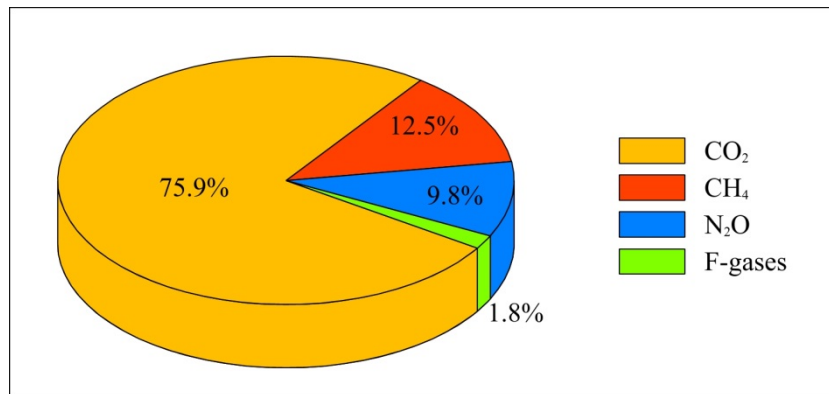


Figure 2.8: Share of greenhouse gas (GHG) emissions by species in Hungary in 2010

Figure 2.7 and Figure 2.8. show the percentage of each emitted greenhouse gases in 2010 in EU, and in Hungary, respectively.

Nitrogen oxides (NO_x):

The main anthropogenic sources of nitrogen oxides are transport and public electricity and heat sector (Figure 2.9). In combustion equipments the NO_x are formed during the combustion process at high temperatures by the oxidation of nitrogen content of fuel and combustion air. In a first phase only NO is formed while the NO₂ is mainly formed after the combustion in exhaust process when more O₂ is present and into the atmosphere. The total yearly emission of Nitrogen oxides in EU27 was 11 199 Gg in 2006, which means a 35% reduction between 1990 and 2006 (EEA, 2008).

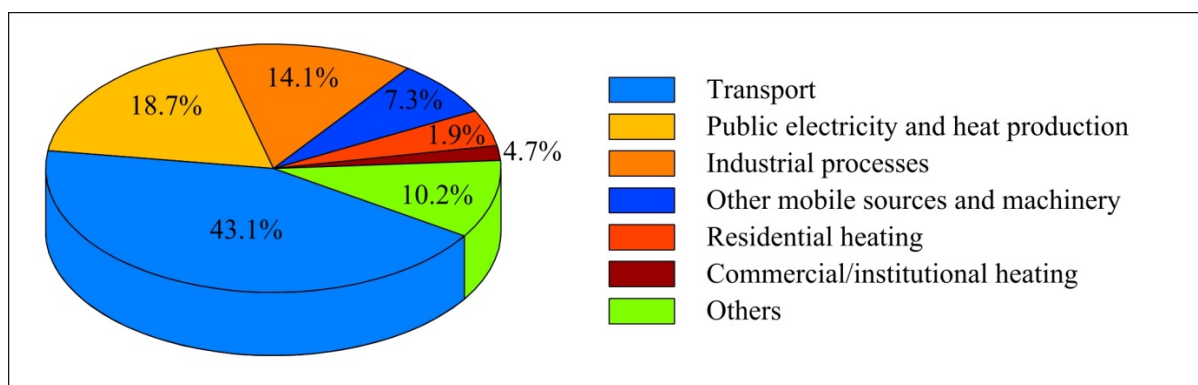


Figure 2.9: Emission sources of nitrogen oxides (NO_x) in 2006 in EU27. Emission data are calculated by the estimations of member countries.

Carbon monoxide (CO):

Carbon monoxide is mainly produced as an intermediary product of combustion processes. In the EU-27, total emissions of CO was 30 200 Gg in 2006. This is a result of a large decrease by just over 53% between 1990 and 2006 (EEA, 2008). Contributions to total CO emission by different sectors in the European Union can be seen in Figure 2.10. Main sources of carbon dioxide are transport and residential heating.

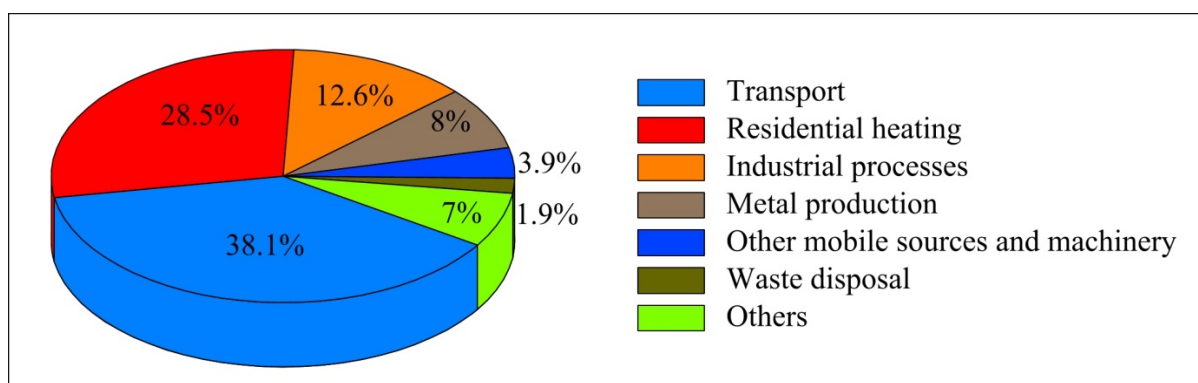


Figure 2.10: Emission sources of Carbon monoxide (CO) in 2006 in EU27. Emission data are calculated by the estimations of member countries.

Non methane volatile organic compounds (NMVOC):

The Earth's vegetation naturally releases huge amounts of organic gases into the air. As plants assimilate carbon dioxide into biomass through photosynthesis, a fraction of this carbon leaks out in to the atmosphere, predominantly in highly reduced forms such as isoprene and terpenes. In addition to emissions from natural sources, several anthropogenic processes result in the emission of organic compounds such as carbonyls, alcohols, alkanes, alkenes, esters, aromatics, ethers and amides. Biogenic sources in total are considered to be approximately ten times larger than the sum of anthropogenic emissions including fossil fuel emissions and biomass burning (Williams and Koppmann, 2007). At the same time, human made emission can play important role in local atmospheric chemistry, e.g. in ozone production (see Chapter 8). The anthropogenic contribution to organic emissions in the atmosphere is originated from transport, other exploitation of fossil fuels, product use and paint applications (Figure 2.11).

In Europe, the total NMVOC emission of EU27 was 9 391 Gg in 2006 (EEA, 2008). The NMVOC emission is decreased by 44% in Europe since 1990.

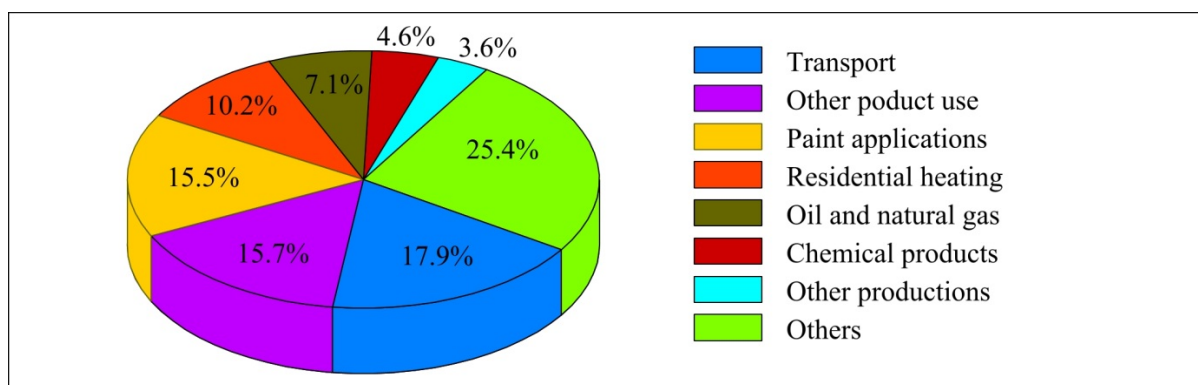


Figure 2.11: Emission sources of non-methane volatile organic compounds (NMVOC) in 2006 in EU27. Emission data are calculated by the estimations of member countries.

Sulphur oxides (SO_x):

Sulphur components are released into the atmosphere by both natural and anthropogenic sources. Human made emissions however are more significant than natural sources (Möller, 1994). Anthropogenic sulphur emission is principally originated from fossil fuel combustion. Total SO_x emission was 7 946 Gg in 2006 in EU countries (EEA, 2008). Due to the rigid emission reduction strategies in Europe, SO_x emission have decreased continuously in the last decades (about 70% decrease have realized in SO_x emission since 1990, when total SO_x emission was 26 217 Gg). Main anthropogenic sources of sulphur compounds is public electricity and heat production, which accounts for more than 58 % of total emissions, and manufacturing industries and constructions (about 14% of total SO_x emissions) (Figure 2.12).

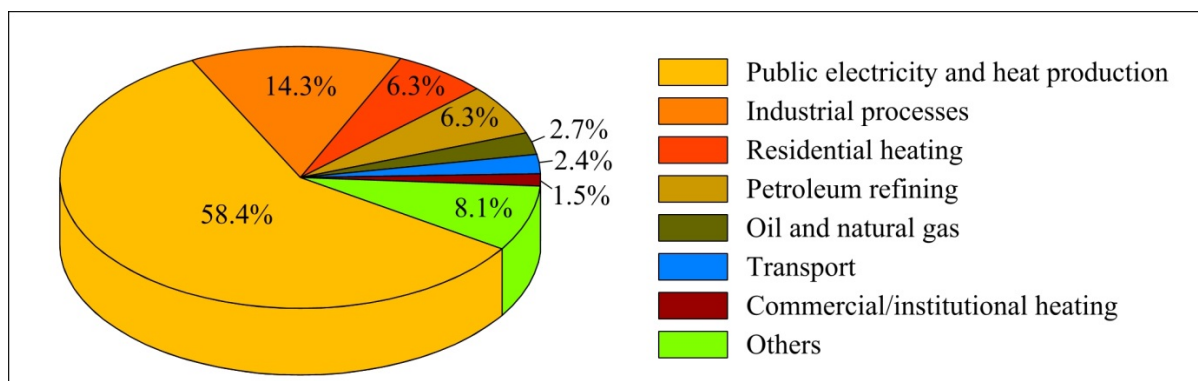


Figure 2.12: Emission sources of sulphur oxides (SO_x) in 2006 in EU27. Emission data are calculated by the estimations of member countries.

Ammonia (NH₃):

The major sources for atmospheric ammonia are agricultural activities. Close to the emission sources, acute exposures to NH₃ can result in visible foliar injury on vegetation. NH₃ is deposited rapidly within the first 4–5 km from its sources in the function of weather and plant conditions (see e.g.: Horváth, et al., 2005). However, NH₃ is a very important alkaline constituent in the atmosphere. It reacts with acidic substances such as sulphuric acid (H₂SO₄), nitric acid (HNO₃), nitrous acid (HNO₂), or hydrochloric acid (HCl) to form NH₄ ammonium salts that occur predominantly in the fine particle (size < 2.5 μm) fraction causing regional scale problems (see e.g.: Krupa, 2003).

Total ammonia emission was 4 001 Gg in 2006 in the European Union countries (EEA, 2008). This value shows a 22% decrease compared to the emission in 1990 (5 118 Gg). The two most important key categories of NH₃ are manure management and direct soil emission, which contributed approximately 70% and 23% respectively of total EU27 emissions in 2006. Agriculture thus contributed more than 90 % of total EU27 ammonia emissions in 2006 (Figure 2.13).

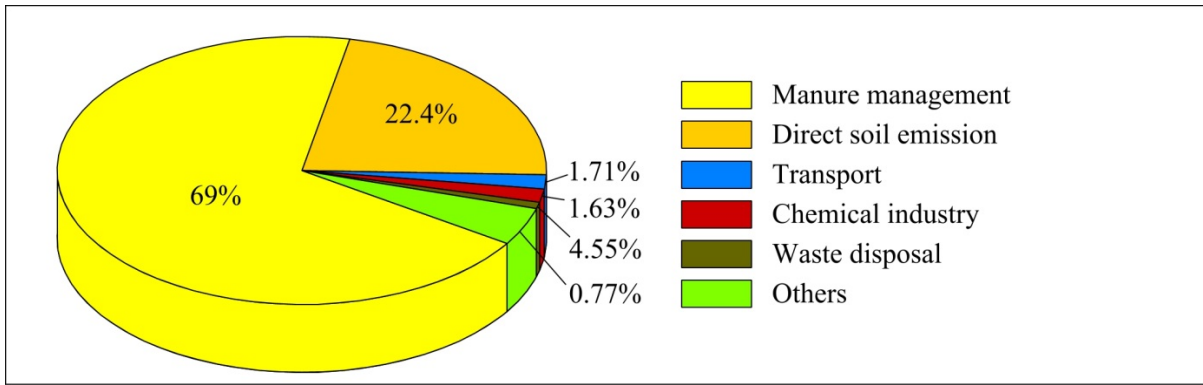


Figure 2.13: Emission sources of ammonia (NH₃) in 2006 in EU27. Emission data are calculated by the estimations of member countries.

Particulate matter:

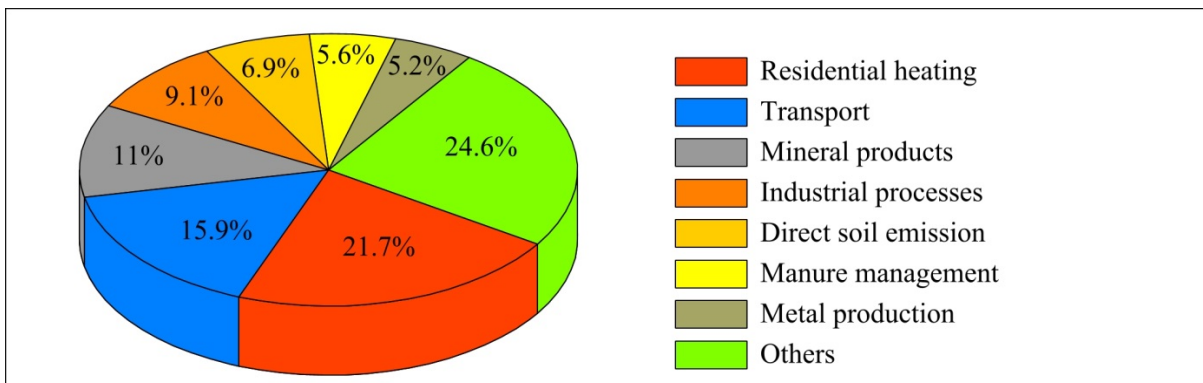


Figure 2.14: Emission sources of particulate matter, PM10 in 2006 in EU27. Emission data are calculated by the estimations of member countries.

Next to the natural sources of primary aerosol particles (see Chapter 9), a huge number of different size particles are also released into the atmosphere by several various anthropogenic processes. The total PM10 emission was 1 555 Gg in EU27, in 2006 (EEA, 2008). Almost 60% of this emission occurs in energy-related sectors, with a further 13% of emissions occurring in the agriculture sector (Figure 2.14).

Total PM2.5 emissions was 1 044 Gg in EU-7, in 2006 (EEA, 2008). In 2006, PM2.5 emissions from the residential category contributed approximately 30% to total emissions (Figure 2.15). Other main sources were road transportation (18%) and manufacturing industries (11%). Both PM10 and PM2.5 emission have decreased since 1990 with about a 10% in Europe.

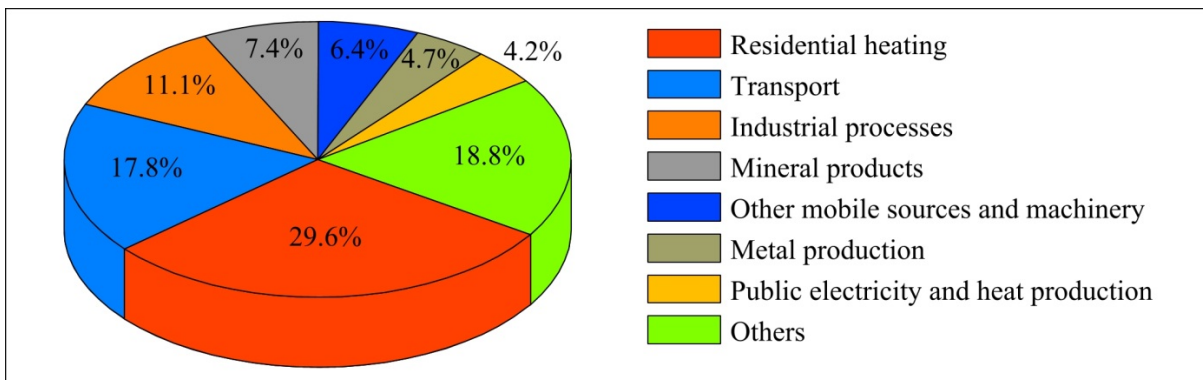


Figure 2.15: Emission sources of particulate matter, PM_{2.5} in 2006 in EU27. Emission data are calculated by the estimations of member countries.

References

EEA Technical report, 2008: *Annual European Community LRTAP Convention emission inventory report 1990–2006 Submission to EMEP through the Executive Secretary of the UNECE*. EEA Technical report. No 7/2008. ISBN 978-92-9167-366-7.

EEA Technical report, 2009: *EMEP/EEA air pollutant emission inventory guidebook 2009. Technical guidance to prepare national emission inventories*. EEA Technical report. No 9/2009. ISBN 978-92-9213-034-3.

EEA Technical report, 2012: *Greenhouse gas emission trends and projections in Europe 2012. Tracking progress towards Kyoto and 2020 targets*. EEA Report. No 6/2012. ISBN 978-92-9213-331-3.

Horváth, L., Asztalos, M., Führer, E., Mészáros, R., and Weidinger, T.. 2005. *Measurement of ammonia exchange over grassland in the Hungarian Great Plain In: Agricultural and Forest Meteorology*. 130. 282-298.

IPCC, 2001: *Climate Change 2001: The Scientific Basis. Contribution of Working Group I to the Third Assessment Report of the Intergovernmental Panel on Climate Change*. Houghton J.T., Ding Y., Griggs D.J., Noguer M., van der Linden P.J., Dai X., Maskell K., and Johnson C.A.. (eds.). Cambridge University Press, Cambridge, United Kingdom and New York, NY, USA. 881pp. ISBN 0521 80767 0.

Krupa, S.V.. 2003. *Effects of atmospheric ammonia (NH₃) on terrestrial vegetation: a review. Environment Pollution*. 124. 179-221.

Möller, D.. 1994. *Global sulfur and nitrogen biogeochemical cycles. In: Boutron, F (ed) Topics in atmospheric and terrestrial physics and chemistry*. Vo. 2. 125-156. ISBN 2-86883-287-3.

Williams, J. and Koppmann, R.. 2007. *Volatile Organic Compounds in the Atmosphere: An Overview, in Koppmann, R (ed): Volatile Organic Compounds in the Atmosphere*. Blackwell Publishing Ltd., Singapore. Vo. 1-32. 125-156. ISBN 978-1-4051-3115-5.

<http://www.ceip.at/ceip/>

<http://www.epa.gov/air/emissions/>

Chapter 3. Basics of the reaction kinetics

Chemical kinetics studies the speed with which a chemical reaction occurs and the factors that affect this speed. This information is especially useful for determining how a reaction occurs. Let's consider the following chemical reaction:



Here letters A, B, C, and D represent chemical species involved in the chemical transformation. ν_a , ν_b , ν_c , and ν_d are the stoichiometric coefficient for the given reaction.

The speed of a reaction is the rate at which the concentrations of reactants and products change. The term rate of reaction (r) occurring in a closed system under isochoric conditions, without a build-up of reaction intermediates can be written in the form (Atkins, 1997):

$$r = \frac{1}{\nu_i} \frac{dc_i}{dt} \quad (3.2)$$

where c_i is the concentration and ν_i is the stoichiometric coefficient of reactants and products, respectively. (Note: The rate of a reaction is always positive. Stoichiometric coefficients for products are positive and for reactants are negative in reaction kinetics. Moreover, stoichiometric coefficients are not always cardinal numbers.)

The effect of concentration on the rate is isolated as

$$r = kf(c_i) \quad (3.3)$$

where the specific rate k , called reaction rate coefficient, is independent of concentration but does depend on temperature, catalysts, and other factors. The law of mass action states that the rate is proportional to the concentrations of the reactants and has a form

$$r = kc_A^\alpha c_B^\beta \quad (3.4)$$

Here exponents α , β are empirical and identifies the order of the reaction, and they can be determined from reaction kinetics measurements. Importantly, they are identical with the stoichiometric coefficients when the stoichiometric equation truly represents the mechanism of reaction i.e. the reaction is an elementary reaction.

3.1. Differential rate law

In many reactions, the rate of reaction changes as the reaction progresses. Initially the rate of reaction is relatively large, while at very long times the rate of reaction decreases to zero (at which point the reaction is complete). In order to characterize the kinetic behaviour of a reaction, it is desirable to determine how the rate of reaction varies as the reaction progresses. A rate law is a mathematical equation that describes the progress of the reaction (3.4). In general, rate laws must be determined experimentally as we discuss earlier. Unless a reaction is an elementary reaction, it is not possible to predict the rate law from the overall chemical equation. There are two forms of a rate law for chemical kinetics: the differential rate law and the integrated rate law.

The differential rate law relates the rate of reaction to the concentrations of the various species in the system. Differential rate laws can take on many different forms, especially for complicated chemical reactions. Each rate law contains the reaction rate coefficient. The units for the rate coefficient depend upon the rate law, because the rate always has units of $\text{mole L}^{-1} \text{s}^{-1}$ and the concentration always has units of mole L^{-1} . There are some examples of different differential rate laws.

First-Order Reaction:

For a first-order reaction, the rate of reaction is directly proportional to the concentration of one of the reactants. Differential rate law: $r = k c_A$; the rate coefficient, k , has units of s^{-1} .

Second-Order Reaction:

For a second-order reaction, the rate of reaction is directly proportional to the square of the concentration of one of the reactants. Differential rate law: $r = k c_A^2$; the rate coefficient, k , has units of $L \text{ mole}^{-1} s^{-1}$.

3.2. Integrated rate law

The differential rate law describes how the rate of reaction varies with the concentrations of various species, usually reactants, in the system. The rate of reaction is proportional to the rates of change in concentrations of the reactants and products; that is, the rate is proportional to a derivative of a concentration. To illustrate this point, consider the reaction



The rate of reaction, r , from equation (2) (using that the stoichiometric coefficient for species A is -1) is given by

$$r = -\frac{dc_A}{dt}. \quad (3.6)$$

Suppose this reaction obeys a first-order rate law, i.e. $r = k [A]$. This rate law can also be written as

$$r = -\frac{dc_A}{dt} = k c_A. \quad (3.7)$$

This equation is a first order ordinary differential equation that relates the rate of change in a concentration to the concentration itself. Integration of this equation produces the corresponding *integrated rate law*, which relates the concentration to time. Let's solve this (3.7) simply differential equation with the following initial condition: $c_A(t=0) = c_0$. After the separation of variables we get the following equation:

$$\int_{c_0}^{c_A} \frac{dc_A}{c_A} = -k \int_0^t dt. \quad (3.8)$$

Integrating both sides we provide the integrated rate law for a first order reaction (Figure 3.1):

$$c_{A1} = c_0 e^{-kt}. \quad (3.9)$$

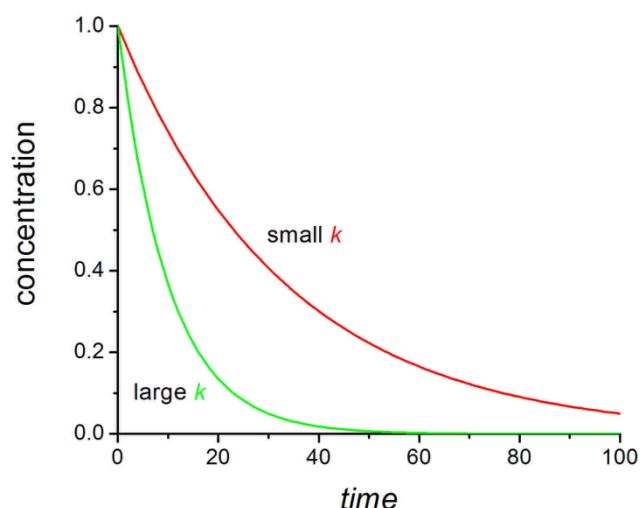


Figure 3.1: Integrated rate law: dependence of concentration in time

3.3. Three-body reaction

There are several reactions in the atmosphere, where a third „non-reactive” compound is involved. A *three-body* reaction is a reaction of two species A and B to yield one single product species AB. This reaction requires a *third body* (M) to stabilize the excited product AB* by collision:



The third body M could be any inert molecule (in the atmosphere, generally N₂ and O₂) that can remove the excess energy from AB* and eventually dissipate it. We can write the overall (net) reaction as



to emphasize the need for a third body.

3.4. Photochemical reaction (Photolysis)

A photolysis reaction involves the breaking of a chemical bond in a molecule by an incident photon (Pilling and Seakin, 1995, Bozó, 2009, Mészáros, 1997). The reaction is written



and the rate of this reaction is calculated as

$$r = kc_A \quad (3.10)$$

where k is the photolysis rate coefficient.

Consider an elemental slab of air of vertical thickness dz and unit horizontal area. The slab contains $[X]dz$ molecules of X (where $[X]$ denotes the number density). A photon incident on a molecule of X has a probability σ_x / A of

being absorbed, where A is the cross-sectional area of the molecule and σ_x is the absorption cross-section (units of $\text{cm}^2 \text{ molecule}^{-1}$) which defines the absorption characteristics of X. The molecules of X in the elemental slab absorb a fraction $\sigma_x [X] dz$ of the incoming photons. We define the actinic flux I as the number of photons crossing the unit horizontal area per unit time from any direction ($\text{photons cm}^{-2} \text{ s}^{-1}$) and the quantum yield q_x (units of molecules photon) as the probability that absorption of a photon will cause photolysis of the molecule X. The number of molecules of X photolyzed per unit time in the slab is $q_x \sigma_x [X] I dz$. To obtain the photolysis rate constant k , we divide by the number $[X] dz$ of molecules of X in the slab:

$$k = q_x \sigma_x I \quad (3.11)$$

Absorption cross-sections and quantum yields vary with wavelength. For polychromatic radiation, as in the atmosphere, equation (3.11) must be integrated over the wavelength spectrum:

$$k = \int_{\lambda} q_x(\lambda) \sigma_x(\lambda) I_{\lambda} d\lambda \quad (3.12)$$

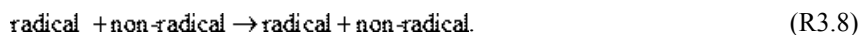
where I_{λ} is the actinic flux distribution function.

3.5. Radicals in the atmosphere

Radicals are defined as chemical species with an unpaired electron in the outer (valence) shell. Because of this unpaired electron, radicals have high free energies and are much more reactive than non-radical species whose electrons are all paired up. Because radicals have high free energies, their formation from non-radical species is in general endothermic; an external source of energy is required. In the atmosphere, this source of energy is supplied by solar radiation:



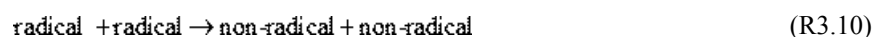
Generation of radicals by reaction (R3.7) provides the initiation step for radical reaction chains which are propagated by subsequent reactions of radicals with non-radical species:



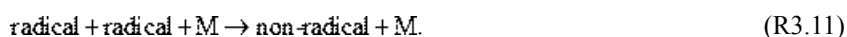
Importantly, any reaction of a radical with a non-radical must always produce a radical in order to conserve the total odd number of electrons. The radical produced in (R3.8) goes on to react with another non-radical, propagating the chain, and in this manner a large number of non-radicals can be processed through the chain. During the propagation cycle, a non-radical species produced by a reaction of type (R3.8) may photolyze following (R3.7) to produce additional radicals; the photolysis is called a branching reaction as it accelerates (or "branches") the chain by augmenting the pool of radicals.



Termination of the chain requires reactions taking place between radicals:



or



Termination reactions are generally slower than propagation reactions because radicals are present at low concentrations and collisions between radicals are therefore relatively infrequent. In subsequent chapters we will encounter many types of radical-assisted chains following the general schematic (reactions R3.7-R3.10). Due to the critical importance of solar radiation in initiating radical-assisted chain mechanisms in the atmosphere, these mechanisms are often referred to as photochemical (Jacob, 1999).

3.6. Arrhenius Equation

It is easy to imagine, especially in the gas phase, that at higher temperature a given chemical reaction will proceed faster due to higher collision rate. This results in a higher kinetic energy, which has an effect on the activation energy of the reaction. The activation energy (E_a) is the amount of a minimal energy required to ensure that a reaction happens (Turányi, 2010).

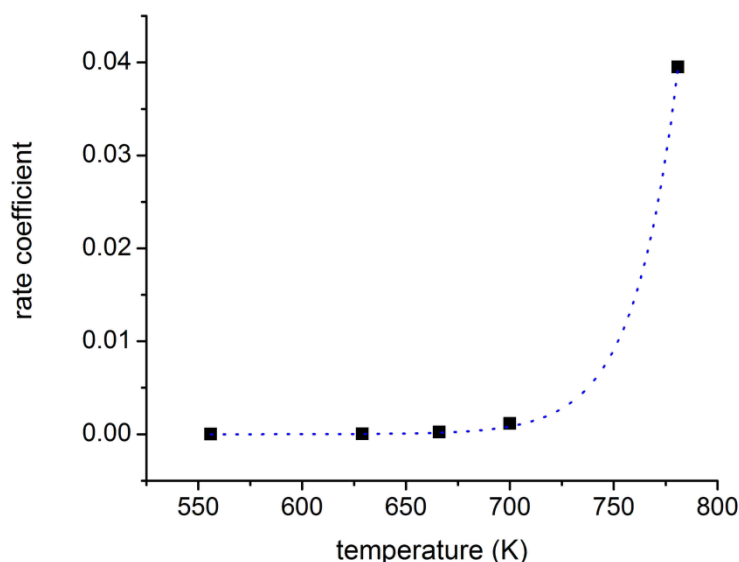


Figure 3.2: Dependence of rate coefficient on thermodynamic temperature

The rate of the chemical reactions depends on the concentrations of reagents, which can vary during the reaction and the rate coefficient (Figure 3.2). Arrhenius equation describes the effect of a change of temperature on the rate coefficient and therefore on the rate of the reaction:

$$k = A e^{-\frac{E_a}{RT}}, \quad (3.13)$$

where A is the pre-exponential factor or the steric factor, which includes factors like the frequency of collisions and their orientation. It varies slightly with temperature, although not much. It is often taken as constant across small temperature ranges. E_a is the activation energy, R is universal gas constant, and T is the thermodynamic temperature, respectively. The former form (13) can be written equivalently as

$$\ln k = \ln A - \frac{E_a}{R} \frac{1}{T}. \quad (3.14)$$

This is the so-called Arrhenius plot, where there is a linear correlation between $\ln k$ and $1/T$ (Figure 1.3). The slope and the intercept of (14) provide activation energy and pre-exponential factor, respectively.

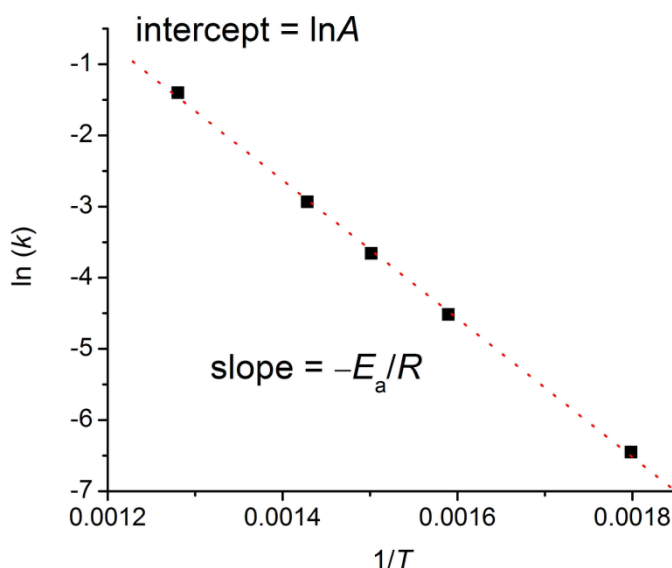


Figure 3.3: Arrhenius plot

3.7. Half-life

The variation in concentration with time provides a detailed description of how fast a reaction is occurring. In many circumstances, though, it is desirable to have a simple, approximate measure of the reaction rate, and the half-life ($t_{1/2}$) provides such a measure. The half-life is the time it takes for one-half of the original amount of material to react (assuming the compound in question is a limiting reactant). If the initial concentration of a reactant A is 1.0 mole L^{-1} , the half-life is the time at which $c_A = 0.5 \text{ mole L}^{-1}$. Intuitively, the faster the reaction, the shorter the half-life. The rate of the reaction is proportional to the rate coefficient; thus the larger the rate constant, the shorter the half-life. Dependence of the half-time on the rate coefficient could be complicated, however, for first order reactions $t_{1/2} = \frac{\ln 2}{k}$, and the half-time does not depend on the initial concentration of A (reagent).

3.8. Reaction mechanism

A reaction mechanism is a set of elementary reactions by which overall chemical change occurs (Turányi, 2010). Let's have an example; the formation of the ozone in stratosphere can be described by the Chapman mechanism, where ozone formation and destruction from oxygen species occur. The set of elementary reactions which describes the ozone formation is the following:



We can consider reactions (R3.12) and (R3.13) as a chemical mechanism for ozone formation in the stratosphere, where the overall (net) reaction is $2\text{O}_2 + h\nu \rightarrow \text{O}_3 + \text{O}$. The net reaction is just shows the transformation of reagents to products, and it reflects the mass conservation. However, equations (R3.12) and (R3.13) – a chemical mechanism – present a sequent of “real” (elementary) steps, which contributes to products formation. The ozone destruction can be written in a set of reactions:



Similarly, the net process is $2\text{O}_2 + h\nu \rightarrow 3\text{O}_2$. The rate constants for reaction (R.312) and (R3.14) depend on light intensity, which in this case is the light intensity of the sun.

A reaction intermediate, an intermediate or intermediate species is a molecular entity that is formed from the reactants and reacts further to give the directly observed products of a chemical reaction. If the reaction mechanism includes these elementary steps:



The chemical species X^* is an intermediate or intermediate species.

3.9. The quasi steady-state approximation (QSSA)

The quasi-steady-state approximation (QSSA) in chemical kinetics is a mathematical way of simplifying the differential equations describing some chemical kinetic systems (Seinfeld and Pandis, 2006). QSSA provides an as-

sumption that there is no change in concentrations in time for all intermediates ($\frac{dc_{\text{X}}}{dt} = 0$). We will illustrate this concept using the Chapman mechanism (R3.18-21). The first step (Step I) is the determination of the reaction rates (3.4) for all elementary steps in the mechanism. In our example this will be:



The second step (Step II) of QSSA is the determination of the intermediates from the mechanism. In this example we can relatively easily find the intermediates; O and O_3 are the intermediate species. In the next step (Step III) we should express the rate of the concentration change for all intermediates, to do this task we should use the definition of reaction rate (3.2). From reactions (R3.18-21) the rates of formation of O and O_3 can be expressed as

$$\frac{dc_{\text{O}}}{dt} = 2k_1 c_{\text{O}_2} - k_2 c_{\text{O}} c_{\text{O}_2} + k_3 c_{\text{O}_3} - k_4 c_{\text{O}} c_{\text{O}_3} \quad (\text{3.15})$$

$$\frac{dc_{\text{O}_3}}{dt} = k_2 c_{\text{O}} c_{\text{O}_2} - k_3 c_{\text{O}_3} - k_4 c_{\text{O}} c_{\text{O}_3} \quad (\text{3.16})$$

We can use the steady-state approximation to solve for the concentration of O and O_3 (Step IV). The steady state approximation assumes that after an initial time period, the concentration of the reaction intermediates remain a constant with time, i.e. the rate of change of the intermediate's concentration with time is zero. Hence, using the steady state approximation:

$$\frac{dc_{\text{O}}}{dt} = \frac{dc_{\text{O}_3}}{dt} = 0 \quad (\text{3.17})$$

thus

$$2k_1 c_{\text{O}_2} - k_2 c_{\text{O}} c_{\text{O}_2} + k_3 c_{\text{O}_3} - k_4 c_{\text{O}} c_{\text{O}_3} = 0 \quad (\text{3.18})$$

$$k_2 c_{\text{O}} c_{\text{O}_2} - k_3 c_{\text{O}_3} - k_4 c_{\text{O}} c_{\text{O}_3} = 0 \quad (\text{3.19})$$

We can see that using the QSSA two ordinary differential equations can be reduced to two algebraic equations. Solving algebraic equations either numerically or analytically is much easier compared to ordinary differential equations. This fact is a power of the QSSA. We can solve for c_{O} and c_{O_3} :

$$c_{\text{O}} = \frac{2k_1c_{\text{O}_2} + k_3c_{\text{O}_3}}{k_2c_{\text{O}_2} + k_4c_{\text{O}_3}} \quad (3.20)$$

$$c_{\text{O}_3} = \frac{k_2c_{\text{O}}c_{\text{O}_2}}{k_3 + k_4c_{\text{O}}} \quad (3.21)$$

Equation (3.21) can be rearranged:

$$c_{\text{O}_3} = \frac{k_2c_{\text{O}_2} / k_4}{\left[k_3 / (k_4c_{\text{O}}) \right] + 1} \quad (3.22)$$

These two equations (3.21) and (3.22) provide the steady state concentration for the intermediates. If we know that $c_{\text{O}} \sim 10^7$ molecule/cm³ and $c_{\text{O}_3} \sim 10^{13}$ molecule/cm³ and $\frac{k_3}{k_4} \sim 10^{12}$, we find that $\frac{k_3}{k_4c_{\text{O}}} \gg 1$. Hence the equation (31) can be simplified to

$$c_{\text{O}_3} = \frac{k_2c_{\text{O}}c_{\text{O}_2}}{k_3} \quad (3.23)$$

Equation (3.23) indicates that the concentration of O₃ in the atmosphere depends proportionately on the rate of reaction (R.319) and inversely on k_3 , the rate constant for the photolysis of ozone by the UV light from the Sun.

3.10. Application of a reaction mechanism

There are several reaction mechanisms, which describe chemical transformation occurring in the atmosphere. These can differ from each other depending on what type of detailed description is needed. One of these mechanisms is the CBM Leeds (Table 3.1, Heard et al., 1998), which describe the photochemical air pollution formation in the troposphere. Elementary reactions in the mechanism are either thermal or photochemical reactions. We can construct a set of ordinary differential equations (ODEs) from a reaction mechanism, which describes the temporal variation of chemical species. These ODEs can be solved by various numerical methods with appropriate initial conditions. Figures 3.4–3.11 show the variation of different compounds involved in the mechanism in winter and summer.

Table 3.1: CBM Leeds mechanism

Reactions			Reaction rate coefficients (k_i)	
NO ₂ + hv	→	NO+O	$k_1=1.45 \cdot 10^{-2} \times \exp(-0.4/ \cos\phi_z)$	(R1)
O + O ₂ · M	→	O ₃	$k_2=1.4 \cdot 10^3 \times \exp(1175/ T_k)$	(R2)
O ₃ + NO	→	NO ₂	$k_3=1.8 \cdot 10^{-12} \times \exp(-1370/ T_k)$	(R3)
O + NO ₂	→	NO	$k_4=9.3 \times 10^{-12}$	(R4)
O ₃ + NO ₂	→	NO ₃	$k_5=1.2 \cdot 10^{-13} \times \exp(-2450/ T_k)$	(R5)
O ₃ + hv	→	O	$k_6=7.865 \cdot 10^{-4} \times \exp(-0.4/ \cos\phi_z)$	(R6)
O ₃ + hv	→	O ¹ D	$k_7=2.0 \cdot 10^{-4} \times \exp(-1.4/ \cos\phi_z)$	(R7)
O ¹ D (+M)	→	O	$k_8=1.9 \cdot 10^8 \times \exp(390/ T_k)$	(R8)
O ¹ D + H ₂ O	→	OH + OH	$k_9=2.2 \cdot 10^{-10}$	(R9)
O ₃ +HO ₂	→	OH	$k_{10}=1.4 \cdot 10^{-14} \times \exp(-580/ T_k)$	(R10)
NO ₃ + hv	→	0.89(NO ₂ +O) 0.11NO	+ $k_{11}=4.91 \cdot 10^{-1} \times \exp(-0.4/ \cos\phi_z)$	(R11)

$\text{NO}_3 + \text{NO}$	\rightarrow	$\text{NO}_2 + \text{NO}_2$	$k_{12}=1.3 \cdot 10^{-11} \times \exp(250/ T_k)$	(R12)
$\text{NO}_3 + \text{NO}_2 (+\text{M})$	\rightarrow	N_2O_5	$k_{13}=5.3 \cdot 10^{-13} \times \exp(256/ T_k)$	(R13)
$\text{N}_2\text{O}_5 + \text{H}_2\text{O}$	\rightarrow	$\text{HNO}_3 + \text{HNO}_3$	$k_{14}=1.3 \cdot 10^{-21}$	(R14)
$\text{N}_2\text{O}_5 + \text{NO}_3$	\rightarrow	NO_2	$k_{15}=3.5 \cdot 10^{14} \times \exp(-10897/ T_k)$	(R15)
$\text{NO} + \text{NO}$	\rightarrow	$\text{NO}_2 + \text{NO}_2$	$k_{16}=1.8 \cdot 10^{-20} \times \exp(530/ T_k)$	(R16)
$\text{OH} + \text{NO} (+\text{M})$	\rightarrow	HONO	$k_{17}=4.5 \cdot 10^{-13} \times \exp(806/ T_k)$	(R17)
$\text{HONO} + \text{h}\nu$	\rightarrow	$\text{OH} + \text{NO}$	$k_{18}=2.86 \cdot 10^{-3} \times \exp(-0.4/ \cos\phi_z)$	(R18)
$\text{OH} + \text{NO}_2 (+\text{M})$	\rightarrow	HNO_3	$k_{19}=1.0 \cdot 10^{-12} \times \exp(713/ T_k)$	(R19)
$\text{HO}_2 + \text{NO}$	\rightarrow	$\text{OH} + \text{NO}_2$	$k_{20}=3.7 \cdot 10^{-12} \times \exp(240/ T_k)$	(R20)
$\text{HO}_2 + \text{HO}_2$	\rightarrow	H_2O_2	$k_{21}=5.9 \cdot 10^{-14} \times \exp(1150/ T_k)$	(R21)
$\text{HO}_2 + \text{HO}_2$ + H_2O	\rightarrow	H_2O_2	$k_{22}=2.2 \cdot 10^{-38} \times \exp(5800/ T_k)$	(R22)
$\text{OH} + \text{CO}$	\rightarrow	HO_2	$k_{23}=2.2 \cdot 10^{-13}$	(R23)
$\text{FORM} + \text{OH}$	\rightarrow	$\text{HO}_2 + \text{CO}$	$k_{24}=1.0 \cdot 10^{-11}$	(R24)
$\text{FORM} + \text{h}\nu$	\rightarrow	$2 \text{HO}_2 + \text{CO}$	$k_{25}=5.40 \cdot 10^{-5} \times \exp(-0.79/ \cos\phi_z)$	(R25)
$\text{FORM} + \text{h}\nu$	\rightarrow	CO	$k_{26}=6.65 \cdot 10^{-5} \times \exp(-0.6/ \cos\phi_z)$	(R26)
$\text{ALD2} + \text{OH}$	\rightarrow	C2O3	$k_{27}=7.0 \cdot 10^{-12}$	(R27)
$\text{ALD2} + \text{h}\nu$	\rightarrow	$\text{MEO2} + \text{HO}_2 + \text{CO}$	$k_{28}=1.35 \cdot 10^{-5} \times \exp(-0.94/ \cos\phi_z)$	(R28)
$\text{C2O3} + \text{NO}$	\rightarrow	$\text{NO}_2 + \text{MEO2}$	$k_{29}=5.4 \cdot 10^{-12} \times \exp(250/ T_k)$	(R29)
$\text{C2O3} + \text{NO}_2$	\rightarrow	PAN	$k_{30}=8.0 \cdot 10^{-20} \times \exp(5500/ T_k)$	(R30)
PAN	\rightarrow	$\text{C2O3} + \text{NO}_2$	$k_{31}=9.4 \cdot 10^{16} \times \exp(-14000/ T_k)$	(R31)
$\text{MEO2} + \text{NO}$	\rightarrow	$\text{FORM} + \text{HO}_2 + \text{NO}_2$	$k_{32}=4.2 \cdot 10^{-12} \times \exp(180/ T_k)$	(R32)
$\text{MEO2} + \text{C2O3}$	\rightarrow	$\text{MEO2} + \text{FORM} + \text{HO}_2$	$k_{33}=3.0 \cdot 10^{-12}$	(R33)
$\text{C2O3} + \text{C2O3}$	\rightarrow	2MEO2	$k_{34}=2.5 \cdot 10^{-12}$	(R34)
$\text{MEO2} + \text{HO}_2$	\rightarrow	$0.77(\text{FORM} + \text{HO}_2 + \text{OH})$	$k_{35}=7.5 \cdot 10^{-14} \times \exp(1300/ T_k)$	(R35)
$\text{C2O3} + \text{HO}_2$	\rightarrow	$0.79(\text{MEO2} + \text{OH})$	$k_{36}=6.5 \cdot 10^{-12}$	(R36)
OH	\rightarrow	MEO2	$k_{37}=1.1 \cdot 10^2 \times \exp(-1710/ T_k)$	(R37)
$\text{PAR} + \text{OH}$	\rightarrow	$-\text{NO} + 0.87 \text{NO}_2 + 0.77 \text{ROR} + 0.1(\text{HO}_2 + \text{ALD2})$	$k_{38}=8.1 \cdot 10^{-13}$	(R38)
ROR	\rightarrow	$1.1 \text{ALD2} + 0.94 \text{NO}_2 + 0.96 \text{HO}_2 + 0.2(\text{KET-NO-PAR}) + 0.02 \text{ROR}$	$k_{39}=1.05 \cdot 10^{15} \times \exp(-8000/ T_k)$	(R39)
ROR	\rightarrow	$\text{KET} + \text{HO}_2$	$k_{40}=1.6 \cdot 10^3$	(R40)
$\text{KET} + \text{h}\nu$	\rightarrow	$\text{C2O3} + 0.95(\text{NO}_2 + \text{HO}_2 + \text{ALD2}) - \text{NO}$	$k_{41}=4.35 \cdot 10^{-6} \times \exp(-0.4/ \cos\phi_z)$	(R41)
$\text{OH} + \text{OLE}$	\rightarrow	$\text{MEO2} + \text{ALD2}$	$k_{42}=5.2 \cdot 10^{-12} \times \exp(504/ T_k)$	(R42)
$\text{O}_3 + \text{OLE}$	\rightarrow	$0.5 \text{ALD2} + 0.52 \text{FORM}$	$k_{43}=1.4 \cdot 10^{-14} \times \exp(-2105/ T_k)$	(R43)

		+ 0.12 CO + 0.17 HO ₂ + 0.22 MEO2 + 0.1 OH		
OH + ETH	→	-NO + NO ₂ + 1.56 FORM +HO ₂ + 0.22 ALD2	$k_{44}=2.0 \cdot 10^{-12} \times \exp(411/ T_k)$	(R44)
O ₃ + ETH	→	FORM	$k_{45}=1.25 \cdot 10^{-14} \times \exp(-2633/ T_k)$	(R45)
OH + TOL	→	0.08(-NO + NO ₂) + 0.36 CRES + 0.44 HO ₂ + 0.56 TO2	$k_{46}=2.13 \cdot 10^{-12} \times \exp(322/ T_k)$	(R46)
TO2 + NO	→	0.9(NO ₂ + OPEN+ HO ₂)	$k_{47}=8.1 \cdot 10^{-12}$	(R47)
TO2	→	HO ₂ + CRES	$k_{48}=4.2$	(R48)
OH + CRES	→	0.22 NO ₂ + 0.61 NO + 0.3 OPEN	$k_{49}=4.1 \cdot 10^{-11}$	(R49)
NO ₃ + CRES	→	-NO ₂	$k_{50}=2.2 \cdot 10^{-11}$	(R50)
OH + XYL	→	0.7 HO ₂ + 0.5 (-NO + NO ₂) + 0.2 CRES + 0.8 MGLY + 1.1 PAR + 0.3 TO2	$k_{51}=1.66 \cdot 10^{-11} \times \exp(116/ T_k)$	(R51)
OH + OPEN	→	-NO + NO ₂ + C2O3 + 2(HO ₂ + CO) + FORM	$k_{52}=3.0^{-11}$	(R52)
OPEN + hv	→	C2O3 + CO + HO ₂	$k_{53}=4.88 \cdot 10^{-4} \times \exp(-0.79/ \cos\phi_z)$	(R53)
O ₃ + OPEN	→	0.03 (-NO + NO ₂ + ALD ₂) + 0.62 C2O3 + 0.7(FORM + CO) + 0.08 OH + + 0.75 HO ₂ + 0.2 MGLY	$k_{54}=5.43 \cdot 10^{-17} \times \exp(-500/ T_k)$	(R54)
OH + MGLY	→	NO + NO ₂ + C2O3	$k_{55}=1.7 \cdot 10^{-11}$	(R55)
MGLY + hv	→	C2O3 + CO + HO ₂	$k_{56}=5.2 \cdot 10^{-4} \times \exp(-0.79/ \cos\phi_z)$	(R56)
O + ISOP	→	0.49 HO ₂ + 0.44 ALD2 + 0.6 OLE + 0.25(-NO + NO ₂ + CO) + 0.15 KET + 0.45 PAR + 0.05(MEO2	$K_{57}=1.82 \cdot 10^{-11}$	(R57)

		+ C2O3)		
OH + ISOP	→	-NO + 0.87 (NO ₂ + HO ₂) + FORM + OLE) + 0.58 (KET + PAR) + 0.29 ALD2	$k_{58}=9.6 \cdot 10^{-11}$	(R58)
O ₃ + ISOP	→	FORM + 0.45 ALD2 + 0.65 OLE + 0.35 CO + 0.2(PAR+KET)	$k_{59}=1.2 \cdot 10^{-17}$	(R59)

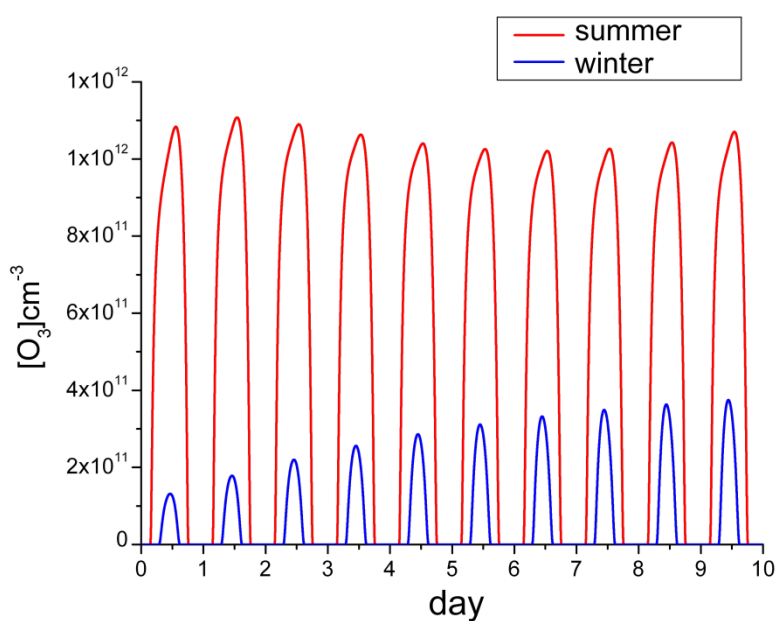


Figure 3.4: Results of the numerical simulations using CBM Leeds mechanism – variation of ozone in summer and winter time

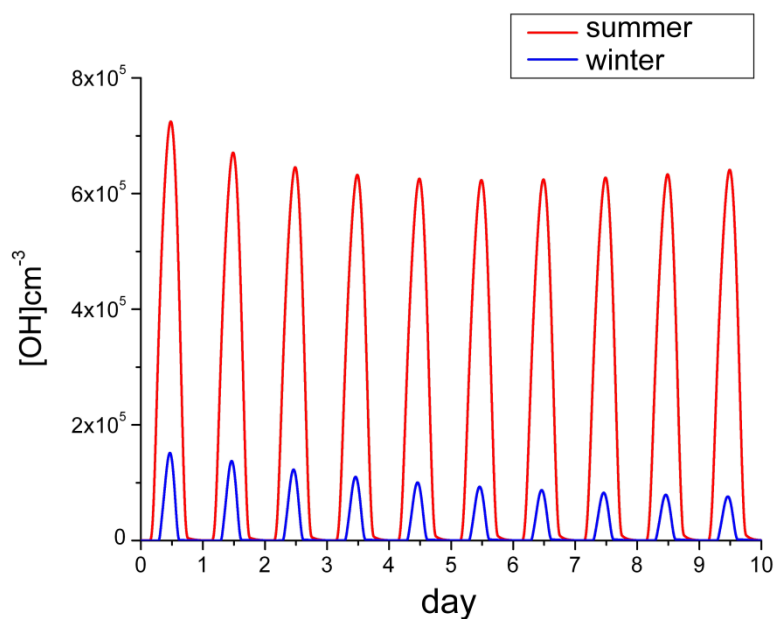


Figure 3.5: Results of the numerical simulations using CBM Leeds mechanism – variation of OH radical in summer and winter time

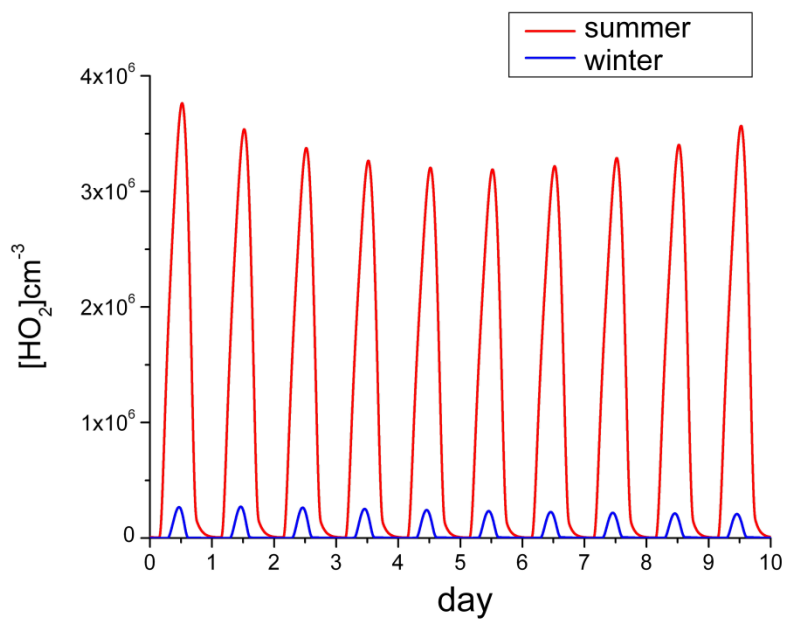


Figure 3.6: Results of the numerical simulations using CBM Leeds mechanism – variation of HO₂ radical in summer and winter time.

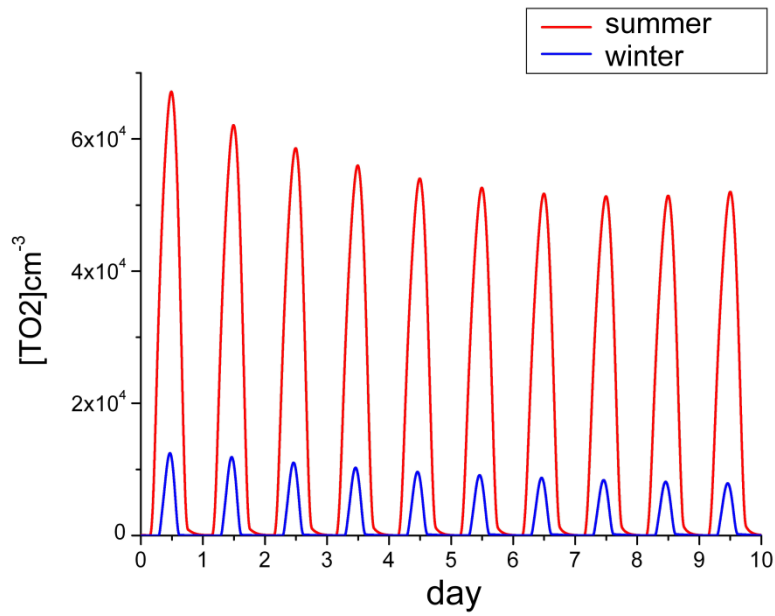


Figure 3.7: Results of the numerical simulations using CBM Leeds mechanism – variation of TO2 species in summer and winter time.

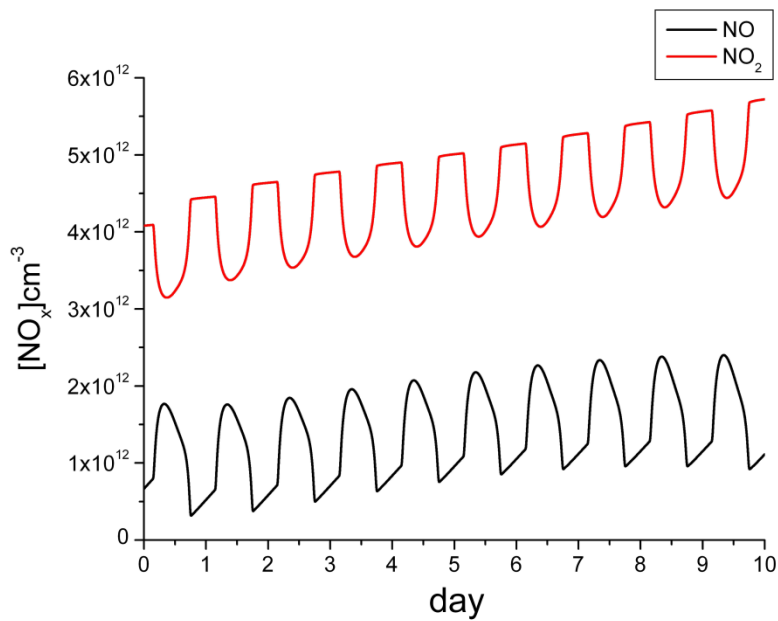


Figure 3.8: Results of the numerical simulations using CBM Leeds mechanism – variation of NO_x in summer time.

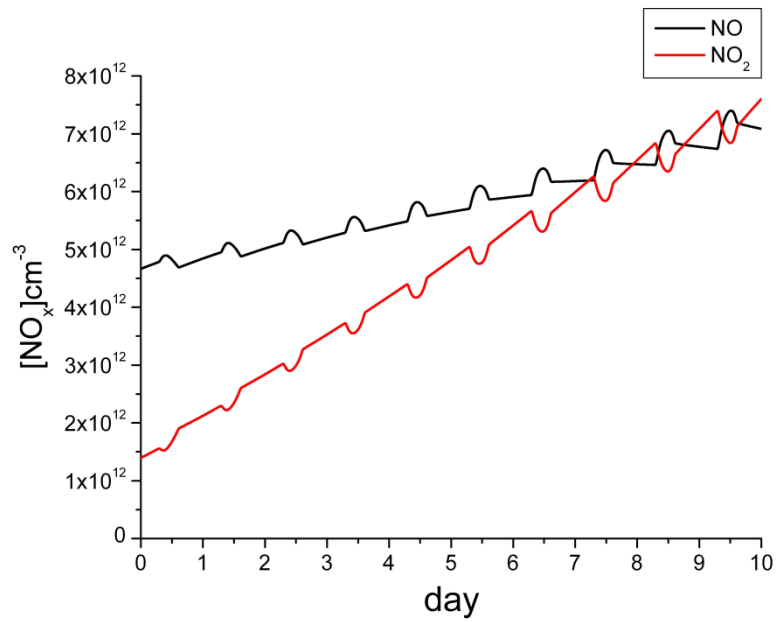


Figure 3.9: Results of the numerical simulations using CBM Leeds mechanism – variation of NO_x in winter time.

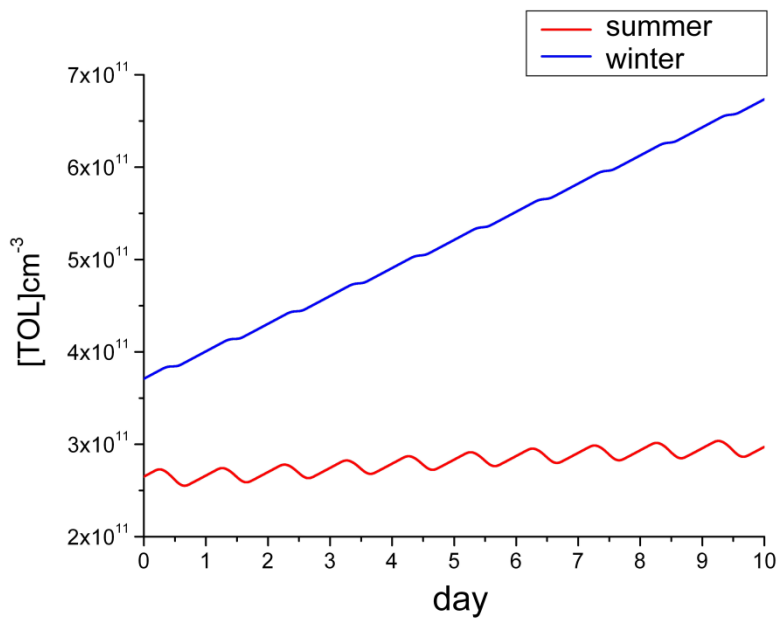


Figure 3.10: Results of the numerical simulations using CBM Leeds mechanism – variation of TOL (toluene) species in summer and winter time.

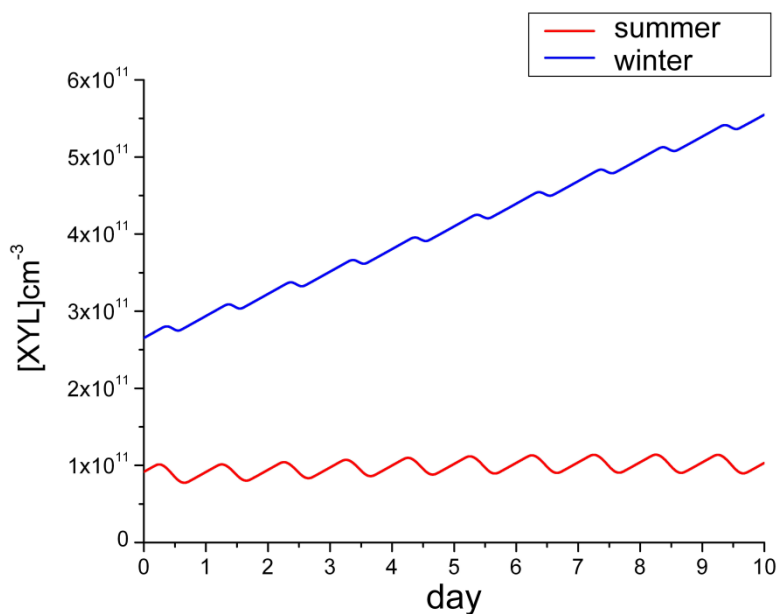


Figure 3.11: Results of the numerical simulations using CBM Leeds mechanism – variation of XYL (xylol) species in summer and winter time.

References

- Atkins P.W., de Paula J., and Atkins P.. 1997. *Physical Chemistry*. Macmillan Higher Education.
- Heard A.C., Pilling M.J., and Tomlin A.S.. 1998. *Mechanism reduction techniques applied to tropospheric chemistry* In: *Atmospheric Environment*. 32. 1059-1073.
- Jacob, D.J.. 1999. *Introduction to Atmospheric Chemistry*. Princeton University Press.
- Mészáros E.. 1977. *The Basics of Atmospheric Chemistry, (In Hungarian)*. Akadémiai Kiadó.
- Pilling M.J. and Seakin P.W.. 1995. *Reaction Kinetics (Oxford Science Publications)*. Oxford University Press, USA.
- Seinfeld J.H. and Pandis S.N.. 2006. *Atmospheric Chemistry and Physics: From Air Pollution to Climate Change*. Wiley.
- Turányi T.. 2010. *Investigation of reaction mechanisms (In Hungarian)*. Akadémiai Kiadó.

Chapter 4. Reactions of air pollutants in the atmosphere

4.1 General notes

Chemical composition of the troposphere has a relative constant composition of gases like oxygen, nitrogen, carbon dioxide and other compounds (Sharma, 2007). The air is utilized by organisms in the process of respiration to liberate chemical energy from organic substances during oxidation. The presence of nitrogen, oxygen and carbon dioxide in the air is of great importance, because these compounds keep cycling in nature between organisms and their environment through various cycles (e.g., carbon, nitrogen and water cycles).

Oxygen (O₂) is available in sufficient amount near to the surface (Figure 4.1), it becomes scarce only at higher altitude, deep in ground and in water soaked soil. Oxygen dissolved in water is used by aquatic organisms. Some of the oxygen is absorbed from the air, while some is also released by plants growing in water. The amount of oxygen dissolved in water depends on the temperature and hydrostatic pressure (depth of the water). Warm water has a lower capacity to dissolved oxygen than the cold one.

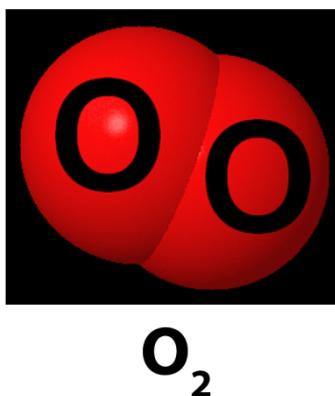


Figure 4.1: Chemical structure of oxygen molecule.

Carbon dioxide (CO₂) provides carbon supply for the plants for photosynthesis. Atmospheric nitrogen (N₂) is directly used by some nitrogen fixing bacteria of some plants' roots. Plants differ in their requirement of aeration. Reduced aeration of soil brings about a number of morphological and physiological effects on plants. Excess of carbon dioxide in soil air may produce some toxic substances like hydrogen sulphide (H₂S), bicarbonates of iron and manganese, acetic acid, oxalic acid and other organic acids. Sometimes carbon dioxide itself has toxic and lethal effects on plants and some soil organisms.

In aquatic habitants the medium is generally deficient in oxygen content. This is due to the fact that much of dissolved oxygen in water defuses in the atmosphere. Carbon dioxide is about 200 times more soluble in water than oxygen. The solubility of these gases also depends on temperature and salinity of the water. The solubility of both these gases decreases in water as a result of increase in temperature and salinity. Thus the oxygen content of lakes is closely related to their thermal stratifications and salinity.

4.2 Reactions of atmospheric oxygen

Oxygen in the troposphere plays an important role in the processes taking place on earth's surface. Oxygen takes part in energy producing reaction like burning of fossil fuels, e.g., oxidation of methane:



Atmospheric oxygen is also used by aerobic organisms in the degradation of organic compounds or in oxidative weathering processes:



The carbon dioxide and water can be utilized by the green plants in the process of photosynthesis and oxygen is again returned back to the atmosphere (Figure 4.2):

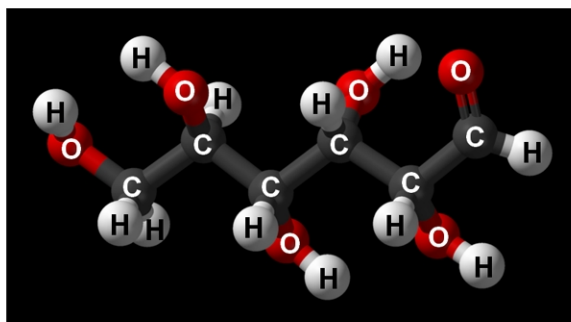
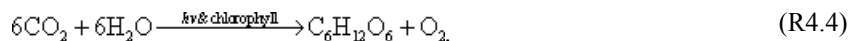


Figure 4.2: Chemical structure of glucose.

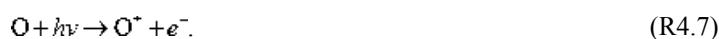
Because of the effect of ionizing radiation, oxygen in the higher atmosphere can exist in some other forms, which are different from those stable forms in lower levels. Therefore, in addition to O_2 (molecular oxygen), the upper atmosphere has also O (oxygen atom), O_2^* (excited oxygen molecule) and O_3 (ozone). The atomic oxygen is very reactive and stable primarily in the thermosphere. It is obtained by a photochemical reaction



Due to this photodissociation of oxygen according to the above reaction and high energy solar radiation molecular oxygen is practically do not exist at very high altitudes. Less than 10% of the oxygen in the atmosphere is present as molecular oxygen (O_2) at altitude exceeding approximately 400 km. Excited oxygen atom can be formed according to reaction



The excited oxygen atom emits visible light at 636 nm, 630 nm and 558 nm wavelengths. Ultraviolet radiation (UV) reacts with oxygen atoms and forms oxygen ions (O^+)



This positively charged oxygen atom can react further at the higher atmosphere



The species O_2^* is also formed in the ionosphere by the absorption of UV radiation



Ozone (O_3) is one of the most important chemical species in the atmosphere (Figure 4.3), because it absorbs harmful ultraviolet radiation and thus protecting living beings from the lethal effects of this ionizing UV radiation. Ozone absorbs UV light strongly in the region of 220 nm and 330 nm. The absorption causes decomposition of ozone. Life existed only in the oceans early in the planet's history where the harmful UV radiation was absorbed and scattered by the water. Photosynthesis in ocean plants then converted CO_2 and H_2O into O_2 (R4.4). When the ocean became saturated with oxygen, the amount of oxygen in the atmosphere gradually increased. Gas-phase oxygen was consumed by two mechanisms: (i) new life forms used O_2 and sugars for metabolism, and (ii) O_3 was formed by the photochemical destruction of molecular oxygen. As concentrations of ozone in the atmosphere began to increase, less UV radiation reached the Earth's surface. Because the ozone absorbed the DNA damaging (ionizing) radiation, therefore, life could slowly begin to exist on the Earth's surface (Figure 4.4).

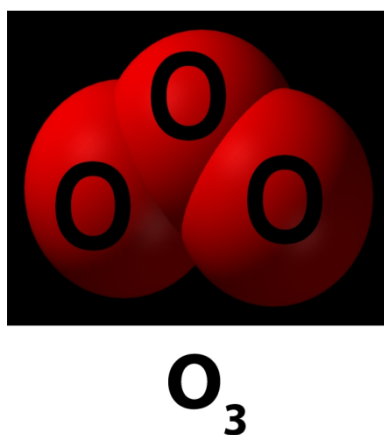


Figure 4.3: Chemical structure of ozone.

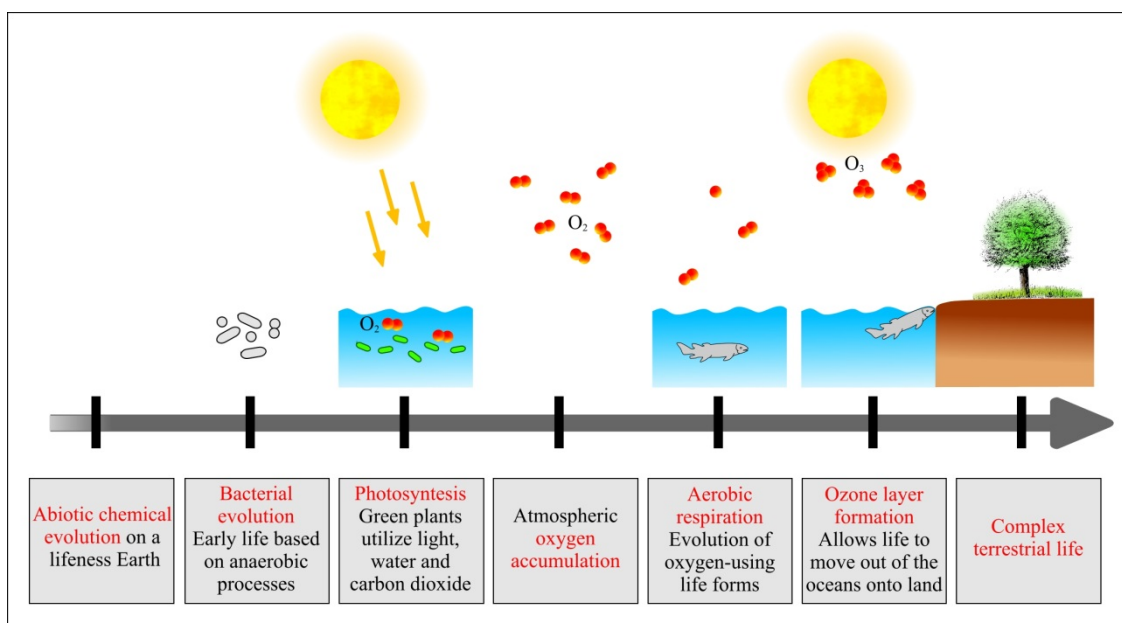


Figure 4.4: Life evolution on the Earth.

4.3 General reactions in the troposphere and stratosphere

Some reactions in the atmosphere involve major gases and occur on global scale, however, others involve trace chemical species on smaller scales (e.g., continental, regional, local scales). Composition of the troposphere shows high variability in mixing ratios of reactive trace species. These compounds are present in low concentration and many of them have short residence time and they are very reactive. Nitrogen oxide (NO) is generated during the combustion processes (e.g., fossil fuel burning, forest fires, lightning discharges)



Nitrogen oxide can be oxidized further producing nitrogen dioxide (NO₂)



It should be noted that, however, the concentration of oxygen is the highest in the atmosphere reaction above (R4.12) would not produce a significant amount of nitrogen dioxide, because this reaction kinetically is very slow. Actually, O₂ is not the most important oxidant for this oxidation reaction. There are other very reactive species, which have the major effect in the oxidation of nitrogen oxide and are present in photochemical smog: ozone (O₃), peroxy radicals (ROO•) and oxyradicals (RO•)

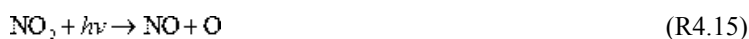


One important tropospheric photochemical reaction is the decomposition of nitrogen dioxide



The atomic oxygen produced in this reaction reacts with molecular oxygen to produce ozone, and this is only the significant pathway to produce ozone in the troposphere.

Radicals also play a very significant role in many atmospheric chemical reactions because of their high affinity to react. The most important radical that plays a very crucial role in many atmospheric chemical reactions is the hydroxyl radical (OH•). This reactive species forms from the following consecutive steps involving photochemical reactions



Atomic oxygen produced in the reaction (R4.15) is ground state oxygen, while oxygen atom produced in reaction (R4.17) is in excited state. For reaction (R4.15) radiation in the visible range supplies sufficient energy, however, in reaction (R4.18) higher energy (UV) radiation is required. Excited state oxygen atoms are essential to form OH• radical with water.

Hydroxyl radical can react with various stable species in the atmosphere and provides other reactive compounds



The hydrogen (H•) and methyl (CH₃•) radicals formed react further



The peroxy radical ($\text{CH}_3\text{OO}\cdot$) is an important oxidant in the oxidation of nitric acid (Seinfeld and Pandis, 2006).

We should remember that many important atmospheric processes are mostly photochemical processes. The energy of solar radiation increases with increasing altitude, therefore photochemistry becomes even more important in the upper atmosphere. Radicals play a dominant role in many atmospheric reactions and the hydroxyl radical is the most reactive compound and it contributes to the oxidative nature of photochemical smog.

A detailed description of reactions of chemical species of carbon, nitrogen, sulphur and oxygen is provided in Chapters 5–8.

References

Seinfeld J.H. and Pandis S.N.. 2006. *Atmospheric Chemistry and Physics: From Air Pollution to Climate Change*. Wiley.

Sharma A.. 2007. *Environmental Chemistry*. GOEL Publishing House, Meerut.

Chapter 5. Biogeochemical cycle of carbon

Carbon, a substantial element for the biosphere, is often referred to as the "building block of life" because living organisms are all based on carbon. Carbon compounds can exist in solid (e.g. diamonds or coal), liquid (e.g. crude oil), or gas (e.g. carbon dioxide) forms. There are three naturally occurring isotopes, with ^{12}C and ^{13}C being stable, while ^{14}C is radioactive, decaying with a half-life of about 5,730 years.

Carbon is stored in and exchanged among four most relevant pools (or reservoirs). In the carbon cycle carbon moves between the hydrosphere, the atmosphere, the geosphere and the biosphere (terrestrial ecosystems). In the non-living pools, carbon is stored as carbonate (CaCO_3 , Figure 5.1) rocks, dead organic matter, such as humus in soil, fossil fuels from dead organic matter, carbon dioxide (CO_2 , Figure 5.2), carbon monoxide (CO , Figure 5.3) carbon dioxide dissolved in water to form HCO_3^- .

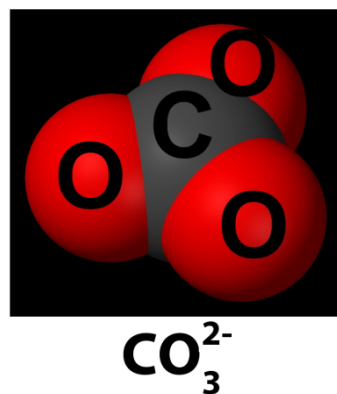


Figure 5.1: Chemical structure of carbonate ion.

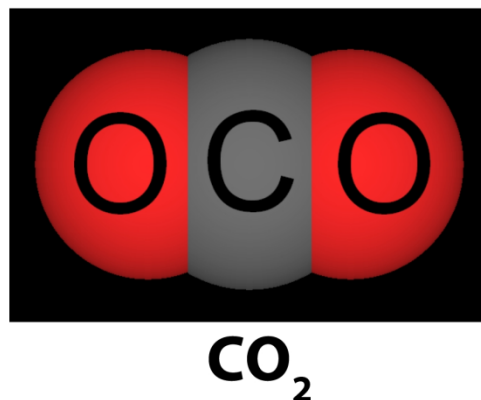


Figure 5.2: Chemical structure of carbon dioxide.

Large continuous carbon fluxes are present among these pools. In atmospheric chemistry the fluxes are considered from the point of view of the atmosphere, usually positive fluxes mean emission to the atmosphere (i.e. the pool where the carbon originates from acts as *source*), negative fluxes mean carbon uptake (i.e. the pool acts as a *sink*). The carbon pools can act both as sources or sinks of carbon, i.e. releasing or absorbing carbon to/from the atmosphere. Usually pools are sources and sinks simultaneously, i.e. carbon is emitted from the pool to the atmosphere in a certain process, and taken up via another process. The system is considered to be in the state of dynamic equilibrium, if the positive fluxes match negative fluxes on longterm average so that the pool size remain constant.

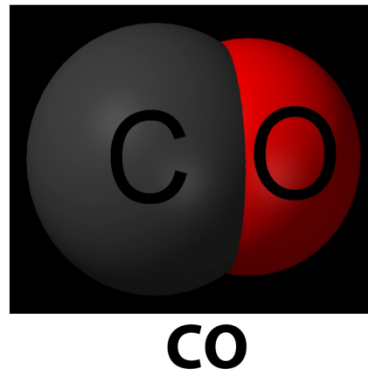


Figure 5.3: Chemical structure of carbon monoxide.

5.1. The natural carbon cycle

Both carbon dioxide (CO_2) and methane (CH_4 , Figure 5.4) play an important role in carbon cycle representing enormous ocean-atmosphere and surface-atmosphere carbon fluxes which had been constant around 280 ppm in the preindustrial era, up until 1750.

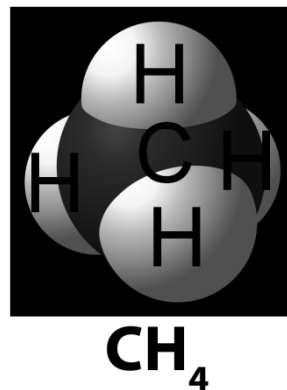


Figure 5.4: Chemical structure of methane.

Carbon dioxide is a long-lived GHG (LLGHG) in the atmosphere. Prehistoric concentrations of CO_2 reconstructed from ice cores showed that previous elevation in CO_2 concentrations during interglacial periods happened gradually by only a few Gt C per decade. The overall variation in CO_2 concentration between glacial interglacial periods barely exceeded 100 ppm. Current high concentrations of CO_2 have not been reached in the last 15 million years.

The carbon budget can be described as the balance or imbalance between sources and sinks of carbon. The most important natural sources of carbon are the ocean, biosphere respiration, geological sources. The gross terrestrial carbon flux transfers ca. 120 Gt C yr^{-1} , the ocean-atmosphere flux is around 90 Gt C yr^{-1} under natural circumstances (black arrows on Figure 5.5). The balance between sources and sinks, i.e. the carbon budget (longterm net flux averaged for a decade or longer time frame) is less than 0.1 Gt C yr^{-1} under undisturbed natural conditions.

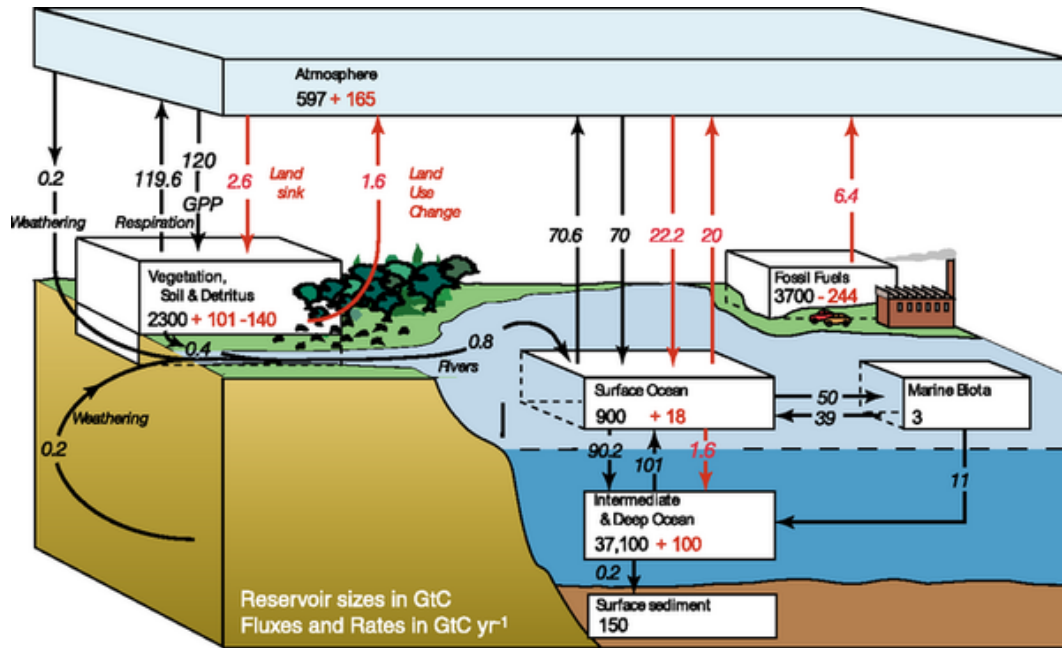


Figure 5.5: The global carbon cycle for the 1990s, showing the main annual fluxes in GtC yr^{-1} : pre-industrial ‘natural’ fluxes in black and ‘anthropogenic’ fluxes in red (modified from Sarmiento and Gruber, 2006, with changes in pool sizes from Sabine et al., 2004a). The net terrestrial loss of -39 GtC is inferred from cumulative fossil fuel emissions minus atmospheric increase minus ocean storage. The loss of -140 GtC from the ‘vegetation, soil and detritus’ compartment represents the cumulative emissions from land use change (Houghton, 2003), and requires a terrestrial biosphere sink of 101 GtC (in Sabine et al., given only as ranges of -140 to -80 GtC and 61 to 141 GtC , respectively; other uncertainties given in their Table 1). Net anthropogenic exchanges with the atmosphere are from Column 5 ‘AR4’ in Table 7.1. Gross fluxes generally have uncertainties of more than $\pm 20\%$ but fractional amounts have been retained to achieve overall balance when including estimates in fractions of GtC yr^{-1} for riverine transport, weathering, deep ocean burial, etc. ‘GPP’ is annual gross (terrestrial) primary production. Atmospheric carbon content and all cumulative fluxes since 1750 are as of end 1994. Source: IPCC AR4 Fig. 7.3.

5.1.1. Terrestrial processes

Carbon is taken up by the biosphere through autotrophs, which are organisms capable of synthesizing their own nutrients from inorganic substances. There are two types of autotrophs between which the main difference lies in the source of energy they use for the synthesis. Photoautotrophs (most autotrophs, such as green plants, certain algae, and photosynthetic bacteria) use light for energy. Chemoautotrophs (e.g. chemosynthetic bacteria) use energy from chemical reactions, e.g. from oxidization of electron donors.)

Most of the terrestrial CO_2 flux takes place through terrestrial vegetation that absorbs CO_2 via the photosynthesis, although most of that amount is respired back to the atmosphere (Figure 5.5). The most important land carbon pools are the terrestrial vegetation, soil and detritus. The carbon fluxes between the atmosphere and these pools take place on relatively small time scales, therefore this part of the carbon cycle is sometimes referred to as the *fast carbon cycle*. On the shortest time scales of seconds to minutes, plants take carbon out of the atmosphere through photosynthesis and release it back into the atmosphere via respiration.

The amount of CO_2 that is converted to carbohydrates in the photosynthesis is known as *gross primary production* (GPP). Part of this carbon is assimilated to support plant growth and functioning, the other part is respired. The annual difference between GPP and autotrophic respiration (R_a), i.e. the annual plant growth, is called *net primary production* (NPP, equation (5.1)). Terrestrial photosynthesis is estimated to be around 120 Gt C yr^{-1} (see Figure 5.5)

$$\text{NPP} = \text{GPP} - R_a \quad (5.1)$$

On longer time scales, most dead biomass moves to the soil organic matter and detritus pools, where it can be stored for years, decades or centuries. Several soil organic matter pools with different residence times can be defined. Eventually this carbon is respired back to the atmosphere by soil microbes and fungi, decomposed at a rate depending on their chemical composition and environmental circumstances (moisture, temperature etc.). When oxygen is present aerobic respiration occurs, which releases carbon dioxide. In the oxygen limited environment anaerobic respiration occurs, producing methane instead of CO₂.

Carbon entering the terrestrial biosphere via photosynthesis is emitted back via (i) autotrophic respiration, (ii) heterotrophic respiration (decomposers and herbivores) (iii) fires (combustion). The net ecosystem production shows the net amount of carbon removed from (or released to) the atmosphere i.e. gained (or lost) by the ecosystem when no other disturbances (carbon loss of the ecosystem) are considered.

$$\text{NEP} = \text{NPP} - \text{Rh} \quad (5.2)$$

Taking into account other carbon losses, e.g. transport of biomass from agricultural lands, fires etc. shows us the carbon sequestered by the terrestrial biosphere, the net biome production (NBP). In a system being in equilibrium, NBP should be zero.

5.1.2. Oceanic processes

The ocean is another major sink of carbon, under natural circumstances it removes CO₂ equivalent to ca. 70 Gt C yr⁻¹ from the atmosphere (Figure 5.5). Before the industrial revolution, the ocean contained about 60 times as much carbon as the atmosphere and 20 times as much carbon as the terrestrial biosphere/soil compartment.

There are different processes involved in the removal of CO₂ transporting carbon to different depths associated with different residence times. Because of the speed of the participating processes, this part is sometimes referred as the *slow carbon cycle*. Oceanic carbon exists in several forms: as *dissolved inorganic carbon* (DIC), *dissolved organic carbon* (DOC), and *particulate organic carbon* (POC) (living and dead). Basically three main processes govern carbon absorption: the *solubility pump* (CO₂ exchange driven by solubility of atmospheric CO₂), the *organic carbon pump* (driven by photosynthetic uptake by marine biota and sinking of this carbon as organic particles to deeper layers) and the *CaCO₃ counter pump* (driven by release of CO₂ during the formation of CaCO₃ shells). The organic carbon pump and carbonate pump processes are the so-called biological pumps, while the solubility pump is sometimes referred as the physical pump (Figure 5.6).

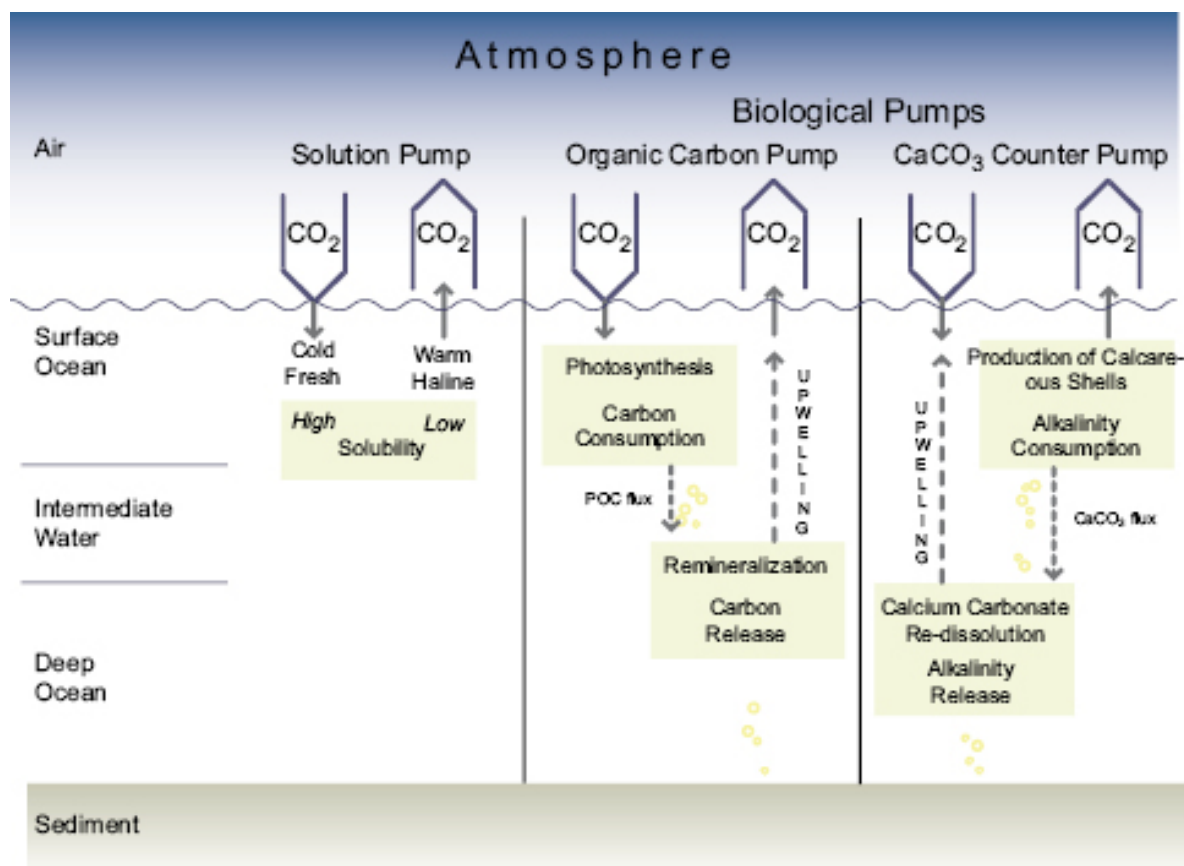
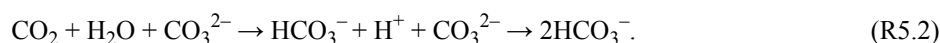


Figure 5.6: Physical pump and biological pump. Three main ocean carbon pumps govern the regulation of natural atmospheric CO₂ changes by the ocean (Heinze et al., 1991): the solubility pump, the organic carbon pump and the CaCO₃ ‘counter pump’. The oceanic uptake of anthropogenic CO₂ is dominated by inorganic carbon uptake at the ocean surface and physical transport of anthropogenic carbon from the surface to deeper layers. For a constant ocean circulation, to first order, the biological carbon pumps remain unaffected because nutrient cycling does not change. If the ocean circulation slows down, anthropogenic carbon uptake is dominated by inorganic buffering and physical transport as before, but the marine particle flux can reach greater depths if its sinking speed does not change, leading to a biologically induced negative feedback that is expected to be smaller than the positive feedback associated with a slower physical downward mixing of anthropogenic carbon. Source IPCC AR4 Fig. 7.10

The solubility pump

The marine carbonate buffer system allows the ocean to take up CO₂ far in excess of its potential uptake capacity based on solubility alone, and in doing so controls the pH of the ocean. This control is achieved by a series of reactions that transform carbon added as CO₂ into bicarbonate (HCO₃⁻) and carbonate (CO₃²⁻). These three dissolved forms are collectively known as DIC. CO₂ is a weakly acidic gas and the minerals dissolved in the ocean have over geologic time created a slightly alkaline ocean (surface pH 7.9 to 8.25). When it dissolves, it reacts with water to form carbonic acid, which dissociates into a hydrogen ion (H⁺) and a HCO₃⁻ ion, with some of the H⁺ then reacting with CO₃²⁻ to form a second HCO₃⁻ ion

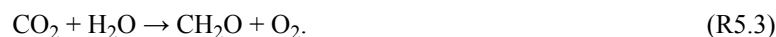


The air-sea exchange of CO₂ is determined largely by the air-sea gradient in pCO₂ between atmosphere and ocean. Equilibration of surface ocean and atmosphere occurs on a time scale of roughly one year. Gas exchange rates increase with wind speed and depend on other factors such as precipitation, heat flux, sea ice and surfactants. The magnitudes and uncertainties in local gas exchange rates are maximal at high wind speeds. In contrast, the equilibrium values for partitioning of CO₂ between air and seawater and associated seawater pH values are well established.

Cold, CO₂ rich waters near the poles during local winters (the lower temperature the higher the solubility) and more dense, therefore sink to greater depths with the Meridional Overturning Circulation creating the solubility pump.

Organic carbon pump

The organic carbon pump (Figure 5.6) is the process in which CO₂ is incorporated to organic matter in the photosynthesis. Part of the particulate organic carbon sinks to deeper layers where it gets decomposed and respired by bacteria and transported back to surface layers by marine circulation as DIC. Other part of POC sinks deeper and settles on the bottom of the ocean to be stored there with thousand years of residence time. The efficient organic pump performs a net carbon removal from the atmosphere also decreasing the total carbon content in the surface layers by developing organic matter in the photosynthesis



The efficiency of the organic pump is limited via the photosynthesis by the availability of light, nutrients and oxygen. Figure 5.7 shows an example of ocean primary productivity in a period of year 2001 based on MODIS imagery.

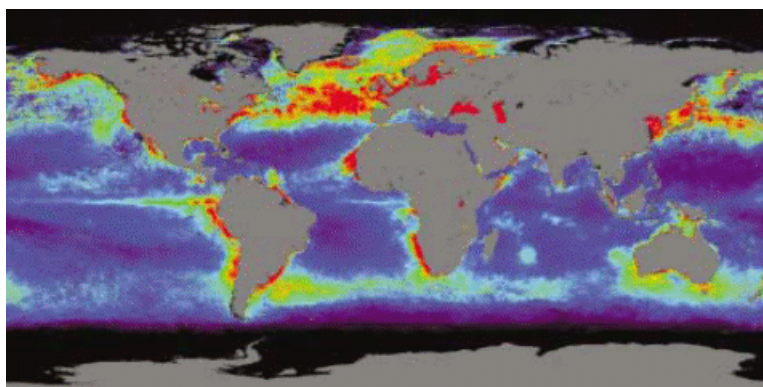
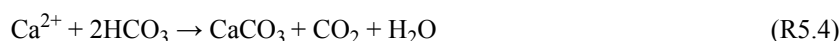


Figure 5.7: The global carbon cycle is greatly influenced by ocean primary productivity, the rate of carbon dioxide uptake via marine plant photosynthesis minus the rate that carbon dioxide is put back into the ocean's carbon reservoir through respiration. This MODIS composite from May 9 to June 9, 2001 shows how variable the rates of carbon exchange are across the Earth's oceans. Productivity tends to be high at northern and southern latitudes, where mixing from deep ocean waters brings up nutrients, and at the margins of continents, where currents draw up nutrients in the shallower waters of the continental shelves. Black areas indicate regions where productivity could not be calculated, typically because of clouds or sea ice. Image credit: MODIS Ocean Team/Ocean Primary Productivity, Wayne Esaias, Principal Investigator, NASA-GSFC; Kevin Turpie, SAIC/GSC.

Carbonate pump

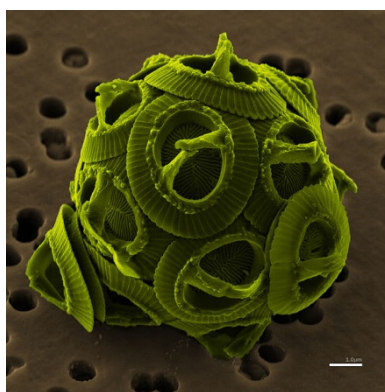
The other component of the biological pump is based on the formation of carbonate and silicate shells, the ions are used by diatoms (silica-secreting organisms, e.g. Figure 5.8) and coccolithophorids (carbonate-secreting organisms, e.g. Figure 5.9) The carbonate ions produced in chemical weathering of carbonate rocks and the solution of CO₂ in surface seawater play important role in the biological pump as well. The production of solid CaCO₃ (that is, "carbonate precipitation") occurs in the surface waters of the ocean, both organically - by organisms that build their shells from CaCO₃ - and inorganically according to the chemical equilibrium in the oceans according to the following chemical equation:



In the reaction above to form one CaCO₃, one CO₂ is produced, which means that although the DIC concentration is decreased in this process, CO₂ partial pressure will increase affecting solubility of atmospheric CO₂ in the surface ocean. In contrary, the formation of silica shells does not produce CO₂, hence being a more effective process regarding carbon sequestration.



Figure 5.8: Diatom

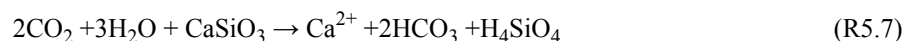
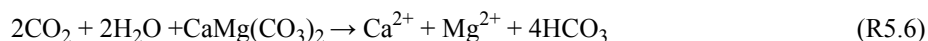
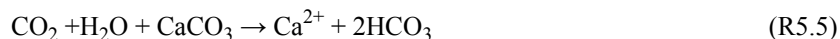
Figure 5.9: Coccolithophorid. *Gephyrocapsa oceanica* Kamptner from Mie Prefecture, Japan. SEM:JEOL JSM-6330F. Scale bar = 1.0 µm. (Source: wikipedia)

5.1.3 Geological processes

On still longer time scales, organic matter that became buried in deep sediments (and protected from decay) is slowly transformed into deposits of coal, oil and natural gas, the fossil fuels we use today. When we burn these substances, carbon that has been stored for millions of years is released once again to the atmosphere in the form of CO_2 .

Silicate weathering and atmospheric CO_2

A small amount of carbon is absorbed in the process of weathering and carried to the ocean by surface water and stored there for longer term. Chemical weathering of rocks are represented by reactions (R5.5) and (R5.6) for carbonates, and reactions (R5.7) and (R5.8) for silicates



In longterm control of atmospheric CO_2 weathering plays an important role (Fig 5.5). CO_2 dissolved in surface waters participates in weathering of rocks (R5.5 – R5.8). The ions produced in the weathering process are carried away to the ocean by rivers where they are used by marine biota to form carbonate and silicate tissues. After sinking to the ocean sediment the weathering products are built in carbonate rocks in the sea crust where the carbon can be stored for several thousand years.

5.2 Methane

At room temperature and standard pressure, methane is a colorless, odorless gas. In the atmosphere it is a „well mixed” greenhouse gas due to its relatively long lifetime in the atmosphere, and it belongs to the group of long-lived greenhouse gases (LLGHGs). Once emitted, CH₄ remains in the atmosphere for approximately 8.4 years before removal. Methane is a potent GHG hence being of great interest among atmospheric scientists.

5.2.1 Sources and sinks of atmospheric methane

Sources

Methane has biogenic and non-biogenic (geological) natural sources. The most important biogenic source is anaerobic decomposition on wetlands, where methane is produced through anaerobic decomposition in soils and sediments. Warm temperatures and moist environments are especially favourable for methane production.

Slow decomposition rates generally cause nontidal wetlands to accumulate carbon as dead soil organic matter and/or peat; in other words, these systems act as an atmospheric CO₂ sink. This source is highly sensitive to temperature so that changes in the global climate toward warmer conditions could, depending on the moisture changes, lead to significant increases in CH₄ emissions and a positive feedback causing further warming. A significant drying of current wetland areas however would lead to diminished CH₄ emissions and most likely to a net release of CO₂ to the atmosphere.

Microorganisms breaking down difficult to digest material in the guts of ruminant livestock and termites produce methane that is then released during defecation. Non biogenic sources of methane are permafrost, glaciers, and ice cores. Large amounts of methane is stored in permafrost areas being released when melting. Frozen soils can be a source that slowly releases methane trapped in frozen environments as global temperatures rise.

Mass burning of organic matter releases huge amounts of methane into the atmosphere. Additional natural sources include termites, oceans, vegetation and CH₄ hydrates. Methane is stored in large amounts in deep ocean deposits in form of methane hydrate. Methane hydrate is a solid form of methane combined with water under low temperatures (less than 25°C) and moderate pressure (greater than 3–5 MPa). These circumstances can be found around 300–500 m depth. With increasing temperature or decreasing pressure the methane hydrate stored in deep oceans can be released in large amounts calling scientists' attention to warming climate.

Sinks

Hydroxyl radical ($\cdot\text{OH}$) in the atmosphere is the largest sink for atmospheric methane as well as one of the most significant sources of water vapor in the upper atmosphere



Because tropospheric reactions with $\cdot\text{OH}$ is the main sink of CH₄ the abundance of $\cdot\text{OH}$ regulates lifetime of methane. Reducing quantities of atmospheric $\cdot\text{OH}$ as a result of biomass

burning therefore increases lifetime of methane. Isoprene, an organic carbon compound emitted by vegetation competes with methane for $\cdot\text{OH}$, therefore isoprene increases lifetime of CH₄ by lowering $\cdot\text{OH}$ concentration.

CH₄ is lost to the stratosphere when it reacts with $\cdot\text{OH}$, Cl and O(¹D). Methane oxidation is a source of water in the stratosphere



Water vapor is important being a greenhouse gas and stratospheric ozone chemistry. Some of the methane in soils is metabolized by methanotrophs (methane-consuming microorganisms). Biological CH₄ oxidation in drier soil is carried out by microorganisms that use methane in their metabolism (methanotrophs) under aerobic conditions, producing carbon dioxide and water



Under anaerobic condition methane is oxidized in the following reaction combining with nitrate/nitrites



Methane also reacts with natural chlorine gas in the atmosphere to produce chloromethane and hydrochloric acid (HCl). This process is known as free radical halogenations.

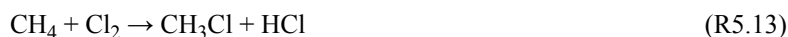


Table 5.1: Atmospheric sources and sinks of methane (IPCC AR4 2007)

		Emission [Tg(CH ₄) yr ⁻¹]
	Total sources	582
	Imbalance	+1
Sinks	Soils	30
	Tropospheric OH	511
	Stratospheric loss	40
	Total sink	581

5.3 Human disruption of carbon cycle

Human activities have altered the natural cycles of GHGs. The natural carbon cycle has been shifted toward accumulation in the atmosphere. Human activities accounting for the majority of anthropogenic carbon compound emission include fossil fuel burning, land use change (most importantly deforestation, increasing agricultural lands) emitting CO₂ and methane as well.

In the contemporary cycle of methane, natural sources of account for 40% of the annual emissions while anthropogenic emissions account for the other 60% of methane released to the atmosphere. The atmospheric abundance of methane before the industrial era has varied from lows of about 400 ppb during glacial periods to highs of about 700 ppb during interglacials based on examination of ice cores. Based on the latest analysis of WMO GAW program, in 2011, the global average abundance of CH₄ is 1813±2 ppb. Present atmospheric levels of CH₄ are unprecedented in at least the last 650 kyr. The growth rate of CH₄ decreased from ~13 ppb/yr during the early 1980s to near zero during 1999–2006. Since 2007, atmospheric CH₄ has been increasing again, with a nearly constant rate during 3 years.

Methane (CH₄) sources to the atmosphere generated by human activities exceed CH₄ sources from natural systems. Between 1960 and 1999, CH₄ concentrations grew an average of at least six times faster than over any 40-year period of the two millennia before 1800, despite a near-zero growth rate since 1980. The human activities that produce CH₄ include energy production from coal and natural gas, waste disposal in landfills, raising ruminant animals (e.g., cattle and sheep), rice agriculture and biomass burning. At the same time, wetlands and rice paddies emit about 175 Tg CH₄ annually. The warmer and moister the rice field, the more methane is produced.

Waste water treatment facilities are responsible for CH₄ emissions as anaerobic treatment of organic compounds in the water results in the production of methane. Decaying organic matter and anaerobic conditions cause landfills to be a significant source of methane.

In 2011, CO₂ concentration in the atmosphere reached 390.9±0.1 ppm (based on WMO GAW measurements), which means an increase of 140% compared to preindustrial level. The additional CO₂ emitted to the atmosphere by human activities (the *anthropogenic CO₂*) has altered the natural carbon cycle. Since the beginning of the industrial era, human activity released large amount of carbon mainly from the longterm pools due to fossil fuel burning. Main sources of anthropogenic emissions include (i) CO₂ from fossil fuel burning and cement production, newly

released from hundreds of millions of years of geological storage (ii) deforestation and turning lands into agricultural fields releasing carbon, which has been stored for decades to centuries. As a result, net land-atmosphere and ocean-atmosphere fluxes have become significantly different from zero (also see red arrows in Fig. 5.5). This latter component of human induced carbon emission associated with land use change is the most uncertain part of anthropogenic emission estimations.

Arrhenius was the first who proposed the idea that CO₂ emitted from fossil fuel burning and combustion can be large enough to cause global temperature increase due to the greenhouse effect. The first continuous measurement of atmospheric CO₂ concentration started in 1958 at Mauna Loa Observatory Hawaii by Charles David Keeling. Keeling's measurements showed the first significant evidence of rapidly increasing carbon dioxide levels in the atmosphere. Many scientists credit Keeling's graph (Fig 5.10) with first bringing the world's attention to the current increase of carbon dioxide in the atmosphere, which, based on Arrhenius' theory can lead to a global temperature change.

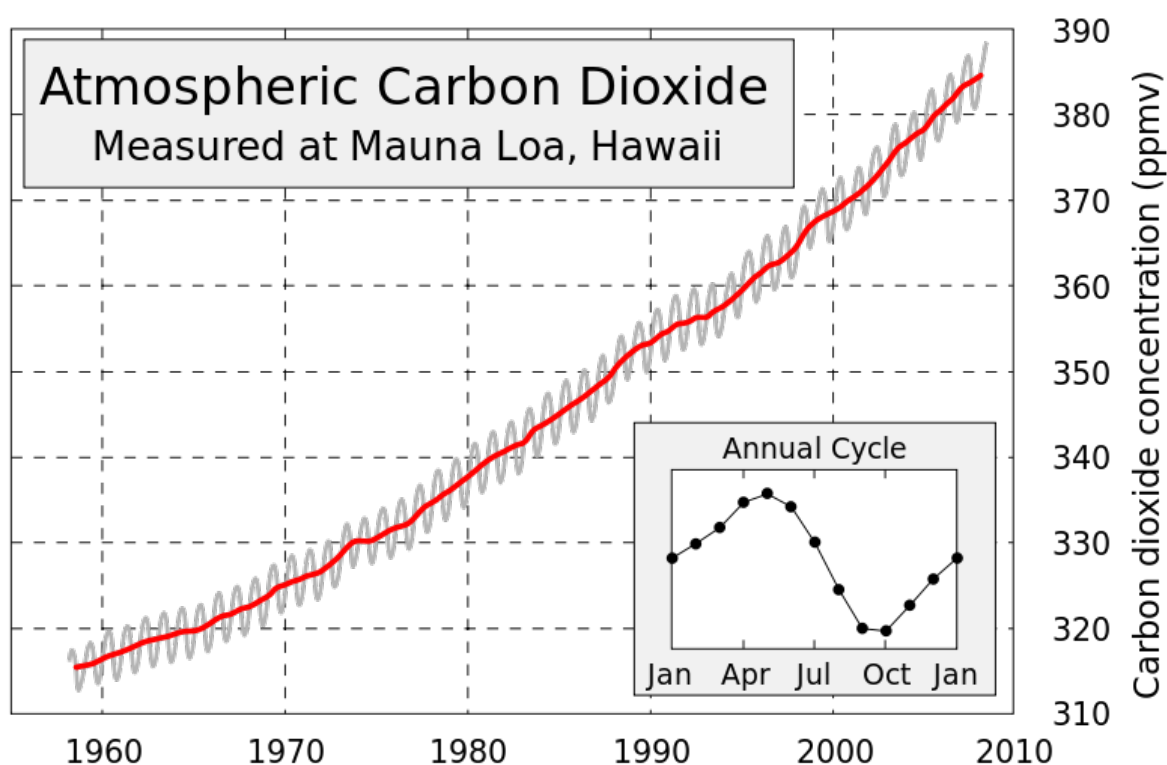


Figure 5.10: The Keeling curve. source: Wikipedia

This figure shows the history of atmospheric carbon dioxide concentrations as directly measured at Mauna Loa, Hawaii. This curve is known as the Keeling curve, and is an essential piece of evidence of the man-made increases in greenhouse gases that are believed to be the cause of global warming. The longest such record exists at Mauna Loa, but these measurements have been independently confirmed at many other sites around the world. The annual fluctuation in carbon dioxide is caused by seasonal variations in carbon dioxide uptake by land plants. Since many more forests are concentrated in the Northern Hemisphere, more carbon dioxide is removed from the atmosphere during Northern Hemisphere summer than Southern Hemisphere summer. This annual cycle is shown in the inset figure by taking the average concentration for each month across all measured years. The grey curve shows the average monthly concentrations, and red curve is a moving 12 month average.

The increase in atmospheric CO₂ concentration is known to be caused by human activities because the character of CO₂ in the atmosphere, in particular the ratio of its heavy to light carbon atoms, has changed in a way that can be attributed to addition of fossil fuel carbon. In addition, the ratio of oxygen to nitrogen in the atmosphere has declined as CO₂ has increased; this is as expected because oxygen is depleted when fossil fuels are burned. A heavy form of carbon, the carbon-13 isotope, is less abundant in vegetation and hence in fossil fuels that were formed from past vegetation, and is more abundant in carbon in the oceans and in volcanic or geothermal emissions. The relative amount of the carbon-13 isotope in the atmosphere has been declining, showing that the added carbon

comes from fossil fuels and vegetation. Carbon also has a rare radioactive isotope, carbon-14, which is present in atmospheric CO₂ but absent in fossil fuels. Prior to atmospheric testing of nuclear weapons, decreases in the relative amount of carbon-14 showed that fossil fuel carbon was being added to the atmosphere.

Atmospheric CO₂ concentration however increases with half of the rate of anthropogenic emissions. The fraction of anthropogenic emission that remains in the atmosphere is known as the airborne fraction. The airborne fraction, considering anthropogenic emissions to be relatively well constrained can be good indicators short and longterm changes in CO₂ sink processes.

According to the original theory, the residual sink (formerly the 'missing sink') takes up about half of the anthropogenic emission. The residual sink is the increased carbon absorbing capacity of terrestrial vegetation and oceans as a response to changing environment, increasing CO₂ burden of the atmosphere. In other words, net carbon balance, i.e. NBP of terrestrial ecosystems is negative (meaning uptake). Estimation of carbon amount taken up by the residual sink greatly depends on our assumptions on land use change emissions, as the residual sink is determined using inverse modeling. Careful analysis reveals that the global uptake of anthropogenic carbon dioxide emissions by carbon sinks has doubled during the past 50 years – but the fractions of this absorbed by land and by sea remain unclear. A drawback of the net uptake of CO₂ by the ocean, is ocean acidification. It makes seawater more acidic with potentially large impacts on the ocean food chain.

Although terrestrial vegetation is currently a net sink of CO₂, aboveground biomass cannot increase indefinitely. Ultimately the most important storage place for organic carbon is the soil, and it holds the greatest potential to act as a longterm sink for atmospheric CO₂. Changes in soil carbon storage, however will not occur in isolation from changes in other trace gas exchanges which raises important scientific questions for GHG mitigation efforts.

The appropriate knowledge of the responses these processes give to climate variability is critical to assess the effect of global change to their capacity to absorb CO₂ and hence moderate atmospheric increase of CO₂.

Factors affecting absorbing capacities of terrestrial vegetation and oceans: (i) direct climatic effects (precipitation, temperature, radiation changes) (ii) changes in atmospheric constituents ('CO₂ fertilization', nutrient deposition (N, P), damage caused by pollutants) (iii) land use change (deforestation, afforestation, agricultural management practices).

(i) Direct climatic effects

Climate and the carbon cycle is closely coupled, as it is best shown by glacial-interglacial cycles (Figure 5.11). During glacial periods, CO₂ concentration is lower compared to interglacials suggesting the close coupling with temperature. Dissolved carbon is released from oceans as CO₂ in higher temperatures and gets dissolved in lower temperatures. Atmospheric CO₂ level responds to short term climate variability as well such as the El Nino-Southern Oscillation and Arctic Oscillation and even to climate perturbation from volcanic eruptions.

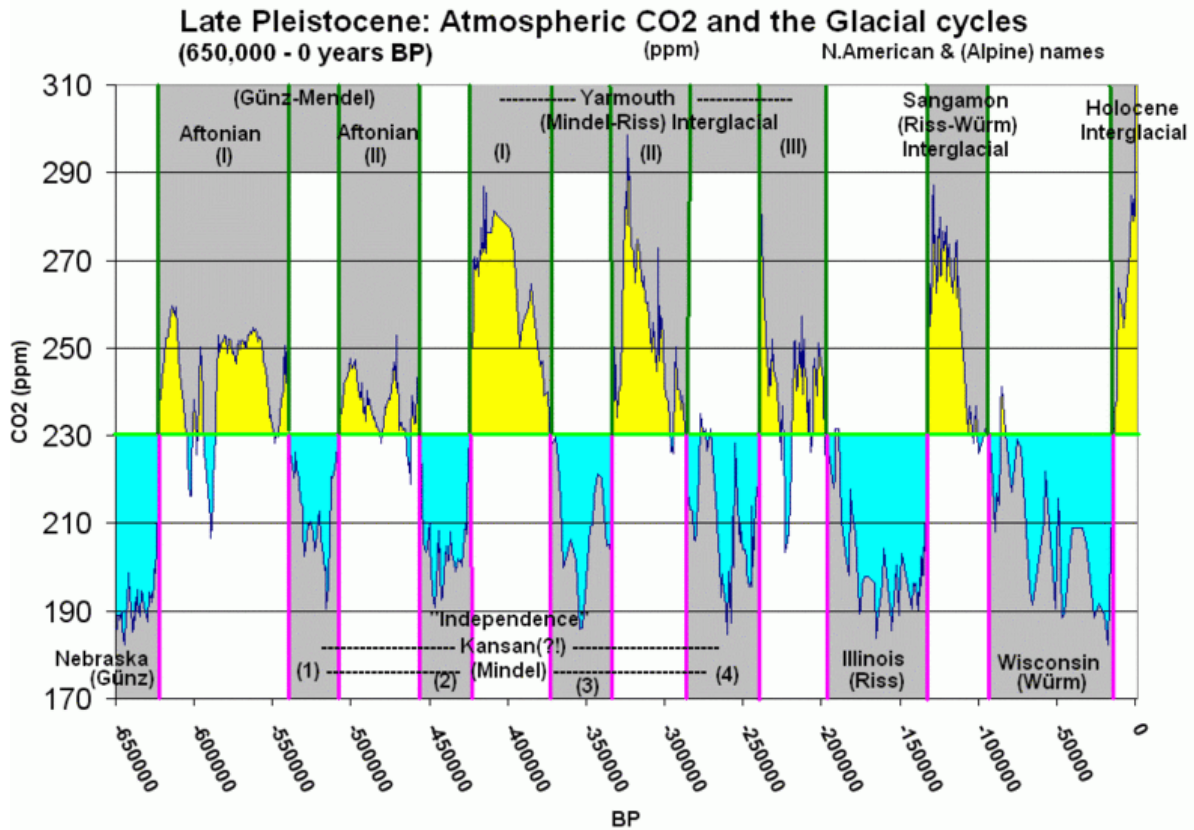


Figure 5.11 This graph shows the newest Ice Core data for Atmospheric CO₂ from air bubbles in the ice. 230 ppm is marked as a transition level and colored "glacial periods" blue and interglacial periods yellow. There's a clear 80,000–110,000 period of repeating glacier even if they vary in quality. Human deforestation and burning of fossil fuel has raised atmospheric CO₂ to over 380 ppm in the last century, well above pre-industrialized levels, and "off the scale" of this graph top.

(ii) Changes in atmosphere chemical composition

There are numerous ways for atmospheric concentration of CO₂ to influence ecosystem functioning. In the FACE (Free-Air Carbon Dioxide Enrichment) experiments, the effect of elevated CO₂ concentration on ecosystems was examined performing in-situ measurements. One would expect an increase in assimilation when more CO₂ is available for the photosynthesis. However, this CO₂ fertilization can be overruled by environmental or nutrient limitations.

(iii) Land-use change

Land cover and land use changes occur naturally due to e.g. changes in climate, or caused by human activity such as agricultural management or appearance of new diseases.

Currently 1/3 of the total anthropogenic CO₂ emission is related to deforestation especially on the tropics. Emission due to land use change is currently the most uncertain part of the anthropogenic carbon emission estimations. Agricultural management practices can influence carbon sequestration by agricultural soils when applied properly. Atmosphere-ocean carbon fluxes are influenced by several factors depending on the scale of the processes involved. The effectiveness of the solubility pump is governed by the intensity of ocean circulation, sea surface temperature, salinity, ocean stratification, ice cover. The biological pump is basically determined by the amount of the sinking part of POC and DOC, influenced by nutrient supply, ocean circulation.

Table 5.2: The contemporary carbon budget. Source: IPCC Table 7.1

The global carbon budget (GtC yr^{-1}); errors represent ± 1 standard deviation uncertainty estimates and not interannual variability, which is larger. The atmospheric increase (first line) results from fluxes to and from the atmosphere: positive fluxes are inputs to the atmosphere (emissions); negative fluxes are losses from the atmosphere (sinks); and numbers in parentheses are ranges. Note that the total sink of anthropogenic CO_2 is well constrained. Thus, the ocean-to-atmosphere and land-to-atmosphere fluxes are negatively correlated: if one is larger, the other must be smaller to match the total sink, and vice versa.

Carbon budget (2000–2005)	
(GtC yr ⁻¹)	
AR4	
Atmospheric Increase	4.1 ± 0.1
Emissions (fossil + cement)	7.2 ± 0.3
Net ocean-to-atmosphere flux	-2.2 ± 0.5
Net land-to-atmosphere flux	-0.9 ± 0.6
Partitioned as follows	
Land use change flux	n.a.
Residual terrestrial sink	n.a.

5.4 Carbon cycle research in Hungary

Carbon cycle related research including measurements has a long tradition in Hungary going back to decades and is carried out by several research groups by now. An overview of the history and results of these activities for CO_2 and non- CO_2 GHGs is provided by Haszpra (ed) (2011).

Eddy covariance (EC) technique is used at three sites in Hungary to monitor ecosystem-atmosphere CO_2 exchange over grasslands and croplands (Table 5.3). EC measurements started at Hegyhátsál site in 1997 to monitor CO_2 fluxes over a heterogeneous agricultural landscape. The measurements are unique in the country being the only measurements over cropland and due to the measurements height, which is 82 m providing regional scale information on the surrounding area. CO_2 mixing ratio measurements started in 1994 at the site, followed by measurements of other GHGs (CH_4 , CO , H_2 , N_2O , SF_6).

Soil CO_2 and CH_4 emissions were measured at sites of different soil and vegetation type including agricultural land (Tóth et al., 2010), grassland (Horváth et al., 2008).

Table 5.3. Eddy covariance monitoring sites in Hungary

Site name and ID	coordinates	vegetation	measurement height	period
Bugac HU-Bug	46.6917, 19.6017	grass	4 m	2002–
Hegyhátsál HU-He1	46.9559, 16.6520	cropland	82 m	1997–
Hegyhátsál 2 HU-He2	46.9558, 16.6556	grass	3 m	1998–2000
Mátra HU-Mat	47.8418, 19.7260	grass	4 m	2002–

References

Barcza Z.. 2001. *Long term atmosphere/biosphere exchange of CO_2 in Hungary - Ph.D. Thesis* <http://nimbus.elte.hu/~bzoli/thesis>. Eötvös Loránd University, Department of Meteorology, Budapest.

Haszpra L.. 2011. *Atmospheric Greenhouse Gases: The Hungarian Perspective*. ISBN 978-90-481-9949-5 (Print). ISBN 978-90-481-9950-1 (Online).

- Haszpra L.. 1995. *Carbon dioxide concentration measurements at a rural site in Hungary*. Tellus. 47B:14-22.
- Haszpra L., Barcza Z., Bakwin P.S., Berger B.W., Davis K.J., and Weidinger T.. 2001. *Measuring system for the long-term monitoring of biosphere/atmosphere exchange of carbon dioxide*. J Geophys Res. 106D:3057-3070..
- Horváth L., Grosz B., Machon A., Balogh J., Pintér K., and Czóbel S.. 2008. *Influence of soil type on N₂O and CH₄ soil fluxes and in Hungarian grasslands, IPCC Fourth Assessment Report: Climate Change*. Commun Ecol. Volume 9. Supplement 1. 75-80.. 10.1556/ComEc.9.2008.S.11.
- National Inventory Report for 1985-2006 Hungary (available online: http://klima.kvvm.hu/documents/32/NIR_HUN_080415.pdf)*. Hungarian Meteorological Service, Greenhouse Gas Inventory Division. 2008.
- Tóth E., Barcza Z., Birkás M., Gelybó Gy., Zsembeli J., Bottlik L., Davis K.J., Haszpra L., Kem A., Kljun N., Koós S., Kovács Gy., Stingli A., and Farkas Cs.. 2010. *Measurements and estimations of biosphere-atmosphere exchange of greenhouse gases - Arable lands*. In: Haszpra L (ed.): *Atmospheric Greenhouse Gases: The Hungarian Perspective* Springer. ISBN: 978-90-481-9949-5.
- http://www.wmo.int/pages/prog/arep/gaw/ghg/documents/GHG_Bulletin_No.8_en.pdf

Chapter 6. Nitrogen compounds

Nitrogen is the main constituent of the Earth's atmosphere. Molecular nitrogen (N_2) is a colorless odorless gas, with an atmospheric abundance of 78% (Figure 6.1). Nitrogen compounds play an important role in atmospheric chemistry, and some chemical forms are potent greenhouse gases.

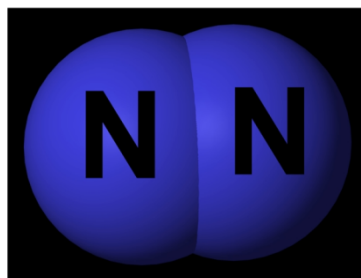


Figure 6.1: Chemical structure of nitrogen molecule

Besides carbon, hydrogen and oxygen, nitrogen is among the most important elements for the biosphere. It can be found in proteins, nucleic acids, vitamins, enzymes and other organic compounds.

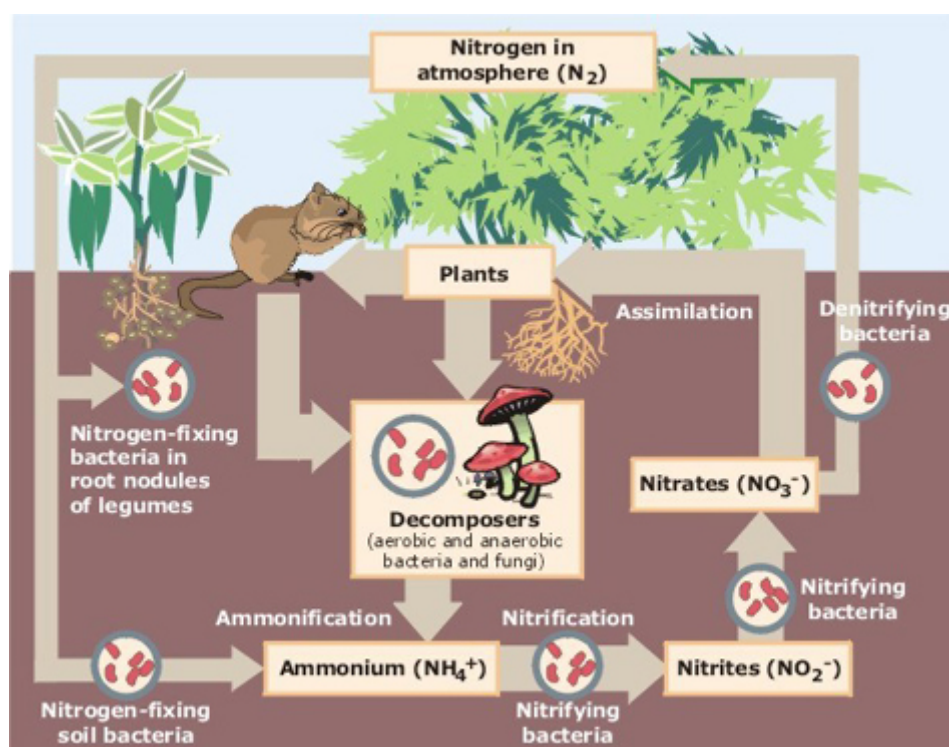


Figure 6.2: Schematic representation of the nitrogen cycle. Source: Wikipedia

However, N_2 is relatively inert, therefore plants and animals are not capable of assimilating atmospheric nitrogen directly, it has to be transformed to chemical forms consumable for living organisms. Nitrogen nutrient limitation therefore frequently occurs in case of various ecosystems making the nitrogen cycle one of the most studied nutrient cycle in ecology.

The atmospheric N cycle includes three basic processes: nitrogen fixation, gaseous nitrogen emission and deposition of nitrogen compounds (Figure 6.2). Some long lived nitrogen compounds have stratospheric sink as well.

6.1. Nitrogen fixation

Nitrogen fixation is the chemical process that transforms N_2 to other nitrogen species that are consumable for living organisms. Plants are able to take up nitrogen in reduced form of ammonia (NH_3 , Figure 6.3), nitrates (NO_3). Two natural ways of nitrogen fixation exist: atmospheric and biological nitrogen fixation.

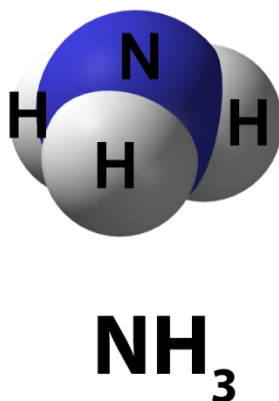


Figure 6.3: Chemical structure of ammonia.

(i) Atmospheric nitrogen fixation. First, the dissociation of N_2 molecule is required to allow N to combine with other elements. However, N_2 being a stable chemical form, the dissociation is a highly energetic process. Therefore N fixation occurs when considerable amount of energy is provided e.g. by lightning. In the subsequent reaction, N combines with atmospheric O or H atoms to form nitric oxides (NO, Figure 6.4) or ammonia (NH_3). These species can reach the land surface via wet deposition with rain.

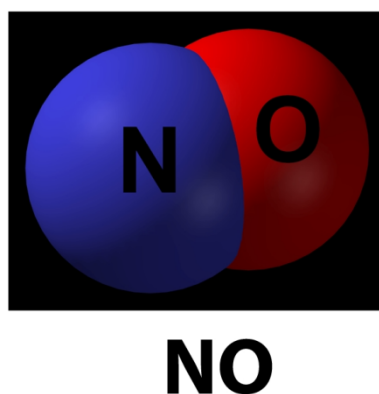


Figure 6.4: Chemical structure of nitrogen oxide.

(ii) Biological N fixation BNF: Diazotrophs are organisms in the soil that do not need fixed nitrogen, but they fix nitrogen in their metabolism. There are two types of diazotrophs: symbiotic and free living (non-symbiotic) diazotrophs. A part of plants are supplied with consumable nitrogen nutrition by root symbionts such as legumes or nodule forming bacteria (Rhizobia). Rhizobia (Azorhizobium, Bradyrhizobium, Mesorhizobium, Rhizobium, Sinorhizobium) are very well studied plant symbionts.

Majority of nitrogen fixation happens via biological processes: Rhizobia require inorganic nutrients for their metabolism in which N_2 is converted to ammonia by the nitrogenase enzyme:



The legume family (Fabaceae) are important in nitrogen fixation as they are well known to associate with symbiotic rhizobia (Figure 6.5, Figure 6.6, Figure 6.7). These plants are produced agriculturally (beans, peas, etc.) but also occur in natural ecosystems (e.g. white clover).



Figure 6.5: Rhizobia nodules on cowpea, pea and soybean roots. Source: Wikipedia



Figure 6.6 Rhizobia nodules on pea roots. Photo credit László Kődöböcz.



Figure 6.7 Rhizobia nodules on soybean roots. Photo credit László Kődöböcz.

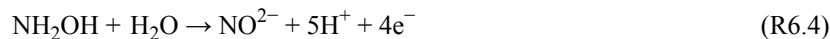
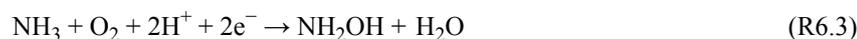
Free living nitrogen fixing organisms are also present in soils, supplying plants with reduced form of nitrogen. Many bacteria, fungi are capable of producing the nitrogenase enzyme. Cyanobacteria is one of the free living nitrogen fixing bacteria, but note that cyanobacteria also has symbiotic form.

Role of micorhizza in nitrogen fixation Abuscular micorhizza is another root symbiont; these fungi help plants to take up nutrients from the soil. It is associated with the majority of terrestrial plants, and probably played important role in the colonization of the land surface by plants.

6.2. Nitrification

Once nitrogen is fixed it can either be assimilated and transformed to organic compounds, or further processed by heterotrophic nitrifying bacteria. Nitrification includes two subsequent oxidative reaction of ammonium (NH_4^+) or ammonia (NH_3) to nitrate (NO_3). Nitrifying bacteria are the most frequent in locations where more ammonia

is present. In the first step, NH_3 is oxidized to nitrite (NO_2^-), this process is called nitrosifying (R6.2-R6.4). In the second step this nitrite is oxidized to nitrate (NO_3^-), which is then available for assimilation by plants.

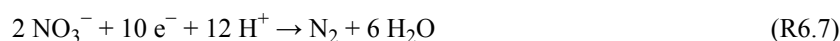


Nitrifying (oxidizing nitrites to nitrates)



6.3. Denitrification

The process that releases nitrogen back to the atmosphere is called denitrification. In this process molecular nitrogen is produced in nitrate reduction (Figure 6.2, R6.6, R6.7). This is the reverse process of nitrification: nitrates are reduced to nitrites and then to ammonia. Denitrification is carried out by soil bacteria under both anaerobic and aerobic conditions. In soils with high organic matter content and anaerobic conditions, denitrification is more intense. The nitrogen produced in this process is emitted to the atmosphere, causing a loss for the soils. On local scale, this means the depletion of an important and frequently limiting nutrient, therefore denitrification is an undesirable process on managed lands.



6.4. Nitrogen deposition

In the atmosphere deposition of nitrogen compounds is the sink process of nitrogen. Nitrogen compounds can get to the surface via both wet and dry deposition pathways determined by the solubility of the compound. Depending on the chemical form, nitrogen can serve as nutrient deposited to land surface or can have detrimental or toxic effects such as acidification. For more information on deposition pathways see Chapter 12.

In wet deposition ammonium (NH_4^+), nitrate (NO_3^-), etc. is carried to the surface predominantly by rain and snow. Connected to precipitation, spatial distribution of wet deposition is highly variable.

Dry deposition of nitrogen means the removal of gases NH_3 , NO_2 , HNO_3 (Figure 6.8) and particulate NH_4^+ and NO_3^- and organic compounds (e.g. peroxyacetyl nitrate: PAN, Figure 6.9), organic acids, nitrogen containing aerosols, etc.

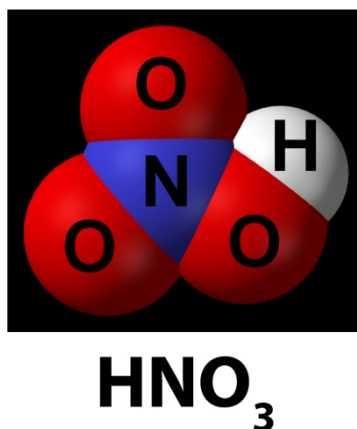
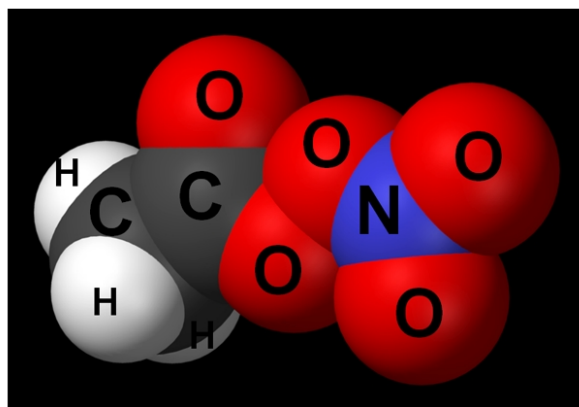


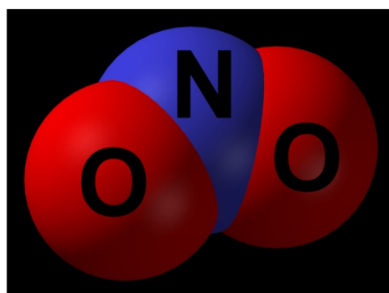
Figure 6.8: Chemical structure of nitric acid.



PAN

Figure 6.9: Chemical structure of peroxyacetyl nitrate.

Nitrogen deposited on the vegetation surface can get to the stomata. Nitrogen uptake by leaves (in form of NO, NO₂ (Figure 6.10), HNO₃, PAN, isoprene nitrates and gaseous amines) are negligible compared to atmospheric abundance but an important pathway of plant N supply. Nitrogen deposition influences carbon sequestration capacity of the terrestrial vegetation, being nitrogen the major constraint of plant development in most geographic locations.



NO₂

Figure 6.10: Chemical structure of nitrogen dioxide.

6.5. Anthropogenic sources of nitrogen compounds

Human induced emission of nitrogen trace compounds is equal or in some cases even exceeds contributions of natural sources. The three main anthropogenic source types are (i) direct agricultural emissions, (ii) emissions from livestock, (iii) indirect agricultural emissions. Industrial emission e.g. from wastewater treatment, fossil fuel and biomass combustion also contributes to anthropogenic emission. Nitrogen oxides are emitted to the atmosphere from fossil fuel burning and play important role in ozone chemistry. Emission of nitrous oxide (N₂O, Figure 6.11) related to anthropogenic activity mostly due to the enhancement of natural processes, increasing rate of nitrification-denitrification as a result of fertilization.

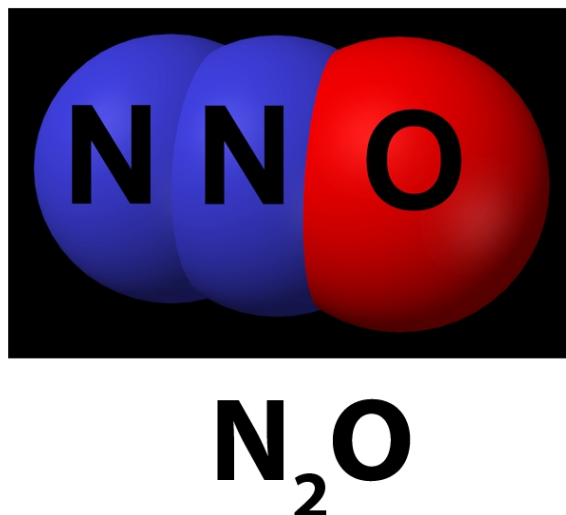


Figure 6.11: Chemical structure of dinitrogen oxide (nitrous oxide).

Nitrogen is essential to synthesize e.g. nucleotids for DNA or RNA and amino acids for proteins, which are basic building blocks of plants. Nitrogen and phosphorous limitations are the most common constraints of soil fertility in agriculture, therefore fertilizers containing nitrogen compounds are widely used in agricultural management. Agriculture is a main source of nitrogen compounds. Large amounts of ammonia and nitrogen is emitted due to fertilizer application, and from livestock waste (manure and urine).

The nitrogen related to fertilization used to increase plant productivity may lead to increased CO₂ uptake but induce emission of N₂O also an important GHG. Nitrogen fertilizers are useful to increase crop yield, but nitrogen pollution originated from crop production have detrimental effects on aqueous ecosystems, lead to acidification, eutrophication and GHG emission that contributes to radiative forcing. Agricultural nitrate and phosphate pollution also endangers freshwater quality. This polluting process is considered to be the main stress factor in marine and coastal ecosystems. For a sustainable agriculture farmers need to optimize fertilizer amount and management techniques in order to maximize yield and profit and minimize nitrogen emission and possibly to increase carbon sequestration as well. Nitrogen availability in a certain region depends on different factors: history of agriculture in the area, management techniques applied, atmospheric nitrogen deposition, several soil factors.

The problem of nitrogen limitation and harmful effects of the applied fertilizers show the importance of legumes in agriculture. Although most of the above ground nitrogen is harvested, some of the fixed nitrogen accumulates belowground fertilizing the soil before the next crop. Therefore using legumes in crop rotations is a popular way to improve soil fertility in environmentally conscious management systems not using fertilizers.

The effects of increased nitrogen emission include

1. decreased atmospheric visibility due to ammonium aerosols (fine particulate matter [PM]);
2. elevated ozone concentrations;
3. ozone and PM affects human health (e.g. respiratory diseases, cancer);
4. increases in radiative forcing and global climate change;
5. decreased agricultural productivity due to ozone deposition;
6. ecosystem acidification and eutrophication; and
7. decreasing ecosystem biodiversity.

6.6 Atmospheric reactions of nitrogen species

Nitrogen compounds, especially NO_x when sunlight is available play an important role in tropospheric photochemistry catalyzing O₃ production in the troposphere. Tropospheric ozone production is limited by NO_x abundance, but heavily polluted areas experience higher ozone concentrations. Nitrogen oxides also will interact with volatile organic compounds to form ozone. In Chapter 8 ozone chemistry is described in more details.

Nitrous oxide (N₂O) is a key nitrogen compound in environmental sciences due to its properties as greenhouse gas, and also because of its role in stratospheric ozone destruction. Because it has a relatively long residence time without major tropospheric sink, it can get to the stratosphere where it responds to UV light by photodissociation to N₂ and O or – less likely – combines with O producing 2NO. This latter gas is has a key role in photocatalytic destruction of stratospheric ozone. In this sense, N₂O can be considered as a long lifetime carrier of NO. The environmental significance of N₂O is also indicated by the fact that emission of this gas is regulated by the Kyoto protocol.

Atmospheric concentration of nitrogen compounds is monitored regularly in Hungary and also a national emission inventory has been presented for the period 1986–2006.

References

- Melillo J.M., Field C.B., and Moldan B.. 2003. *Interactions of the Major Biogeochemical Cycles: Global Change and Human Impact*. Island Press. ISBN 978-1559630665.
- IPCC, 2007: *Fourth Assessment Report: Climate Change 2007: The Physical Science Basis Contribution of Working Group I to the Fourth Assessment Report of the Intergovernmental Panel on Climate Change*. 2007. Solomon S., Qin D., Manning M., Chen Z., Marquis M., Averyt K.B., Tignor M., and Miller H.L.. (eds.). Cambridge University Press, Cambridge, United Kingdom and New York, NY, USA.
- Haszpra L.. 2003. *Atmospheric Greenhouse Gases: The Hungarian Perspective*, Springer. ISBN 978-90-481-9949-5 (Print). ISBN 978-90-481-9950-1 (Online).
- Horváth L., Grosz B., Machon A., Balogh J., Pintér K., and Czóbel S.. 2008. *Influence of soil type on N₂O and CH₄ soil fluxes and in Hungarian grasslands*. Commun Ecol. 9 (Suppl). 75-80. doi: 10.1556/Com.Ec.9.2008.S11.
- Wagner S.C.. 2012. *Biological Nitrogen Fixation In: Nature Education Knowledge*. 3. (10). 15.

Chapter 7. Sulphur compounds

There are several sulphuric compounds in the atmosphere: sulphur dioxide (SO₂), sulphur trioxide (SO₃) – we can group these two chemical species as SO_x – hydrogen sulphide (H₂S), carbonyl sulphide (COS), carbon disulfide (CS₂), and sulphates (SO₄²⁻) (Figure 7.1–7.6).

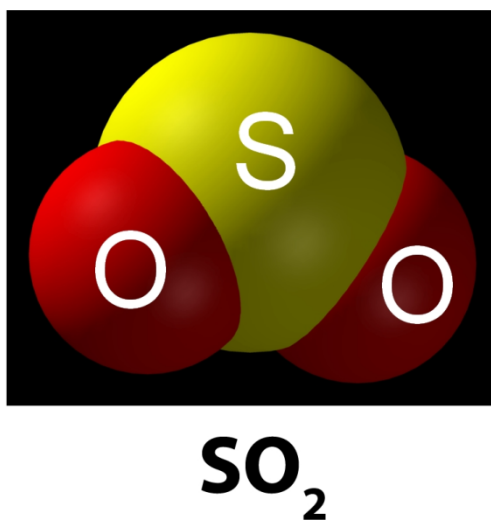


Figure 7.1: Chemical structure of sulphur compounds – sulphur dioxide (Source: Wikipedia).

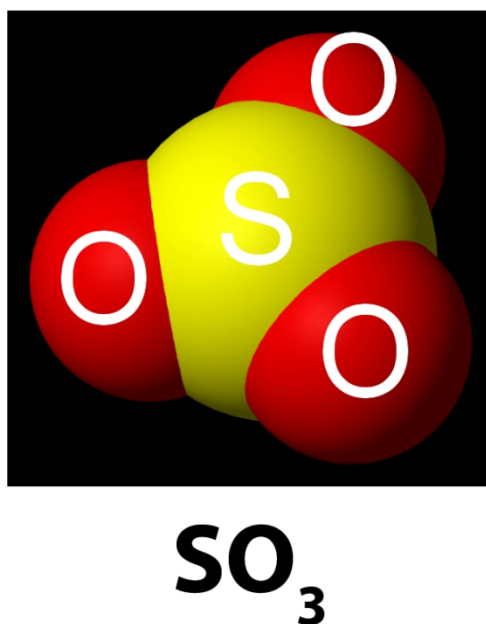


Figure 7.2: Chemical structure of sulphur compounds – sulphur trioxide (Source: Wikipedia).

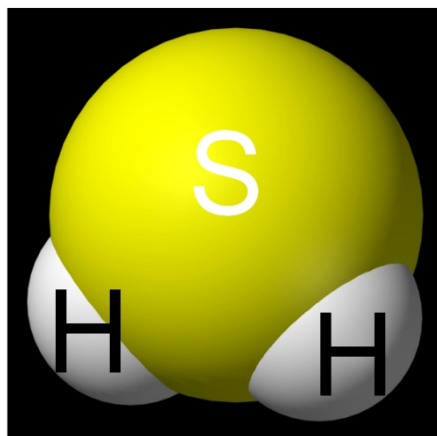


Figure 7.3: Chemical structure of sulphur compounds – hydrogen sulphide (Source: Wikipedia).

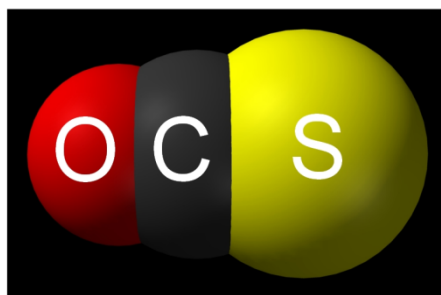


Figure 7.4: Chemical structure of sulphur compounds – carbonyl sulphide (Source: Wikipedia).

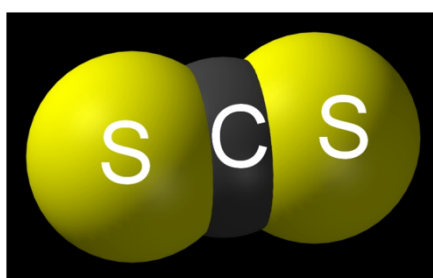


Figure 7.5: Chemical structure of sulphur compounds – carbon disulphide (Source: Wikipedia).

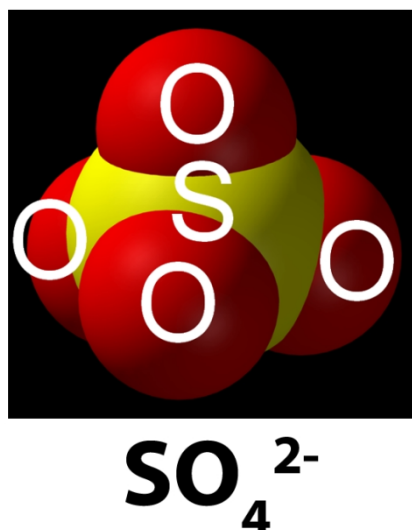
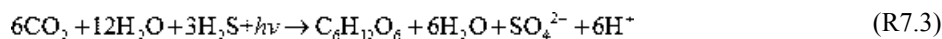
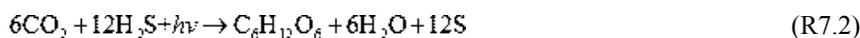


Figure 7.6: Chemical structure of sulphur compounds – sulphate ion (Source: Wikipedia).

Sulphur is an essential element of living matter (amino acids and proteins). Sulphur exists in various forms in the Earth such as elemental sulphur, sulphides, sulphites, sulphates and other species. Sulphur mainly exists in the form of elemental sulphur, sulphides, and sulphates (Seinfeld and Pandis, 2006). Combustion of fossil fuels, emission from oceans due to activity of microorganisms, volcanic eruptions, and decomposition of living matters are the main sources of sulphur in the atmosphere. Sulphur dioxide and hydrogen sulphide are mostly emitted into the troposphere. H_2S undergoes oxidation producing SO_2 followed by oxidation of SO_2 to sulphuric acid (H_2SO_4 or SO_4^{2-}). Sulphuric acid dissolves in water, thus the sulphur content is carried back to soil. Sulphate ion can be absorbed by plant and incorporated into organic compounds (amino acids). The sulphur bounded in amino acids is transferred from the producers (plants) to consumer (animals, humans). Excretion and the death of consumers carry sulphur back to the soil and water bodies, where it can be used by special bacteria. The $-\text{SH}$ (thiol group or a sulphhydryl group) of amino acids (e.g., cysteine) gets separated as H_2S . Several groups of bacteria can use hydrogen sulphide as fuel, oxidizing it to elemental sulphur or to sulphate by using dissolved oxygen, metal oxides (e.g., Fe oxyhydroxides and Mn oxides) or nitrate as oxidant. Hydrogen sulphide can be oxidized in an aerobic condition to SO_4^{2-} by bacteria adapted to perform this change



and the formed sulphate ion can be used again by autotrophs (Figure 7.7). In anaerobic condition some photosynthetic bacteria can use hydrogen sulphide to form carbohydrates and oxidize it to elemental sulphur or sulphate



Other bacteria can transform elemental sulphur to sulphate. This reaction is fast in the presence of molecular oxygen



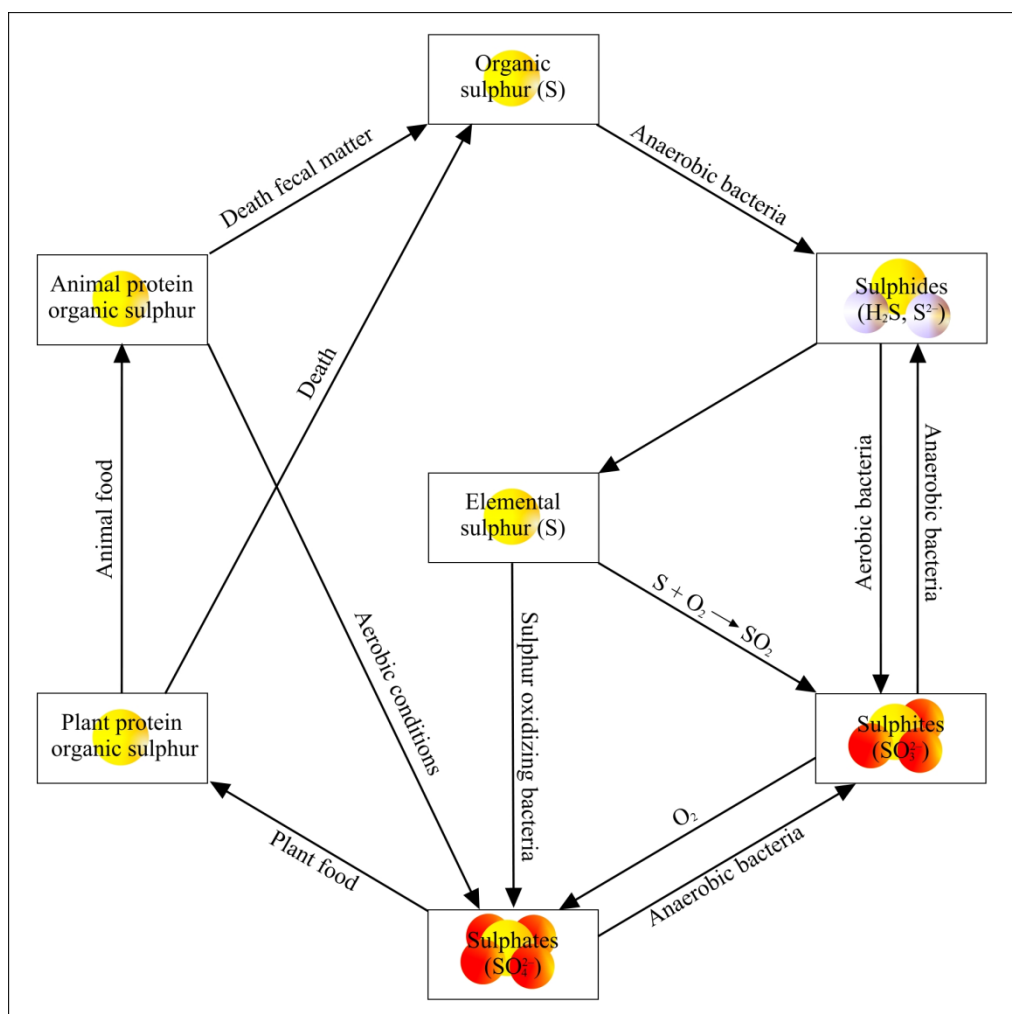


Figure 7.7: The sulphur cycle.

7.1. Sulphur oxides (SO_x)

SO₂ is one of the most important contributors to air pollution. Sulphur in low concentration is essential for living organisms, but it becomes harmful when its concentration is increased. There are two sources: natural and anthropogenic. Natural sources (e.g., volcanoes) provide about two thirds of the sulphur oxides pollution on the Earth, while the smaller amount is from anthropogenic sources. Among anthropogenic sources, fossil fuel combustion accounts for ~ 75% of the total SO_x emission.

7.1.1. Reaction sulphur dioxide in the atmosphere

In the atmosphere, SO₂ does not remain in the gas phase for a long time. It reacts with water in the atmosphere in the presence of radiation to form sulphuric acid, which finally can deposit (wash out) with rain water causing acid rain. Sulphuric acid production from SO₂ oxidation proceeds via a series of radical reactions. First, sulphur dioxide reacts with an OH radical, which is normally produced from water vapour via reaction with electronically excited atomic oxygen, which in turn is formed from ozone photolysis



The HSO₃ radical then rapidly reacts with molecular oxygen to yield either SO₃ and HO₂ or an intermediate complex HSO₅ (Kurten et al., 2009):



where M denotes a collision partner (typically molecular nitrogen or oxygen). The $\text{HSO}_3 \cdot$ radical may also decompose to SO_3 and $\text{HO}_2 \cdot$, or it may react with other compounds.



The produced SO_3 reacts with water (catalyzed by another water molecule) to yield sulphuric acid:



In the daytime, the photochemically generated radicals react as catalyst in these reactions. Sunny weather enhances the rate of conversion to acid, and this rate of conversion to acid decreases fast after sunset.

SO_2 undergoes several chemical reactions in the atmosphere forming particulate matter and aerosols, which are scavenged from the air. Sulphur dioxide and trioxide are transformed and washed out from the atmosphere in the form of sulphuric acid. Increasing concentration of sulphuric acid in the troposphere involves the occurrence of acid rain. A number of factors such as temperature, radiation intensity, and humidity can affect these reactions. Sulphur dioxide reacts through several ways in the atmosphere: (i) Photochemical reactions; (ii) Chemical reactions in the presence of NO_x and hydrocarbons; (iii) Chemical reactions in water phase and on solid aerosol particles. If fuel (e.g., coal) contains sulphur, its burning forms SO_2



Sulphuric acid in the atmosphere reacts with ammonia (NH_3) and metal salts (e.g., NaCl) producing sulphates



In relatively humid conditions sulphur dioxide may be oxidized by reactions taking place inside the water phase in aerosol particles. These reactions proceed faster in the presence of ammonia and catalyst such as Fe(II) , Ni(II) , Mn(II) , and Cu(II)



Oxidation rate of sulphur dioxide is more intense in a photochemically active air containing sulphur dioxide, VOCs, and NO_x , and this process results in more pronounced formation of aerosol particles. Sulphur dioxide, aerosols, soot particles, ammonium sulphate and water are the major components of the London smog. This smog has reductive chemical nature. SO_2 is a strongly irritating gas, which has effects on both living and man-made environment. For humans this gas is very dangerous because causes irritation (~ 5 ppm) and increases airway resistance in the respiratory tract. Sulphur dioxide damages crops and plant growth due to killing leaf tissues causing necrosis.

7.2. Hydrogen sulphide (H_2S)

Small amounts of hydrogen sulphide occur in crude petroleum, but natural gas can contain up to 90%. Volcanoes and some hot springs (as well as cold springs) emit some H_2S , where it probably arises via the hydrolysis of sulphide minerals, i.e. $\text{MS} + \text{H}_2\text{O} \rightarrow \text{MO} + \text{H}_2\text{S}$. Hydrogen sulphide can be present naturally in water, often as a result of the action of sulphate-reducing bacteria. About 10% of total global emissions of H_2S is due to human activity. The largest industrial emission of H_2S is from petroleum refineries. The hydrodesulphurization process liberates sulphur from petroleum by the action of hydrogen. The resulting H_2S is converted to elemental sulphur by partial combustion via the Claus process, which is a major source of elemental sulphur. Hydrogen sulphide

arises from anywhere where elemental sulphur comes in contact with organic material, especially at high temperatures.

7.3. Carbonyl sulphide (COS)

Carbonyl sulphide is the most abundant sulphur compound naturally present in the atmosphere (0.5 ± 0.05 ppb), because it is emitted from oceans, volcanoes and sea vents. COS is a significant compound in the global sulphur cycle. Analysis of ice cores from Antarctica and air trapped in snow above glaciers provided how the COS concentration changed during the past few centuries. These measurements provided an understanding of the relative importance of anthropogenic and natural sources of this gas to the atmosphere. Some carbonyl sulphide that is transported into the stratospheric sulphate layer is oxidized to sulphuric acid. Sulphuric acid forms particulate which affects energy balance due to light scattering. The long atmospheric lifetime of carbonyl sulphide makes it the major source of stratospheric sulphate. COS is also removed from the atmosphere by vegetation by enzymes associated with the uptake of carbon dioxide during photosynthesis and by hydrolysis in ocean waters.

The largest anthropogenic sources of carbonyl sulphide release include its primary use as a chemical intermediate and as a byproduct of carbon disulfide production. However, it is also released from automobiles, coal-fired power plants, biomass combustion, fish processing, combustion of refuse and plastics, petroleum manufacture, and manufacture of synthetic fibers, starch, and rubber. The average total worldwide release of carbonyl sulphide to the atmosphere has been estimated at about 3 million tons/year, of which less than one third was related to human activity.

7.4 Carbon disulfide (CS₂)

Very small amounts of carbon disulfide occur in coal tar and in crude petroleum. Carbon disulfide is a natural product of anaerobic biodegradation and is released to the atmosphere from oceans and landmasses as well as geothermal sources. The ocean appears to be a major source of carbon disulfide. Coastal and marshland areas of high biological activity are also major sources. Carbon disulfide reacts with the hydroxyl radical (OH•) in the atmosphere, with the effective rate constant depending on O₂ concentration and pressure. Based on the literature rate constant the estimated lifetime of carbon disulfide due to its reaction with the hydroxyl radical is about 12 days. Carbon disulfide is released naturally into the atmosphere through various sources, including the metabolic processes of plants, the decaying of animal feces, from volcanoes, and also as a byproduct of oil and gas processing.

References

- Kurten T., Berndt T., and Stratmann F.. 2009. *Hydration increases the lifetime of HSO₅ and enhances its ability to act as a nucleation precursor – a computational study* In: *Atmos. Chem. Phys.* 9. 3357-3369.
- Seinfeld J.H. and Pandis S.N.. 2006. *Atmospheric Chemistry and Physics: From Air Pollution to Climate Change*. Wiley.

Chapter 8. Ozone

Ozone (O_3) is a tri-atomic molecule consisting of three oxygen atoms was discovered and first published by a German-Swiss chemist, Christian Friedrich Schönbein in 1840. It is a toxic, oxidative, unstable gas with pungent odour (Schönbein denominated ozone after its characteristic odour from the Greek word „ozein”, which is meaning, “to smell”. Ozone has a greater oxidation potential than oxygen. About 90% of atmospheric ozone can be found in the stratosphere, particularly between 19 and 30 km above the Earth’s surface, and only about 10% of total ozone is located in the troposphere, especially near ground level.

Ozone plays important role in radiation balance of the atmosphere and in the formation of photochemical air pollution, too. Stratospheric ozone, sometimes called as ozone layer, filters out the incoming ultraviolet radiation in the bands between 210 and 290 nm to protect the live. In the troposphere, it works as a greenhouse gas. Near ground level, ozone can affect harmfully both vegetation and human life (see Chapter 13).

8.1. Stratospheric ozone

8.1.1. A short history

After the discovery of ozone by Schönbein, Walter Hartley recognized in 1881 that a sharp cut-off in radiation spectrum between 210 and 290 nm (called Hartley band) correspond to the absorption of ultraviolet radiation by ozone. In 1993, Albert Wigand obtained solar spectra from a balloon at 9000 m, and he found essentially the same cut-off as at the sea level. John William Strutt (better known as Lord Rayleigh) showed in 1918 that ozone in the lowest layer of the atmosphere is not enough for uv absorption, and assumed that most of the atmospheric ozone can be found above 10 km over the surface. In 1921, Charles Fabry and Henry Buisson published the results of their ozone column measurement. They found that the mean thickness of atmospheric ozone is about 3 mm, but this value varies from day to day. First ozone spectrophotometer was developed by Gordon Miller Bourne Dobson in 1924, and regular measurements of ozone abundance started in 1925. This instrument measures the total ozone in a column of air overhead. The amounts of ozone are regularly reported in thickness of the total column ozone, commonly known as Dobson Units (DU). This measure is defined as the amount of ozone contained in a vertical column of base 1 cm^2 at standard air pressure and temperature. The world average is about 300 DU, and it varies geographically from about 230 to 500 DU.

Just a few years after first measurements with Dobson spectrophotometer, Paul Götz discovered a method, called Umkehr-effect, for determining the vertical profile of ozone concentration. This effect is observed when the ratio of the measured intensities of scattered zenith skylight at two different wavelengths (311 and 332 nm) is plotted against the increasing zenith angle of the Sun between 60° and 90° . The ratio increases with increasing zenith angle up to about 86° , then a reversal (Umkehr) occurs. The spectrally different changes in zenith sky uv radiation around Sun rises and sets are controlled by the ozone vertical distribution.

In 1930, Sydney Chapman proposed a theory to describe the natural balance (production and destruction) of stratospheric ozone.

8.1.2. Natural balance of stratospheric ozone

Ozone (O_3) can be found in the earth’s atmosphere from the ground up to about 100 km, but most of the ozone (about 90%) resides in the stratosphere (between about 10 and 50 km above the Earth’s surface). This stratospheric ozone is commonly known as the „ozone layer”. The ozone concentration maximum varies with latitudes, but can be localized at an altitude around 20 km. The maximum concentration varies here between 4 and 8 ppm. Typical vertical profile of ozone can be seen in Figure 8.1.

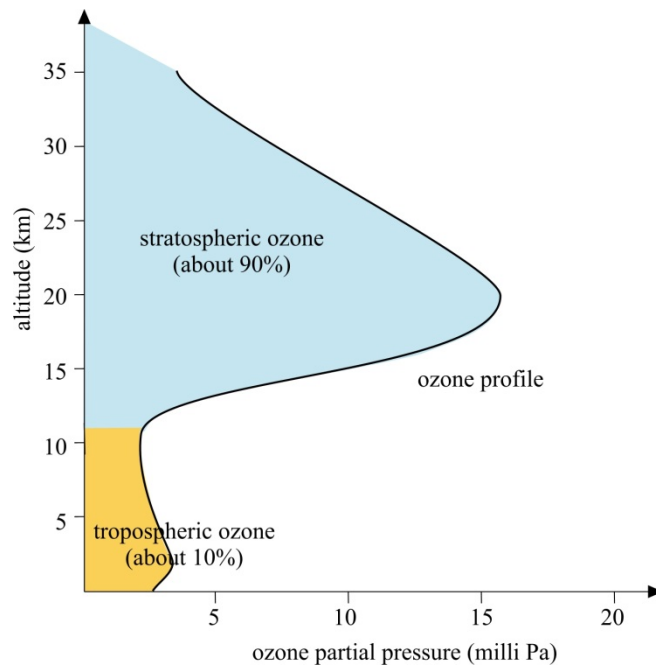
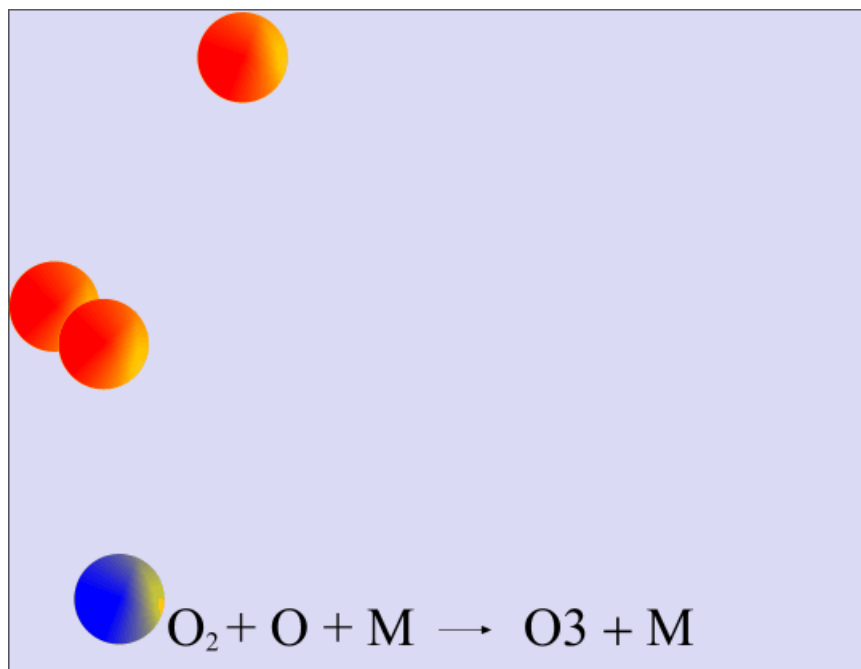


Figure 8.1: Ozone in the atmosphere

Figure 8.2: Production of ozone from an oxygen atom and an oxygen molecule in the presence of a third molecule (usually N_2 , or another O_2).

Ozone is constantly produced and destroyed in a natural cycle. Ozone is formed from a single recombination reaction of an atomic oxygen and a molecular oxygen (Figure 8.2.) in the presence of a third body M, which is required to carry away the energy released in the reaction (M is usually O_2 or N_2):



Here, O atoms are the fundamental triplet state $\text{O}({}^3\text{P})$, which are highly reactive due to their two unpaired electrons. They combine rapidly with O_2 to form ozone.

The net production of oxygen atoms results almost exclusively from the photodissociation of molecular oxygen (Figure 8.3). The bond energy of the oxygen molecule (498 kJ mol^{-1}) corresponds to the energy of a 242 nm uv photon, therefore only photons of wavelengths less than 242 nm can photolyze these molecules:

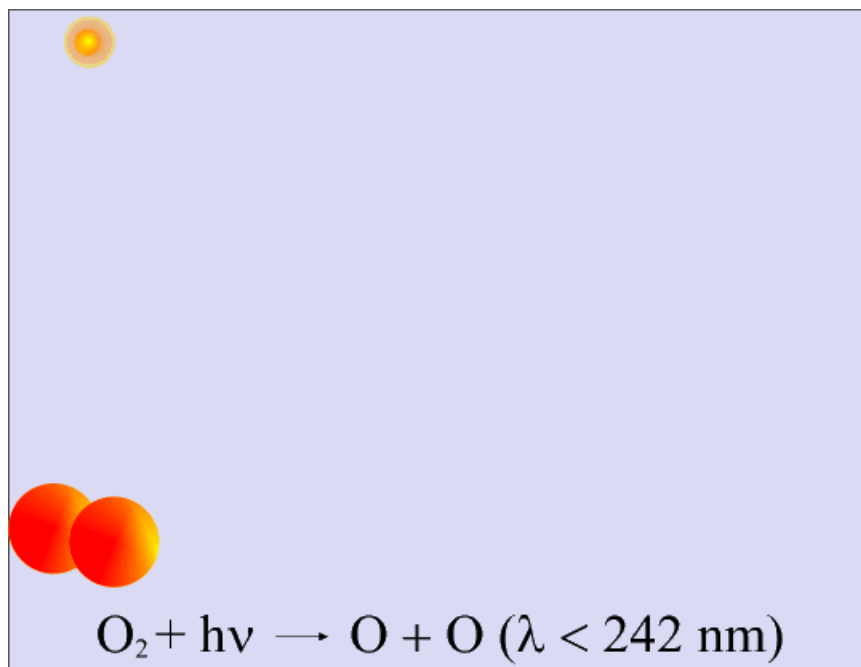
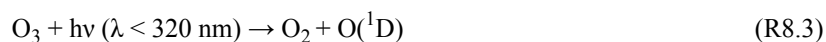
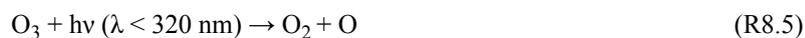


Figure 8.3: Photodissociation of oxygen molecule into to oxygen atoms

Ozone molecule produced in reaction (R8.1) absorbs solar radiation and decomposes back to O_2 and O (Figure 8.4.). Because the bonds in the O_3 molecule are weaker (364 kJ mol^{-1}) than those in the O_2 molecule, photolysis is achieved with lower-energy photons (in the wavelength range of 240 to 320 nm):



Net:



where $\text{O}({}^1\text{D})$ is the O atom in an excited singlet state which is rapidly stabilized to $\text{O}({}^3\text{P})$ by collision with N_2 or O_2 .

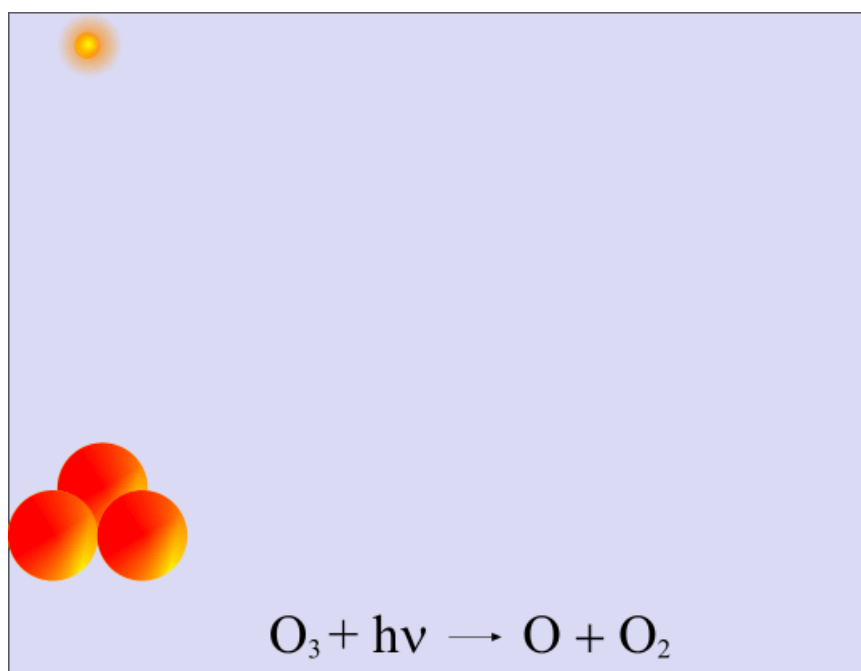


Figure 8.4: Destruction of ozone (O_3) molecule by solar ultraviolet radiation ($\lambda < 320 \text{ nm}$). The result is one oxygen molecule and one excited oxygen atom.

Reactions (R8.1) and (R8.3) are very fast. This dissociation and recombination cycle taking place continuously and occur in less than 100 s throughout the stratosphere. During this cycle, solar uv radiation breaks ozone molecule and oxygen atom reacts an oxygen molecule. This process converts uv radiation to thermal energy, heating the stratosphere.

Additionally, ozone can react with atomic oxygen to regenerate two oxygen molecules:



However, stratospheric ozone concentration calculated by Chapman scheme is much greater than the observed one. The reaction (R8.6) could only account for about 20% of odd oxygen (O and O_3) loss in the stratosphere. Since the 1970s, it is well known that ozone is mainly removed in natural stratosphere through catalytic cycles. During these catalytic cycles, several ozone molecules destructed, while the catalyst that started the reaction is reformed to continue the process (Figure 8.5). Several catalytic cycles are important in ozone chemistry, involving homogeneous gas-phase reactions of active radical species from hydrogen (HO_x), nitrogen (NO_x) and chlorine (ClO_x) families. In the lower stratosphere, cycles catalyzed by bromine (BrO) also contribute to the ozone loss. A large variability of possible catalytic cycles can be described generally by the following reactions:



Net:



where X = H, OH, NO, Cl, Br, or F as catalysts.

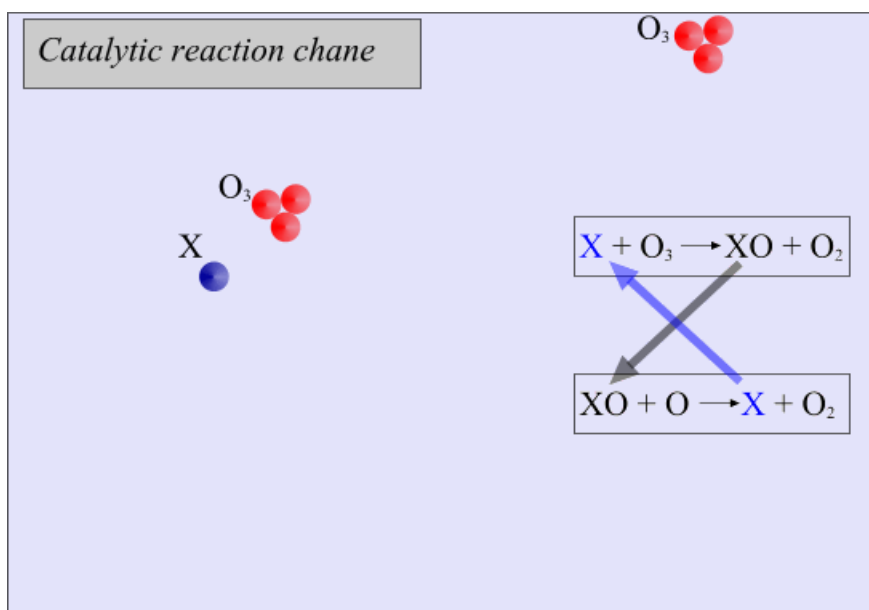


Figure 8.5: A catalytic reaction chain in the stratosphere. One catalyst can destroy several ozone molecules.

8.1.3. Circulation patterns in the stratosphere

The spatial distribution of stratospheric ozone is controlled also by dynamical processes. Most of the ozone is produced in the tropical stratosphere, where solar radiation is strongest and reaction (R8.2) is the most effective. At the same time, higher stratospheric ozone concentration can be observed outside this tropical source region. This picture is a result of a slow atmospheric circulation, called Brewer–Dobson circulation (see e.g. in Gerber, 2012). Brewer–Dobson circulation (BDC) characterizes the transport of mass through the stratosphere. First, in the tropics, the air is rising from the troposphere, then is drifting poleward in the mid latitudes, and finally is descending in the mid and high latitudes. Descending air can be transported back into the troposphere in the mid latitudes, while it can be accumulated in the lower stratosphere at higher latitudes. Due to this circulation pattern, the total ozone column varies in a wide range, from about 220 Dobson Units over tropical region, to above 450 Dobson Units in polar region. This general distribution however has a daily, seasonal and interannual variability, especially during ozone hole events (see later).

8.1.4. Gas-phase chemistry in the stratosphere

The behaviour of the stratospheric ozone layer depends on the chemical reactions, which govern the formation, chemical transformation and removal processes of chemically active components. Several chemical species slowly diffusing from the surface through the troposphere, and they can reach the stratosphere.

Nitrogen oxides (NO and NO₂) dominate the balance between ozone production and destruction in the natural stratosphere. The main source of nitrogen species is nitrous oxide (N₂O) emitted from soil:



Additionally, significant amount of NO are emitted directly to the lower stratosphere by the exhaust gases of aircrafts. The main ozone destruction cycle in the middle stratosphere (25–35 km) is the following:



In the upper stratosphere, odd hydrogen species play important role in the ozone destruction. The main sources of the hydroxyl-radical (OH) and subsequently of hydrogen (H) and hydroperoxyl (HO₂) radicals are the reactions of excited atomic oxygen with water vapour and methane:



and the ozone destruction mechanism if hydrogen species:



or in the lower stratosphere, where atomic oxygen is much less abundant, due to the rapid formation of ozone (R8.4):



Additionally, in the lower stratosphere the coupling between the odd nitrogen and odd hydrogen chemistry can lead to a net production of ozone.

Chlorine species have also a key role in the stratospheric chemistry. However, the major chlorine compounds at the surface (Cl_2 , HCl , NaCl) emitted from oceans and continuous volcanic activity are water soluble and they have a very short lifetime. They removed from the lower atmosphere to the surface by wet deposition (see. Chapter 12) during a few days and they cannot transferred to the stratosphere. The only known natural source of stratospheric chlorine is methylchloride (CH_3Cl) produced by micro-organisms in the ocean. However, methylchloride is only produced about 20% of stratospheric chlorine.

In the 1970's, it became clear that the most important cause for the depletion of stratospheric ozone is the growth in the anthropogenic chlorofluorocarbon gases. The chemically inert chlorofluorocarbons may remain in the atmosphere for 40 – 150 years, and their photodissociation in stratosphere produce significant amounts of chlorine radicals (Molina and Rowland, 1974). The most significant chlorofluorocarbons are CFCl_3 (CFC11), CF_2Cl_2 (CFC12), carbon-tetrachloride (CCl_4), methylchloroform (CH_3CCl_3) while chlorine radicals (ClO_x) are chlorine (Cl) and chlorine monoxide (ClO). Chlorine formation can be described generally as:



The catalytic chain reaction leading to the net destruction of O_3 and O related to chlorine compounds:



This ozone depletion by chlorine radicals occurs especially about 30 km above the surface. In the lower part of stratosphere, the effects of chlorine radicals on ozone depletion are moderated due to the strong chemical interactions between chlorine radicals and other compounds. The presence of nitric-oxide (NO) can hinder the ozone depletion, as it reacts with ClO :



Resulting nitrogen dioxide (NO_2) takes part in the formation of ozone, which moderates the ozone depletion mechanisms. Additionally, further chemical reactions between ClO_x , and NO_x - HO_x can lead to convert the catalysts into less reactive reservoir species which do not react with ozone.





These reservoir species, such as chlorine nitrate (ClONO_2), hypochloric acid (HOCl) or chlorhydric acid (HCl) can slowly transported downward to the troposphere, where they can dissolved and removed into the surface by wet deposition. However, HCl is only a temporary reservoir in the stratosphere, as chlorine can be formed again through the reaction with hydroxyl radical:



Brominated hydrocarbons (halons) from anthropogenic sources can also reach the stratosphere, where bromine catalyst can be formed during photodissociation processes. These bromine catalysts (active bromine – Br , or hypobromite – BrO) can also take part in ozone depletion, similarly, as chlorine compound.

8.1.5. Polar ozone chemistry

Significant seasonal ozone depletion was observed in the lower stratosphere (between 15 and 22 km) over Antarctica during the Southern Hemisphere spring (Farman et al., 1985). Each year for the past few decades during the period between September and November, the stratospheric ozone layer in the southern polar region was destroyed rapidly causing a large area, where total column ozone decreased below 220 Dobson Unit. This region is known as the „ozone hole”.

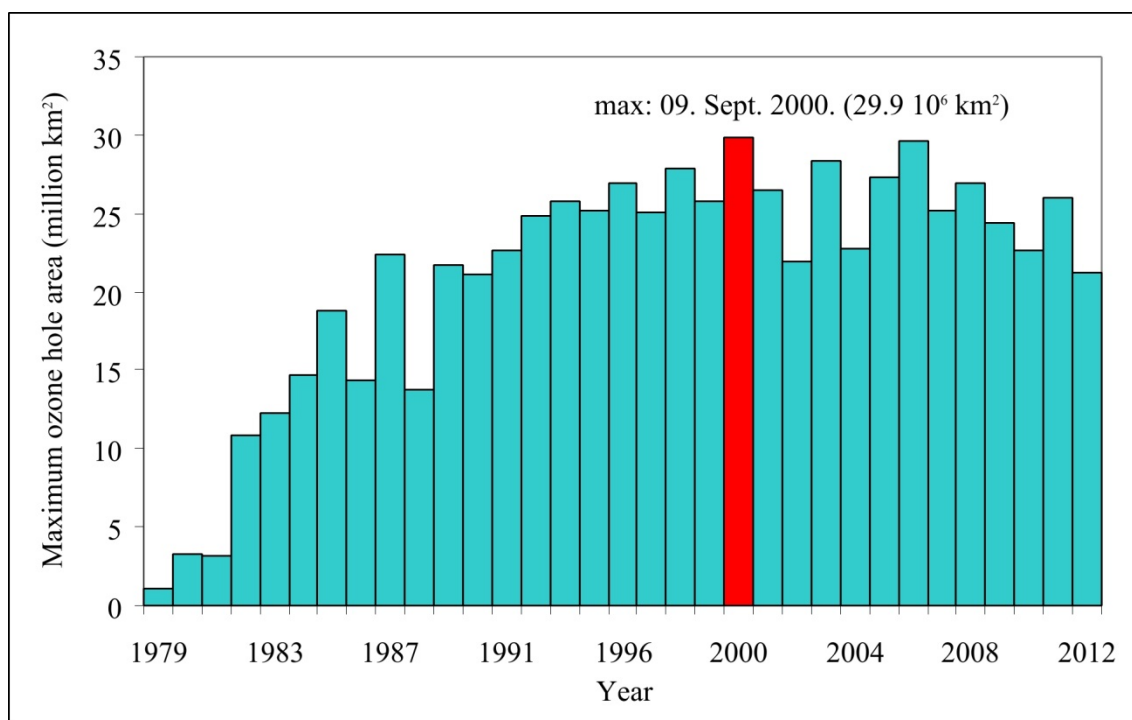


Figure 8.6: The maximum of the daily ozone hole size for each year from 1979 to 2012. (Source of the data: <http://ozonewatch.gsfc.nasa.gov>)

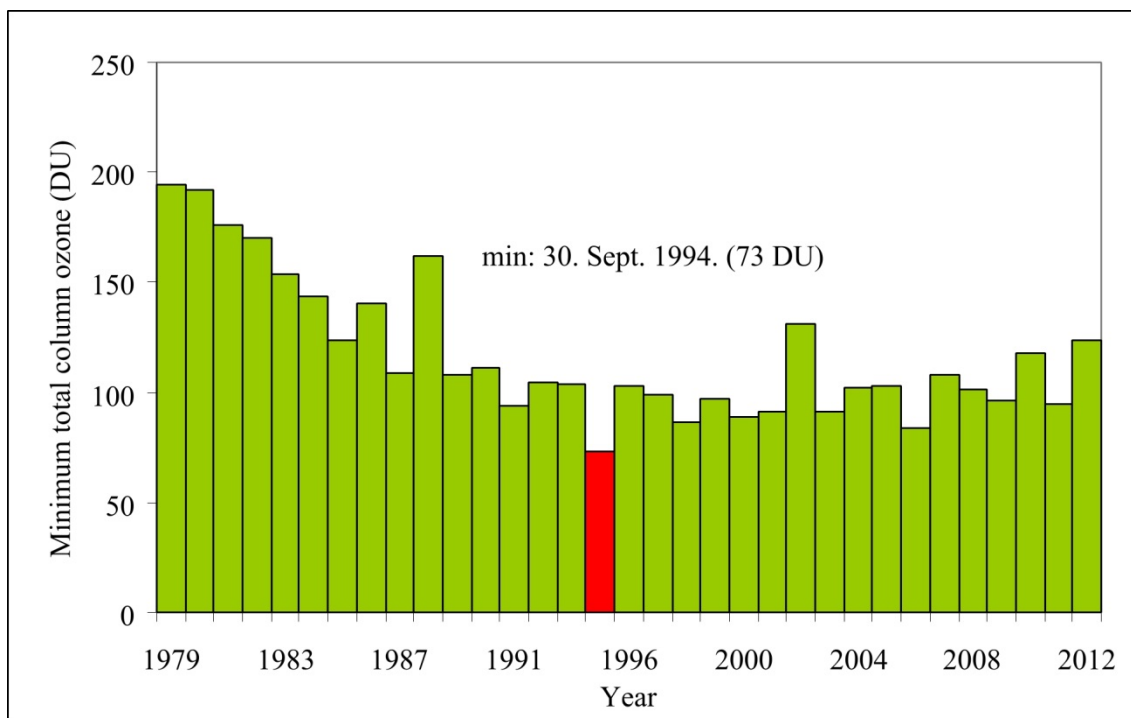


Figure 8.7: The minimum of the daily total column ozone minimum for each year from 1979 to 2012. (Source of the data: <http://ozonewatch.gsfc.nasa.gov/>)

Figure 8.6 shows the yearly maximum extension of ozone hole from 1979, while Figure 8.7 presents the minimum total ozone column for each year from 1979. The border of the ozone hole is represented by a line with a constant value of 220 Dobson Units. This value was chosen since total ozone values of less than 220 DU were not found over Antarctica before 1979 (measurements started in the 1950's). This reduced ozone level is a result of the ozone loss by chlorine and bromine compounds. However, the atomic oxygen, O, has very low concentrations at this region, which limits the efficiency of the formerly described catalytic reaction chains. In that case, other type catalytic reactions become the dominant.

In the polar stratosphere, heterogeneous chemical reactions are extremely important in ozone depletion. Besides of these reactions, dynamical and radiative processes are also responsible for the emergence of the ozone hole.

Over the polar region (above about 65 °C), an isolated, quasi-cylindrical, dynamically stable persistent area, called polar vortex is formed in the mid and upper troposphere and in the lower stratosphere. This cold vortex is strongest during winter and weaker or can disappear in summer. Due to the different geographical conditions, the polar vortex is less perturbed, therefore more pronounced and persistent in the Southern Hemisphere than over the Arctic region. During the polar winter, at very low temperature, different types polar stratospheric clouds (PSCs) can be formed in the polar vortex between altitude of 15 and 25 km. Type I PSCs are formed at temperature below -78 °C and composed by supercooled solution of nitric acid, sulphuric acid and water ice ($\text{HNO}_3\text{-H}_2\text{SO}_4\text{-H}_2\text{O}$) or condensed nitric acid trihydrate (NAT – $\text{HNO}_3\text{-3 H}_2\text{O}$). Type II PCs are less common, and contains water ice particles that form when temperature drops below -88 °C. PSCs are mainly formed over Antarctica, in the polar vortex, but they are less frequent in the Arctic stratosphere, because the temperature in this region is on average about 10 °C warmer than in the Antarctic lower stratosphere. Therefore, ozone depletion is less significant over the Northern polar region.

Polar stratospheric clouds plays important role in ozone depletion (Crutzen and Arnold, 1986). Heterogeneous chemical reactions, which convert inactive chlorine compound to ozone destroying radicals can take place on the component of PSCc. Additionally, the sedimentation of nitric acid (HNO_3) particles from polar stratospheric clouds leads indirectly to the removal active nitrogen species (this process is called denoxification). As NO_2 can react with ClO to form reservoir chlorine nitrate (ClONO_2) species, the removal of NO_2 helps maintain large levels of ozone-destroying ClO.

The heterogeneous reactions in the polar stratosphere (Molina et al., 1987; Isaksen, 1994) involving HCl, ClONO₂, HOCl, N₂O₅ and H₂O are responsible for the conversion of reservoir species into reactive forms of chlorine, and also for removal of reactive nitrogen species into more stable forms (such as HNO₃):



Due to the heterogeneous chemistry, active species of chlorine (and also bromine) accumulated in the polar vortex. Then, after polar sunrise, the re-appearing solar radiation starts the photochemical activity, which leads to intensive ozone depletion in polar stratosphere during the polar spring. Chlorine reservoirs (such as molecular chlorine - Cl₂) photodissociated rapidly by ultraviolet and visible radiation into chlorine atoms:



which initiates catalytic reaction chains, as chlorine atoms react with ozone to produce ClO. Due to the low solar elevation angles, atomic oxygen is not present in the polar stratosphere, therefore the ozone destruction occurs through the following catalytic chain:



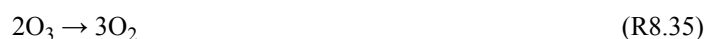
Net:



Similar catalytic bromine cycles can occur involving Bromine compound:



Net:

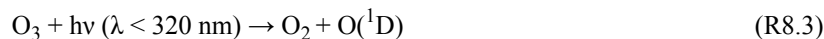


8.2 Tropospheric ozone

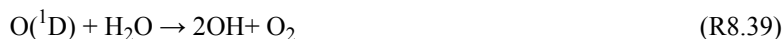
Tropospheric ozone is only about 10% of the total amount of ozone contained in a vertical column in the atmosphere. However, this relatively small amount of tropospheric ozone has a great importance because it's important role in the formation of photochemical air pollution and its oxidizing impact in the near surface layer (e.g. Krupa and Manning, 1988).

Tropospheric ozone is a direct greenhouse gas. Ozone abundances in the troposphere typically vary from less than 10 ppb over remote tropical oceans up to about 100 ppb in the upper troposphere, and often exceed 100 ppb downwind of polluted metropolitan regions (IPCC, 2001).

The absorption of solar ultraviolet radiation of wavelength shorter than 320 nm by ozone occurs in the troposphere similarly as in the stratosphere (see above). This photochemical reaction leads to the production of excited $O(^1D)$ atoms:



This excited $O(^1D)$ atoms have higher energy than ground state oxygen atoms, thus it has enough energy to react with water vapour to produce hydroxyl radicals (OH):



In this way, ozone is the precursor of OH, which is responsible for the oxidation of several species, such as carbon monoxide (CO) or alkanes (denoted as RH):



8.2.1. Global tropospheric ozone budget

Ozone is a secondary air pollutant that is not emitted directly to the atmosphere. Ozone can enter the troposphere from the stratosphere, where it forms by reactions (R8.1–R8.2). The most active regions of stratosphere-troposphere exchange of ozone are in cyclonic regions of the upper troposphere, near the disturbed tropopause. The major sources of tropospheric ozone, however, are chemical reactions, when it forms from its precursor compounds, such as reactive hydrocarbons and nitrogen oxides. Globally annual average of photochemical destruction of tropospheric ozone is comparable with the production. Another sink process of tropospheric ozone is dry deposition, when ozone is settling from the atmosphere to different surfaces (see Chapter 12). Globally averaged annual tropospheric ozone budget and major processes related to the life of tropospheric ozone can be seen in Figure 8.8.

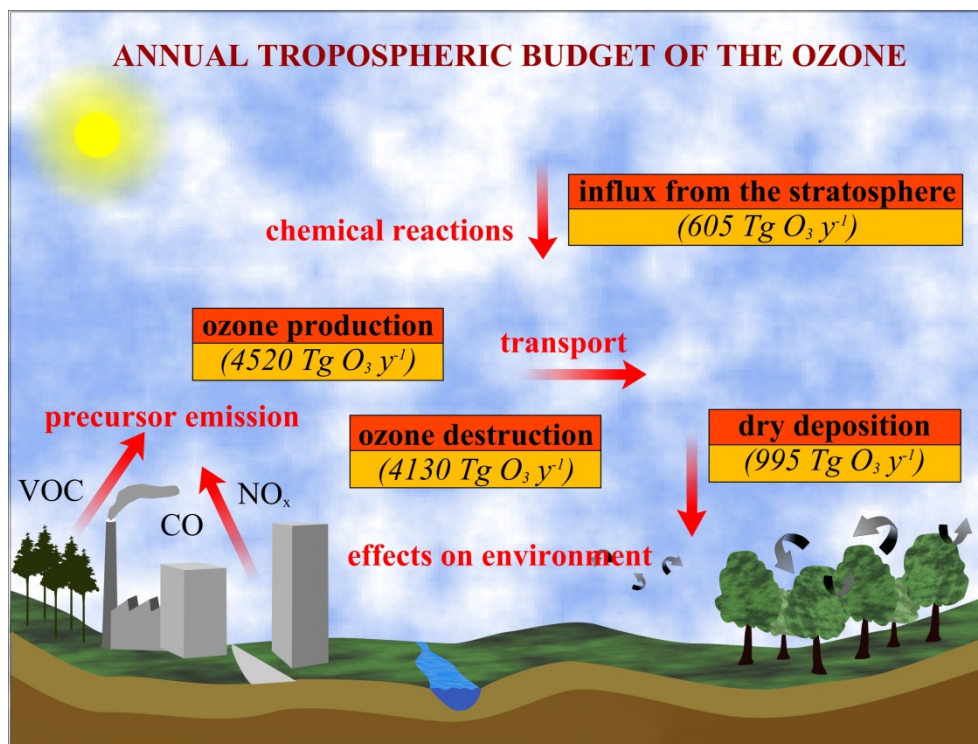


Figure 8.8: Annual tropospheric budget of the ozone. Source of data: Guicherit and Roemer, 2000.

8.2.2. Ozone production in the troposphere

Ozone can form by the recombination of an oxygen molecule and an oxygen atom, similarly as in the stratosphere (reaction R8.1). Nevertheless, O atom cannot form in the troposphere by the photodissociation of molecular oxygen (reaction R8.2), because this reaction requires short wavelength ($\lambda < 242$ nm) which is not available in the troposphere (due to the absorption by stratospheric ozone). In the troposphere, nitrogen dioxide is the only known compound that can produce O atom during its photodissociation at available radiation:



In the presence of NO, O₃ reacts with it, which reaction destroys the ozone and reproduces the NO₂:



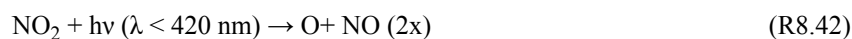
This means that reaction (R8.42)–(R8.44) themselves do not result net ozone production, because these reactions only recycle O₃ and NO_x. Net ozone production occurs, when other precursors, such as carbon monoxide (CO), methane (CH₄), non-methane hydrocarbons (NMHC) or certain other organic compounds (volatile organic compounds – VOC) are present in the atmosphere. Ozone production can be simulated by a simple reaction scheme, through the oxidation of carbon monoxide, when nitric oxide is available. In this reaction chain OH, HO₂, NO and NO₂ participate as catalysts:



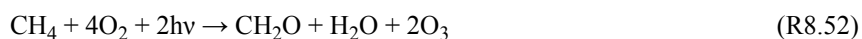
net:



Similar reactions chain occurs with the oxidation of methane in NO rich environment, when ozone and formaldehyde (CH₂O) are formed rapidly:



net:



Formaldehyde photodissociates to generate other radicals, which can participate further ozone productions.

Instead of methane, other organic compounds (NMHC, VOC) can also be participated in this reaction chain, where carbonyl species or a ketone formed next to the ozone. A schematic pattern of tropospheric ozone production can be seen if Figure 8.9.

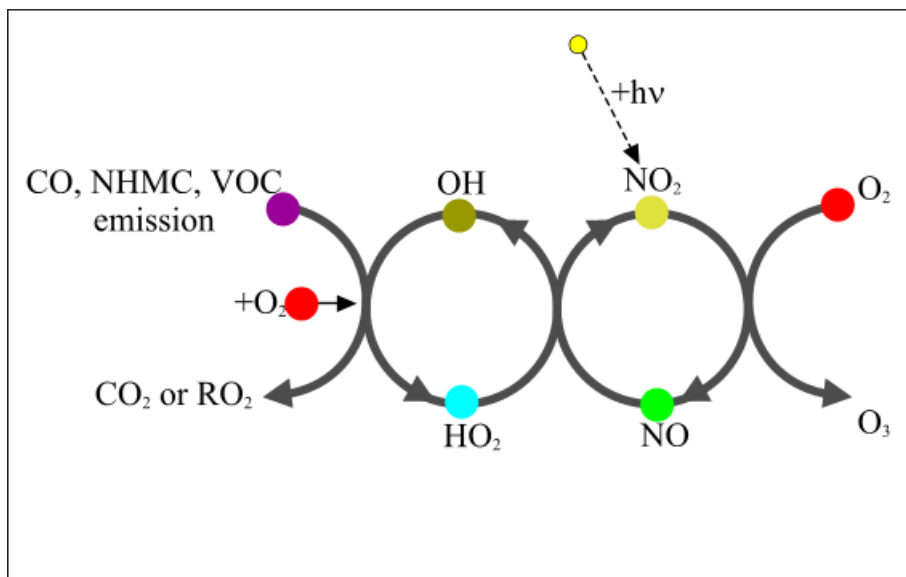


Figure 8.9: Schematic picture of photochemical ozone formation in the troposphere

8.2.3. Sinks of the tropospheric ozone

Primary loss processes of tropospheric ozone are the photochemical reaction (R8.3), when O_3 molecules dissociate by solar radiation. In NO rich environment, the reaction (R8.44) governs the ozone destruction. On the other hand, in NO-poor environment, the oxidation of carbon dioxide can lead to ozone loss. In that case, after the reactions (R8.40) and (R8.45) the generated HO_2 can react with ozone (instead of reaction R8.46):



Further ozone can be destroyed by the direct reaction with OH radical:



Next to chemical destructions ozone can be removed from the atmosphere by dry deposition. This process is more intense during unstable atmospheric stratification. After movement from near surface layer by turbulent diffusion, ozone can react with the receiving surface. Many plants are extremely sensitive to ozone and can be damaged (see details in Chapter 13).

8.2.4. Spatial and temporal variability of ozone in the near surface layer

The background surface ozone concentration increased steadily worldwide in the last decades of 20th century (Vingarzan, 2004). Spatial and temporal distributions of ozone concentrations, however, show large variability. Background ozone concentration at a given place and time results from a combination of formation, transport,

destruction and dry deposition and affected by elevation, too. Higher concentrations typically occur at sites located in the free troposphere (Figure 8.10).

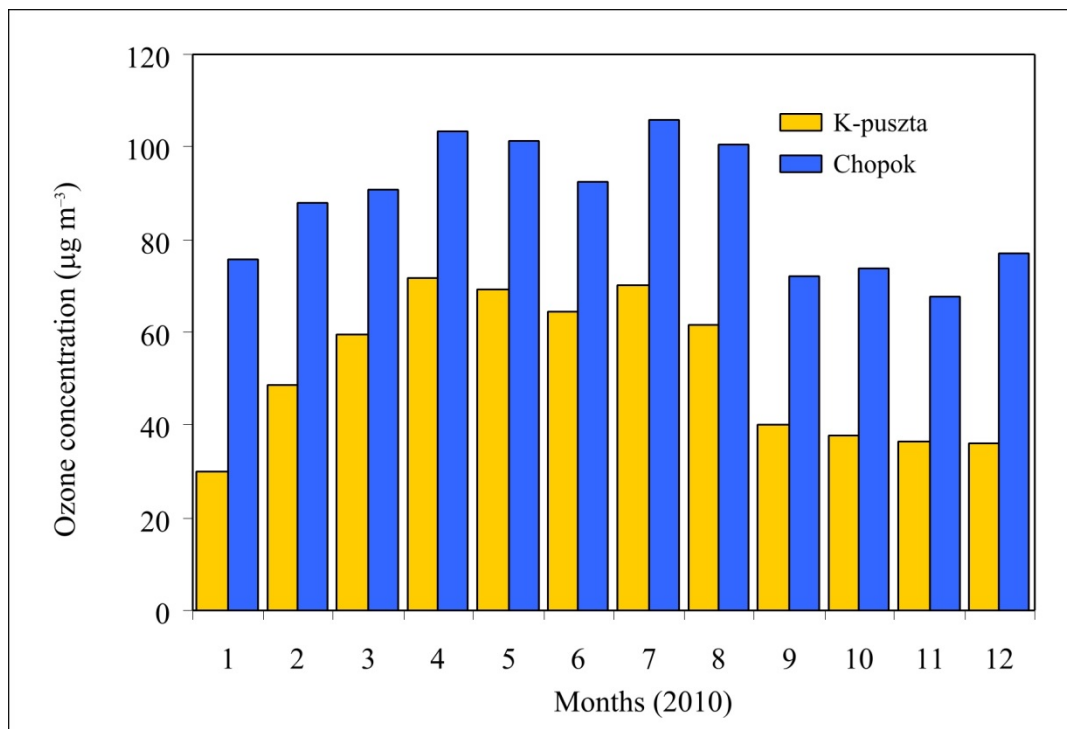


Figure 8.10: Average monthly ozone concentrations in 2010 at two EMEP (European Monitoring and Evaluation Programme) measuring station: K-puszta (Hungary, $\varphi = 46^{\circ}58'$, $\lambda = 19^{\circ}35'$, $h = 125$ m) and Chopok (Slovakia, $\varphi = 48^{\circ}56'$, $\lambda = 19^{\circ}35'$, $h = 2008$ m). Source of data: <http://www.nilu.no/projects/ccc/onlinedata/>

Seasonal cycle of tropospheric ozone is also well-defined in Figure 8.10. Higher values can be observable in summer period due to the more intense photochemical reactions.

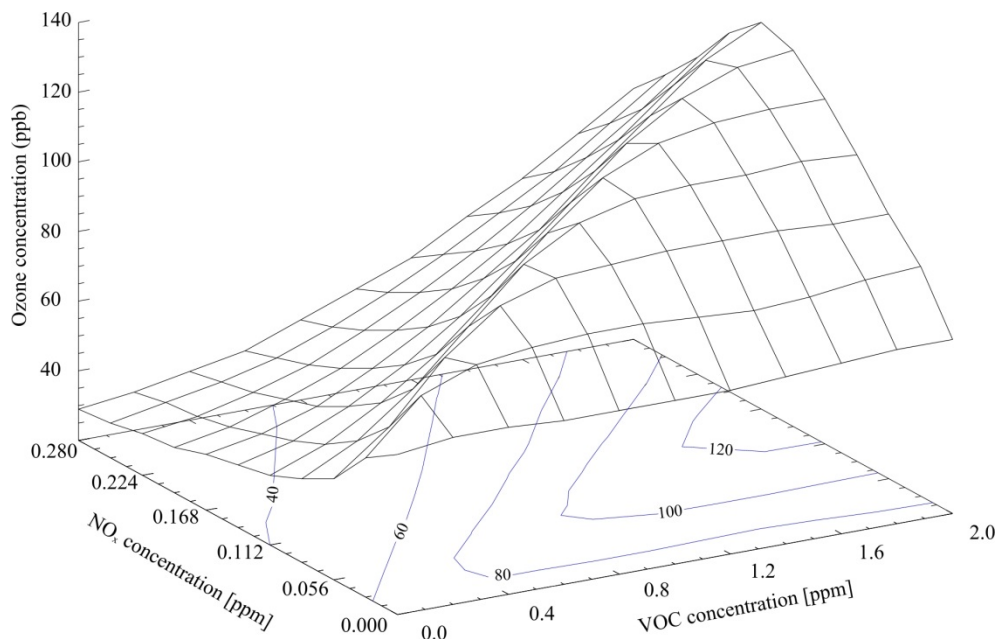


Figure 8.11: Modelled ozone concentration with different ratio of NO_x and VOC concentration

Near surface ozone is produced mainly in the urban environment due to the high emission of ozone precursor compounds. The ozone production depends on the rate of the precursors concentrations. Figure 8.11 shows a result

of a model simulation. The ozone concentrations were simulated by a simple box model in the function of NO_x and VOC concentrations. It seems that ozone concentration increasing with increase VOC concentration. Concentration of nitrogen compounds, however can affect both the ozone production and destruction. High NO emission in the city causes ozone destruction.

When the air mass from the city is transported to far away by the wind, higher ozone concentrations can be formed in rural NO-poor environment. Additionally biogenic emission of ozone precursors (e.g. isoprene emitted by trees) can cause further increase in ozone concentration. Hence, higher ozone concentrations most frequently occur in rural environment (Figure 8.12).

Surface ozone concentration has also a typical diurnal cycle. Highest values occur in the afternoon, when photochemical activity is more intense. The production during the day is also related to the daily course of precursor emissions. Typical diurnal cycle of the ozone concentration measured in an urban site is presented in Figure 8.13. This figure also shows a significant difference between a summer and a winter month. However, the daily variation of ozone concentration is similar in each period.

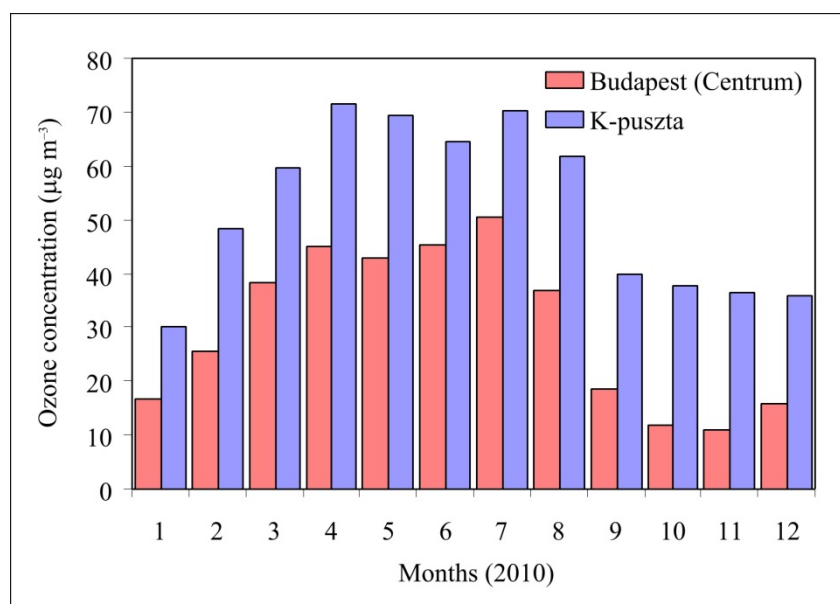


Figure 8.12: Average monthly ozone concentrations in 2010 in urban and rural environment. Data obtained from an urban measuring site of Hungarian Air Quality Monitoring System (Budapest centrum - Kosztolányi Dezső tér) and from a background measuring site of European Monitoring and Evaluation Programme (K-puszta) operated by Hungarian Meteorological Service. Sources of data: <http://www.nilu.no/projects/ccc/onlinedata/> and

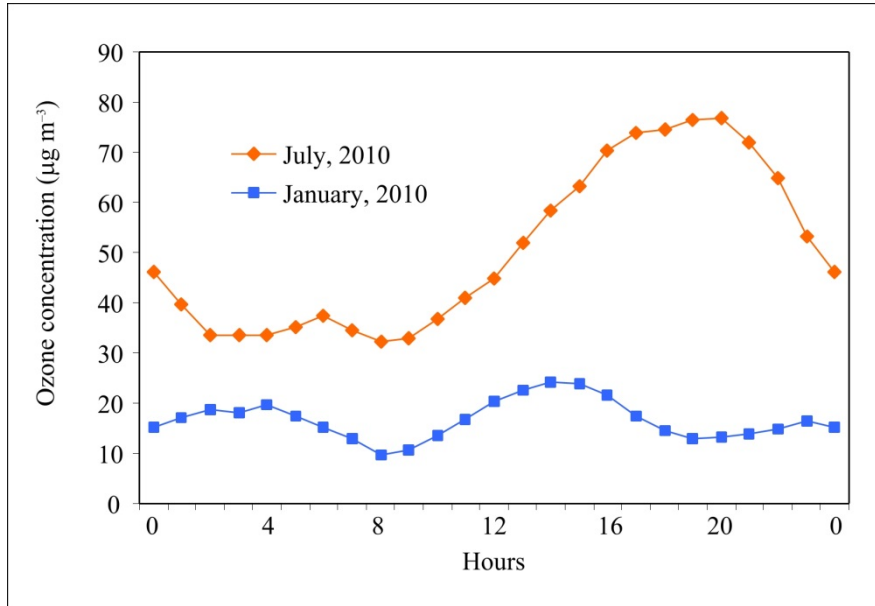


Figure 8.13: Average diurnal variation of ozone concentration in July and January, 2010. Data obtained from an urban measuring site of Hungarian Air Quality Monitoring System (Budapest centrum – Kosztolányi Dezső tér). Source of data:

Similar temporal variation can be found in background ozone concentration. The highest concentration values occur in spring and summer in the early afternoon hours, while the lowest ones in winter in the case of stable stratification (Figure 8.14).

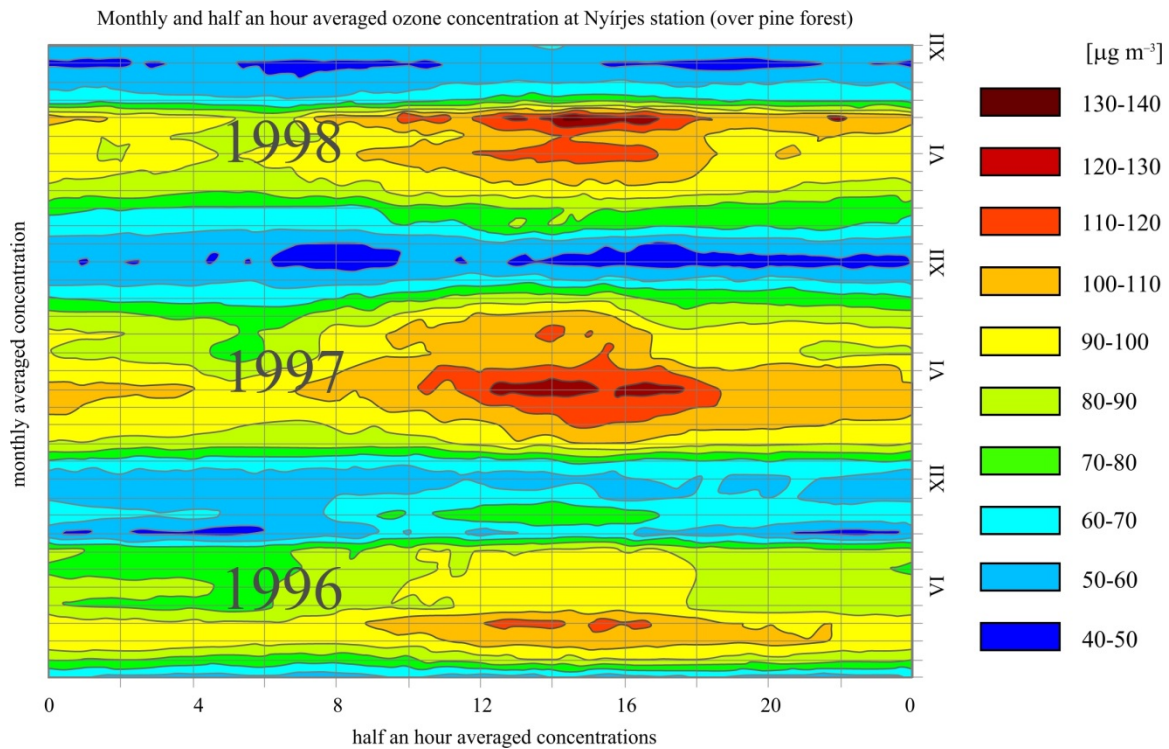


Figure 8.14: Temporal variability of background ozone concentration at Nyírjes station (Mátra Mountain) from 1996 to 1998.

References

- Crutzen P.J. and Arnold F.. 1986. *Nitric acid cloud formation in the winter Antarctic stratosphere: a major cause for the springtime ozone hole* In: *Nature*. 324. 651.
- Farman J.C., Gardiner B.G., and Shanklin J.D.. 1985. *Large losses of total ozone in Antarctica reveal seasonal ClOx/NOx interactions* In: *Nature*. 315. 217-210.
- Gerber E.P.. 2012. *Stratospheric versus Tropospheric Control of the Strength and Structure of the Brewer-Dobson Circulation* In: *Journal of the Atmospheric Sciences*. 69. 2857-2877.
- Guicherit R. and Roemer M.. 2000. *Tropospheric ozone trends*. *Chemosphere – Global Change Science*. 2. 167-183.
- Climate Change 2001: The Scientific Basis. Contribution of Working Group I to the Third Assessment Report of the Intergovernmental Panel on Climate Change*. Houghton J.T., Ding Y., Griggs D.J., Noguer M., van der Linden P.J., Dai X., Maskell K., and Johnson C.A.. (eds.). Cambridge University Press, Cambridge, United Kingdom and New York, NY, USA. 881. ISBN 0521 80767 0.
- Isaksen I.S.A.. 1994. *Reduction of stratospheric ozone from chlorine and bromine emission, and the effect on tropospheric chemistry*. In: *Boutron, F (ed) Topics in atmospheric and terrestrial physics and chemistry*. 251-270. ISBN 2-86883-241-5.
- Krupa S.V. and Manning W.J.. 1988. *Atmospheric ozone: formation and effects on vegetation* In: *Environmental Pollution* . 50. 101-137.
- Molina M.J. and Rowland F.S.. 1974. *Stratospheric sink for chlorofluoromethanes: chlorine atom catalyzed destruction of ozone* In: *Nature*. 249. 810-814.
- Molina M.J., Tso T.L., Molina L.T., and Wang F.C.. 1987. *Antarctic stratospheric chemistry of chlorine nitrate, hydrogen chloride, and ice: release of active chlorine* In: *Science*. 238. 1253-1257.
- Vingarzan R.. 2004. *A review of surface ozone background levels and trends* In: *Atmospheric Environment* . 38. 3431-3442.
- Error: no bibliography entry: d0e12890 found in <http://docbook.sourceforge.net/release/bibliography/bibliography.xml>
- Error: no bibliography entry: d0e12894 found in <http://docbook.sourceforge.net/release/bibliography/bibliography.xml>
- Error: no bibliography entry: d0e12898 found in <http://docbook.sourceforge.net/release/bibliography/bibliography.xml>

Chapter 9. Aerosol particles

Aerosol is a system of solid or liquid particles suspended by a mixture of gases. The term aerosols covers a wide spectrum of small particles, like sea salt particles, mineral dust, pollen, drops of sulphuric acid and many others. Aerosols have a great impact on several atmospheric phenomena, Earth's climate and on biosphere. During their atmospheric residence, different size solid and liquid particles influence the radiation and energy budget of the Earth's, the hydrological cycle, atmospheric circulation and the abundance of trace gases. Aerosol particles can be characterized by their concentration, size distribution, structure and chemical composition, which are highly variable both temporally and spatially.

9.1. Sources and sinks of atmospheric aerosols

After the emission of aerosol particles, they undergo various physical and chemical processes. During these processes, size, composition and structure of particles can be changed. Finally, they can be removed from the atmosphere to the surfaces by dry or wet deposition processes (Figure 9.1).

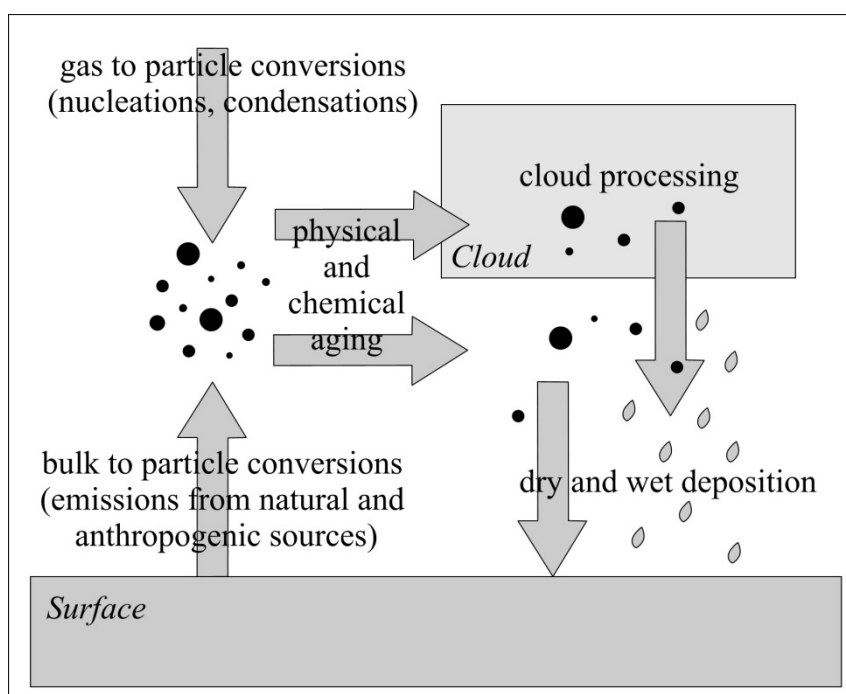


Figure 9.1: Atmospheric cycles of aerosol particles

9.1.1. Sources of aerosol particles

Aerosols originate from a wide variety of natural and anthropogenic sources. Various aerosol particles are generated through a combination of physical, chemical and biological processes. Based on the formation processes, different source types can be distinguished. Primary particles emitted directly to the atmosphere as liquids or solids, through a wide range of processes (Bulk-to-Particle Conversion, BPC). Some particles formed by nucleation¹ and condensation² of precursor gases (Gas-To-Particle Conversation, GPC), and others from the reactions of dissolved substance in cloud droplets.

During Bulk-to-Particle Conversion, many different aerosol particles are generated from solid or liquid base materials. Oceans and dry continental regions are the two main natural sources of atmospheric aerosol. A large amount

¹ Nucleation: generally defined as creation of molecular embryos or clusters prior to formation of a new phase during the transformation of vapor → liquid → solid. Nucleation can occur within the original phase (homogeneous nucleation), or on another phase, e.g. on a small particles (heterogeneous nucleation).

² Condensation: gas to liquid phase change.

of water droplets and sea salts are released to the atmosphere through sea spray and air bubbles at the surface of the seas (Figure 9.2).

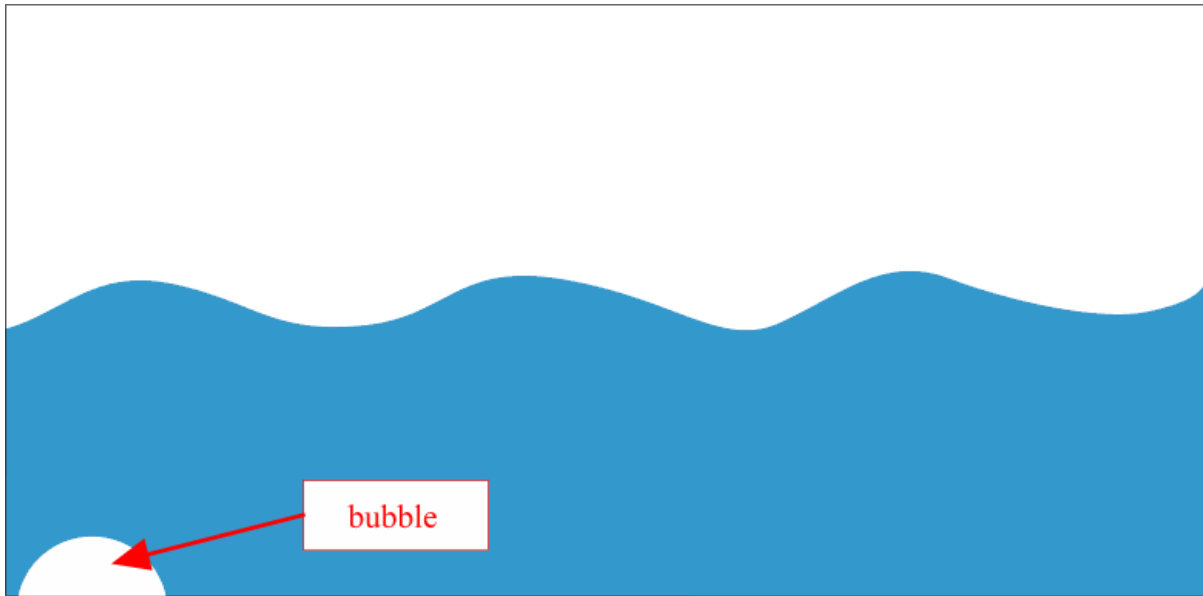


Figure 9.2: Droplet formation during the bursting of small bubble

As a water droplet evaporates, the salt is left suspended into the atmosphere forming a maritime aerosol particle (e.g. sodium-chloride (NaCl), magnesium sulphate (MgSO₄)). Other major source of primary particles is the windblown mineral dust from dry continental area, like deserts and semi arid regions. Further natural sources are volcanic ash, clay particles from soil erosion and biological materials (plant debris, pollen etc.). Additionally, different particles are formed by anthropogenic activities, like biomass burning, combustion of fossil fuel or industrial activities (Table 9.1).

Aerosol particles originated during Gas-To-Particle Conversion (e.g., sulphates, secondary organics) are not directly emitted, but are formed in the atmosphere from gaseous precursors (Table 9.2). Two basic processes can cause the formation of these secondary particles: an existing particle may grow through material condensing from gas phase, or new particle may forms through homogeneous nucleation.

Some other particles can form or transform by cloud droplets. When a cloud condensation nucleus³ as an aerosol particle dissolves in the water, and then reacts with other substances, it can build new aerosol substance and form a new aerosol particle when the water evaporates.

Table 9.1: Primary particle emissions (Tg / year) Source: IPCC (2001)

Sources	Range
Carbonaceous aerosols	66 – 217
Organic Matter:	
Biomass burning	45 – 80
Fossil fuel	10 – 30
Biogenic	0 – 90
Black carbon:	
Biomass burning	5 – 9
Fossil fuel	6 – 8
Aircraft	0.006

³ Cloud condensation nuclei (CCN): hygroscopic aerosol particles that can serve as nuclei of atmospheric cloud droplets, that is, particles on which water vapour condenses.

Industrial dust	40 – 130
Sea salt	1000 – 6000
Mineral (soil) dust	1000 – 3000

Table 9.2: Annual source strength for present day emissions of aerosol precursors (Tg N, S or C /year). Source: IPCC (2001)

Sources	Range
NO _x (Tg N y ⁻¹)	28 – 58
Fossil fuel	21.0
Aircraft	0.4 – 0.9
Biomass burning	2 – 12
Agricultural soil	0 – 4
Natural soil	3 – 8
Lightning	2 – 12
NH ₃ (Tg N y ⁻¹)	40 – 70
Domestic animals	10 – 30
Agriculture	6 – 18
Human	1.3 – 6.9
Biomass burning	3 – 8
Fossil fuel and industry	0.1 – 0.5
Natural soils	1 – 10
Wild animals	0 – 1
Oceans	3 – 16
SO ₂ (Tg S y ⁻¹)	67 – 130
Fossil fuel and industry	60 – 100
Aircraft	0.03 – 1.0
Biomass burning	1 – 6
Volcanoes	6 – 20
DMS and H ₂ S (Tg S y ⁻¹)	12 – 42
Oceans	13 – 36
Land biota and soils	0.4 – 5.6
Volatile organic emissions (Tg C y ⁻¹)	100 – 560
Anthropogenic	60 – 160
Terpenes	40 – 400

9.1.2. Sink processes

Aerosols can be removed from the atmosphere by different ways in the function of their size and disposition. Two main types of removing processes of aerosol particles are wet and dry deposition (see e.g. Sportisse, 2007; Petroff et al., 2008). In an annual global mean, about 80–90% of aerosol particles are removed from the atmosphere by in-cloud and below-cloud scavenging (wet deposition). Remaining part of particles is removed by different ways of dry deposition.

Wet deposition processes (the main sink of atmospheric aerosol particles):

Rain-out and washout: a part of cloud droplets form precipitation which reaches Earth's surface removing aerosols from cloud and from the column of air below the cloud.

Cloud deposition: deposition form of aerosols in high elevation ecosystems due to interception of cloud droplets by vegetation.

Dry deposition processes (less important on a global scale):

Turbulent diffusion: for larger particles (with a diameter larger than 1 μm) eddy diffusivity becomes important.

Gravitational settling (sedimentation): larger particles are influenced more by gravity and fall back to the surface. This process becomes increasingly important for particle sizes above 1 μm .

Impaction: if a particle cannot follow the flow streamline around an obstacle (e.g. a larger particle), small particle can hit this obstacle (Figure 9.3).

Interception: if an object is not directly in the path of particle moving in the gas stream (as in case of impaction), but particle approaches the edge of the obstacles, it may be collected by the obstacle (Figure 9.4).

Brownian diffusion: randomly moving smaller particles bump each other (thermal coagulation⁴) or to a larger obstacles (Figure 9.5). This process dominates for particle sizes below 0.2 μm . Brownian diffusion coefficients increase as particle diameter decreases. Additionally, in a very thin (about 1 mm) layer over the surface, the Brownian diffusion becomes more important for larger particles too.

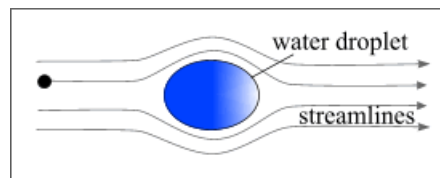


Figure 9.3: Impaction of an aerosol particle on an obstacle (for example on a larger water droplet)

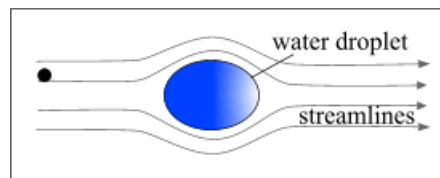


Figure 9.4: Particle interception by an obstacle (for example by a larger water droplet)

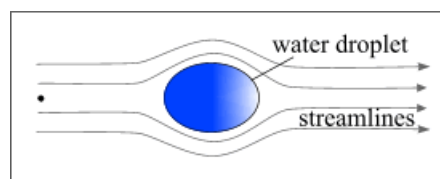


Figure 9.5: Brownian diffusion of a small aerosol particle

9.2 Physical and chemical characteristics of aerosols

The environmental impacts of atmospheric particles depend on their physical, chemical properties, lifetimes and abundances. The concentration, size distribution and composition of atmospheric aerosol particles are highly variable both temporally and spatially.

⁴ Particle coagulation: a process, in which small particles collide with each other and coalesce completely to form a larger particle.

9.2.1. Concentrations:

Different measures are commonly used to describe the aerosol concentration: these are number, area volume and mass concentrations (Table 9.3).

Table 9.3: Commonly used measures of aerosol concentration

Name	Unit	Description
Number concentration	cm^{-3}	N
Area concentration	$\mu\text{m}^2 \text{cm}^{-3}$	$4 r^2 \pi N$
Volume concentration	$\mu\text{m}^3 \text{cm}^{-3}$	$4/3 r^3 \pi N$
Mass concentration	$\mu\text{g m}^{-3}$	$4/3 r^3 \pi N \rho$

Table 9.4: Number concentration and mass concentration of aerosol particles at different locations (source: Heintzenber, 1994).

Location	Number concentration (cm^{-3})	Mass concentration ($\mu\text{g m}^{-3}$)
Urban	$10^5 - 10^7$	$10^1 - 10^4$
Rural	$10^3 - 10^4$	$10^1 - 10^2$
Remote maritime	10^2	$10^1 - 10^2$
Polar	$10^0 - 10^3$	$10^{-1} - 10^1$

In the lower troposphere, the total particle number concentration typically varies in the range of about 10^2 – 10^5 cm^{-3} , and typical mass concentration varies between 1 and $100 \mu\text{g m}^{-3}$ (Table 9.4). Aerosol concentrations in the free troposphere are typically 1–2 orders of magnitude lower than in the atmospheric boundary layer.

PM_x (particulate matter with diameter smaller than $x \mu\text{m}$) is another often-used measure to describe the aerosol mass concentration. $\text{PM}(2.5)$ and $\text{PM}(10)$ are routinely monitored values.

9.2.2. Size distribution:

Aerosol particles in the atmosphere have widely variable shapes. Their dimensions are usually characterized by a particle diameter, which span over four orders of magnitude, from a few nanometers to around $100 \mu\text{m}$. Particle size is one of the most important parameters to describe the behaviour of aerosols, affecting both their lifetime, physical and chemical properties. Distribution of aerosol particles is generally defined by their number, surface or volume (Figure 9.6).

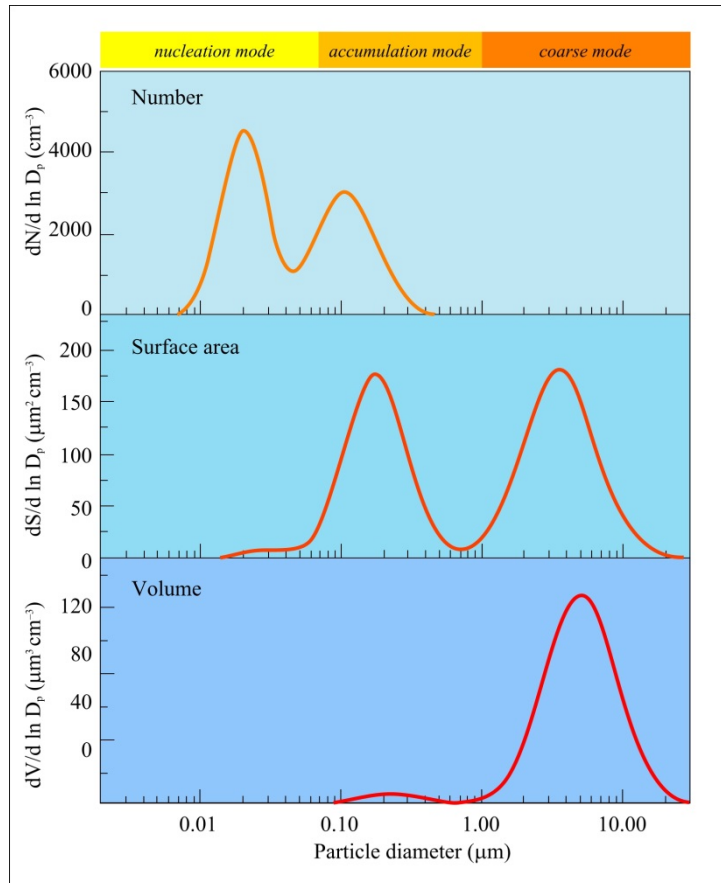


Figure 9.6: Number, surface and volume distributions of aerosol particles. The areas below the curves correspond to the total aerosol number, surface and volume, respectively.

Based on particle distributions, different groups of atmospheric particles can be separated:

- nucleation (Aitken) mode (particle diameter $< 0.1 \mu\text{m}$),
- accumulation mode (particle diameter: $0.1 \mu\text{m} > d > 1 \mu\text{m}$),
- coarse mode (particle diameter $d > 1 \mu\text{m}$).

Aerosol particles below $0.1 \mu\text{m}$ in diameter constitute the *nucleation (or Aitken) mode*. The smallest range of these particles (with particle diameter is lower than $0.01 \mu\text{m}$) sometimes called ultrafine mode. These particles are produced by homogeneous and heterogeneous nucleation processes (Figure 9.7). They can form during natural gas-to particle condensation (Figure 9.8) or during condensation of hot vapour in combustion processes. Due to their rapid coagulation (Figure 9.9) or random impaction onto surfaces, the lifetime of these small particles is very short (order of minutes to hours).

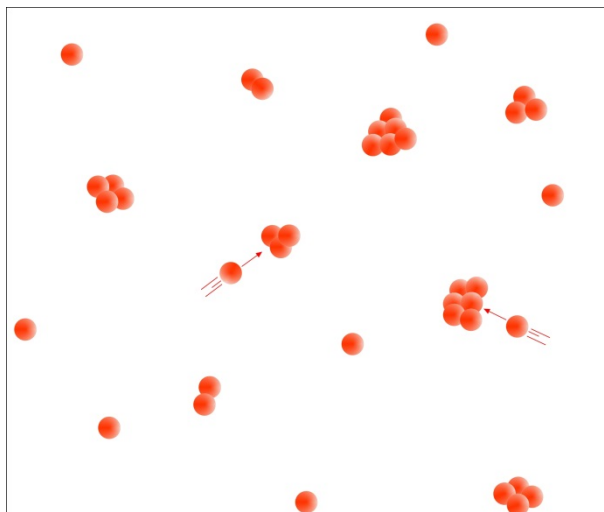


Figure 9.7: Homogeneous nucleation of aerosol particles

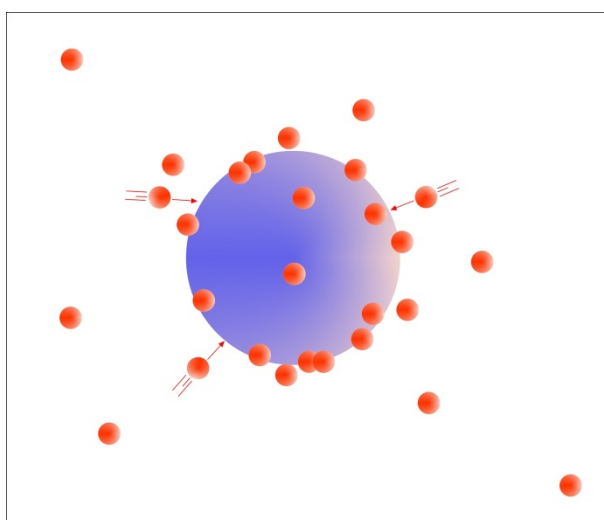


Figure 9.8: Condensation of aerosol particles

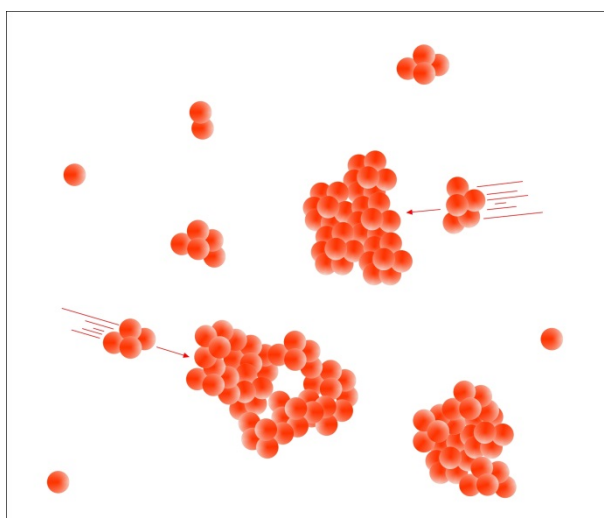


Figure 9.9: Coagulation of aerosol particles

Larger aerosol particles in the size range 0.1 to 1 μm in diameter can accumulate in the atmosphere because their removal mechanisms are least efficient. Their lifetime in the atmosphere is 7–10 days and during this period they can be transported to a long distance from their sources. Particles belonging to this accumulation mode are formed mainly by coagulation (Figure 9.9) of smaller particles or condensation of vapours onto existing particles, and during these mechanisms they grow into this size range. At the same time, they can also be emitted to the atmosphere from different sources, mainly from incomplete combustion. Accumulation particles removed from the atmosphere mainly by wet deposition.

The Coarse mode contains particles with diameter larger than 1.0 μm . These particles are mostly emitted to the atmosphere during mechanical processes from both natural and anthropogenic sources (e.g. sea-salt particles from ocean surface, soil and mineral dust, biological materials). Due to their relatively large mass, they have short atmospheric lifetimes because of their rapid sedimentation.

The distribution of atmospheric aerosol particles can be seen in Figure 9.6. Small particles in nucleation mode constitute the majority of atmospheric particles by number. However due to their small sizes, their contribution to the total mass of aerosols is very small (around a few percent). The Accumulation mode particles have the greatest surface area. The mass or volume concentration is dominated by the aerosols in coarse and accumulation modes. Size, area and volume distributions of aerosol particles show characteristic patterns at different locations (e.g. urban, rural, remote continental or marine regions).

9.2.3. Chemical composition

The atmospheric aerosol has a very complex and variable chemical composition. Due to the various sources and transformations, each particle has individual composition. Atmospheric aerosols are generally composed of variable amounts of sulphate, nitrate, ammonium, sea salt, crustal elements and carbonaceous compounds (elemental and organic carbon) and other organic materials. Fine particles predominantly contain sulphate, nitrate, ammonium, elemental and organic carbon and certain trace metals (e.g. lead, cadmium, nickel, copper etc.). The primary components of coarse particle fraction are dust, crustal elements, nitrate, sodium, chloride and biogenic organic particles (e.g. pollen, spores, plant fragments etc.).

The main precursors of sulphate component (SO_4^{2-}) in the troposphere are sulphur dioxide (SO_2) emitted from anthropogenic sources and volcanoes, and dimethyl sulphide (DMS) from biogenic sources, especially from marine planktons. In the stratosphere, sulphate aerosols are mostly converted from carbonyl sulphide (COS).

Nitrate (NO_3^-) is formed mainly from the oxidation of atmospheric nitrogen dioxide (NO_2). Ammonium salts are also common components of atmospheric aerosols. They are formed during the reactions between ammonia (NH_3) and various acids, like sulphuric (H_2SO_4) and nitric acids (HNO_3). When atmospheric ammonia neutralises these acids, ammonium sulphate ($(\text{NH}_4)_2\text{SO}_4$), and ammonium nitrate (NH_4NO_3) particles are formed. Main source of chloride (Cl^-) is sea spray, but ammonium chloride (NH_4Cl) particles form also during the reaction between ammonia and hydrochloric acid (HCl).

Carbonaceous materials constitute a large but highly variable fraction of the atmospheric aerosol. The carbonaceous fraction of the aerosols consists of both elemental carbon (EC) or black carbon (BC) and organic carbon (OC). The ratio of elemental to total carbon (EC+OC) is strongly dependent on the sources. The main sources of elemental carbon particles are biomass and fossil fuel burning. Particles containing organic carbon can be emitted directly to the atmosphere also from biomass burning or combustion processes and by secondary organic aerosol (SOA) formation during the atmospheric oxidation of biogenic or anthropogenic volatile organic compounds (VOC).

Typical chemical composition of aerosols can vary at different locations, times, weather conditions and particle size fractions. Figure 9.10, Figure 9.11 and Figure 9.12 show the relative abundance of different chemical components of fine particles in different locations, in urban area, in rural region and in a remote site, respectively.

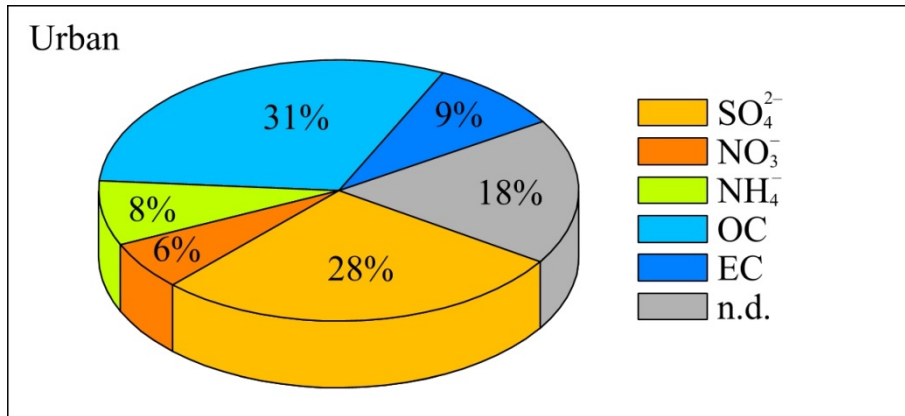


Figure 9.10: Average fine particle composition of aerosol types in urban area. Data correspond to mass fraction in % of the total fine particle mass concentration. OC = organic carbon, EC = elementary carbon. Source of data: Heitzenberg, 1994.

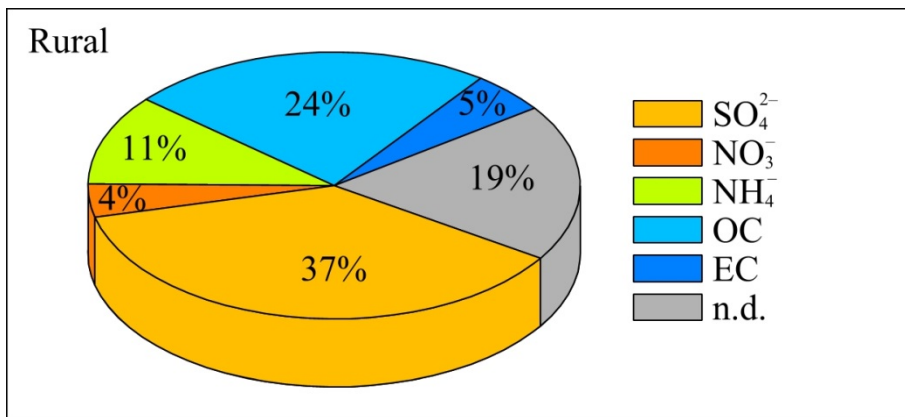


Figure 9.11: Average fine particle composition of aerosol types in rural continental region. Data correspond to mass fraction in % of the total fine particle mass concentration. OC = organic carbon, EC = elementary carbon. Source of data: Heitzenberg, 1994.

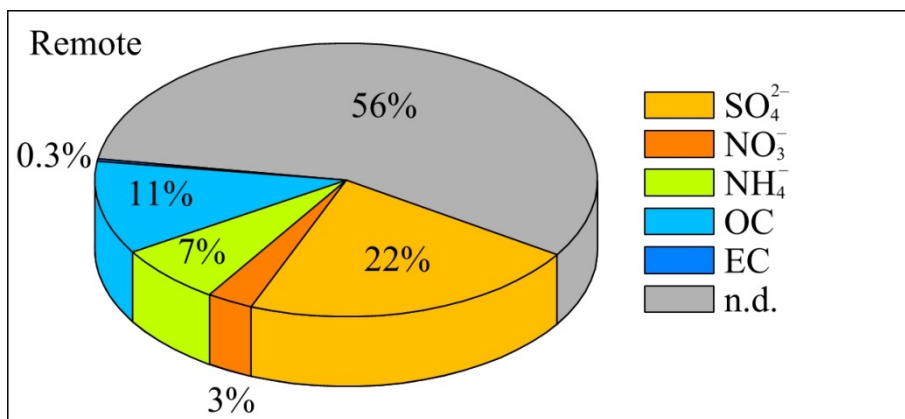


Figure 9.12: Average fine particle composition of aerosol types in remote region. Data correspond to mass fraction in % of the total fine particle mass concentration. OC = organic carbon, EC = elementary carbon. Source of data: Heitzenberg, 1994.

9.2.4. Water solubility

Atmospheric particles can also be categorized by their water solubility, that is, how well they dissolve in water. In continental regions, about 80% of smaller particles are water-soluble. However, some types of coarse particles are also water soluble, like sea salt particles over oceans. Most water-soluble aerosol components are hygroscopic and they can absorb water. If aerosol particles consisting of water-soluble material, the uptake of atmospheric water vapour can result in an aqueous solution droplet. During this process, the size of the particle increases by hygroscopic growth, even when relative humidity is lower than 100%. Highly soluble particles are for example ammonium sulphate, ammonium nitrate and sodium chloride. These particles are efficient cloud condensation nuclei (CCN).

Several particles are poorly soluble or insoluble in water. Insoluble aerosols for example particles derived from soil dust or volcanoes (e.g. metal oxides, silicates, clay minerals).

9.2.5. Atmospheric lifetime

The lifetime of atmospheric aerosol particles depends on their properties (size, chemical composition, etc.) and on altitude range, too (Figure 9.13). In the atmospheric boundary layer (lower troposphere), the residence time of aerosol particles is usually less than a week, often on the order of a day, depending on aerosol properties and meteorological conditions. In the free troposphere, the typical particle lifetime is 3–10 days on average. During this time, a particle can easily be transported to a long distance. Therefore, there is a large variability in particle concentration, reflecting the geographical distribution of sources and sinks. The stratosphere also contains aerosol particles, which have much longer lifetimes (up to 1 year), than in the tropospheric particles, due to the lack of precipitation.

Smaller particles are efficiently removed by coagulation with other particles. Therefore, their lifetime is very short (in a range of ten minutes to day). Similarly, the large particles spend only a short time in the atmosphere due to sedimentation. Particles in the accumulation mode have the longest lifetime (7–10 days on average), as in this range, both the Brownian diffusion and sedimentation are less important. These particles are removed from the atmosphere predominantly by wet deposition.

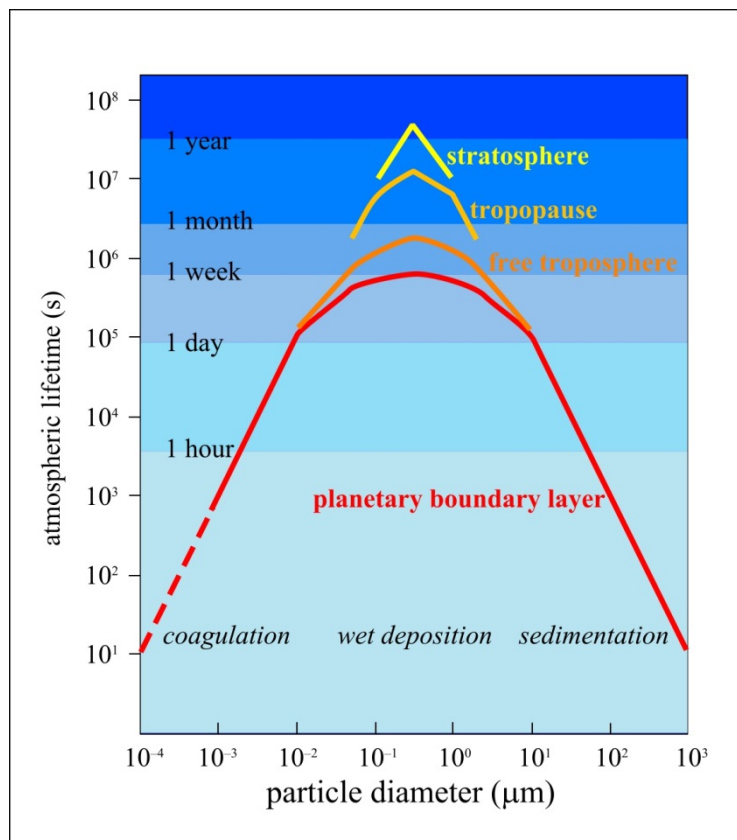


Figure 9.13: Atmospheric lifetime of different size particles at different levels of the atmosphere (after Jaenicke, 1980)

Table 9.5 summarises the sources and formations as well as the main physical and chemical properties of different size aerosol particles.

Table 9.5: Main properties of different aerosol particles (Adapted from Wilson and Suh, 1997):

	Nucleation mode	Accumulation mode	Coarse mode
	(Fine particles)	(Coarse particles)	
Size:	$d < 0.1 \mu\text{m}$	$0.1 \mu\text{m} > d > 1 \mu\text{m}$	$d > 0.1 \mu\text{m}$
Sources:	Combustion Gas-to Particle conversion Chemical reactions	Combustion Gas-to Particle conversion Chemical reactions	Dust Soil Biological sources Ocean spray
Formation	Chemical reactions Nucleation Condensation Coagulation	Nucleation Condensation Coagulation Evaporation of droplet	Mechanical disruption of surface Suspension ^a of dust Evaporation of ocean spray Chemical reactions
Composition	Sulphate Elemental carbon Trace metals, Low-volatility organic compounds	Sulphate Nitrate Ammonium Elemental Carbon Organic Component Trace metals (Pb, Cd, V, Ni, Cu, Zn, Fe, etc.)	Dust Ash Crustal elements Sea salt Nitrate Biogenic organic particles
Solubility	Largely soluble, hygroscopic	Largely soluble, hygroscopic	Largely insoluble, non-hygroscopic
Travel distance	<a few 10 of km	a few 100 to 1000 of km	<a few 10 of km (sometimes larger)
Typical atmospheric lifetime	Minutes to hours	Days to weeks	Minutes to days
Sinks	Growth into accumulation mode, wet and dry deposition	Wet deposition, dry deposition (Brownian diffusion, turbulence)	Wet deposition, dry deposition (sedimentation, turbulence)

^a Suspension: (in atmospheric chemistry :) a dispersion of fine solid or liquid particles in the atmosphere. Dust is an example of atmospheric suspension.

9.3. Effects of atmospheric aerosols

Atmospheric aerosol particles play important role in radiation budget of the Earth's as they scatter and absorb both shortwave solar radiation and longwave terrestrial radiation. They are also highly involved in the formation of

clouds and precipitation since they operate as cloud condensation and ice nuclei (CCN and IN⁵). Aerosols can form the abundance and distribution of atmospheric trace gases by complex chemical reactions, and can affect significantly the cycles of nitrogen, sulphur, and atmospheric oxidants. Aerosol particles in the upper atmosphere, where the major part of atmospheric ozone forms, can modify the ozone removal (Mészáros, 2000). Additionally, particles are major elements of lower tropospheric air quality, and can influence harmfully the environment and human health.

Aerosols play important role in the balance of the Earth's climate. Due to the increasing anthropogenic emission of aerosols since the industrial revolution, they can also effect the global climate change. However, the effects of aerosols on climate are not one-way, moreover excessively uncertain. The climate forcing by aerosols can be realized in two ways, basically: in direct and indirect radiative forcing.

9.3.1. Direct effects: direct radiative forcing due the scattering radiation.

Aerosol particles reflected a part of shortwave solar radiation back into the space, cooling the Earth's atmosphere. This cooling effect of aerosols, especially by sulphate components may be compensated by the absorption of longwave terrestrial radiation primarily by elemental (black) carbon aerosols and dust particles. The global, annual mean radiative forcing still less certain and is estimated $-0.4 \pm 0.2 \text{ W m}^{-2}$ for sulphate, $-0.05 \pm 0.05 \text{ W m}^{-2}$ for fossil fuel organic carbon, $+0.2 \pm 0.15 \text{ W m}^{-2}$ for fossil fuel black carbon, $+0.03 \pm 0.12 \text{ W m}^{-2}$ for biomass burning, $-0.1 \pm 0.1 \text{ W m}^{-2}$ for nitrate and $-0.1 \pm 0.2 \text{ W m}^{-2}$ for mineral dust (IPCC, 2007). A large volcanic eruption can greatly increase the concentration of stratospheric sulphate aerosols, thereby increasing the negative radiative forcing. However, a single, large eruption can cool our atmosphere only for a few years.

9.3.2. Indirect effects: indirect radiative forcing through cloud formation effects

Aerosol particles can also affect the radiation balance by formation of cloud droplets. Cloud droplets are formed in the troposphere by condensation of water vapour onto aerosol particles (cloud condensation nuclei, or ice nuclei) when the relative humidity exceeds the saturation level. Without these particles, a very large supersaturation (about 400%) would be necessary for the homogeneous condensation of water vapour.

The properties and the number of particles can affect the formation and the characteristic of clouds and precipitation in many ways (Lohmann and Feichter, 2005). The increased number of aerosol particles, and therefore the increased cloud optical thickness decrease the net surface solar radiation. The more numerous smaller cloud particles reflect more solar radiation (called albedo effect or Twomey effect). Smaller particles decrease the precipitation efficiency, thereby prolonging cloud lifetime. The absorption of solar radiation by soot particles may cause evaporation of cloud particles (semi-direct effect). In mixed-phased clouds, smaller cloud droplets delay the beginning of freezing and decrease the riming efficiency. However, more ice nuclei increase the precipitation efficiency.

Anthropogenic aerosols effects on water clouds through the cloud albedo effect cause a negative radiative forcing of -0.3 to -1.8 W m^{-2} (IPCC, 2007).

References

Heintzenber J.. 1994. *The life cycle of the atmospheric aerosol*. In: *Boutron, F (ed) Topics in atmospheric and terrestrial physics and chemistry*. 251-270. ISBN 2-86883-241-5.

Climate Change 2001: The Scientific Basis. Contribution of Working Group I to the Third Assessment Report of the Intergovernmental Panel on Climate Change. Houghton J.T., Ding Y., Griggs D.J., Noguer M., van der Linden P.J., Dai X., Maskell K., and Johnson C.A.. (eds.). Cambridge University Press, Cambridge, United Kingdom and New York, NY, USA. 881. ISBN 0521 80767 0.

⁵ Ice nuclei (IN): aerosol particles that can serve as nuclei of ice crystals.

- Climate Change 2007: The Physical Science Basis. Contribution of Working Group I to the Fourth Assessment Report of the Intergovernmental Panel on Climate Change.* Solomon S., Qin D., Manning M., Chen Z., Marquis M., Averyt K.B., Tignor M., and Miller H.L. (eds.). Cambridge University Press, Cambridge, United Kingdom and New York, NY, USA. 996. ISBN 978 0521 88009-1.
- Jaenicke R.. 1980. *Atmospheric aerosols and global climate* In: *Journal of Aerosol Sciences*. 11. 577-588.
- Lohmann U. and Feichter J.. 2005. *Global indirect aerosol effects: a review* In: *Atmospheric Chemistry and Physics*. 5. 715-737.
- Mészáros E.. 2000. *Fundamentals of Atmospheric Aerosol Chemistry*. Akadémiai Kiadó, Budapest. 308. ISBN 9630576246.
- Petroff A., Mailliat A., Amielh M., and Anselmet F.. 2008. *Aerosol dry deposition on vegetative canopies. Part I: Review of present knowledge* In: *Atmospheric Environment*. 42. 3625-3653.
- Pöschl U.. 2005. *Atmospheric Aerosols: Composition, Transformation, Climate and Health Effects* In: *Angewandte Chemie International Edition*. 44. 7520-7540.
- Sportisse B.. 2007. *A review of parameterizations for modelling dry deposition and scavenging of radionuclides* In: *Atmospheric Environment*. 41. 2683–2698.
- Wilson W.E. and Suh H. H.. 1997. *Fine Particles and Coarse Particles: Concentration Relationships Relevant to Epidemiologic Studies* In: *Journal of the Air & Waste Management Association*. 47. 12. 1238-1249.

Chapter 10. Dispersion of air pollutants

10.1. Introduction

There are many accidents and natural events, where harmful and toxic chemical species can be emitted into the atmosphere (e.g., accidental release at nuclear power plant (NPP), volcano's eruptions, forest fires). These air pollutants can travel hundreds and thousands kilometres from their release points across the globe depending on their chemical (chemical composition) and physical (e.g., solubility in water, size distribution for aerosol particles) properties, and they affect the human health and result in a long-term effect on our environment. Moreover, such incidents could have huge economical impact. For example the eruption of Eyjafjallajökull in Iceland over a period of six days in April, 2010 caused enormous disruption to air travel in most part of Europe because of the closure of airspace. Estimated lost of airlines was about US\$1.7 billion.

It is important to note that model simulations must have a high degree of accuracy and must be achieved faster than real time to be of use them in an effective decision support. Therefore, accurate and fast simulation of dispersion of toxic chemical substances or radionuclides in the atmosphere is one of the most important and challenging tasks in atmospheric sciences. Chernobyl disaster and an increased demand from the society have stimulated the development of accidental release programs and complex decision making softwares (e.g., RODOS). Underestimating the maximum concentrations of air pollutants may have serious health consequences, and conversely, applying remediation measures in regions where significant dosage will not be received would waste valuable resources and may have significant social implications if evacuation or other interventions is required. This demand and extreme pressure from the society and business bodies can be illustrated by the following statement by Giovanni Bisignani, chief executive of IATA, during the Eyjafjallajökull incidents: "Airspace was being closed based on theoretical models, not on facts. Test flights by our members showed that the models were wrong."

Dispersion of air pollutants in the troposphere is mainly governed by advection (wind) field, however, other processes like turbulent diffusion (turbulence) or radioactive decay, chemical reaction and deposition of air pollutants play important role in the spatiotemporal evolution of dispersion pattern. Development of models requires complex thinking and interaction of researchers from different fields. For simulating the dispersion of air pollutants, various modelling approaches have been developed. The main aim of this chapter is to provide a comprehensive review of air pollution modelling. The chapter is structured as follows. Section 2 provides an overview of air pollution modelling. Following 3 sections describe Gaussian, Lagrangian and Eulerian dispersion models with their advantages and drawbacks. Finally, section 6 discusses computational fluid dynamics models for environmental modelling.

10.2. Overview of air dispersion modelling

10.2.1. The transport equation

In a selected V_I volume of the fluid, mass conservation of the component described with c concentration can be expressed as:

$$\frac{d}{dt} \iiint_{V_I} c dV = - \oint_{\partial V_I} c \vec{v} d\vec{A} + \iiint_{V_I} S_c dV - \oint_{\partial V_I} (-D_c \nabla c) \cdot \vec{n} dA \quad (10.1)$$

Where \vec{v} is the wind vector, S_c is the source term and D_c is the diffusion coefficient. Equation (10.1) represents the change of the total mass of the material within volume V_I as the sum of the advective flux through the borders of the volume, source terms inside the volume, and the diffusive flux. In dispersion models, wind field and other meteorological data is obtained from measurement or a numerical weather prognostic (NWP) model, thus the only unknown term in equation (10.1) is the c concentration field. We can transform equation (10.1) into a differential form using Gauss' formula and generalizing the integrates to any V_I volumes:

$$\frac{\partial c}{\partial t} = -\nabla \cdot (c\vec{v}) + S_c + \nabla \cdot (D_c \nabla c) \quad (10.2)$$

This is the dispersion equation that describes advection, source and molecular diffusion processes. Dry and wet deposition, chemical or radioactive decay is part of the S_c term, while gravitational settling can be added as an extra advection component. Turbulent diffusion, however, is not represented in equation (2).

Turbulence is usually taken into account with Reynold's theory that splits the wind and concentration field into time-averaged and turbulent perturbation values:

$$\vec{v} = \bar{\vec{v}} + \vec{v}' \quad (10.3)$$

$$c = \bar{c} + c' \quad (10.4)$$

From equations (10.2) and (10.3, 10.4) we can construct a dispersion equation that represents both time-averaged and perturbation components:

$$\frac{\partial \bar{c}}{\partial t} + \frac{\partial c'}{\partial t} = -\nabla(\bar{v}\bar{c}) - \nabla(\bar{w}c') - \nabla(\bar{v}'c') - \nabla(\bar{v}'c') + S_c + \nabla(D_e \nabla \bar{c}) + \nabla(D_e \nabla c') \quad (10.5)$$

Time averaging equation (10.5) will eliminate all the components that contain a single perturbation term, as the Reynolds model is based on the assumption that turbulent perturbations' time average is zero. However, not all perturbations will disappear as the covariance term's time average is not necessarily 0:

$$\frac{\partial \bar{c}}{\partial t} = -\nabla(\bar{v}\bar{c}) - \nabla(\bar{w}c') + S_c + \nabla(D_e \nabla \bar{c}) \quad (10.6)$$

We can here conclude that dispersion equation (10.5) for turbulent flows can be written in the same form as equation (10.2) with the addition of three eddy covariance terms. Writing the turbulent components explicitly and assuming an isotropic molecular diffusion, equation (10.6) can be rewritten in a form that is widely used in atmospheric dispersion modelling:

$$\frac{\partial \bar{c}}{\partial t} = -\nabla(\bar{v}\bar{c}) + S_c + D_e \nabla^2 \bar{c} - \frac{\partial(\overline{u'c'})}{\partial x} - \frac{\partial(\overline{v'c'})}{\partial y} - \frac{\partial(\overline{w'c'})}{\partial z} \quad (10.7)$$

The right side of equation (10.7) describes advection, source terms, molecular diffusion and horizontal and vertical turbulent fluxes. In the atmosphere, turbulent mixing is magnitudes more efficient than molecular diffusion thus the third component of equation (10.6) can usually be neglected. However, in the laminar layer within 0.1 – 3 cm of the ground, turbulence is very weak, therefore molecular diffusion gets a large importance in the investigation of soil-atmosphere fluxes and deposition processes, often treated as a resistance term.

Equation (10.7) involves four new variables in the equation. There are two ways for the closure of the turbulent dispersion equation: either we construct new transport equations for the turbulent fluxes or we use parameterization to express the turbulent fluxes with time-averaged concentration and wind values. The former approach leads to the Reynolds Stress Models (RSM), while the latter is the widely used gradient transport theory, or K-theory. These are presented in details in Stull (1988), here we provide a brief outline of their results.

As an analogy of Fick's law for molecular diffusion, gradient transport theory is based on the assumption that the x directional turbulent flux is proportional to the first component of the gradient of the concentration field:

$$\overline{u'c'} = -K_x \frac{\partial \bar{c}}{\partial x}, \quad (10.8)$$

where K_x is the x directional turbulent diffusion coefficient or eddy diffusivity. Using this approach equation (10.7) results in a form where turbulent fluxes are expressed as an additional diffusion term:

$$\frac{\partial \bar{c}}{\partial t} = -\nabla(\bar{v}\bar{c}) + S_c + D_e \nabla^2 \bar{c} + \nabla(\underline{K} \nabla \bar{c}), \quad (10.9)$$

where \underline{K} is a diagonal matrix of the K_x, K_y, K_z eddy diffusivities. Due to the different atmospheric turbulent processes in horizontal and vertical direction, \underline{K} cannot be assumed to be isotropic. Furthermore, while D_c is a property of the chemical species, \underline{K} is a property of the flow, thus it varies in both space and time. Assuming an incompressible fluid and isotropic horizontal turbulence and neglecting the molecular diffusion, the dispersion equation can be written in a form:

$$\frac{\partial \bar{c}}{\partial t} = -\bar{v} \nabla \bar{c} + S_c + \nabla_k (K_k \nabla_k \bar{c}) + \frac{\partial}{\partial z} K_z \frac{\partial \bar{c}}{\partial z}, \quad (10.10)$$

where ∇_k is the horizontal divergence operator, K_h is the horizontal and K_z is the vertical eddy diffusivity. These two parameters need to be estimated at each grid point and timestep through various parameterizations.

Reynolds Stress Models (RSM) construct new transport equations for the turbulent fluxes based on the turbulent kinetic energy and dissipation values (Launder et al., 1975). This approach has larger computational cost than gradient transport models, however, its results proved to be more accurate in several microscale cases (Rossi and Iaccarino, 2009, Chen, 1996). While RSMs have been successfully applied in CFD-based microscale atmospheric models (Riddle et al., 2004), on meso- and macroscale, computationally more efficient eddy diffusivity approach is used (Draxler and Hess, 1998, Lagzi et al., 2009).

The dispersion equation (10.10) can be solved numerically with spatial discretization of variables on a grid, which is often referred to as the Eulerian approach. Under some assumptions, (10.10) can also be solved analytically and provides a Gaussian distribution that is widely used in Gaussian dispersion models. A stochastic solution also exists where instead of solving the partial differential equation (PDE), equation (10.10), the concentration field is given as a superposition of a large number of drifting particles (Lagrangian approach).

10.2.2. Turbulence parameterization

Turbulence is a key process in dispersion simulations: while downwind dispersion is usually dominated by advection, crosswind or even upwind turbulent mixing is magnitudes more efficient than molecular diffusion. Turbulence is treated on different scales: macroscale turbulence, with a scale larger than the numerical weather prediction (NWP) model's grid resolution, is computed explicitly within the NWP thus it is taken into account in the advection term. Subgrid-scale turbulence causes a velocity and concentration fluctuation, often referred to as turbulent diffusion. We note that subgrid-scale velocity fluctuation also has an effect on the large scale flow through turbulent viscosity. This effect is treated with various turbulence parameterizations in the NWP models.

Atmospheric dispersion can be regarded as a sum of two main effects: the mechanical turbulence caused by wind shear, and the thermal turbulence caused by buoyancy. Their characteristics and dependence on measurable variables is very different (Table 10.1).

Mechanical turbulence estimates rely on 3D wind field measurement data to obtain wind shear values. Surface roughness also has an important role in generating mechanical turbulence through friction in the ground layer. Surface roughness is usually measured with the z_0 roughness length, a characteristic length of surface obstacles. Typical roughness lengths of different surfaces are shown in table 10.2. The models make the difference between complex terrain and surface roughness upon the scale of the problem: while the flow around large scale geometry covered with multiple grid points is computed explicitly in the model, sub-grid scale geometry is treated as roughness and parameterized through its effect on turbulence.

Table 10.1: Parameters that affect turbulence patterns in the planetary boundary layer (PBL)

Mechanical turbulence (wind shear)	Thermal turbulence (buoyancy)
3D PBL wind field	3D PBL (potential) temperature field
Surface roughness	Sun elevation
Complex terrain	Cloud cover
	Albedo
	Surface land use (sensible heat)

	Surface evapotranspiration (latent heat)
--	------------------------------------------

Table 10.2: Typical roughness length and albedo values of different surfaces

Surface	Roughness length	Albedo
Open water	1 mm	0.1
Fresh snow	5 mm	0.9
Flat terrain with low grass	5 cm	0.25
High crops	25 cm	0.2
Forest	1 m	0.15
Buildings	several meters	0.05

Thermal turbulence depends largely on the atmospheric stability and the surface's radiation budget. Under stable conditions, thermal turbulence is low, and mixing is determined by the wind shear strength. On the other hand, in a convective boundary layer (CBL), thermal turbulence has a significant role in dispersion processes. Surface parameters, like albedo (Table 10.2) or potential evapotranspiration have a large importance in the estimation of sensible and latent heat fluxes that determine the thermal turbulence intensity.

The strength of the turbulence can be described using various measures. One of them is eddy diffusivities (m^2s^{-1}) that represent a diffusion coefficient in the dispersion equation (10.10). Another approach is to estimate the u' , v' , w' wind fluctuation components (equation 10.3), and calculate the turbulent kinetic energy (TKE , Jkg^{-1}) that describe the time-averaged energy of subgrid-scale turbulent eddies (Stull, 1988):

$$TKE = \frac{1}{2} (\overline{u'^2} + \overline{v'^2} + \overline{w'^2}) \quad (10.11)$$

While eddy diffusivities and turbulent kinetic energy explicitly describe turbulence intensity, there are dispersion-oriented characteristics that try to estimate the mixing efficiency instead of describing the turbulence itself. Mixing efficiency is often treated as the deviation of a Gaussian plume, which is widely used in Gaussian and puff models. Lagrangian models use a stochastic random-walk simulation for mixing.

As both wind and temperature changes in space and time, atmospheric turbulence is a non-homogenous, non-stationary field. Furthermore, thermal turbulence is highly anisotropic, which means a difficult challenge for turbulence models especially in a convective boundary layer and leads to the separated treatment of horizontal and vertical turbulence in equation (R10.10). While horizontal dispersion is usually dominated by advection, vertical mixing of the planetary boundary layer (PBL) is caused by turbulence because of the large vertical wind shear and temperature gradients, together with the fairly low vertical wind speeds. This means that vertical turbulence is a key process in atmospheric dispersion simulations, and requires sophisticated methods to estimate its strength.

The vertical profile of vertical eddy diffusivity is presented in Figure 10.1 after Kumar and Sharan (2012). It can be seen that far from the ground, turbulence intensity decreases with height thus the h planetary boundary layer height can be defined as the elevation where turbulence becomes neglectable. On the other hand, near-ground turbulence intensity fast increases with height, and reaches its maximum value at the elevation approximately 30–40 % of the PBL height. Near-zero eddy diffusivity at the top of the PBL means that there is no vertical mixing upward, thus pollutants released from the surface will stay in the boundary layer. The PBL height and the advection speed together determine the volume in which the pollutant can dilute within a specified time, thus they have a very significant effect on concentration estimates.

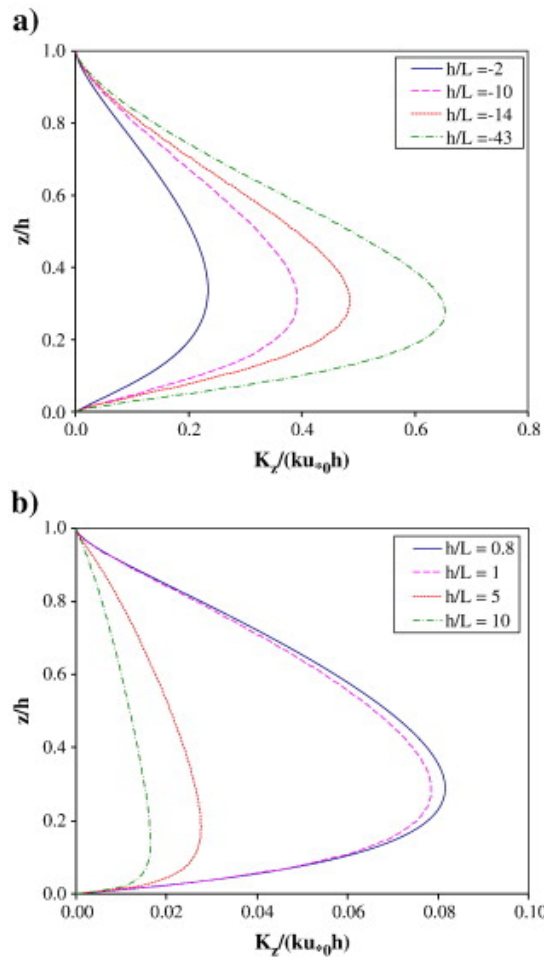


Figure 10.1: Profiles of the normalized vertical eddy diffusivity for different normalized planetary boundary layer heights under (a) unstable conditions and (b) stable conditions from Ref. (Kumar and Sharan, 2012), where h is the planetary boundary layer height and L is the Monin–Obukhov-length, respectively.

Table 10.3: Typical PBL height values

	Night	Day
Spring	150 m	1700 m
Summer	150 m	1900 m
Autumn	150 m	1200 m
Winter	100 m	500 m

PBL height has a strong diurnal and annual variability: it extends over 2000 m on convective summer days, however, it can shrink to a few 10 meters on clear nights (Table 10.3). A key process is the collapse of the mixed layer approximately one hour before sunset, when heat fluxes from the surface are stopped and thermal turbulence is ceased (Figure 10.2). The night time stable boundary layer keeps the surface-based pollutants close to the ground, while the residual layer is detached from the surface until approximately one hour after sunrise.

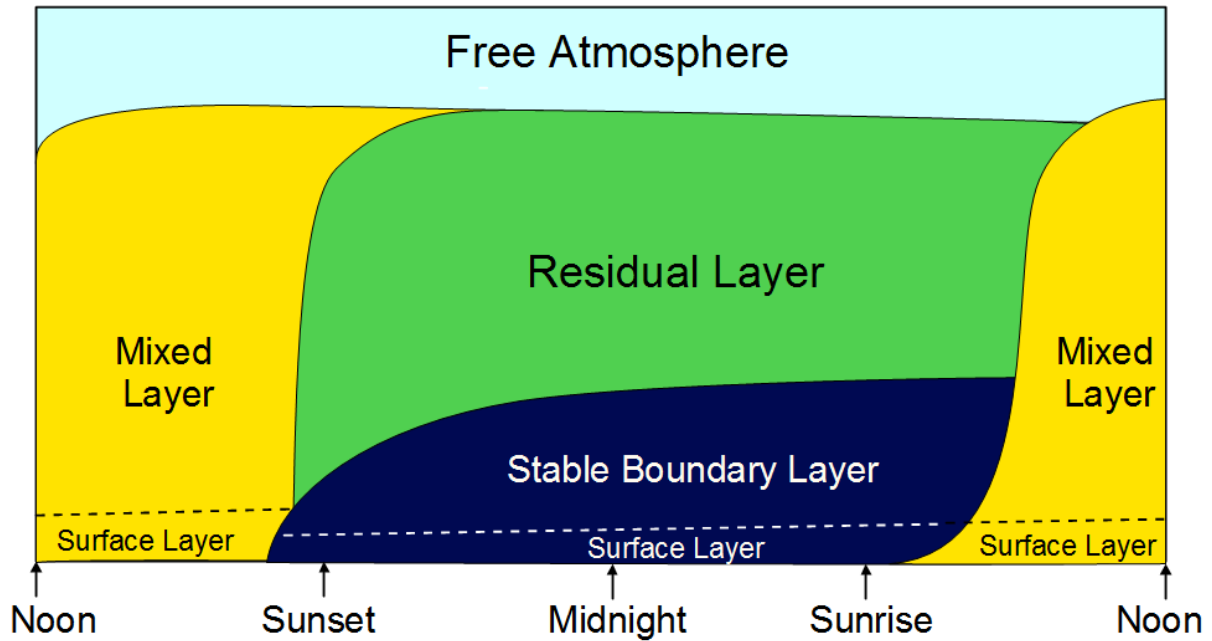


Figure 10.2: A typical daily cycle of the planetary boundary layer in fair weather (after Stull, 1988).

10.2.2.1. Stability classes

Atmospheric turbulence is determined by wind shear and thermal stratification. In the early years of dispersion modelling, it was an obvious solution to define categories based on easily measurable wind and radiation characteristics like albedo, cloud cover and sun elevation. The most popular stability classification is Pasquill's method that defines six categories: from the very unstable A to the very stable F class (Table 10.4). Pasquill took into account wind speed, sun elevation and cloud cover data to determine the stability class that provided pre-defined mixing efficiency values. Despite the fact that this classification can handle only six discrete values of turbulence intensity, Pasquill's method was used for scientific and regulatory purposes for many decades (Turner, 1997, Sriram et al., 2006).

Table 10.4: Pasquill's stability classes from the very unstable (A) to the very stable (F) atmosphere. Note: neutral (D) class has to be used for overcast conditions and within one hour after sunrise / before sunset. [Source: <http://ready.arl.noaa.gov/READYpgclass.php>]

Surface wind speed	Daytime insolation			Night time	
	Strong	Moderate	Slight	Thin overcast or max. 3 octas low cloud	Min. 4 octas low cloud
< 2 m/s	A	A – B	B	E	F
2 – 3 m/s	A – B	B	C	E	F
3 – 5 m/s	B	B – C	C	D	E
5 – 6 m/s	C	C – D	D	D	D
> 6 m/s	C	D	D	D	D

10.2.2.2. Richardson number

The difference between thermal and mechanical turbulence can be regarded as a separation of the subgrid-scale turbulent energy to potential (buoyant) and kinetic energy. Their ratio is described with the gradient Richardson number:

$$Ri = \frac{-\frac{g}{\rho} \frac{\partial \rho}{\partial z}}{\left(\frac{\partial u}{\partial z}\right)^2 + \left(\frac{\partial v}{\partial z}\right)^2}, \quad (10.12)$$

where ρ is density and g is the gravitational acceleration. The numerator of equation (10.12) describes buoyancy, while the denominator is the wind shear term. It can be observed that the buoyancy can take both positive and negative values, representing both the unstable stratification that generates turbulence, and the stable stratification that destroys turbulence. The wind shear term, however, can take only positive values as it is always a generator of turbulence. The buoyancy term is the square of the Brunt-Vaisala-frequency, and is often written with more practical potential temperature gradients instead of density (Stull, 1988).

Richardson number gives a first-guess estimate on atmospheric stability and turbulence intensity. In the $Ri < 0$ case, unstable stratification develops thermal turbulence, which describes a convective boundary layer (CBL). Zero Richardson number means a neutral stratification, thus only mechanical turbulence is present. If the Richardson number is positive, but less than a critical Ri_c value ($0 < Ri < Ri_c$), mechanical turbulence overrides stable stratification that leads to a mechanic turbulence dominated boundary layer. For Richardson numbers larger than Ri_c , atmospheric stability destroys mechanical turbulence and results in a stable boundary layer (SBL). Estimates for the critical Richardson number are in a range 0.15-0.5, but it was also showed that taking qualitative difference between turbulence patterns based on a pre-defined critical value can lead to unrealistic results. However, in many cases, when surface characteristics and fluxes are not available to perform more sophisticated simulations, the Richardson number is used to estimate the turbulence intensity and/or PBL height.

10.2.2.3. Monin–Obukhov-theory

Monin and Obukhov developed a theory in 1954 for atmospheric turbulence that fully described vertical profiles of turbulence intensities. Their basic idea was to combine the vertical turbulent momentum and heat fluxes into a single number with dimension of length, the so called Monin–Obukhov-length

$$L = -\frac{\left\{-\overline{u'w'}\right\}^{\frac{3}{2}}}{\kappa \frac{g}{T} \overline{T'w'}}, \quad (10.13)$$

where T' , u' , w' are the temperature, horizontal and vertical wind turbulent fluctuations, T is the temperature and κ is the von Karman constant, usually taken equal to 0.4 (Stull, 1988). Equation (10.13) is valid for dry air, however, for moist air, virtual temperature or virtual potential temperature is used (Stull, 1988). Hardly measurable turbulent fluxes can be estimated with the definition of two parameters: the u^* friction velocity and the q turbulent heat flux. Using these new parameters, the Monin–Obukhov-length can be expressed as a function of measurable variables (Foken, 2006)

$$L = -\frac{u^{*3}}{\kappa \frac{g}{T} \frac{q}{c_p \rho}}, \quad (10.14)$$

where c_p is the specific heat and ρ is the density of the air. There are different methods for the determination of u^* and q using net radiation components and (potential) temperature gradient, which largely differ in the convective and in the stable boundary layer.

The Monin–Obukhov-length in (10.13) is a reference scale for boundary layer turbulence, thus any z height can be given with the dimensionless z/L parameter. The z/L is not only a new vertical coordinate, but also a stability parameter: at any given z height, turbulence intensity can be described with the z/L value (Figure 10.1).

Monin and Obukhov defined universal functions for neutral, stable and unstable cases that describe vertical profiles of wind and temperature as a function of the z/L height (Foken, 2006). The u^* friction velocity is often also computed as a function of z/L using an iterative solution (Cimorelli et al., 2005). The turbulent momentum and heat fluxes are given explicitly from the u^* and q values (as in equations 10.13-10.14), however, dispersion models require

eddy diffusivity profiles as well. These are obtained through model-dependent parameterizations using the u^* value, the vertical wind and temperature profile provided by the Monin–Obukhov-theory and the universal functions of z/L that describe stability. The Monin–Obukhov-theory was validated against numerous measurement and advanced computational fluid dynamics datasets, and although some weaknesses were shown, it still means the most reliable basis for all fields of atmospheric modelling (Foken, 2006).

10.2.3. Chemical reactions and radioactive decay

Chemical transformation of air pollutants can be diversified and complex especially in the troposphere or stratosphere, where thermal as well as photochemical reactions can occur. Photochemical reactions can produce radicals, which have high affinity to react with other chemical compounds in the atmosphere. This driving force and rich variety of atmospheric components can really provide a complex network of chemical reactions. Formation of air pollutants can be described by reaction mechanisms. A reaction mechanism is a set of elementary reactions by which overall chemical change occurs. Variation of concentrations of air pollutants in the atmosphere can be constructed from the rate equations and can be calculated by a set of ordinary differential equations (ODEs)

$$\frac{dc_i}{dt} = \sum_n k_n \prod_i c_i^{\alpha_n^i}, \quad (10.15)$$

where k_n is the chemical rate constant for n^{th} reaction and α_n^i is the order of reaction in respect for a given chemical species. Usually, for a thermal reaction the rate constant is a “real” constant, however, for a photochemical reaction the rate constant depends on light intensity, and this dependence can be expressed through the annual and diurnal variation of the solar zenith angle (θ)

$$k_{\text{photo}} = a \exp(-b \sec \theta), \quad (10.16)$$

where a and b are parameters depending on the given photolytic reaction.

Radioactive decay in environmental models can be interpreted as a first order chemical reaction

$$\frac{dc_i}{dt} = -kc_i. \quad (10.17)$$

Solution of this equation (10.17) is an exponential function in time. Radioactive decay constant (k) is an inherent property of the radionuclides. Models can take into account consecutive decays with different decay constants, which is mathematically not a complicated task. Equations (10.16, 10.17) are added to the source term (S_c) of atmospheric transport equations (10.10). Models using concentration field (e.g., Eulerian model) can easily handle this mean field description of the concentrations described by ODEs.

However, if we consider dispersion of air pollutants as a dispersion of individual particles, using deposition, chemical and decay rate constants could be meaningless, because these quantities represent “bulk” properties of the system. Here we deal with individual particles, where macroscopic parameters can hardly be used. We can overcome this problem using probabilistic nature for first order reaction, radioactive decay and deposition. The probability that individual particles during a time step Δt will transform, decay or deposit can be estimated by the following relation

$$p = 1 - e^{-k\Delta t}, \quad (10.18)$$

where k is either the “macroscopic” radioactive decay constant (first order rate constant) or wet or dry deposition constant. Thus we can connect microscopic event to macroscopic properties and constants.

10.3. Gaussian dispersion models

10.3.1. Theory and limitations of Gaussian models

The turbulent diffusion equation (10.10) is a partial differential equation that can be solved with various numerical methods. Assuming a homogenous, steady-state flow and a steady-state point source, equation (10.10) can also be analytically integrated and results the well-known Gaussian plume distribution

$$c(x, y, z) = \frac{Q}{2\pi\sigma_y\sigma_z u} \exp\left(\frac{-y^2}{2\sigma_y^2}\right) \left(\exp\left(\frac{-(z-h)^2}{2\sigma_z^2}\right) + \exp\left(\frac{-(z+h)^2}{2\sigma_z^2}\right) \right) \quad (10.19)$$

where c is a concentration at a given position, Q is the source term, x is the downwind, y is the crosswind and z is the vertical direction and u is the wind speed at the h height of the release. The σ_y , σ_z deviations describe the crosswind and vertical mixing of the pollutant, thus they are constructed from the K_h , K_z values of equation (10.10). Equation (10.19) describes a mixing process that results a Gaussian concentration distribution both in crosswind and in vertical direction, centered at the line downwind from the source (Figure 10.3). The last term of equation (10.19) expresses a total reflection from the ground, therefore this formula does not count with dry and wet deposition. Adding a third vertical component to the equation, total reflection from an inversion layer can also be computed. Gravitational settling and chemical or radioactive decay are neglected.

One can observe that the x downwind distance from the source does not appear in equation (10.19). It originates from the obvious assumption that advection is more dominant than diffusion, that, however, can cause large error in situations with low wind speeds where a three-dimensional diffusion dominates. Unfortunately, these situations proved to have been the most dangerous ones in real-life atmospheric dispersion problems as they were often connected to stably stratified atmosphere or low-level inversions (Sharan and Gopalakrishnan, 1997).

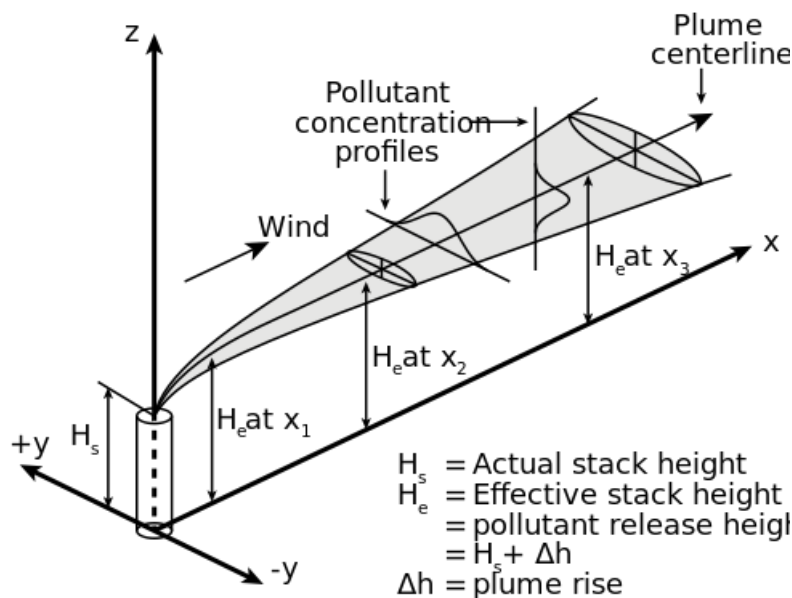


Figure 10.3: Schematic figure of a Gaussian plume. The H_e effective stack height and the crosswind and vertical deviation of the profile are the key parameters of the model. (Source: Wikipedia)

Table 10.5: Features and assumptions of most Gaussian dispersion models

<i>Represented in most Gaussian models</i>	<i>Not represented in most Gaussian models</i>
Advection	Wind shear
Horizontal turbulent diffusion	Change of wind over time

Vertical turbulent diffusion	Change of source parameters over time
Reflection from ground	Wet and dry deposition
Reflection from inversion layer	Gravitational settling
Elevated source	Chemical reactions
Buoyancy (effective stack height)	Radioactive decay
Multiple source points	Complex terrain
	3D diffusion (low-wind case)

Besides turbulence, the elevation of the source, often referred to as stack height is a key parameter of a Gaussian model, because ground concentrations are computed in an analytical way assuming the maximum concentration in the stack height (Figure 10.3). If buoyant pollutants are present, the horizontal advection starts from considerably higher than the stack's top due to the buoyant rise of the released gas. It led to the definition of the effective stack height that is the stack height added to the buoyant plume rise. Both empirical and theoretical formulas exist to compute the plume rise using the temperature, specific heat capacity, release speed and flux of the material as input data, which can be successfully used even in extremely buoyant cases like pool fires. We note that in situations where buoyant pollutants and a low-level thermal inversion are present, more sophisticated simulations are required to estimate the penetration of the inversion layer by the plume.

10.3.2. History of development

The greatest advantage of Gaussian models is that they have an extremely fast, almost immediate response time. Their calculation is based only on solving a single formula (equation 10.11 or similar) for every receptor point, and the model's computational cost mainly consists of meteorological data pre-processing and turbulence parameterization. Depending on the complexity of these submodules, the model's runtime can be extremely reduced that enables its application in real-time GIS-based decision support software.

Gaussian dispersion models have become a uniquely efficient tool of air quality management for the past decades, especially in the early years when high performance computers had an unreachable price for environmental protection organizations and authorities. They have been successfully used for a wide range of studies of air quality in urban and industrial areas. However, industrial incidents like the ones in Seveso, Bhopal and Chernobyl showed out some critical weaknesses of Gaussian models, and strongly motivated the development of more advanced simulations to satisfy the scientific and public interest in the safety of atmospheric environment.

Although the toxic gas release in Seveso, Italy in 1976 happened during daytime in weakly unstable conditions, Gaussian models couldn't perform well because of the strong horizontal wind shear and fast changing wind direction. As exact deposition maps became available, Cavallaro et al. (1982) managed to give a better computational result with a statistical method that estimated dispersion directions driven by measured wind vectors, which can be regarded as a Lagrangian approach. Eight years later, another serious accident happened in Bhopal, India. The high number of victims warned the world that release of toxic heavy gas in a situation where low-level night time inversion is present can cause catastrophic consequences. Because of the low wind speed, fast settling pollutant and strong temperature inversion connected with local scale terrain effects, it was impossible to obtain reliable results from Gaussian models, however, later simulations with advanced Lagrangian software showed a good agreement with measurements.

Inspired by the serious accidents and the more and more efficient computers, there were large efforts to develop Gaussian models in a way that they could provide more accurate air quality forecasts as well as to take into account some of the unrepresented physical processes (Table 10.5). It led to some respectable results like the more sophisticated treatment of vertical mixing in convective boundary layer or the parameterization of complex terrain effects. Due to the developments, today's advanced Gaussian dispersion models like AERMOD, CTDM or ADMS still have a significant role in environmental modelling.

While the incidents in Seveso and Bhopal and other air pollution episodes were concentrated on a local scale, the Chernobyl accident in 1986 had serious consequences in several countries and the radioactive I-131 gas was measured globally (Pudykiewicz, 1988). It was clear that the steady-state assumption of Gaussian models couldn't handle continental scale dispersion processes, however, existing Eulerian and Lagrangian models provided precious

information in the estimation of the impact of the accident (Pudykiewicz, 1988). The fast development of computers and NWP-s allowed researchers to create more and more efficient dispersion simulations using girded meteorological data. Eulerian and Lagrangian models are state-of-the-art tools of recent atmospheric dispersion simulations (Mészáros et al., 2010, Dacre et al., 2011).

10.3.3. Advanced Gaussian models

AERMOD is an open-source Gaussian air dispersion model developed by the *US Environmental Protection Agency* (EPA). It has a sophisticated turbulence parameterization based on the Monin–Obukhov-theory, and has built-in models to handle complex terrain and urban boundary layer (Cimorelli et al., 2005). It uses the *Plume Rise Model Enhancements* (PRIME) algorithm that gives a hard approximation of complicated turbulent processes like the downwash effect near the source. Although AERMOD uses the steady-state approximation for the flow and the source, it can be used within 10–100 km distance as a long-term statistical tool through its meteorological preprocessor, AERMET. AERMET assimilates detailed surface and meteorological data from both surface measurements and upper air soundings and enables the model to perform several model runs from which time averaged concentrations can be estimated through a certain period. AERMOD is a powerful tool to carry out impact studies of planned or existing industrial sites as well as to estimate the average load on environmental protection or agricultural areas. Besides AERMOD, EPA also developed the *Complex Terrain Dispersion Model* (CTDM), which can estimate concentration patterns in mountain regions without solving the complex mesoscale flow field.

In Europe, the British ADMS model has become the most popular for air quality simulations. It provides a wide range of parameterizations for complex effects like coastal circulations, complex terrain, deposition processes and radioactive decay. Like AERMOD, it can be used in statistical mode to obtain long-term average loads for impact studies. *UK Met Office* and *Cambridge Environmental Research Consultants* (CERC) also developed the ADMS-Urban module that aims to provide air quality forecasts for cities as an alternative of costly and time consuming computational fluid dynamics (CFD) modelling. The basic idea behind ADMS-Urban is to create the complex concentration field of a city as a superposition of plumes from different point, line and field sources based on emission estimates and a built-in chemistry model.

There are several other Gaussian models available like CALINE3 for highway air pollution, OCD for coastal areas, BLP and ISC for industrial sites or ALOHA for accidental and heavy gas releases. They are widely used by authorities, environmental protection organizations and industry for impact studies and health risk investigations. Their fast runtime allows users to make long-term statistical simulations (Leelössy et al., 2011) or detailed sensitivity studies (Bubbico and Mazzarotta, 2008), and provide immediate first-guess information if an accidental release occurs. They are often coupled with GIS software to create an efficient decision support tool for risk management.

10.4. Lagrangian models

Lagrangian models are based on the idea that pollutant particles in the atmosphere move along trajectories determined by the wind field, the buoyancy and the turbulence effects. Calculating these trajectories means an ODE instead the original dispersion PDE problem that is computationally easy to solve. The final distribution of many particles gives a stochastic estimation of the concentration field. The models either estimate the particle as a single drifting point, and the final distribution of numerous particles is used to estimate concentration fields (trajectory models), or assume a Gaussian dispersion inside each particle and the final concentration field is given as a superposition of these Gaussian distributions (puff models).

The Lagrangian approach has the advantage against Eulerian models that no grid is used for computation, thus spatial discretization errors like numerical diffusion are avoided. The result can be interpolated to any grid which means that the model error is independent of the output resolution. Deposition and radioactivity can be taken into account as a time-dependent decay term within each particle (Stohl et al., 2005), however, the treatment of chemical reactions can only be carried out if concentration field is available on a grid. Therefore reactive materials require an interpolation on a grid at each timestep that introduces spatial truncation errors and numerical diffusion in the model.

Lagrangian models are exceptionally efficient close to the source, where girded computations would require a very fine resolution to handle large gradients. On the other hand, long-range simulations require progressively more particles that causes a much faster increase of computational cost with the domain size than for the Eulerian models.

To unite the advantages of both approaches, nested models have been developed that use a Lagrangian model near the source, but interpolate the variables on a grid to perform Eulerian dispersion and chemistry simulations for larger distances.

10.4.1. Calculation of trajectories

The trajectory equation for a single particle is written as an ordinary differential equation

$$\frac{d\vec{r}}{dt} = \vec{v} + \vec{v}_t, \quad (10.20)$$

where \vec{r} is the position of the particle, \vec{v} is the grid-scale particle speed including advection, settling and buoyancy, while \vec{v}_t is the turbulent wind fluctuation vector. Some models present a third term to describe subgrid mesoscale wind fluctuations (Stohl et al., 2005). The turbulent fluctuation term can be estimated as a random walk in a viscous fluid, which is described by the Langevin equation

$$dw_t = -\frac{w_t}{T_L} dt + \sqrt{\frac{2\sigma_w^2}{T_L}} dW, \quad (10.21)$$

where T_L is a Lagrangian integration time step, σ_w is the vertical turbulent velocity fluctuation and dW represents a white noise process with mean zero and variance dt . A similar equation can be written for the horizontal fluctuations. The last component of equation (10.21) describes a random walk, while the first component is a memory term that represents autocorrelation. The T_L Lagrangian timescale is a key parameter and is often given explicitly, or computed from velocity fluctuations (Stohl et al., 2005). At large T_L values, autocorrelation becomes low, and the turbulent diffusion can be estimated as an uncorrelated random walk, that gives a reasonable estimation only for long distance simulations. However, in some models only this simple random walk process is implemented. Velocity fluctuations are computed from eddy diffusivities, or defined through parameterizations using the Monin-Obukhov-theory (Stohl et al., 2005).

The easiest way to handle anisotropic turbulence is to solve separated Langevin equations for each wind component using different wind fluctuations and Lagrangian timescales (Stohl et al., 2005). This way we neglect cross-correlations between turbulent fluctuations that proved to be a reasonable assumption for meso- and macroscale simulations. The Langevin equation (10.21) assumes Gaussian turbulence, thus it is only valid in case of isotropic turbulence and neutral stratification. Several approaches were presented to modify equation (10.21) in order to take into account mesoscale horizontal wind shear, buoyancy and convective boundary layer turbulence effects (McNider et al., 1988, Luhar and Britter, 1989, Pozorski and Minier, 1998, Stohl and Thomson, 1999).

When solving the trajectory equation numerically, temporal discretization of equations (10.20-10.21) is carried out. Equation (10.21) is usually solved with a first-order scheme (Stohl et al., 2005), however, applications of higher order Runge-Kutta methods are also present. Discretization of equation (10.21) is presented in Pozorski and Minier (1998). We note that for numerical representation of the white noise process in equation (10.21), an efficient random number generator is also needed that can significantly increase the computational cost of the model.

10.4.2. Puff models

Puff models are an intersection between Gaussian and Lagrangian dispersion models. They hold the assumption that the concentration pattern can be well described with a Gaussian distribution; however, the centreline of a plume is not a straight downwind direction, but a Lagrangian trajectory (Figure 10.4). This way they can take into account temporal and spatial wind changes. Puff models split the released mass of pollutants into small units, “puffs”, and then compute the trajectories of all the puffs in a Lagrangian way (through equation 10.19), but keep a Gaussian concentration pattern inside each puff. The final concentration field is given as a superposition of all the puffs’ concentration distributions:

$$c(x, y, z) = \frac{Q\Delta t}{(2\pi)^{\frac{3}{2}}} \sum_{k=1}^N \frac{1}{\sigma_{xk}\sigma_{yk}\sigma_{zk}} \exp\left(-\frac{(x_k-x)^2}{2\sigma_{xk}^2} - \frac{(y_k-y)^2}{2\sigma_{yk}^2} - \frac{(z_k-z)^2}{2\sigma_{zk}^2}\right) \quad (10.22)$$

where $Q\Delta t$ is the source term, N is the number of puffs, (x_k, y_k, z_k) is the position of the k^{th} puff and σ_{xk} is the x -directional deviation of the Gaussian distribution inside the k -th puff. Equation (10.22) is very similar to the equation (10.19) with the difference that at the puff models, a sum of many components is calculated. Reflection from the ground and the inversion layer can be added to the equation in a way presented in equation (10.19), however, it describes only the reflection inside the puff. In a complete 3D model, reflection of the trajectory of the puff also has to be computed. Deposition and decay can be treated within each puff in the same way as in the Gaussian models. The effect of buoyancy can be estimated with the plume rise parameterization, or with both trajectory and in-puff treatment. Taking a time-dependent source strength in Q multiplied with the Δt release frequency of puffs, the temporal variability of the source can be represented in the model.

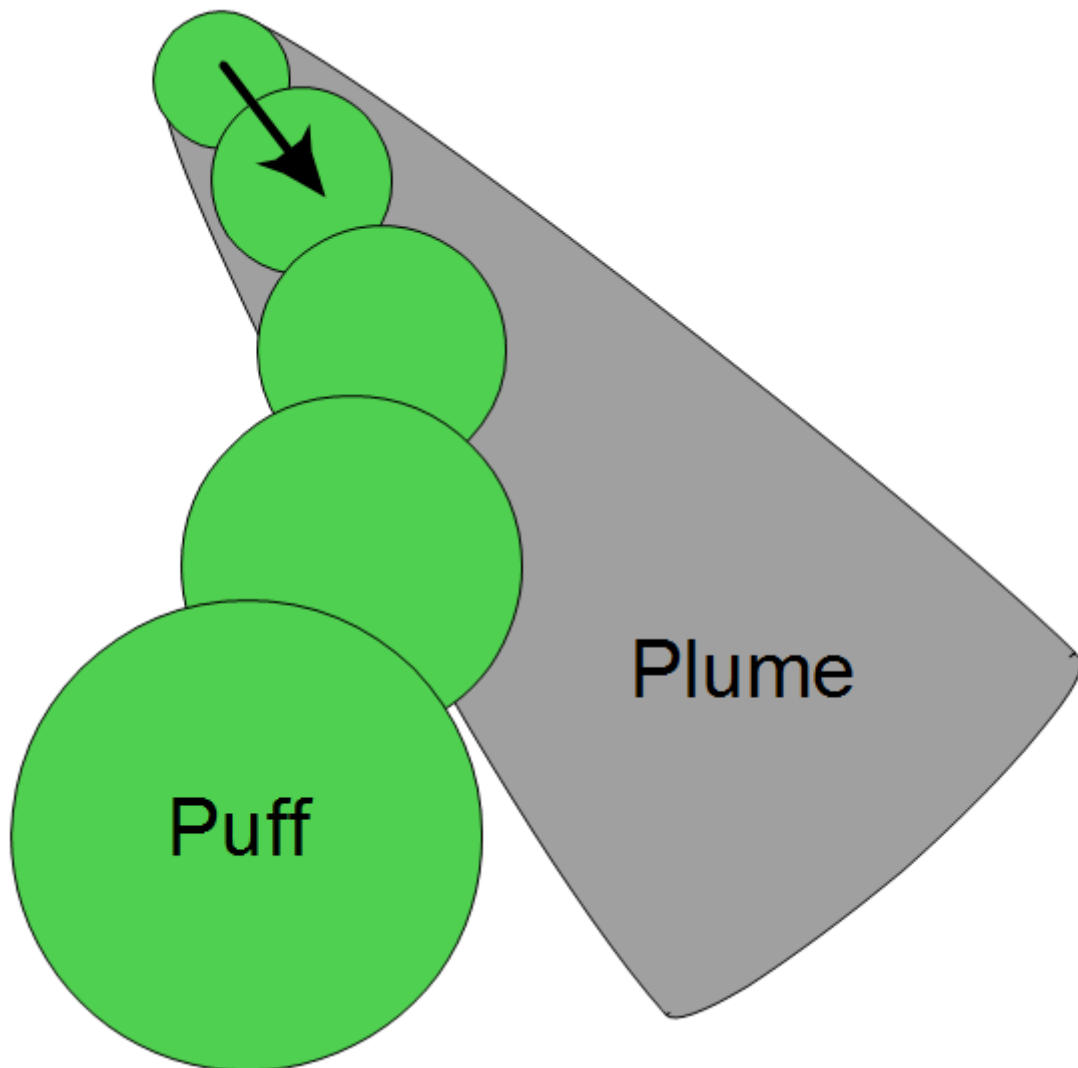


Figure 10.4: Schematic representation of Gaussian plume and puff models. Puff models still estimate a Gaussian dispersion, but are able to take into account temporal and spatial wind changes.

Puff models calculate the effect of turbulence in two different ways: with a stochastic random-walk approach in the trajectories of the puffs (equation (10.20)); and through the deviation of a normal distribution inside each puff (equation (10.22)). It can be interpreted as a separated treatment of large-scale and sub-puff-scale turbulence. In long-range simulations, as the puffs grow due to diffusion while travelling along their trajectories, initially small puffs will reach a size where the wind shear becomes significant. To deal with this issue, developers introduced a

puff-splitting technique that mass-consistently splits a puff into two parts if it reaches either a maximum size or a minimum sub-puff scale wind shear.

There are models like RAPTAD that encounter with both trajectory and puff turbulence. However, most of the softwares simplify the calculation with neglecting one of the turbulent processes. As the simplest approach, CALPUFF and RIMPUFF compute Gaussian turbulence deviations inside the puffs, but neglects large-scale turbulence and only advective trajectories are given. A more sophisticated solution is presented in HYSPLIT, where stochastic random-walk motion of the puff is used only in vertical direction, while horizontally a two-dimensional in-puff Gaussian distribution is assumed. The NAME model can be run both in point-particle (only random walk) and puff mode. We note that if the in-puff Gaussian turbulence is neglected (deviation is zero), the puff can be treated as a single point particle, which leads to the trajectory models.

Puff models were the first tools to simulate long-range atmospheric dispersion processes, as they were developed from existing Gaussian models, but were able to encounter with changing wind and emission data. In Europe, the Danish models, DERMA and RIMPUFF are widely used in risk management for case and sensitivity studies. RIMPUFF is part of the RODOS (*Realtime Online Decision Support*) system, the European framework for nuclear security. In the US, the CALPUFF was designated (besides AERMOD) as a preferred model of the Environmental Protection Agency. CALPUFF was successfully used worldwide in various environmental protection and public health investigations as well as for regulatory purposes. The RAPTAD model was developed for mesoscale simulations around complex terrain, and was also applicated for nuclear risk management and microscale dispersion problems.

The HYSPLIT model, developed by the *NOAA Air Resources Laboratory*, is one of the most widely used dispersion softwares. It provides an easy-to-use online interface for single trajectory simulations in order to give a fast estimation of atmospheric dispersion pathways or source regions. It also offers a mixture of a vertical trajectory and a horizontal puff model to determine concentration levels.

10.4.3. Trajectory models

Trajectory models are based on a stochastic simulation of a large number of drifting point-particles that represent a fraction of the released mass of pollutants (Figures 10.5, 10.6, and 10.7). Instead of using the Gaussian assumption, they solve all scales of turbulence explicitly above the T_L Lagrangian timescale using the (10.20 and 10.21) trajectory and Langevin equations. They provide a sophisticated treatment of turbulent diffusion without solving partial differential equations, however, to obtain reliable results from a stochastic model, the calculation of a large number of single trajectories is needed that increases the computational cost. When the final particle distribution is available, either the concentration field can be given with a simple box-counting model, or cluster analyses can be performed to determine the most affected areas.

NOAA HYSPLIT MODEL
 Forward trajectory starting at 0000 UTC 08 Jan 13
 GDAS Meteorological Data

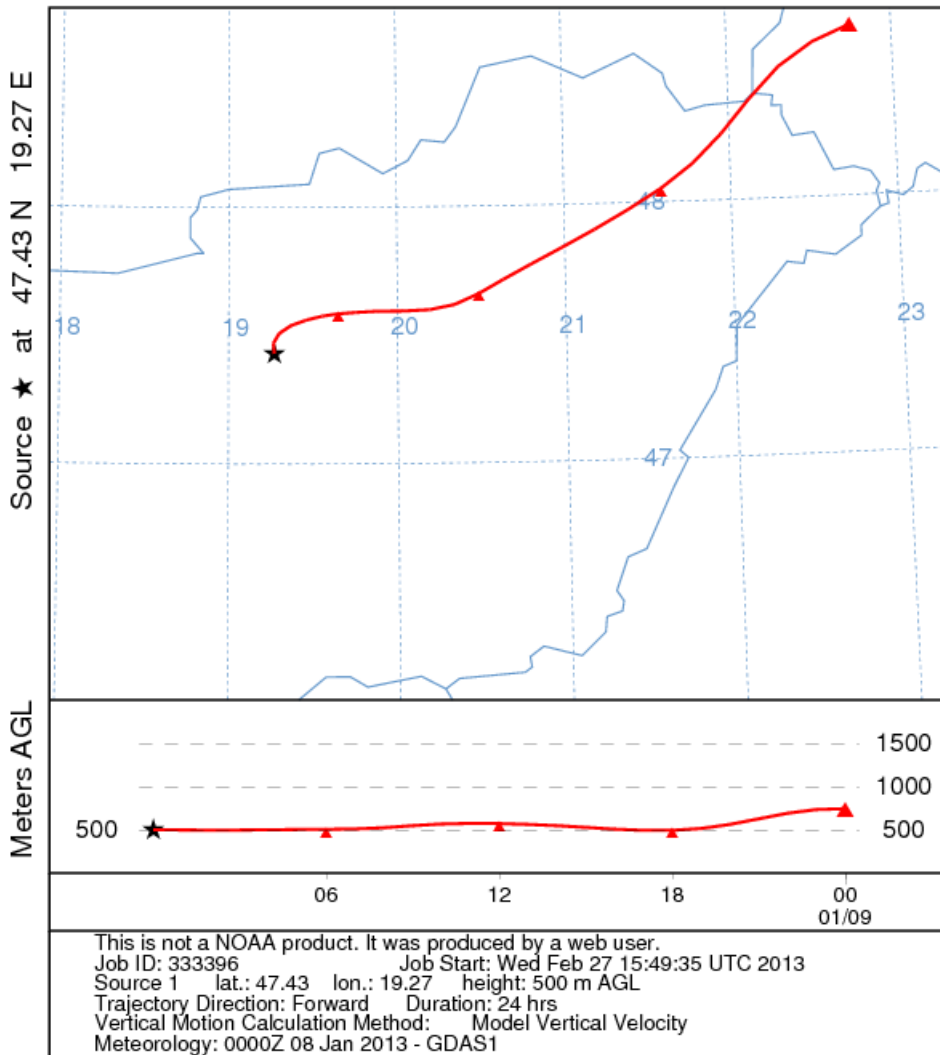


Figure 10.5: Air mass (or single particle) trajectory in the HYSPLIT model.

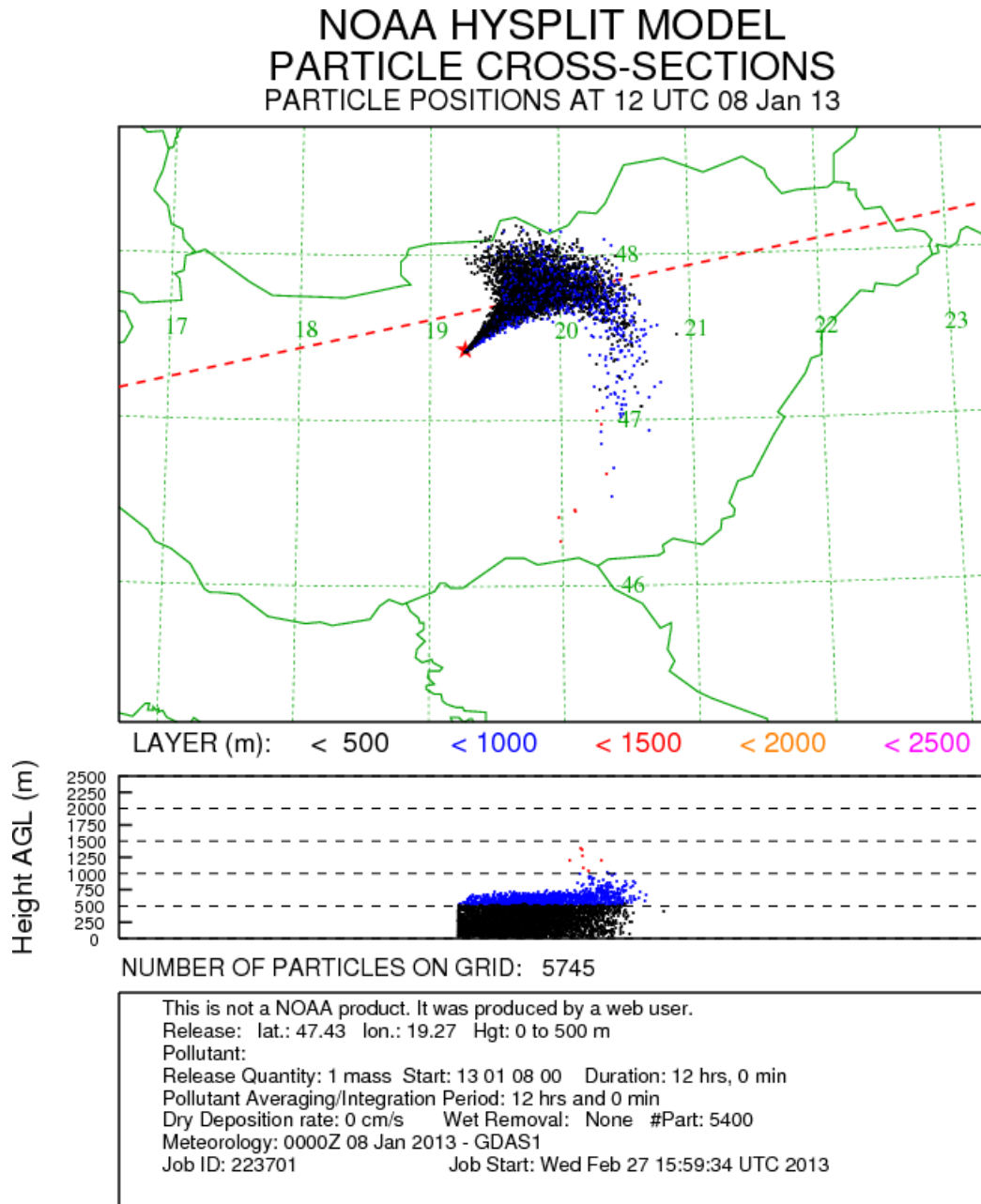


Figure 10.6: Dispersion of particles in the HYSPLIT model.

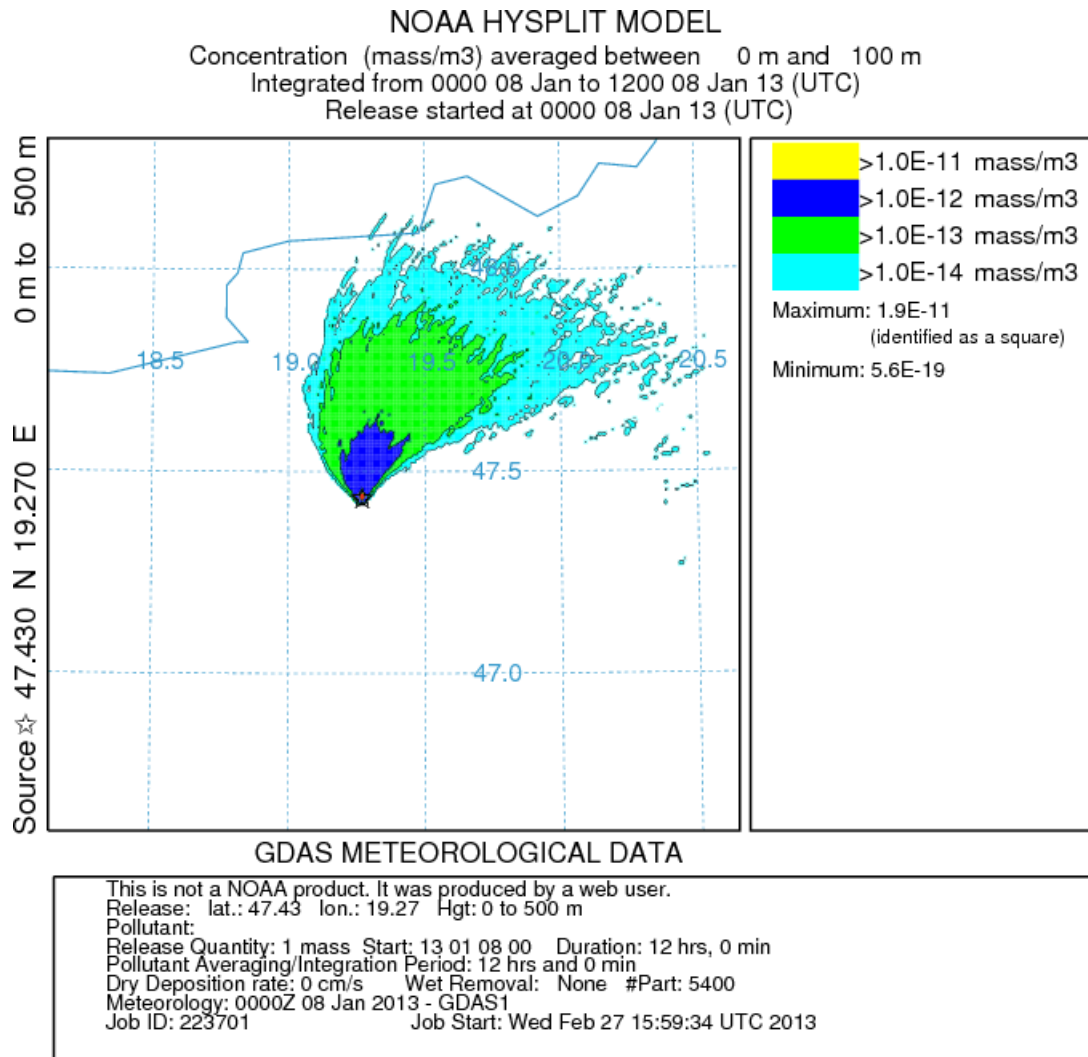


Figure 10.7: Averaged concentration of an air pollutant using particles (from Figure 10.6) in the HYSPLIT model.

Modern computers allow the computation of millions of long-range trajectories within a reasonable time that made trajectory models the state-of-the-art tools of regional to global scale atmospheric dispersion simulations. The British NAME and the open-source Austrian FLEXPART are well validated, popular models successfully used worldwide for dispersion simulations. They provided reliable and fast information for authorities and scientists in recent air pollution episodes like the 2001 airborne foot-and-mouth disease epidemic (Mikkelsen et al., 2003), the Eyjafjallajökull eruption in 2010 (Dacre et al., 2011) or the Fukushima nuclear accident in 2011 (Stohl et al., 2011).

Trajectory models are often used in backward mode in order to identify source regions or provide an estimation of the mass of the released material. While it is easy to compute backward advective trajectories using an archived NWP wind field, the irreversibility of turbulent diffusion and deposition has to be carefully treated. In backward simulations, the final distribution obtained from the random walk of many trajectories represents sensitivity, and not a concentration field (Stohl et al., 2005). In other words, while in forward mode random walk describes a physical process (i.e. turbulent diffusion), in backward mode, random walk is used to describe the uncertainty of the trajectory caused by turbulent diffusion and deposition. The output of backward simulations is a source-receptor sensitivity field that provides probabilities of possible source locations. Once the most probable source locations are known, the estimation of the mass of released material has to be carried out (Stohl et al., 2011). It is usually performed with Monte-Carlo methods calculating multiple groups of forward trajectories with different source terms, or Eulerian inverse modelling.

We note that a simplification of trajectory models also exists that compute single trajectories to determine the main direction of the dispersion. These models don't estimate concentration, but provide a fast and easy-to-use first-guess of the affected areas. Single trajectory calculations can be easily carried out using a numerical weather pre-

diction model's wind field. A single trajectory gives few information of the turbulence, thus the method provides reliable results only in advection dominated, large distance and free atmosphere simulations. Near-source or boundary layer modelling requires large number of trajectories to estimate the effect of turbulent diffusion.

10.5. Eulerian models

10.5.1. Solving atmospheric transport equations

The main idea of any Eulerian models is to solve numerically the atmospheric transport equation (equation 10.9). The atmospheric transport equation is mathematically a second order differential equation, and its solution with the appropriate initial and boundary conditions provides the spatiotemporal evolution of the concentration, i.e., $c = c(t, x)$. There are several numerical methods to solve PDE, one of the most powerful and common method is the so-called "method of lines". The method consists of two steps: (i) spatial discretization and (ii) the temporal integration of the derived ordinary differential equations (ODEs). Spatial discretization of PDE (the atmospheric transport equation) is performed on a mesh (grid). This reduces the PDE to a system of ordinary differential equations (ODEs) in one independent variable, time. The system of ODEs can then be solved as an initial value problem, and a variety of powerful methods and software tools exist for this purpose.

Let's consider a simple and 1D form of the atmospheric transport equation

$$\frac{\partial c}{\partial t} = -u \frac{\partial c}{\partial x} + K_x \frac{\partial^2 c}{\partial x^2} \quad (10.23)$$

This equation describes a simplified situation, where the spread of a pollutant occurs by advection (wind) and turbulent diffusion. We will show the method of lines technique on this example.

Spatial discretization:

There are different discretization techniques (e.g., finite difference method (FDM), finite volume method (FVM), finite element method (FEM)). The basic idea of the spatial discretization is approximating the first and the second order spatial derivatives in (10.23). The simplest one is the finite difference method, and here the derivatives will be approximated by the Taylor's theorem. Let's divide the 1D space equidistantly into N grid point (Figure 10.8). We assume that $c(x, t)$ is at least twice continuously differentiable, and examine its first order Taylor expansion



Figure 10.8: Spatial discretization in 1D.

$$c_{i+1} = c_i + \left. \frac{\partial c}{\partial x} \right|_i \Delta x + \left. \frac{\partial^2 c}{\partial x^2} \right|_i (\Delta x)^2 + O(\Delta x)^3 \quad (10.24)$$

$$c_{i-1} = c_i - \left. \frac{\partial c}{\partial x} \right|_i \Delta x + \left. \frac{\partial^2 c}{\partial x^2} \right|_i (\Delta x)^2 + O(\Delta x)^3 \quad (10.25)$$

It can be seen that the first order derivatives can be easily derived that from (10.24) and (10.25) if we assume $(\Delta x)^2 = 0$, thus

$$\left. \frac{\partial c}{\partial x} \right|_i = \frac{c_{i+1} - c_i}{\Delta x} \quad (\text{forward difference}), \quad (10.26)$$

$$\left. \frac{\partial c}{\partial x} \right|_i = \frac{c_i - c_{i-1}}{\Delta x} \quad (\text{backward difference}). \quad (10.27)$$

Those two approximations have truncation error of $O(\Delta x)$. It is easy to construct other schemes that have smaller truncation error. Let's subtract equation (10.25) from equation (10.24), thus we get the central difference scheme

$$\left. \frac{\partial c}{\partial x} \right|_i = \frac{c_{i+1} - c_{i-1}}{2\Delta x} \quad (\text{central difference}). \quad (10.28)$$

This scheme has truncation error $O(\Delta x)^2$.

For approximation of second order derivatives, let's add equation (10.26) to equation (10.27). It can be seen that the first order derivatives will be eliminated, and we construct a central difference scheme for second order derivatives

$$\left. \frac{\partial^2 c}{\partial x^2} \right|_i = \frac{c_{i+1} - 2c_i + c_{i-1}}{(\Delta x)^2} \quad (\text{central difference}). \quad (10.29)$$

Here the truncation error is $O(\Delta x)^2$.

Temporal integration:

After spatial discretization we obtain a set of ODEs (each ODE describes the variation of concentration in time in a given grid point). The next step is to solve these ODEs (using appropriate initial conditions) with a numerical integrator. There are three numerical integrator schemes: explicit (forward, equation 10.30), implicit (backward, equation 10.31), and Crank–Nicolson (semi-implicit, equation 10.32) method

$$c_i^{t+\Delta t} = c_i^t - u \frac{c_{i+1}^t - c_i^t}{\Delta x} + K_x \frac{c_{i+1}^t - 2c_i^t + c_{i-1}^t}{(\Delta x)^2}, \quad (10.30)$$

$$c_i^{t+\Delta t} = c_i^t - u \frac{c_{i+1}^{t+\Delta t} - c_i^{t+\Delta t}}{\Delta x} + K_x \frac{c_{i+1}^{t+\Delta t} - 2c_i^{t+\Delta t} + c_{i-1}^{t+\Delta t}}{(\Delta x)^2}, \quad (10.31)$$

$$c_i^{t+\Delta t} = c_i^t - u \frac{1}{2} \left[\frac{c_{i+1}^{t+\Delta t} - c_i^{t+\Delta t}}{\Delta x} + \frac{c_{i+1}^t - c_i^t}{\Delta x} \right] \Delta t + K_x \frac{1}{2} \left[\frac{c_{i+1}^{t+\Delta t} - 2c_i^{t+\Delta t} + c_{i-1}^{t+\Delta t}}{(\Delta x)^2} + \frac{c_{i+1}^t - 2c_i^t + c_{i-1}^t}{(\Delta x)^2} \right] \Delta t, \quad (10.32)$$

where c_i^t and $c_i^{t+\Delta t}$ are the concentration at t and $t+\Delta t$, respectively. Δt is the time step (integration step).

10.5.2. Operator splitting

We have seen that the basis of nearly all deterministic air pollution models is a system of partial differential equations, the right-hand side of which contains several terms. These terms describe the different physical/chemical subprocesses of the air pollution transport, namely, advection, diffusion, chemical reactions, deposition and emission. (The definition of a sub-process is not unique. For example, we can call advection one sub-process, but horizontal and vertical advection can be viewed as two different sub-processes as well.) The several different terms on the right-hand side make the model problem rather complicated, especially in complex Eulerian models, where all known sub-processes are taken into account. The high complexity of this system requires the application of numerical solution techniques.

The numerical integration of the transport equations is a rather difficult computational task, especially in large-scale and global Eulerian models, where the number of grid-points can range from a few thousand to a few hundred thousand, and the number of chemical species is typically between 20 and 200. If some readily available solver is applied directly to the system, we cannot obtain a sufficiently accurate numerical solution within reasonable computational time. Therefore, procedures that allow us to lead the solution of the system back to the solution of simpler systems for which sufficiently accurate as well as efficient methods exist, are of great importance.

The problems describing the sub-processes have been thoroughly investigated, and appropriate solution techniques have been developed for their numerical solution. I.e., there exist efficient and accurate methods for the diffusion equation, for the advection equation etc., but not for a system which describe all the sub-processes at the same time. This gives the idea of operator splitting: let us divide the right-hand side of the original system into a few simple terms, and solve the corresponding systems – which are connected to each other through the initial conditions – successively in each time step of the numerical integration. This means that we replace the original model with one in which the different sub-processes take place successively in time. This de-coupling procedure allows us to solve a few simpler systems instead of the original, complicated one.

Operator splitting has been successfully applied in the numerical solution of the Navier-Stokes equations. Splitting is also popular in numerical models of ocean circulation, which typically include multiple time-scale motions. The governing equations of the oceans are split into sub-systems that model the fast and slow motions separately. Further fields where operator splitting is successfully applied include cloud physics, biomathematics, astrophysics, and medical science.

As an example of operator splitting from a complex transport-chemistry model, we introduce a splitting method used in the Danish Eulerian Model (DEM splitting) (Dimov et al., 2008). In this long-range air pollution model the subsystems describe the horizontal advection (1), the horizontal diffusion (2), the chemical reactions to which also emissions are added (3), the deposition (4) and the vertical exchange (5):

$$\frac{\partial c_i^{(1)}}{\partial t} = -\frac{\partial\{uc_i^{(1)}\}}{\partial x} - \frac{\partial\{wc_i^{(1)}\}}{\partial x}, \quad (10.33)$$

$$\frac{\partial c_i^{(2)}}{\partial t} = K_x \frac{\partial^2 c_i^{(2)}}{\partial x^2} + K_y \frac{\partial^2 c_i^{(2)}}{\partial y^2}, \quad (10.34)$$

$$\frac{\partial c_i^{(3)}}{\partial t} = E(\vec{x}) + R(\vec{x}, c_1, c_2, \dots, c_m), \quad (10.35)$$

$$\frac{\partial c_i^{(4)}}{\partial t} = -k_{\text{dry}} c_i^{(4)} - k_{\text{wet}} c_i^{(4)}, \quad (10.36)$$

$$\frac{\partial c_i^{(5)}}{\partial t} = -\frac{\partial\{wc_i^{(5)}\}}{\partial z} + K_z \frac{\partial^2 c_i^{(5)}}{\partial y^2}, \quad (10.37)$$

for $i = 1, \dots, m$, where m is the number of chemical species. In the above splitting procedure, the original system of PDEs has been split into five simpler systems, which are to be solved in each time step one after the other in the following way. Assume that some approximation to the concentration vector (c_1, \dots, c_m) at the beginning of the time step has been found. System (equation 10.33) is solved by using this vector as a starting vector. The obtained solution will serve as the initial vector in the treatment of system (equation 10.34), and so on. The solution of the fifth system is accepted as an approximation to the concentration vector at the end of the time step.

The DEM splitting is based on a separation of the different physical processes of the air pollution transport and the separation of the vertical and horizontal directions for advection and diffusion. An alternative of the DEM splitting is the so-called physical splitting, where the sub-operators belong to the five basic air pollution processes (i.e., advection, diffusion, chemistry, deposition and emission), and there is no directional separation.

Operator splitting has the great advantage that the sub-systems are easier to solve numerically than the original system. We can exploit the special properties of the different sub-systems and apply a suitable method for each. In some situations one of the sub-problems may even be solved analytically (semi-analytical method). On the other hand, this de-coupling procedure may cause inaccuracy in the solution, since we have replaced the original model with one in which the sub-processes take place one after the other. This error is called splitting error. Obviously, the success of operator splitting is primarily determined by the effect of the splitting error. Therefore, further splitting schemes with reduced splitting error have been constructed, such as the Marchuk–Strang splitting or the weighted splitting.

10.6. Computational Fluid Dynamics models

Eulerian and Lagrangian models have become uniquely efficient tools for atmospheric dispersion simulations from meso- to macroscale. These models are tightly connected to numerical weather prognostic (NWP) models that provide wind field and other meteorological data in order to perform dispersion calculations. Grid resolution of NWP models is in a range of 1 to 10 km, however, several dispersion problems are concentrated on a smaller scale. Most importantly, in case of urban air pollution, source and receptor points are often located within a few hundred meters from each other, surrounded by a very complex geometry. Wind field datasets from NWP models have far too coarse resolution to represent the wind field within an urban area, thus existing Eulerian and Lagrangian dispersion models cannot be used.

As urban air quality has become a more and more important part of environmental and health protection, two approaches have been developed to provide air quality forecasts within urban areas: a statistical and a dynamic (CFD) approach. The former tried to determine a statistical correlation between meteorological data and air quality measurement time series. In the years when computational performance did not allow running fine resolution flow simulations for urban areas, this approach provided valuable air quality forecasts for many populated cities. However, the method had the disadvantage that it required detailed and long-term air quality measurement data, thus it was not applicable for fast-developing cities that lacked earlier measurements. Furthermore, changes in the city structure or even impact studies of planned buildings' effect on air quality couldn't be simulated.

The more and more efficient computers led to the rapid development of the Computational Fluid Dynamics (CFD) technology, a general purpose engineering tool for numerical flow simulation. They provide a tool to solve various partial differential equations (PDEs) that enables the user to define the governing equations that best fit to their needs. The basic form of the Navier–Stokes-equation for turbulent incompressible fluids

$$\frac{\partial \vec{v}}{\partial t} + (\vec{v} \nabla) \vec{v} = -\frac{1}{\rho} \nabla p - \vec{g} + \nu_T \nabla^2 \vec{v}, \quad (10.38)$$

where \vec{v} is the wind field, ρ is density, p is pressure, ν_T is the eddy viscosity and \vec{g} is the gravitational acceleration vector. Equation (10.38) is very similar to the one solved in numerical weather prognostic (NWP) models, however, the coordinate system, grid, boundary conditions and physical parameterizations are completely different (Figures 10.9, 10.10).

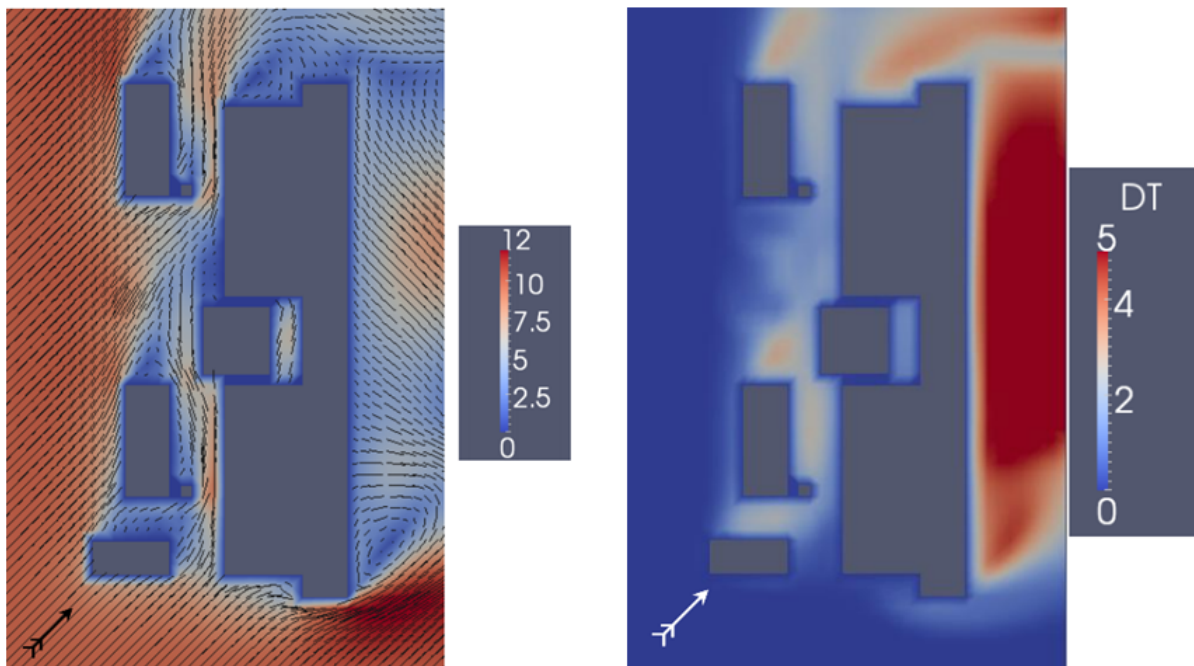


Figure 10.9: Horizontal cross section of the wind field (m/s) and turbulent diffusion coefficient (m^2/s) at 10 m height around the buildings of the Paks Nuclear Power Plant, assuming 10 m/s south-westerly wind. On the lee side, turbulent diffusion dominates over advection.

The flexibility of CFD models' application for different purposes led to their large dominance on all areas of mechanical and environmental engineering as well as microscale dispersion modelling (Balczó et al., 2011).

CFD models consist of four main parts:

1. a mesh generator, that splits the computational domain to cells with a user-defined resolution;
2. a PDE solver, that solves a selected form of the Navier–Stokes and other attached (e.g. dispersion) equations;
3. turbulence model;
4. a visualization tool to create 3D plots and slices of the computed fields.

Key parameters of a CFD model are the mesh, the solver and the turbulence model. While in engineering cases the computationally most efficient tetrahedral mesh and finite element solvers are used, atmospheric simulations are often carried out on hexahedral mesh and/or using finite volume solvers.

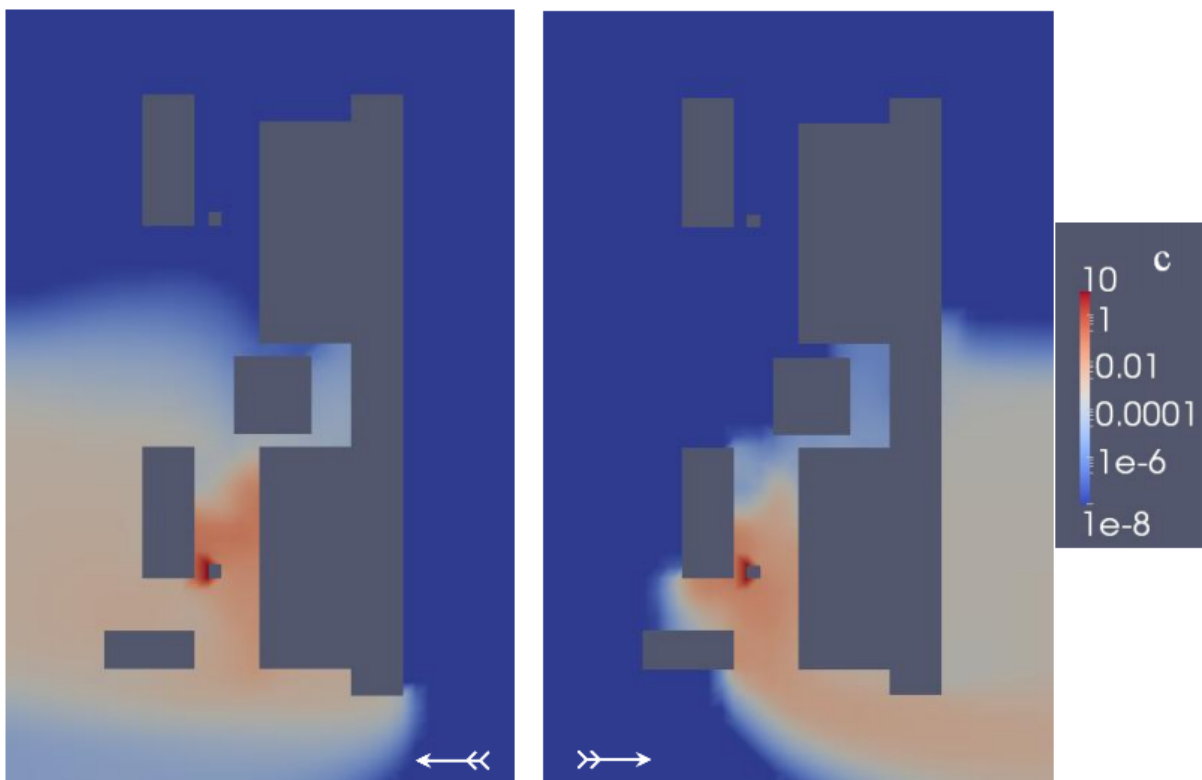


Figure 10.10: Horizontal cross section of concentration field after a hypothetical release from the southern tower at 10 m height at Paks Nuclear Power Plant. If advection dominates at the source point, crosswind dispersion is weak (westerly wind, right). If the source point is in downwash area, cross- and upwind dispersion is significant (easterly wind, left).

As CFD models are often used around complex geometry, a fine grid resolution is required to explicitly calculate turbulence to a very low scale that results in a very large computational cost. However, subgrid-scale turbulence still has to be estimated, which in most cases is assumed to be isotropic. Among the various turbulence models for CFD, the k-e approach has become the most popular for both engineering and atmospheric applications. However, in the atmosphere, anisotropy of turbulence can cause large errors in k-e results, thus modified atmosphere-oriented turbulence closures are applied. A state-of-the-art solution for turbulence modelling is the Large Eddy Simulation (LES), that filters the large scale (anisotropic) and small scale (isotropic) eddies and performs direct simulation on the former one. Despite its huge computational cost, LES has become a popular tool for planetary boundary layer case studies, and its results are often used as a verification dataset for other models.

CFD-based street canyon models are widely used to predict air quality in urban and industrial areas. Atmospheric dispersion and even chemical reactions can be simulated together with the flow on the same grid. Another solution is to use the CFD tools only to provide a stationary wind field, and modify an existing Eulerian or Lagrangian dispersion model to carry out transport simulations using the CFD-based wind data. General purpose computational fluid dynamics packages like ANSYS's Fluent and the open-source OpenFOAM are often used for atmospheric studies, furthermore, several CFD softwares have been designed specifically for atmospheric dispersion and wind engineering studies like the German MISKAM or the French MERCURE.

Baklanov (2000) pointed out several weaknesses that made CFD results less reliable as the scale increased. The convective boundary layer (CBL) usually extends over 1 km and the very fine grid resolution does not allow running the simulation in its whole height within a reasonable computational time. It makes very difficult to take into account atmospheric stability parameters that are dominant in convective cases. Another difficulty is to provide proper boundary conditions for wind and turbulence parameters either from measurement or NWP data. Although nesting CFD into NWP models is difficult due to their different coordinates, governing equations and variables, Tewari et al., 2010 presented promising results using WRF and a three-dimensional CFD code.

While numerical weather prognostic (NWP) and computational fluid dynamics (CFD) models provide reliable wind data for all scales of atmospheric dispersion simulations, their connection proved to be difficult. While recent developments of NWPs achieve more and more detailed resolution, CFD models with enhanced computational capacity, parallel computing and LES simulation for anisotropic turbulence are becoming even better for PBL simulations. Either the modification of an NWP model to perform microscale simulations, or an extension of a CFD software for atmospheric studies holds large possibilities and gaps, and is a direction of extensive research from both meteorological and environmental engineering side (Table 10.6).

Table 10.6: Recommended approaches for different scales and applications of atmospheric dispersion modelling

Application	< 1 km	1 – 10 km	10 – 100 km	100 – 1000 km
Online risk management (fast runtime is important)	-	Gaussian	Puff	Eulerian
Complex terrain	CFD	Lagrangian	Lagrangian	Eulerian
Reactive materials	CFD	Eulerian	Eulerian	Eulerian
Source-receptor sensitivity	CFD	Lagrangian	Lagrangian	Lagrangian
Long-term average loads	-	Gaussian	Gaussian	Eulerian
Free atmosphere dispersion (volcanoes)	-	Lagrangian	Lagrangian	Lagrangian
Convective boundary layer	(CFD)	Lagrangian	Eulerian	Eulerian
Stable boundary layer	CFD	Lagrangian	Eulerian	Eulerian
Urban areas, street canyon	CFD	CFD	Eulerian	Eulerian

References

- Baklanov A.. 2000. *Application of CFD Methods for Modelling in Air Pollution Problems: Possibilities and Gaps* In: *Environmental Monitoring and Assessment*. 65. 181-189.
- Balczó M., Balogh M., Goricsán I., Nagel T., Suda J.M., and Lajos T.. 2011. *Air quality around motorway tunnels in complex terrain: computational fluid dynamics modelling and comparison to wind tunnel data* In: *Időjárás*. 115. 179-204.
- Bubbico R. and Mazzarotta B.. 2008. *Accidental release of toxic chemicals: influence of the main input parameters on consequence calculation* In: *Journal of Hazardous Materials*. 151. 394-406.

- Cavallaro A., Tebaldi G., and Gualdi R.. 1982. *Analysis of Transport and Ground Deposition of the TCDD Emitted on 10 July 1976 from the ICMESA Factory (Seveso, Italy)* In: *Atmospheric Environment*. 16. 731-740.
- Cimorelli A.J., Perry S.G., Venkatram A., Weil J.C., Paine R.J., Wilson R.B., Lee R.F., Peters W.D., and Brode R.W.. 2005. *AERMOD: A dispersion model for industrial source applications. Part I: General model formulation and boundary layer characterization* In: *Journal of Applied Meteorology*. 44. 682-693.
- Dacre H.F., Grant A.L.M., Hogan R.J., Belcher S.E., Thomson D.J., Devenish B.J., Marenco F., Hort M.C., Haywood J.M., Ansmann A., Mattis I., and Clarisse L.. 2011. *Evaluating the structure and magnitude of the ash plume during the initial phase of the 2010 Eyjafjallajökull eruption using lidar observations and NAME simulations* In: *Journal of Geophysical Research*. 116. D00U03.
- Dimov I., Faragó I., Havasi Á., and Zlatev Z.. 2008. *Different splitting techniques with application to air pollution models* In: *International Journal of Environment and Pollution*. 32. 174-199.
- Foken T.. 2006. *50 years of the Monin–Obukhov similarity theory* In: *Boundary-Layer Meteorology*. 119. 431-447.
- Kumar P. and Sharan M.. 2012. *Parameterization of the eddy diffusivity in a dispersion model over homogenous terrain in the atmospheric boundary layer* In: *Atmospheric Research*. 106. 30-43.
- Leelőssy Á., Mészáros R., and Lagzi I.. 2011. *Short and long term dispersion patterns of radionuclides in the atmosphere around the Fukushima Nuclear Power Plant* In: *Journal of Environmental Radioactivity*. 102. 1117-1121.
- Mészáros R., Vincze Cs., and Lagzi I.. 2010. *Simulation of accidental release using a coupled transport (TRES) and numerical weather prediction (ALADIN) model* In: *Időjárás*. 114. 101-120.
- Mikkelsen T., Alexandersen S., Astrup P., Champion H.J., Donaldson A.I., Dunkerley F.N., Gloster J., Sorensen J. H., and Thykier-Nielsen S.. 2003. *Investigation of airborne foot-and-mouth disease virus transmission during low-wind conditions in the early phase of the UK 2001 epidemic* In: *Atmospheric Chemistry and Physics*. 3. 2101-2110.
- Pozorski J. and Minier J-P.. 1998. *On the Lagrangian turbulent dispersion models based on the Langevin equation* In: *International Journal of Multiphase Flow*. 24. 913-945.
- Pudykiewicz J.. 1988. *Numerical simulation of the transport of radioactive cloud from the Chernobyl nuclear accident* In: *Tellus B*. 40B. 241-259.
- Sharan M. and Gopalakrishnan S.G.. 1997. *Bhopal gas accident: a numerical simulation of the gas dispersion event* In: *Environmental Modelling and Software*. 12. 135-141.
- Sriram G., Krishna Mohan N., and Gopaldasamy V.. 2006. *Sensitivity study of Gaussian dispersion models* In: *Journal of Scientific and Industrial Research*. 65. 321-324.
- Stohl A., Forster C., Frank A., Seibert P., and Wotawa G.. 2005. *Technical note: The Lagrangian particle dispersion model FLEXPART version 6.2* In: *Atmospheric Chemistry and Physics*. 5. 4739-4799.
- Stohl A., Seibert P., Wotawa G., Arnold D., Burkhardt J.F., Eckhardt S., Tapia C., Vargas A., and Yasunari T.J.. 2011. *Xenon-133 and caesium-137 releases into the atmosphere from the Fukushima Dai-ichi nuclear power plant: determination of source term, atmospheric dispersion, and deposition* In: *Atmospheric Chemistry and Physics*. 11. 28319-28394.
- Stull R.B.. 1988. *An Introduction to Boundary Layer Meteorology*. Kluwer Academic Publishers.
- Tewari M., Kusaka H., Chen F., Coirier W.J., Kim S., Wyszogrodzki A.A., and Warner T.T.. 2010. *Impact of coupling a microscale computational fluid dynamics model with a mesoscale model on urban scale contaminant transport and dispersion* In: *Atmospheric Research*. 96. 656-664.

Turner D.B.. 1997. *The Long Lifetime of the Dispersion Methods of Pasquill in U.S. Regulatory Air Modelling In: Journal of Applied Meteorology*. 36. 1016-1020.

Chapter 11. Air pollution modelling

11.1. Adaptive gridding

11.1.1. Introduction

In numerical analysis, adaptive mesh refinement is a method of adaptive meshing. Central to any Eulerian method is the manner in which it discretizes the continuous domain of interest into a grid of many individual elements (Garcia-Menendez and Odman, 2011). This grid may be static (e.g., nested grid), established once and for all at the beginning of the computation, or it may be dynamic, tracking the features of the result as the computation progresses. If the computation has features which one wants to track which are much smaller than the overall scale of the problem, and which move in time, then one must either include many more static grids to cover the region of interest, or adopt a dynamic scheme.

Nested-grid modelling techniques have been and still are very popular in atmospheric modelling. In static grid nesting, finer grids are placed or “nested” inside coarser grids. The domain and resolution of each nest are specified prior to the simulation and remain fixed throughout. The nested grid method targets higher resolution for domain features that remain stationary (e.g., terrain, coastline, the location of a power plant or urban area).

The objective of an adaptive grid method is to increase solution accuracy by providing dynamic refinement at regions and instances where accuracy is most dependent on resolution. This can be achieved by restructuring the grid on which solution fields are estimated to better fit the needs of the system being numerically described. Adaptive gridding techniques can be classified as *h*-refinement or *r*-refinement depending on the type of grid restructuring employed. The advantages of a dynamic gridding scheme are: (i) Increased computational savings over a static grid approach; (ii) Increased storage savings over a static grid approach; (iii) Complete control of grid resolution, compared to the fixed resolution of a static grid approach, or the Lagrangian-based adaptivity of smoothed particle hydrodynamics.

H-refinement relies on increasing the total number of grid elements (e.g., nodes or cells) within a base grid for which the original structure remains fixed. The technique, also known as mesh enrichment or local refinement, modifies the grid at regions tagged for increased resolution. Frequently, the method is carried out by subdividing grid elements into smaller self-similar components. In Figure 11.1, the example depicting *h*-refinement shows a single refinement level. A second level of refinement could involve subdividing the refined cells at the center of the domain into four even smaller cells. Generally, a maximum number of refinement levels allowed must be defined.

R-refinement techniques, commonly referred to as mesh moving or global refinement, relocate mesh nodes to regions warranting increased resolution and subsequently increase grid element concentration at the areas with the greatest inaccuracies. However, the total number of grid points is maintained constant. Unlike *h*-refinement, *r*-refinement around a region is necessarily accompanied by coarsening at another. Figure 11.1 shows simple schematics of *h*-refinement and *r*-refinement at the center of a simple nine element grid.

The objective of increasing solution accuracy through adaptive gridding can only be met if adaptation is driven by an efficient indicator of the solution error in a spatial field. The concept of error equidistribution has been used to describe the adaptive grid process; grids are reconfigured to result in an equal amount of error for all grid elements. However, directly quantifying error is not a straightforward task. Quantitative analysis of resolution-induced error in advection algorithms has been previously investigated. For advection schemes, a Fourier method can estimate error (i.e., numerical diffusion) as a function of grid resolution. The estimation becomes much more complex after integrating other physical and chemical processes into the system, particularly nonlinear transformations. Additionally, exact error quantification cannot be used as a refinement driver a priori, as the error itself depends on grid structure after adaptation.

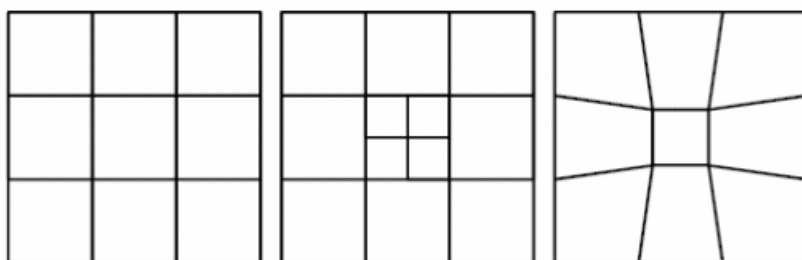


Figure 11.1: Uniform grid (left) and examples of h -refinement (center) and r -refinement (right). Reprinted with permission from Garcia-Menendez and Odman, 2011.

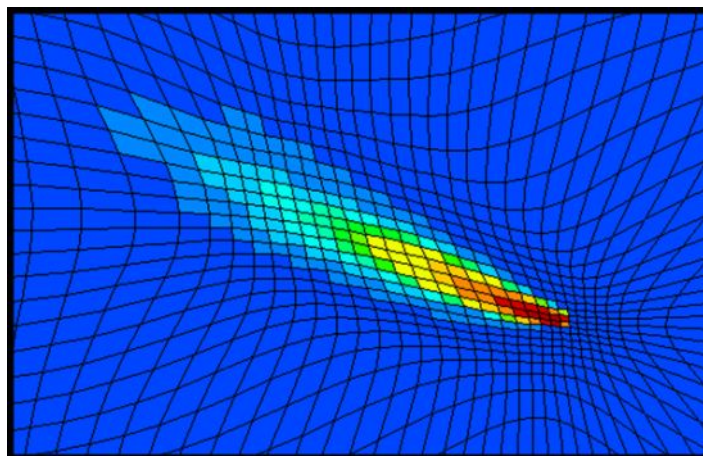


Figure 11.2 R -refinement in use in case of simulating air pollution dispersion from a point source. Reprinted with permission from Garcia-Menendez and Odman, 2011.

11.1.2. Adaptive gridding for simulating photochemical air pollution

Previous EUROTRAC and EUROTRAC2 investigations have shown that ozone is increasing on both a local and regional scale in the European boundary layer and that some of the highest regional ozone concentrations in Europe can be observed in Central Europe, including Hungary. During summer ozone episodes, ozone concentrations can exceed legislative standards in Central Europe (see e.g., <http://www.emep.int>). Ozone and other photo-oxidants can cause damage to human health, natural and agricultural vegetation. Therefore, an important strategic goal is to develop reliable tools to help us estimate these short and long term impacts. Computational models form one set of tools that can be usefully employed to evaluate past episodes and possible future trends in photochemical oxidants. For the computational study of this phenomenon in Hungary, an Eulerian photochemical air pollution model has been developed. This model fully utilizes adaptive gridding methods for modelling chemical transport from multi-scale sources. The model has been elaborated within a flexible framework where both area and point pollution sources can be taken into account with variable resolution, and the chemical transformations can be described by a mechanism of arbitrary complexity. Operational use of the model has revealed that the large cities in the region, Budapest and Vienna emit significant amounts of ozone precursors and highly influence the photo-oxidant concentrations in this region. Budapest, the capital of Hungary, is one of the major sources. This paper reports the latest developments of the model and focuses on the effects of the plume of Budapest on the concentrations of ozone in the surrounding region for a high ozone episode. Although previous studies have used an Eulerian modelling framework to study high ozone concentrations within Europe, this study is the first to describe the photochemical air pollution formation in Hungary in a detailed way, focusing on the emissions of Budapest at high resolution. An emission inventory for Budapest at 1 km resolution and an adaptive grid technique are used to predict the ozone levels in Hungary for the first time.

The model describes the spread of reactive air pollutants in four layers of the troposphere over the Central European region. The vertical mixing of pollutants is approximated by a parameterised description of exchange between the

layers. The horizontal dispersion of species is described within an unstructured triangular Eulerian grid framework. The horizontal grid is adaptive, i.e. continuously changes in space and time to minimize the numerical errors. Transient refinement and de-refinement is invoked as necessary throughout the model run according to the estimated spatial errors. The modelled area is a 980 km × 920 km region of Central Europe with Hungary in the centre. The model describes the horizontal domain using a Cartesian coordinate system through the stereographic polar projection of the curved Earth surface onto a plane. The dispersion of species in the horizontal domain is described by the atmospheric transport–reaction equation in two space dimensions. For n chemical species, an n dimensional set of partial differential equations is formed describing the change of concentrations over time and space. These equations are coupled through the non-linear chemical reaction term.

The four horizontal layers of the model are the surface layer (from surface to 50 m), the mixing layer, the reservoir layer and the free troposphere layer. At night, the mixing layer extends to the height determined by the midnight radiosonde data. During the daytime, the height of the mixing layer is assumed to rise smoothly to the height determined by the noon radiosonde data. In the evening, it collapses to the nighttime level. The reservoir layer, if it exists, extends from the top of the mixing layer to an altitude of 1000 m. Vertical mixing and deposition are parameterised according to the vertical stratification of the atmosphere. The species exchange between the layers (i.e. the vertical transport) is modelled in two ways. Exchange between the mixing and the surface layers due to turbulent diffusion and fumigation at the top of the mixing layer are described by ordinary differential equations. These equations have been defined in our recent article. In this way, species exchange takes place between the mixing layer and the reservoir layer or the upper layer if the reservoir layer does not exist.

The wind speed and direction, relative humidity, temperature, and cloud coverage were determined by the meteorological model ALADIN, which is the numerical weather forecasting model of the Hungarian Meteorological Service. The ALADIN model is a hydrostatic, spectral, limited area model using 24 layers for vertical resolution where initial and boundary conditions are determined from a larger scale weather prediction model ARPEGE (Horányi et al., 1996). The model domain for ALADIN covers the Central European region from latitude 43.1°N to 52.0°N and from longitude 10.35°E to 25.1°E. The time resolution of data is 6 hours and the spatial resolution is 0.10 × 0.15 degrees (approximately 10 km × 10 km). In our model, conservative interpolation methods were used to obtain data relevant to a given spatial point on the unstructured grid from the regularly gridded ALADIN meteorological data.

The dry deposition velocity was calculated using the resistance method that is based on the parameterisation of the surface resistance, the boundary layer resistance and the aerodynamic resistance. The model calculated the Monin–Obuhov length from the data of the ALADIN meteorological model.

For Budapest, the emission inventories for CO, NO_x and VOCs were provided by the local authorities with a spatial resolution of 1 km × 1 km and also include the most significant 63 emission point sources. For Hungary, the National Emission Inventory of spatial resolution 20 km × 20 km was applied which included both area and point sources. Figure 1 shows the emission inventories of NO_x for Budapest and Hungary. Outside Hungary, the emission inventory of EMEP for CO, NO_x and VOCs was used, having a spatial resolution of 50 km × 50 km. The emissions data had to be interpolated onto the unstructured grid following each change to the mesh during refinement. This was achieved using the mass conservative method of overlapping triangles. Point sources are averaged into the appropriate grid cell for their location and hence when the grid is refined the definition of point sources improves.

In the present simulations, the GRS chemical scheme was used, although the model allows the utilization of any other reaction scheme (see Table 11.1). The GRS-scheme is a reduced mechanism that was created using a semi-empirical approach; it contains 7 reactions of 7 species. The GRS scheme was developed by comparison with smog chamber data and has been evaluated by comparison with smog chamber data and predictions from more detailed chemical schemes. Previous studies have shown that the scheme performs well for the prediction of ozone in polluted conditions although it can overpredict ozone concentrations in rural locations. The scheme has been selected in the current application for its computational efficiency and because its accuracy can be assumed to be reasonable in the region of interest i.e. down wind of major NO_x sources. The rate constants were calculated as described by Derwent and Jenkin and were expressed as m th order rate constants with units (molecule cm³) ^{m} s⁻¹. The photolysis rates were parameterized by the following function:

$$J_q = (1 - 0.75N^{3.4}) a_q \exp(-b_q \sec \Theta), \quad (11.1)$$

where Θ is the solar zenith angle, N is the cloud coverage, and a_q, b_q are the rate parameters of reaction q . Temperature dependent rate constants were represented by standard Arrhenius expressions.

The basis of the numerical method is the spatial discretisation of the partial differential equations derived from the atmospheric transport–reaction equation on unstructured triangular meshes. This approach, known as the ‘method of lines’, reduces the set of partial differential equations to a system of ordinary differential equations of one independent variable, time. The model uses the flux limited, cell centred finite volume scheme. The system of ordinary differential equations is integrated by the code SPRINT2D (Hart et al., 1998, Lagzi et al, 2009). Operator splitting is carried out at the level of the non-linear equations by approximating the Jacobian matrix.

The initial unstructured meshes are created from a geometry description using the Geompack mesh generator. These meshes are then refined and coarsened by the Triad adaptivity module. Low and high order solutions are obtained for each species and the difference between them gives a measure of the spatial error. The algorithm identifies the regions of large error by comparison with a user-defined tolerance for the concentration of one or several species. For the i th PDE component on the j th triangle, a local error estimate $e_{i,j}(t)$ is calculated from the difference between the solution using a first order and a second order method. For time dependent PDEs this estimate shows how the spatial error grows locally over a time step. A refinement indicator for the j th triangle is defined by an average scaled error $serr_j$ that is considered over all $npde$ PDEs using user supplied absolute and relative tolerances:

$$serr_j = \sum_{i=1}^{npde} \frac{e_{i,j}(t)}{atol_i / A_j + rtol_i \cdot c_{i,j}}, \quad (11.2)$$

where $atol$ and $rtol$ are the absolute and relative error tolerances, $e_{i,j}(t)$ is the local error estimate of species i over element j , $c_{i,j}$ is the concentration of species i over triangle j and A_j is the area of j th triangle. This formulation for the scaled error provides a flexible way to weight the refinement towards any PDE error. In the calculations presented, a combination of errors in species NO and NO₂ were used as a refinement indicator, because these are primary species and also because their concentrations are very closely related to ozone production. Estimation of the local spatial error of ozone concentration is not an efficient choice, because it would be too late to make refinement decisions on the basis of the detection of a large error in the concentration of a secondary pollutant. On the other hand, concentrations of the VOCs are locally dominated by emissions, and since the available emissions inventory for VOCs has a coarse resolution (50 km × 50 km), the use of VOC concentration as an error indicator is not appropriate. Each triangle that is flagged for refinement is split into four similar triangles. Refined triangles may later be coalesced into the parent triangle when coarsening the mesh.

Table 11.1: The GRS mechanism (T : temperature, Θ solar zenith angle)

Reactions						Reaction rate constants		
ROC	+	h ν	→	RP	+	ROC	$k_1 = 1000\exp(-4710/T)J_3$	[R11.1]
RP	+	NO	→	NO ₂			$k_2 = 3.7098 \times 10^{-12} \exp(242/T)$	[R11.2]
NO ₂	+	H ν	→	NO	+	O ₃	$J_3 = 1.45 \times 10^2 \exp(-0.4 \text{ sec } \Theta)$	[R11.3]
NO	+	O ₃	→	NO ₂			$k_4 = 1.7886 \times 10^{12} \exp(-1370/T)$	[R11.4]
RP	+	RP	→	RP			$k_5 = 6.7673 \times 10^{12}$	[R11.5]
RP	+	NO ₂	→	SGN			$k_6 = 1.00 \times 10^{13}$	[R11.6]
RP	+	NO ₂	→	SNGN			$k_7 = 1.00 \times 10^{13}$	[R11.7]

Table 11.2: Comparisons of CPU times and number of grid cells for each meshing strategy

Grid type	Relative CPU time	Number of grid cells
Coarse	1	353
Adaptive	8.8	353–1276
fine nested	13.2	2298

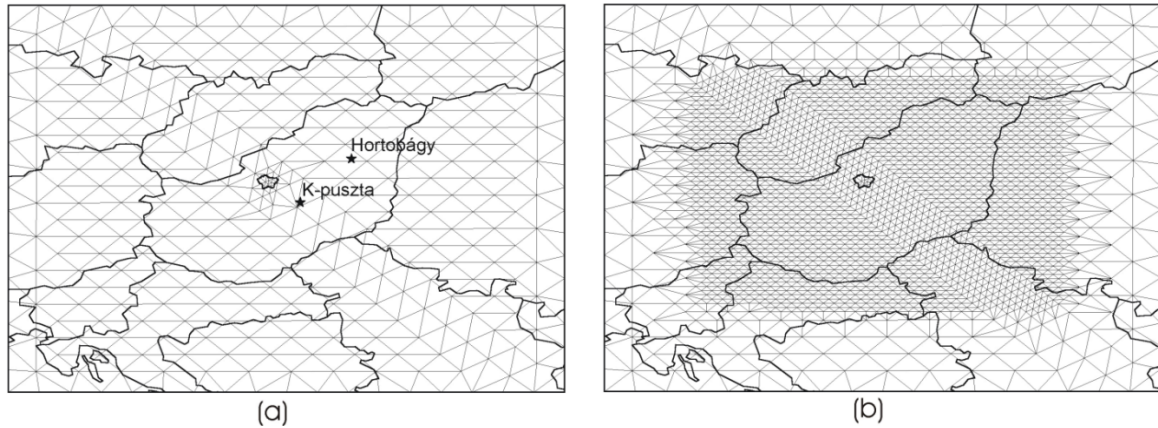


Figure 11.3: The structure of the coarse (level 0; with a nested grid around Budapest) and fine (level 2) grid. The symbols show the monitoring stations of the Hungarian Meteorological Service. The average mesh lengths are 70 km and 17.5 km for the two cases, respectively.

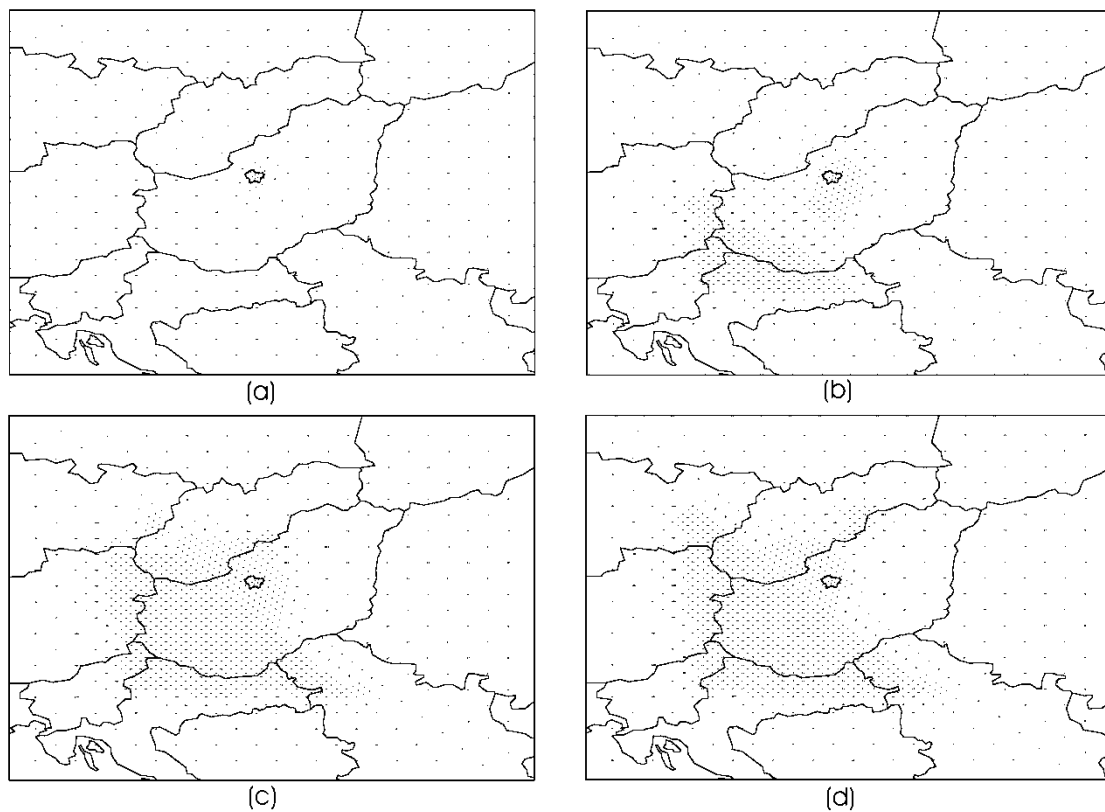


Figure 11.4: *H*-refinement in use in case of simulating photochemical air pollution in Hungary. The time evolution of the adaptive grid: (a) t_0 , (b) t_0+24h , (c) t_0+48h , (d) t_0+72h .

The simulated period was the beginning of August, 1998. During almost the whole period low cloud coverage, low wind speeds and the high temperatures resulted in high photo-oxidant levels in most of Europe. In Hungary, high ozone concentrations were measured at the K-puszta (48°58'N, 19°33'E) and Hortobágy (47°29'N, 20°56'E) monitoring stations of the Hungarian Meteorological Service. Three simulations, corresponding to three different spatial grid structures, were carried out. The first grid was a coarse fixed one that covered a part of Central Europe as seen in Figure 11.3 (a). The resolution of this coarse grid (level 0) was characterized by an edge length of 70 km. The grid structure of the second type was a fixed fine nested grid (level 2) over Hungary, which had an edge size of 17.5 km (see Figure 11.3 (b)). In the adaptive grid simulations, the refinement was restricted to the area of the nested grid in Figure 11.3 (b) and limited to 2 levels. Therefore, the minimum grid size was identical to that

of the fine grid in the nested grid calculations. The initial concentrations of the major species were 0.4 ppb for NO₂, 2.0 ppb for NO, 89.3 ppb for O₃, and 4.1 ppb for VOC. The initial concentrations were equal in each layer across the whole simulated domain.

The simulation period from noon on the 31th of July to midnight on the 3rd of August, 1998, was chosen. Figure 11.4 illustrates the evolution of the adaptive grid in time. The adaptive grid was initially refined around Budapest, which is the main emission source of the primary pollutants in Hungary. High spatial gradients in NO_x concentrations are therefore likely to have formed close to the Budapest region leading to an increase in spatial errors and therefore mesh refinement. This is in part due to the high resolution inventory used in the simulations and raises interesting issues with regards to the influence of mesh resolution within an Eulerian framework. Clearly, where a coarse emissions inventory is used, a certain level of averaging has already taken place, perhaps resulting in a lower sensitivity to solution grid resolution below a certain level, although meteorological events may still lead to steep spatial concentration gradients under certain conditions. The finer the resolution of the emissions inventory, the larger the spatial concentration gradients will be at the edges of the down wind plumes formed. The representation of large point sources represents a particular challenge to Eulerian models. As emissions inventories become finer therefore, the influence of grid resolution on solution accuracy may become more apparent, requiring the use of techniques such as transient grid adaption.

After one and a half simulation days the whole western region of the domain became refined, because this region is more industrialized and emits higher levels of ozone precursors than the other regions of the simulated area. Figure 11.5 shows the calculated ozone concentrations after 3 days of simulation on the 3rd of August, 1998 at 17.00, as a result of three simulations each using a different type of grid. During the simulated period, the southern winds transported the ozone precursors towards the north from Budapest. The simulated ozone concentrations using the fine (Figure 11.5 a) and the adaptive grids (Figure 11.5 b) are very similar. Both simulations show high ozone concentrations in a wide north and northwest region around Budapest, but in the city the ozone concentration is much lower due to the high local NO emissions. In these simulations the plume is bent, follows the direction of the wind and extends up to about 150 km from the city at 17.00. There are significant differences in the predicted peak ozone concentrations between the coarse grid (Figure 11.5 c) and the fine (and adaptive) grid simulations. In general, the simulations using higher resolution grids predict higher peak ozone concentrations than the low resolution ones. The simulations using the coarse grid predict an “ozone ring” around the city and smooth the concentration peaks due to numerical diffusion. The detailed structure of the plume in the South West region of the country is lost in the low resolution simulations.

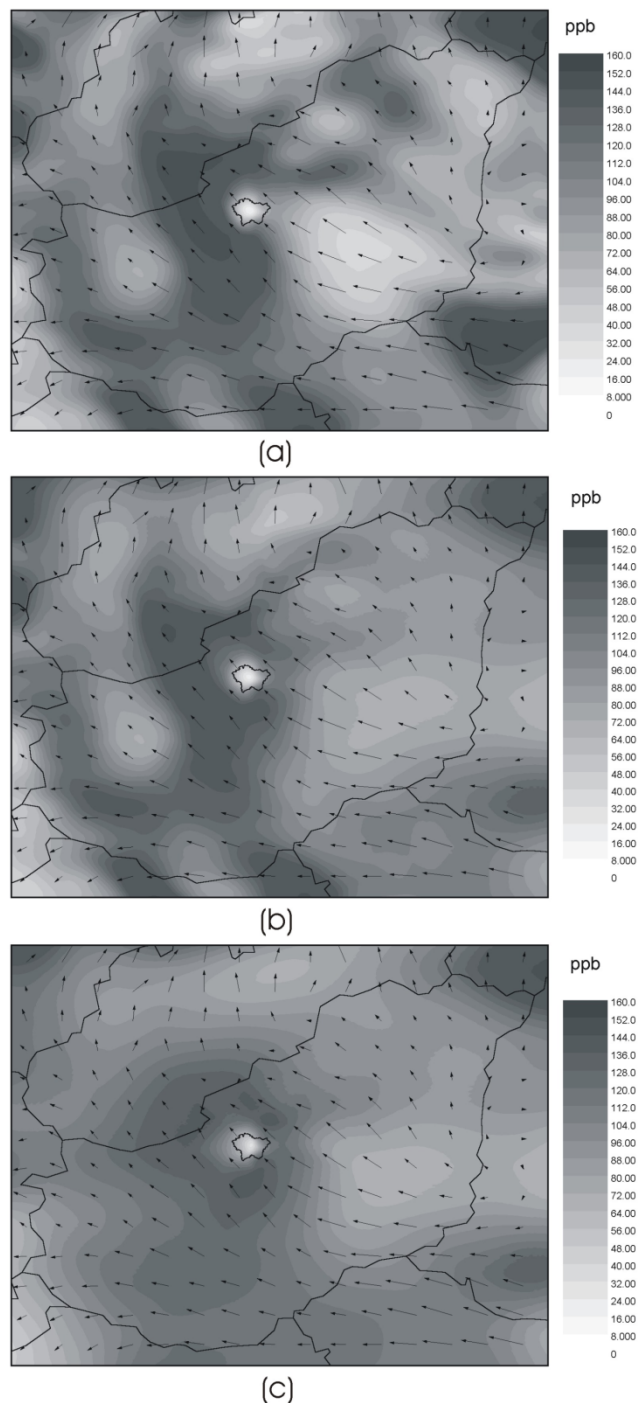


Figure 11.5: Calculated ozone concentrations on the 3rd of August, 1998 at 17.00 with wind field originated from the ALADIN weather prediction model: (a) application of fixed fine nested grid, (b) adaptive grid, (c) fixed coarse grid.

The comparisons of integrated ozone concentrations across the simulation period are displayed in figure 11.6. We obtain very similar integrated ozone patterns using the fixed nested fine and adaptive grids. In both cases a plume shaped region of lowered ozone concentrations is present to the North East of Budapest with a peak of much higher integrated concentrations at the end of the plume close to the Slovakian border. The ability to model this depletion of ozone results from the use of a high-resolution emissions inventory for Budapest coupled with a grid resolution that is high enough to resolve the resulting plumes. This enables the resolution of nitrogen oxide concentrations in this region leading to the depletion of ozone. In the coarse grid simulation, the integrated ozone concentrations are smoothed in comparison and the plume shaped structure is not present. Hence, although the

fixed coarse grid model is the fastest to simulate, it misses key features related to integrated concentrations and would therefore be unsuitable for estimating the long-term impact of ozone.

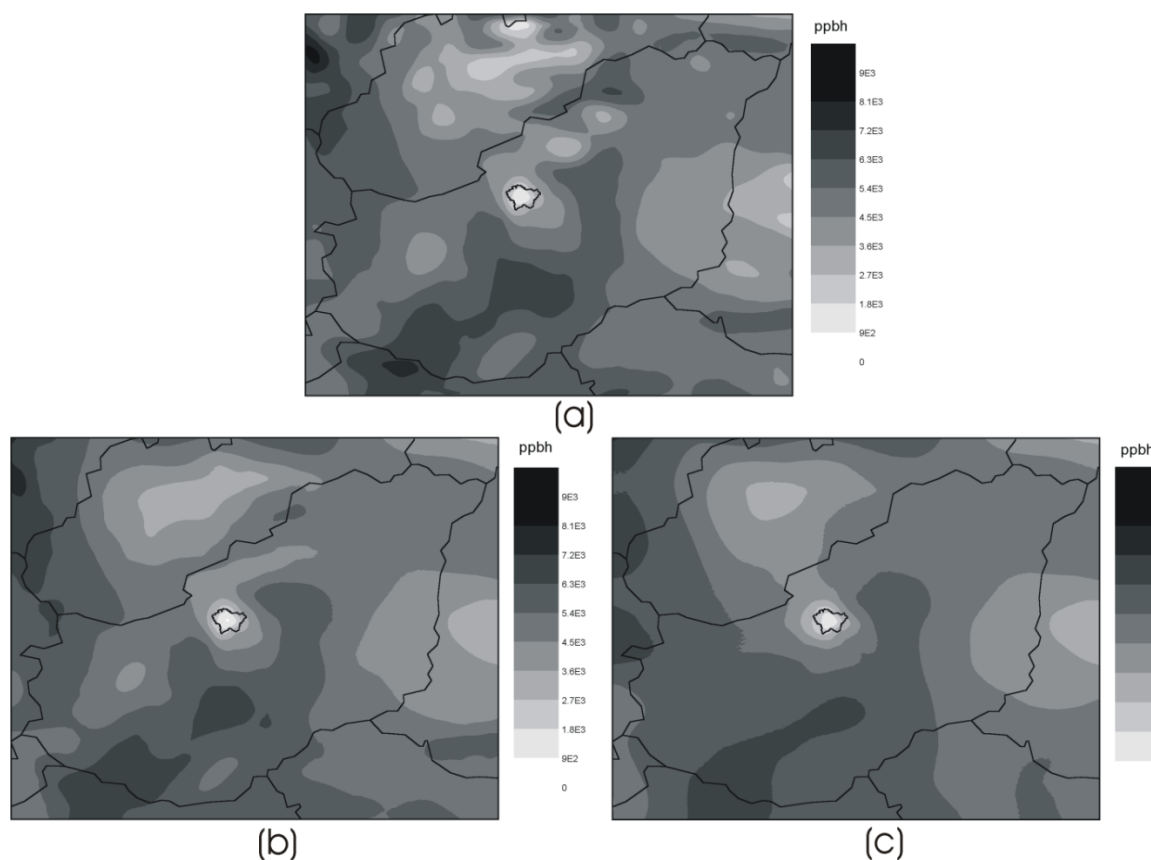


Figure 11.6: Calculated integrated ozone concentrations for the simulation period: (a) application of fixed fine nested grid, (b) adaptive grid, (c) fixed coarse grid.

The ratio of CPU time requirements and number of grid cells for the coarse, adaptive and fine grid models is shown in Table 11.2. The fine and the adaptive models provided similar results, but the former method required 1.5 times more computer time and a significantly higher number of grid cells. Therefore, the adaptive grid model provides an efficient method for the prediction of secondary air pollution formation at the regional scale. Such model could be successfully used for operational purposes due to lower CPU costs.

An adaptive grid model describing the formation and transformation of photochemical oxidants based on triangular unstructured grids has been developed and applied to the simulation of photochemical oxidant formation in Hungary. The model contains a high-resolution emissions inventory for the Budapest region and during the simulation automatically places a finer resolution grid in regions characterized by high concentration gradients and therefore by higher numerical error. Using the adaptive method, grid resolutions of the order of 10 km can be achieved in regional air pollution models without excessive computational effort. The overhead in using such a transient adaptive scheme stem from the need for interpolation of emissions and meteorological data as well as modelled concentrations onto the new grid structure following grid refinement or de-refinement. However, such overheads can be minimized if the grid refinement procedure is not performed for each simulation time-point but is limited to a given time interval which in the current application was 5 minutes. Figure 11.4 demonstrates that in the current application, large parts of the nested domain did not require refinement using the chosen tolerances. If refinement overheads are limited the application therefore shows that transient adaptation can provide an efficient alternative to traditional nested grid approaches.

The simulation of a photochemical episode that occurred during August 1998 demonstrates the influence of precursor emissions from Budapest on down-wind ozone concentrations up to 150 km from the city. The comparison of different grid strategies demonstrates that the use of a coarse grid has a tendency to smooth out key features in both local and integrated ozone concentrations due to numerical diffusion. This results in the underestimation of

both ozone depletion in high NO_x regions, and peak ozone concentrations. The adaptive model predicts similar features to the fixed fine grid model using less CPU time and grid cells. The results therefore indicate the potential for using adaptive models in an operational context for assessing the long-term impact of ozone within Europe.

11.1.3. Adaptive gridding for simulating accidental release

Following the Chernobyl accident most countries in Europe developed national nuclear dispersion or accidental release models linked to weather prediction models of varying types and resolutions. The performance of a number of these models was evaluated against the ETEX European tracer experiments with no overall modelling strategy emerging from this evaluation as being statistically better than another. A comparative discussion of the available model types will be given in the next section. The second ETEX experiment proved to be a challenge for all the codes, since they failed to predict the location of the tracer plume accurately. Clearly therefore, issues still remain as to what is an appropriate strategy for predicting the impact of an accidental release. Sensitivity tests from the ETEX comparisons showed significant impact of both input data (e.g. three dimensional wind-fields and boundary layer descriptions) and model structure, such as the choice of numerical solution method and model resolution on output predictions. Models are not only used for predictive purposes such as exposure assessment, but are also often used to test our understanding of the underlying science that forms the foundation of the models. Improvements in our understanding are often tested by comparison of the models with measured data. If this is the case then one must be sure that changes made to input data to improve predictions are not compensating for errors that actually arise from the numerical solution of the problem. It follows that models used within the decision making and environmental management context must use not only the best available scientific knowledge and data, but also the best available numerical techniques. By this we mean techniques that minimize the errors induced by the choice of numerical solution method rather than the structure of the physical model. Because of the historical development of environmental predictive models and the investment time required to implement new computational solution strategies, unfortunately the most appropriate numerical method is not always used. Therefore, the aim of this work is not to elaborate yet another numerical dispersion simulation code, but to present the practical application of improved numerical methods which may provide useful developments to some existing modelling strategies. The paper presents the use of adaptive Eulerian grid simulations to accidental release problems and it will be shown by comparison with some current numerical computational methods that improvements in accuracy can be made without significant extra computational expense. We present the use of the model for the prediction of hypothetical accidents from the Paks Nuclear Power Plant (NPP) in Central Hungary and we include a discussion of the comparison of the present method with more traditional modelling approaches.

The Chernobyl release provided a large impetus for the development of accidental release models and several inter-comparisons between different model types have been made. The predominant model types are Lagrangian and Eulerian. The former trace air masses, particles with assigned mass, or Gaussian shaped puffs of pollutants along trajectories determined by the wind-field structures. Lagrangian models have the advantage that they can afford to use high spatial resolution although they rely on the interpolation of meteorological data. Their potential disadvantages are that in some cases they neglect important physical processes and often experience problems when strongly diverging flows lead to uncertainties in long-range trajectories. One example of this is discussed by Baklanov et al. (2002) who modelled the potential transport of radionuclides across Europe and Scandinavia from a hypothetical accident in Northern Russia using an isentropic trajectory model. In their 'winter' case studies the isentropic trajectory model simulated much of the deposition when compared to a high-resolution meteorological/dispersion model. In some cases however, additional deposition was predicted by the dispersion model in locations not predicted by the isentropic trajectory model due to the splitting of atmospheric trajectories.

There are several types of Lagrangian trajectory models. One example of a Gaussian puff model is the DERMA model, which uses a multi-puff diffusion parameterization. A Gaussian profile is assumed for the puff in the horizontal direction with complete mixing in the vertical direction within the boundary layer and a Gaussian profile above it. The UK MET office NAME model and the Norwegian SNAP model use a Lagrangian particle formulation, which resolves the trajectories of a large number of particle releases with assigned masses. The NAME model is capable of following a 3D mean wind-field plus a turbulent component with a variety of turbulence parameterizations available ranging from simple eddy diffusion terms to complex random walk descriptions, although the turbulent parameterizations are based on measurements from a single location. Because it does not use a Gaussian puff formulation it can resolve varying wind speeds and directions, skewed turbulence and varying stabilities. The disad-

vantage of this approach is its computational expense, since a large number of particles must be released when compared to the Gaussian puff approach.

Eulerian models use grid based methods and have the advantage that they may take into account fully 3D descriptions of the meteorological fields rather than single trajectories. However, when used traditionally with fixed meshes, Eulerian models show difficulty in resolving steep gradients. This causes particular problems for resolving dispersion from a single point source, which will create very large gradients near the release. If a coarse Eulerian mesh is used then the release is immediately averaged into a large area, which smears out the steep gradients and creates a large amount of numerical diffusion. The result will be to underpredict the maximum concentrations within the near-field plume and to over estimate the plume width. Close to the source the problem could be addressed by nesting a finer resolution grid to better resolve steep gradients. This need to resolve accurately both near and far field dispersion has been noted previously by for example Brandt et al. (1996) who used a combined approach of a Lagrangian mesoscale model coupled with a long range Eulerian transport model in the development of the DREAM model. The approach requires some kind of interpolation procedure between the two grids. A similar approach was also employed through the point source initialization scheme in the Swedish Eulerian model MATCH. The MATCH model uses a Lagrangian particle model for the horizontal transport of the first 10 h after the point source release with vertical transport being described by an Eulerian framework during this time. Quite a large number of particles need to be released per hour to reduce errors in predicting the vertical transport, thus adding to the computational cost. These multi-scale modelling approaches showed significant improvements in predictions close to the release due to the higher resolution Lagrangian models. However, as with the nested Eulerian modelling approach, they still suffer from the drawback that the plume is averaged into the larger Eulerian grid as soon as it leaves the near source region. Brandt et al. (1996) argue that once the plume has left the near-source region the gradients will become sufficiently smooth as to lead to small errors due to numerical diffusion. This ignores however, the fact that steep gradients may persist at plume edges for large distances from the source due to mesoscale processes. Previous studies have shown that high contamination levels or deposition can exist over small areas several hundred kilometres from the source. Brandt et al. (1996) argue that long-range Eulerian models are not suitable for resolving single source releases alone and demonstrate this through the standard Molenkamp test of a rotating passive puff release in a circular wind-field. More recently, however, it has been shown that adaptive Eulerian methods are very capable of resolving the advection of such single source releases since they can automatically refine the mesh in regions where steep gradients exist. Moreover, they can be more efficient than say nested models, since they refine only where high spatial numerical errors are found and not in regions where grid refinement is not necessary for solution accuracy. This means that for the same computational run-time they may allow higher resolution of the grid in important areas. Eulerian models also provide an automatic framework for the description of mixing processes and non-linear chemical reaction terms. This study will therefore show that adaptive grid methods provide a consistent approach to coupling near-field and long-range simulations for single source accidental releases.

It is clear that one of the most crucial inputs to any dispersion model for point source releases is the underlying meteorological data such as wind-field and boundary layer descriptions. The importance of the horizontal resolution of meteorological data has been demonstrated by many of the simulations of the first ETEX experiment (Bryall and Maryon, 1998). The ETEX experiment was an international tracer campaign during which a passive tracer was tracked across Europe over several days from its release in France by monitoring at a large number of meteorological stations. Many numerical simulations were carried out which demonstrated the need for mesoscale weather modelling. Nasstrom and Pace (1998) for example showed that events resolved by a meteorological model of 45 km but not at 225 km resolution had a significant impact on even long-range dispersion of the ETEX plume. Sorensen (1998) showed that the double structure of the first ETEX plume was picked up by their model when using mesoscale weather predictions but not when using coarser resolution ECMWF data. The difference was attributed to a mesoscale horizontal anti-cyclonic eddy that was not resolved within the ECMWF data. The importance of resolving the vertical structure of wind-speeds and directions was demonstrated by the second ETEX experiment where evidence of decoupling of an upper cloud of pollution from the boundary layer plume was observed. In this case significant concentrations were measured behind the path of the plume predicted by most of the models tested. This behaviour has been attributed to the vertical lofting of the plume by the passage of a front, followed by the transport of the pollution cloud in upper levels of the atmosphere at a lower wind speed than in the boundary layer or even perhaps in a different wind-direction. The MET Office NAME model in this case showed a significant amount of mass above the boundary layer for the second ETEX experiment in contrast to the first one where particles were well distributed throughout the boundary layer. Previous simulations point to several important issues relating to the development of an accidental release model. Firstly, a mesoscale meteorological model must be used in order to capture small spatial scale effects such as frontal passages and small scale horizontal eddies.

Secondly, the dispersion model used must be capable of representing, in some way, the possible vertical variations in wind speed and direction, rather than using a single boundary layer description with varying mixing layer height but a single wind-field. Thirdly, the dispersion model must be capable of resolving potentially steep concentration gradients that may be caused by either the single source release or features that may arise due to mesoscale meteorological events. This study will therefore discuss the practical application of an adaptive Eulerian dispersion model when coupled to data from a high resolution mesoscale meteorological model.

This model has been developed within a flexible framework and can therefore simulate both single source accidental releases and photochemical air pollution, where the pollution sources are both area and point sources and the chemical transformations are highly non-linear (Lagzi et al., 2004). A slightly modified version of the model is used here to demonstrate its capacity simulating nuclear dispersion calculations. In the model, the horizontal dispersion of radionuclides is described within an unstructured triangular Eulerian grid framework. The vertical mixing of radionuclides is approximated by a parameterized description of mixing between four layers representing the surface, mixing, reservoir layers and the free troposphere (upper) layer. The horizontal grid is adaptive, i.e. continuously changes in space and time to minimize the numerical errors. The transformation of radionuclides is described within each grid cell by the equations of nuclear decay. Transient refinement and de-refinement is then further invoked as necessary throughout the model run according to spatial errors and chosen refinement criteria. The model domain is represented by an unstructured mesh of triangular elements surrounding each grid point, thus forming a small volume over which the solution is averaged. The model therefore falls into the category of Eulerian models described above, although it is not described by the standard Cartesian mesh approach. The use of adaptivity however, allows the model to overcome the usual problems of the Eulerian approach, since a fine mesh can be used where needed leading to averaging over small volumes. The term ‘unstructured’ represents the fact that each node in the mesh may be surrounded by any number of triangles, whereas in a structured mesh such as a Cartesian mesh, the number of surrounding grid points would be fixed. The use of an unstructured mesh easily enables the adequate resolution of complex solution structures that may be found following point source releases and which may not fall naturally into Cartesian geometrical descriptions. For example, following release, the plume from a point source may be stretched and folded in space due to advection and turbulent mixing. The unstructured triangular mesh then provides an efficient way of adapting around this complex geometry. The initial unstructured triangular meshes used in the model are created from a geometry description using the Geompack mesh generator. The complex nature of atmospheric dispersion problems makes the pre-specification of grid densities very difficult, particularly for forecasting codes where the wind-field is not known in advance. Many complex processes can take place far from the source due to advection, mixing, chemical reactions and deposition, affecting the geometry of the plume and spatial concentration profiles. To this end the model presented here utilizes adaptive gridding techniques, which quantitatively evaluate the accuracy of the numerical solution in space and time and then automatically refine or de-refine the mesh where necessary. As described above, the accuracy of Eulerian models tends to become degraded in regions where the concentration of the pollutant changes steeply in space. The use of transient adaptivity allows us to overcome this problem. It is achieved by using a tree-like data structure with a method of refinement based on the regular subdivision of triangles (local h -refinement). Here an original triangle is split into four similar triangles as shown in Figure 11.7 by connecting the midpoints of the edges.

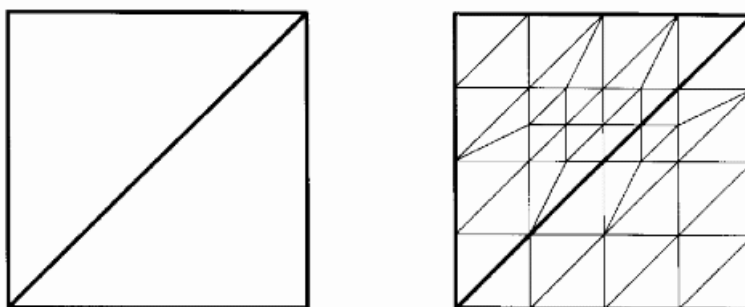


Figure 11.7: Example of local h -refinement in the model.

Hanging or unconnected nodes are removed by joining them with nearby vertices. This finer grid may be later coalesced into the parent triangle to coarsen the mesh if the solution accuracy does not require refinement – for example when the plume has passed or concentration gradients in space are reduced. The use of unstructured meshes allows the model to go from very fine resolution to coarse resolution within small spatial regions. Once a method of refinement has been implemented, a suitable criterion for the application of transient adaptivity must

be chosen. The technique used here is based on the calculation of spatial error estimates, allowing a certain amount of automation to be applied to the refinement process. This is achieved by first calculating some measure of numerical error in each species over each triangle. A reliable method for determining the numerical error is to examine the difference between the solution gained using a high accuracy and a low accuracy numerical method. Over regions of high spatial gradient in concentrations the difference between high and low order solutions will be greater than in regions of relatively smooth solution, and refinement generally takes place in these regions. The use of absolute as well as relative tolerances allows the user to define a species concentration below which high relative accuracy is not required. For the current example the choice of this tolerance may be driven by a minimum concentration of concern from a health point of view for example. An integer refinement level indicator is calculated from the scaled error above to give the number of times the triangle should be refined or de-refined. The choice of tolerances will therefore reflect, to a certain extent, a balance between desired accuracy and available computational resources, since tighter tolerances usually lead to a higher number of grid cells. It is also possible within the code for the user to control the maximum number of levels of adaptivity, thus limiting the minimum grid size in regions of very steep gradients i.e. close to the point source. Since the error is applied at the end of time-step it is too late to make refinement decisions. Methods are therefore used for the prediction of the growth of the spatial error using quadratic interpolants. The spatial error can therefore be used to predict within which regions the grid should be refined or coarsened for the next time-step in order to give good spatial accuracy with the minimum computational resource. The application of adaptive rectangular meshes would be also possible, but would be less effective in terms of the number of nodes required in order to achieve high levels of adaptivity. Although the data structures resulting from an unstructured mesh are somewhat more complicated than those for a regular Cartesian mesh, problems with hanging nodes at boundaries between refinement regions are avoided. The use of a flexible discretization stencil also allows for an arbitrary degree of refinement, which is more difficult to achieve on structured meshes.

The model domain covers Central Europe including Hungary with a domain size of 1550×1500 km. The model describes the domain using a Cartesian coordinate system through the stereographic polar projection of the curved surface onto a flat plane. Global coordinates are transformed by projecting the surface of the Earth, from the opposite pole onto a flat plane located at the North Pole that is perpendicular to the Earth's axis. Due to the orientation of the projection plane this transformation places the Cartesian origin at the North Pole. The model includes four vertical atmospheric layers: a surface layer, a mixing layer, a reservoir layer and the free troposphere (upper) layer. The surface layer extends from ground level to 50 m altitude. Above the surface layer is the mixing layer whose height is determined for 0.00 and 12.00 UTC values by radiosonde measurements in Budapest. The night time values are assumed to be identical to the midnight value while the height between 6.30 and 15.00 were linearly interpolated between the night and the highest daytime values. The reservoir layer, if it exists, extends from the top of the mixing layer to an altitude of 1000 m. Different wind-fields are represented for each layer and vertical mixing and deposition are also parameterized. The local wind speed and direction was considered as a function of space and time. These data were obtained from the mesoscale meteorological model ALADIN, which provides data with a time resolution of 6 h and a spatial resolution of $0.10 \times 0.15^\circ$. The ALADIN model is a hydrostatic, spectral limited area model using 24 vertical layers where initial and boundary conditions are determined from larger scale ECMWF data. The model domain for ALADIN covers the Central European region from latitude 43.1° to 52.0° and longitude 10.35° to 25.1° . The data from ALADIN were interpolated using mass conservative methods to obtain data relevant to a given space and time point on the adaptive model grid. The surface temperature and cloud coverage, relative humidity and wind field for each layer were determined from the ALADIN database. The eddy diffusivity coefficients for the x and y directions were set at $50 \text{ m}^2 \text{ s}^{-1}$ for all species.

The features of the model are illustrated by the simulation of a hypothetical nuclear accident on 2 August 1998, at time 0.00 in the Paks nuclear power plant. The release of $2.985 \text{ kg } ^{131}\text{I}$ isotope is assumed at a height of 10 m for 12 h. This isotope decays to the stable ^{131}Xe with a half-life of 6.948×10^5 s. In the current simulations, only the radioactive decay of ^{131}I was calculated and the change of activity of this isotope was simulated. The model is capable of the simultaneous simulation of the spread of several hundred isotopes, taking into account all radioactive decays.

Figures 11.8 and 11.9 show initial grids for the adaptive and coarse grid calculations. The typical length of a triangle edge is 106 km and around the Paks NPP a somewhat finer resolution initial grid was used. The figure shows that the modelled area includes Hungary and covers the neighbouring countries within about 600 km from the border to all directions. Wind-field maps corresponding to this period indicated that the wind at all heights from the surface to 3000 m blew from south-east in the first 36 h. After this, the wind direction changed to northwest in the Czech Republic and Poland, but was almost unchanged in the other areas. The application of adaptive gridding methods was compared to the application of fixed grids for the hypothetical release described above. Three different fixed

grid schemes were tested: (i) the initial grid (shown in Figure 11.8) was not refined during the calculations; (ii) a high resolution (triangle edge length 6.6 km) nested grid was placed around the source within a $250 \text{ km} \times 250 \text{ km}$ area as shown in Figure 11.9; (iii) resolution (triangle edge length 6.6 km) fixed grid was used within the whole area.



Figure 11.8: Initial grid of the adaptive and coarse grid calculations.

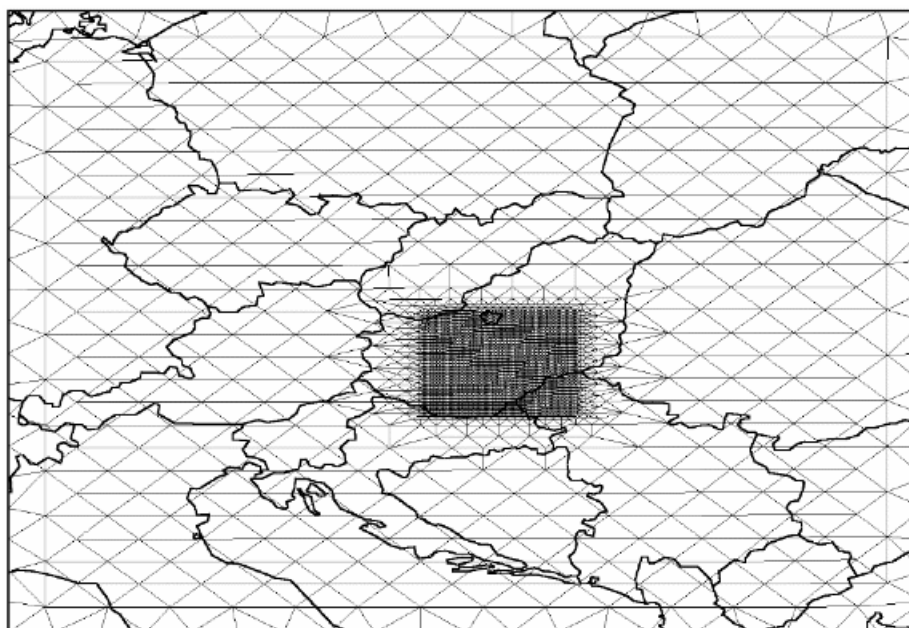


Figure 11.9: Nested fine grid within the coarse grid.

Figure 11.10 e-h show the simulated surface layer activity of isotope ^{131}I using adaptive gridding. A continuous release was assumed in the first 12 h and therefore there is a continuous plume after 12 h (Figure 11.10 e). After 12 h, the cloud is separated from the source and travels towards the northwest (t_0+24 h, Figure 11.10 f). After 36 h (Figures 11.10 g, h) it starts to drift backwards towards the southeast. Figures 11.10 a–d show that the region of increased grid resolution continuously follows the path of the contaminated air. The typical grid size in the non-contaminated area remained at ca 106 km, but in the highly contaminated area it was automatically reduced to 6.6

km (the minimum allowed length at the simulation) by the transient adaptation routine, allowing better spatial resolution in critical areas.

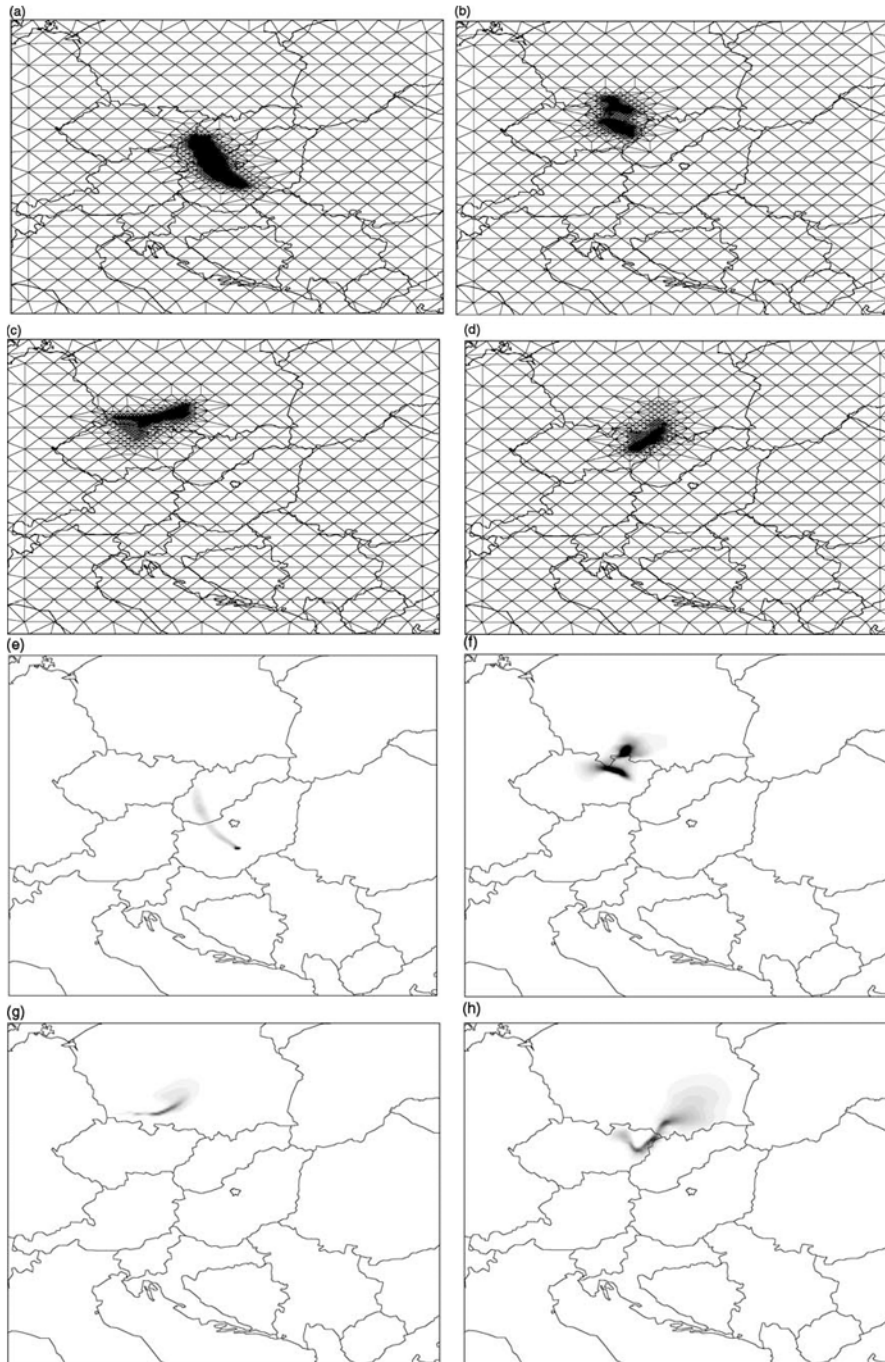


Figure 11.10: Change of the surface layer mesh structure and activity of isotope ^{131}I during the adaptive grid calculations. Simulation started from 2 August 1998, at 0.00. (a)–(d) The adapted mesh at t_0+12 , t_0+24 , t_0+36 , t_0+48 h; (e)–(h) activity in the surface layer at t_0+12 , t_0+24 , t_0+36 , t_0+48 h.

Figures 11.11–11.14 compare the simulation results using the three fixed grid schemes at simulation times 12, 24, 36, and 48 h after the accident. The fine grid calculation has the lowest numerical error and therefore these results are the basis of comparison for the other mesh strategies. The coarse grid calculations show high numerical diffusion at all times. The result is that the initial plume is smeared over a much wider area than in the fine grid simulation as shown in Figure 11.11 a. The nested grid calculation results agree well with the fine grid results while the con-

tamination is in the highly resolved area; however high numerical diffusion appears when the contamination leaves the nested grid. After 24 h of simulation the predictions from the nested grid calculation are more similar to those of the coarse grid calculation than the fine one (Figures 11.12-11.14), showing that the initial advantage of using a nested grid can quickly be lost. The agreement between the adaptive grid solutions (Figure 11.9 e–h) and the fine grid results (Figures 11.11 c, 11.12 c, 11.13 c and 11.14 c) is very good at t_0+12 and t_0+24 h and acceptable at t_0+36 and t_0+48 h simulation times. The shape of the isotope cloud is well predicted with some smearing occurring at the edges. The adaptive grid simulation is significantly closer to the fine grid calculation than both the course and nested grid predictions even after 48 h as shown by comparing figures 11.10 and 11.14.

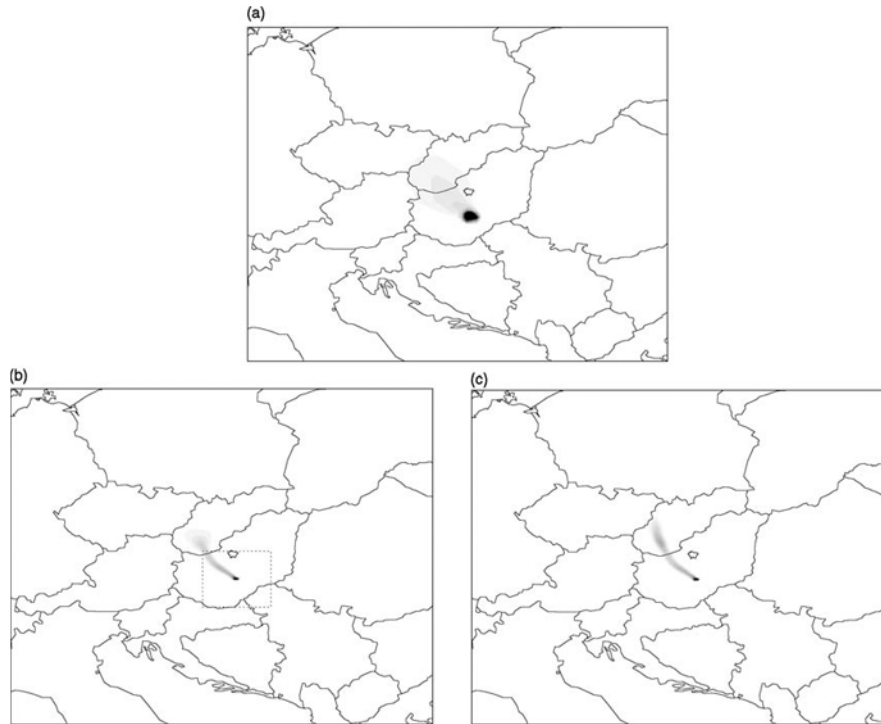


Figure 11.11: Surface layer activity of isotope ^{131}I using three different fixed grid size schemes at t_0+12 ((a) coarse grid; (b) nested grid; (c) fine grid). All simulations started from 2 August 1998 at 0.00 UTC.

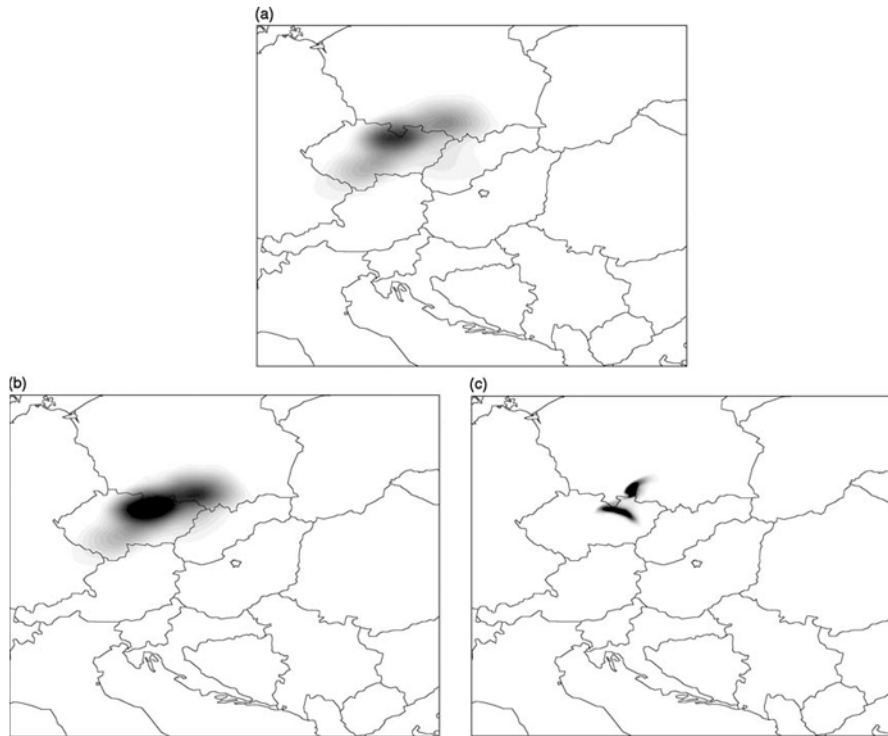


Figure 11.12: Surface layer activity of isotope ^{131}I using three different fixed grid size schemes at t_0+24 ((a) coarse grid; (b) nested grid; (c) fine grid). All simulations started from 2 August 1998 at 0.00 UTC.

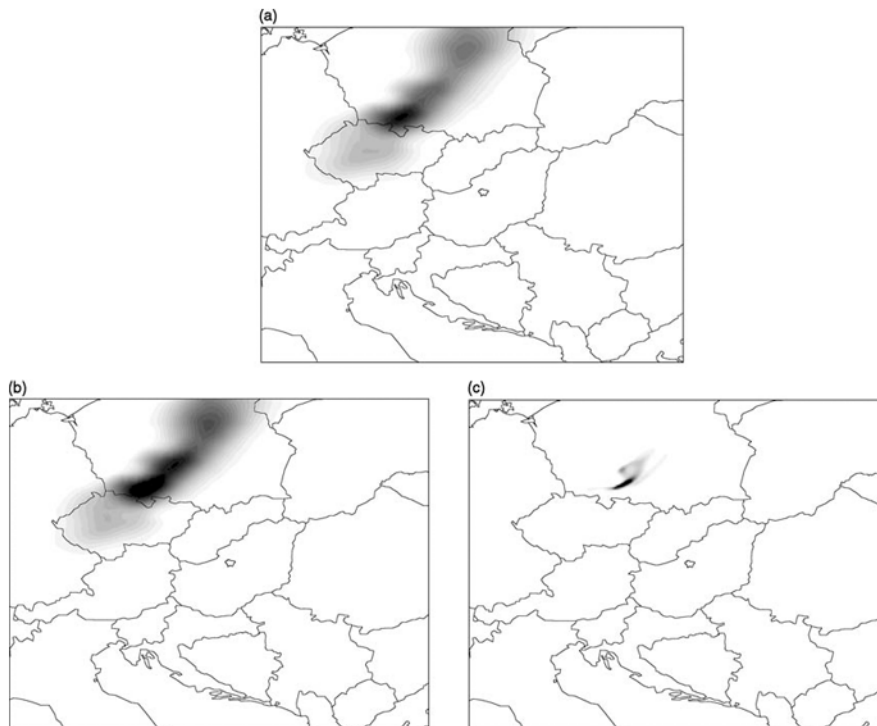


Figure 11.13: Surface layer activity of isotope ^{131}I using three different fixed grid size schemes at t_0+36 ((a) coarse grid; (b) nested grid; (c) fine grid). All simulations started from 2 August 1998 at 0.00 UTC.

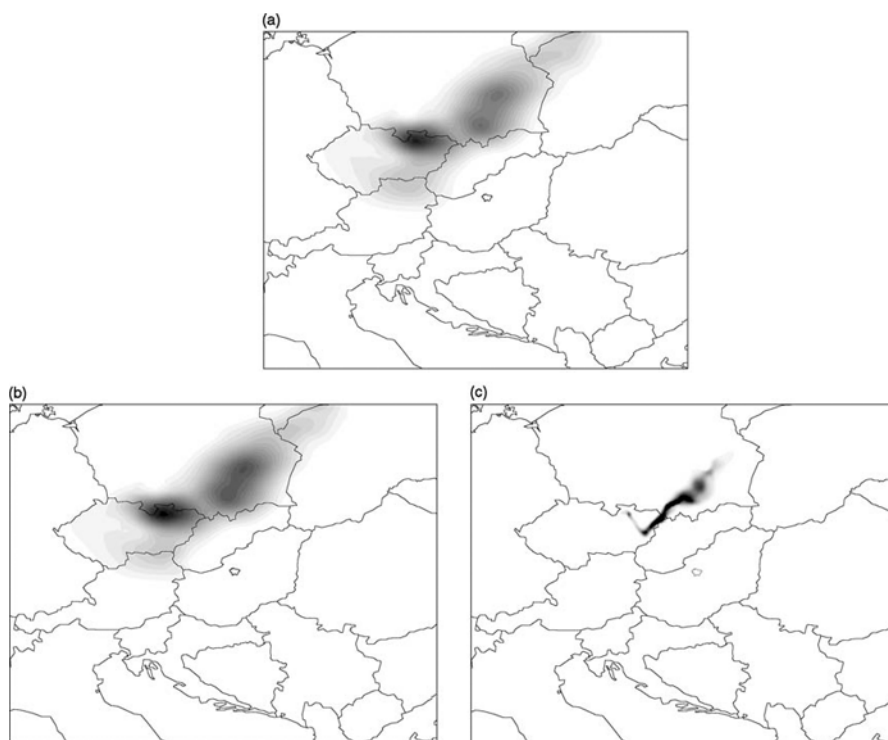


Figure 11.14: activity of isotope ^{131}I using three different fixed grid size schemes at t_0+36 ((a) coarse grid; (b) nested grid; (c) fine grid). All simulations started from 2 August 1998 at 0.00 UTC.

Nuclear dispersion models have to predict accurately both the maximum level of contamination and the expected arrival time of the contamination peak. The four models presented above can be compared not only by using activity maps at fixed times, but also by plotting the time history of activity at a given location. Three cities, all northwest of Paks were selected: Székesfehérvár (located in Hungary, 101 km from Paks), Bratislava (Slovakia, 247 km), Ostrava (Czech Republic, 415 km). Figure 11.15 shows the time dependence of the surface layer activity of ^{131}I in these three cities, calculated by the four gridding schemes. Again, the fine grid calculations were assumed to be the most accurate. At Székesfehérvár, the fine and the nested grid results are identical and the adaptive grid predicted only a slightly higher peak at a slightly earlier arrival time. The coarse grid calculation predicted a much higher double peak arriving much earlier. Bratislava is not affected directly by the plume, as it is well visible from both the fine and the adaptive grid results shown here and in figures 11.10 e and 11.11 c. Because of the smearing of the plume due to numerical diffusion however, the coarse and the nested grid models erroneously predict the appearance of the contamination in Bratislava. In a real situation such a prediction may result in the unnecessary evacuation of the population. In Ostrava, the fine and the adaptive models both predict high contamination at similar arrival times. The nested and the coarse models forecast much lower contamination, which arrives later than predicted by in the fine grid simulations. Based on the latter models, the population may not be evacuated in a dangerous situation. Additionally, the first two models predict the return of the polluted cloud with very good agreement, but such a feature is not present in the coarse and nested simulation results. In all cases the fine and adaptive simulation results were in good qualitative agreement, while the coarse and nested grid simulations would have advised wrong measures in the chosen locations. The ratio of time requirements are 1:30:19:532 for the coarse, adaptive, nested and fine grid models, respectively. The adaptive simulation is therefore only slightly more computationally expensive than the nested grid whilst providing a step change in accuracy. Note, that using the time and space dependent adaptive grid is more time consuming than the application of the fixed nested grid due to the use of the adaptivity algorithm, even though the nested method uses more grid points. There is some overhead therefore in calculating the refinement criteria and interpolating the solution onto the new mesh each time the mesh is updated. However, the fine and the adaptive models provided similar results, but the application of the former required 17.5 times more computer time. The implications could be that given limited computer resources, the adaptive model provides reliable results quickly thus allowing ample time for emergency response. The fine grid model would provide similar results, but possibly too late.

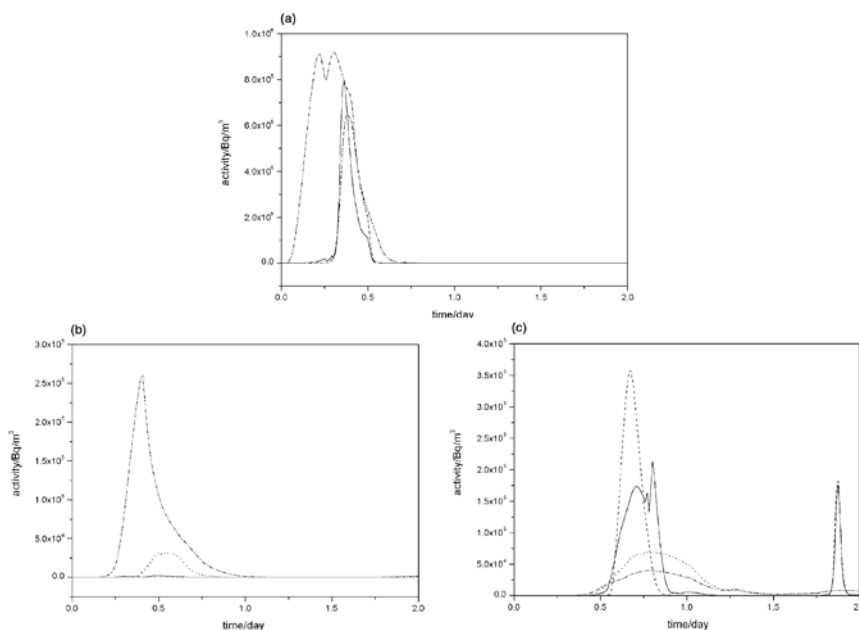


Figure 11.15: Time dependence of the surface layer activity of ^{131}I in three cities in the region, calculated using four different gridding schemes. (a) Székesfehérvár (Hungary, 101 km NW from Paks), (b) Bratislava (Slovakia, 247 km NW), (c) Ostrava (Czech Republic, 415 km NW). Solid line, adaptive grid; dashed line, fine grid; dotted line, nested grid; dash-dot line, coarse grid.

11.2. Parallelization

11.2.1. Introduction

There are numerous solutions to address the issue of high computational requirements. Generally, the solution is using supercomputers, clusters, or grid systems. These systems are built by connecting numerous processors, either by some sort of direct link or by a network connection. Several computing centres can be connected to each other by the internet, thus creating grids. Management and programming of these systems require certain software environments and tools.

11.2.2. Supercomputers, clusters, and Grids

Parallel computers can be roughly classified according to the level at which the hardware supports parallelism. This classification is broadly analogous to the distance between basic computing nodes.

Multicore computing:

A multicore processor is a processor that includes multiple execution units ("cores") on the same chip. These processors differ from superscalar processors, which can issue multiple instructions per cycle from one instruction stream (thread); in contrast, a multicore processor can issue multiple instructions per cycle from multiple instruction streams. Each core in a multicore processor can potentially be superscalar as well - that is, on every cycle, each core can issue multiple instructions from one instruction stream.

Supercomputers (Symmetric multiprocessing):

A symmetric multiprocessor (SMP) is a computer system with multiple identical processors that share memory and connect by a local high-speed computer bus.

Distributed computing:

A distributed computer is a distributed memory computer system in which the processing elements are connected by a network. Distributed computers are highly scalable.

1. Cluster computing:

A cluster is a group of loosely coupled computers that work together closely, so that in some respects they can be regarded as a single computer. Clusters are composed of multiple standalone machines connected by a network. While machines in a cluster do not have to be symmetric, load balancing is more difficult if they are not.

2. Grid computing:

A distributed system consists of multiple computers that communicate through a computer network. The computers interact with each other in order to achieve a common goal. A computer program that runs in a distributed system is called a distributed program, and distributed programming is the process of writing such programs.

In order to parallelise the sequential code of a reaction-diffusion simulation the domain decomposition concept should be followed; the two-dimensional grid is partitioned along the x space direction, so the domain is decomposed into horizontal columns. Therefore, the two-dimensional subdomains can be mapped onto a one-dimensional logical grid of processes. An equal partition of subdomains among the processes gives us a well balanced load during the solution of the reaction-diffusion equations. During the calculation of the diffusion of the chemical species communications are required to exchange information on the boundary concentrations between the nearest neighbour subdomains (Figure 11.16).

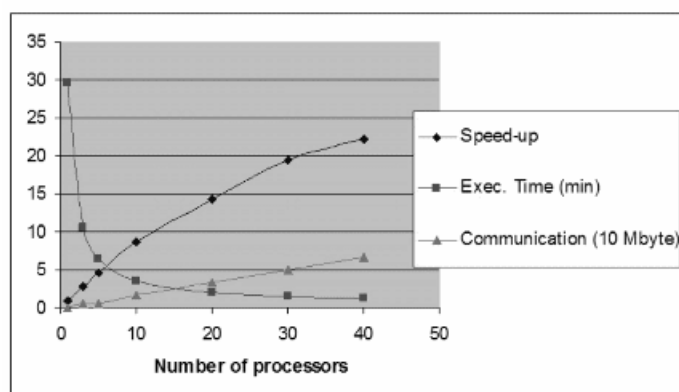


Figure 11.16: A typical performance result of a diffusion problem on Grid.

11.2.3. GPU – Graphical Processing Unit

In the past five years, the technological development of consumer graphics hardware created the possibility to use desktop video cards to solve numerically intensive problems, since their computational capacity far exceeds the capacity of desktop CPUs. Using GPUs (processors of video cards) for general purpose calculations is called GP-GPU. Its main advantage is high cost-effectiveness. Compared to former solutions, there are virtually no extra costs to operate these systems, like high-powered air conditioning, high electric power consumption and the need for a large space (building). Programming GPU is achieved by using library functions designed for 3D computer graphics (games, CAD). Due to this constraint programming such applications is difficult. Recently, NVIDIA addressed this problem by creating a new parallel computing model called CUDA. It is also an extension to the well-known C language. A compiler, a software development kit with utilities and numerous examples, and a complete documentation of the architecture and the language extensions are available.

In this chapter we present an efficient parallelization of the stochastic Lagrangian particle model using CUDA. In this model, each particle can be handled independently, thus being a perfect candidate for parallelization.

11.2.3.1. Lagrangian model

In this model type as discussed earlier, individual particles are released from a point source in each time step. Each particle represents a given mass or activity, and they can be moved in 3D space by advection (wind field) and turbulent diffusion, they can transform to other species (by radioactive decay), and particles can be removed from the atmosphere via dry and wet deposition processes to the surface. This means that the model is continuous in space and discontinuous in time. It was supposed that advection field is deterministic, but the effect of the turbulent diffusion is always stochastic. The new spatial position of particles can be calculated with the following equations (Molnár et al, 2010):

$$X_i^{new} = X_i^{old} + v_i^{adv} \Delta t + \tilde{x}_i, \quad (11.3)$$

where X_i^{new} and X_i^{old} are the spatial coordinates of particles after and before the time step, respectively. v_i^{adv} is the i^{th} coordinate of the wind velocity vector, Δt is the time step (in the model simulation 10 s). The last term in equation (11.3) (\tilde{x}_i) describes the effect of stochastic turbulent processes, and i denotes the spatial dimension ($i = 1, 2, 3$). Stochastic term is calculated by

$$\tilde{x}_i = \{rand\} \sqrt{2K_i \Delta t}, \quad (11.4)$$

Random numbers (*rand*) with normal distribution (with mean 0.0 and variance 1.0) were generated using Mersenne Twister random number generator and a Cartesian Box-Muller transformation. K_i is the turbulent diffusion coefficient in each direction. For horizontal dispersion a constant value was used ($K_x = K_y = 100 \text{ m}^2 \text{ s}^{-1}$). Vertical diffusion coefficient (K_z) depends on the height, and it can be calculated by the Monin–Obukhov theory.

Released particles can decay (radioactive decay) and deposit by dry and wet pathways. The probability that individual particles during a time step Δt will decay or deposit can be estimated by the following relation:

$$p = 1 - e^{-k\Delta t}, \quad (11.5)$$

where k is either the radioactive decay constant or wet or dry deposition constant. These constants depend on the chemical nature of the toxic species. During dry deposition, particles can deposit below the mixing layer height. Wet deposition occurs only in case of precipitation.

11.2.3.2. Parallel application and implementation:

The main concept of CUDA parallel computing model is to operate with tens of thousands of lightweight *threads*, grouped into *thread blocks*. These threads must execute the same function, with different parameters. The function that contains the computations and runs in parallel in many instances is called the *kernel*. Threads in the same thread group can synchronize with each other, by inserting synchronization points in the kernel, which must be reached by all threads in the group before continuing execution. These threads can also share data during execution. This way usually several hundred threads in the same block can work cooperatively. Threads of different thread blocks cannot be synchronized and should be considered to run independently.

It is possible to use a small number of threads and/or small number of blocks to execute a kernel, however, it would be very inefficient. This would utilize only a fraction of the computing power of the GPU. Therefore, CUDA is the best suited to those problems that can be divided into many parts, which can be computed independently (in different blocks), and these should be further divided into smaller cooperating pieces (into threads).

There are several types of memory available in CUDA, designed for different uses in kernels. Proper use of these memories can increase the computation performance. The *global memory* is essentially the random access video memory available on the video card. It may be read or written any time at any location by any of the threads, but to achieve high performance access to global memory should be coalesced, meaning the threads must follow a specific memory access pattern. For the complete (and hardware-revision dependent) description please refer to the Programming Guide. A kernel has access to two cached, read-only memories: the *constant memory* and the *texture memory*. Constant memory may be used to store constants that do not change during kernel execution.

Texture memory may be used efficiently when threads access data with spatial locality in one, two, or three dimensions. It also provides built-in linear interpolation of the data. There is also a parallel data cache available for reading and writing for all the threads of a thread block called the *shared memory*. It makes the cooperative work of threads in a block possible. It is divided into banks. Kernels should be written in a way to avoid bank conflicts, meaning the threads which are executed physically at the same time should access different banks. The Programming Guide presents details how to achieve this.

Memory management and kernel execution is controlled by CUDA library functions in the *host* code (the one which runs on the CPU). While the kernels are executing on the *device*, the CPU continues to execute host code, so CPU and GPU can work in parallel.

Implementing a single-threaded CPU version of the model is straightforward. Assuming that the emission profile (the amount of emitted particles in every time step) for all species and the maximum number of particles released during the simulation are known, activities or masses can be a priori assigned to the particles. The maximum number of particles is the dominant variable that affects simulation time and precision. It is limited only by available memory.

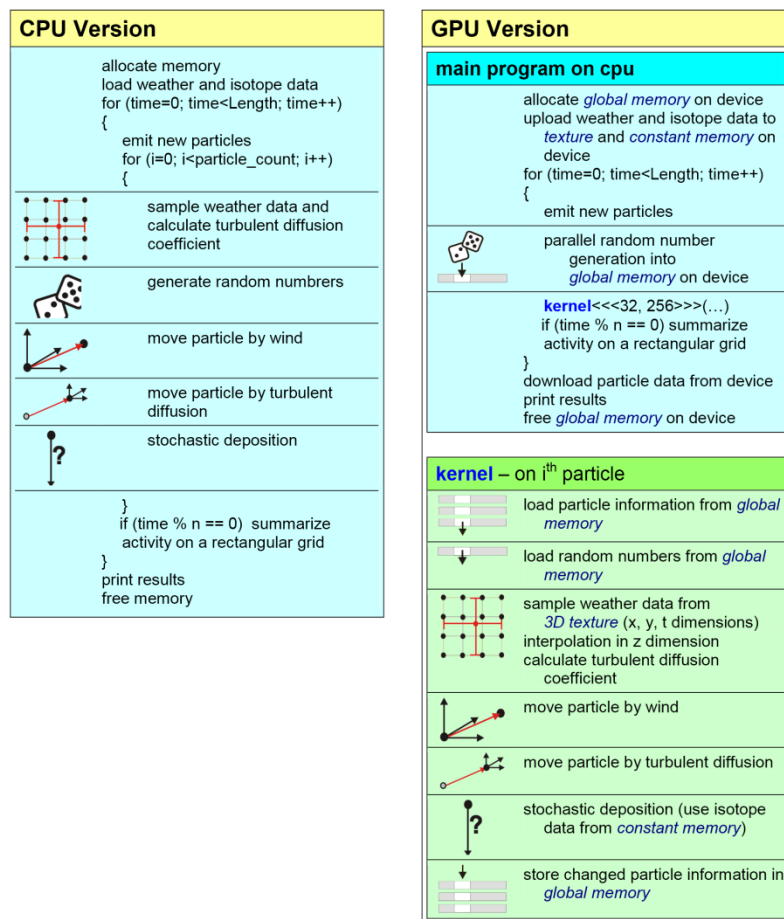


Figure 11.17: Flowchart of the stochastic Lagrangian model on CPU and GPU. A typical performance result of a diffusion problem on Grid.

The main loop is the time evolution of the simulation (Figure 11.17). In every iteration the main steps for every particle are the same: interpolating (sampling) weather data in x , y , z , and time dimensions using linear interpolation, calculating the turbulent diffusion coefficient, moving the particle by the wind, then by turbulent diffusion, and finally testing for dry and wet depositions. Particles may become inactive, meaning they are no longer moved by wind or turbulent diffusion, when the particle is deposited or it reaches the predefined boundaries of the simulated

area. At the end of every n^{th} time step the activity of particles is calculated based on the isotope's half-life and the time since particle was emitted. Activities or masses of particles are summarized on a rectangular grid for visualization and further statistical evaluation. From the technical point of view, the value of n should not be smaller than four, it should be set to the highest number possible to achieve the desired precision of the time-integrated dosage calculation (a post-processing of simulation results).

In the parallelized CUDA version of the program, we utilize the various memory types available. Weather data are loaded into three-dimensional textures, to utilize the hardware-implemented trilinear interpolation. Since the weather data are four-dimensional, an extra interpolation step is necessary. The fourth interpolation must be in z dimension, because the vertical weather information is nonlinear, unlike x , y and time dimensions. Using texture memory is also useful because the plume usually propagates in a specific direction, giving the required spatial locality for the texture cache to work efficiently. Physical constants of the isotopes are loaded to constant memory. Shared memory is used for caching the particle data (position, state information). The data is loaded from global memory to shared memory when a kernel starts, and written back at the end, if data was modified.

The calculations in each time step are done by two kernel functions. First step is generating random numbers, using the Mersenne-Twister random number generator. The implementation is provided by the CUDA SDK. A large buffer (on the GPU) is used to store the numbers, because the random number generator works more efficiently if large amount of numbers is asked for at once. The second step is the main kernel. First, particle information and random numbers are loaded from global memory to shared memory. Second step is sampling the weather data, interpolation in z dimension, and calculating the turbulent diffusion coefficient. These results are stored in shared memory. Next step is moving the particles by wind field and turbulent diffusion, and testing for deposition. This step uses the interpolated weather prediction model outputs and the random numbers for calculation of turbulent motion and stochastic deposition. The final step is writing the changed particle information back to global memory.

Calculation and integration of activities on a rectangular grid is performed by the same way as in the sequential version, and it is calculated on the CPU, while the GPU is processing the next time steps in parallel. It should be noted that this step requires extra memory transfer between device and host and should be done as rarely as possible.

The kernel is configured to execute in 32 blocks, and with 256 threads in each block. The optimal number of threads in a block was found using the CUDA Occupancy Calculator, which is part of the CUDA SDK. All threads process multiple particles, since the number of particles may well exceed the number of threads.

The simulation is clearly limited by memory bandwidth, because there are only relatively few arithmetic operations to update a particle information. Therefore, the most important rule to optimize this simulation in CUDA is to follow the specific memory access pattern to achieve *coalesced* memory reads and writes. High multiprocessor occupancy (number of threads which are executed physically in parallel, compared to the maximum supported number of threads) is also desired to hide memory latency. The highest possible occupancy is 33% because of the high register requirement of the kernel, which is achieved by using 256 threads per block. Shared memory bank conflicts never arise since particles never interact with each other.

We performed simulations with various particle numbers on a 2.33 GHz Core 2 Duo CPU and on two video cards: GeForce 8800 GTS and GeForce 8800 GTX. Figure 11.18 shows the actual speedup gained using the graphics processors. There is no technological difference between the two cards, only computing power and memory speed. The ratio of the speedup with the GTS and the GTX cards well represents the performance difference between them. In both cases the speedup is higher as the particle number is increased. For optimal performance at least half million particles are required. If fewer particles are used, the GPU spends most of the time on initialization for the calculations, synchronizing execution, etc., while the useful calculations actually take less time. In a real application, however, one should use as many particles are allowed by the memory on the video card, which should be several millions of particles.

The speedup achieved is a result of many factors. The memory bandwidth between GPU and video card's RAM is approximately one order of magnitude higher than between CPU and PC's RAM. During GPU calculation access to physical constants and meteorological data is even faster, because constant and texture cache are used. Calculation is also accelerated by the instant trilinear interpolation provided by the GPU. Finally, the random number generation on the GPU is about two orders of magnitude faster than using the CPU.

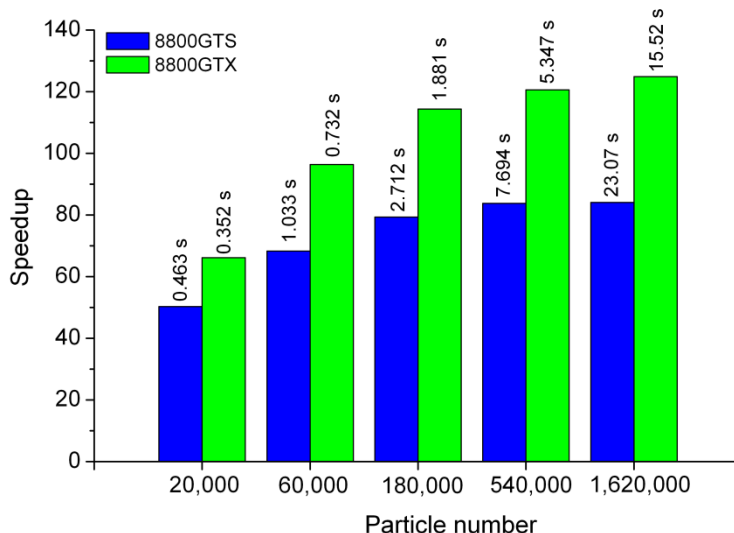


Figure 11.18: The speedup of the applications as a function of released particles using GeForce 8800 GTS and GeForce 8800 GTX video cards.

11.2.3.3. Eulerian model

Solving diffusion or advection-diffusion equations fits well to the architecture of CUDA. The basic ideas are the following. Concentrations of the species in a simulation can be stored in global memory on the device. We can assign computation of the next time level to a kernel function, assigning threads to compute individual grid points. The rectangular space represented by the grid points can easily be splitted to smaller parts, which can be assigned to blocks. Shared memory within a block utilized in the approximation of the spatial derivatives, because this computation requires data which belongs to neighboring grid points (and threads). Physical constants and other parameters of a simulation can be stored in the constant memory (Molnár et al., 2011).

Two very important performance guidelines must be followed to reach maximum performance: accessing (reading or writing) global memory should follow a *coalesced* access pattern, and accesses to the shared memory should be without bank conflicts. CUDA devices from the first generation have very strict rules for achieving coalesced memory access, which result in a computational solution for them and another one for the second generation. However, a solution which is optimized well for the first generation of devices should also run very efficiently on the devices of second generation with minor adjustments to some parameters.

Two different reaction-diffusion problems were chosen and solved using CUDA to illustrate the capability and efficiency of GPU computing. The first one is the pure diffusion, which presents the ‘core’ mechanism in all reaction-diffusion-advection related problems. The second example is an extension of the pure diffusion transport problem with advection. This arises in many areas, especially in air pollution, where the transport of air pollutants consist of two main transport phenomena (advection – transport by wind field and turbulent diffusion).

The first application is a simple diffusion problem without any reactions. Here a chemically inert compound diffused from the centre of the computational domain. During this process the diffusing species can reach outer regions. The simulation of this problem is essentially calculating the Laplacian operator on all of the grid points and updating concentrations every time step. Therefore, it is easier to review the computational solution and performance in this simple case before the main concepts can be applied to more complex simulations.

The main question in computing the Laplacian is how to split the computational job on the domain (grid) to smaller rectangular blocks, which will be assigned to thread blocks, where a single thread updates a single grid point. Using the spatial discretization scheme, data from nineteen grid points should be read to update one point, but since these are neighbouring points, data of every point will be read nineteen times (by its thread and its neighbours) while updating all of the grid. In order to avoid reading so many times from the slow global memory, data should be copied to the shared memory of a thread block. Using this stencil, a rectangular block will require an extra layer of grid points around it to allow computation on all points in the block. To read this data, one way is that after all threads read their corresponding grid points into shared memory, some threads read the extra layer.

The other way is that although all threads read their corresponding grid points to shared memory, the ones on the edge do not compute, and the blocks overlap in every direction. We found that the second approach is generally faster, however it results in a *read redundancy*: grid points where the blocks overlap will be read more than once in a single time step. This measure can be calculated by the following formula:

$$\text{read redundancy} = \frac{\text{width}}{\text{width} - 2} \cdot \frac{\text{height}}{\text{height} - 2} \cdot \frac{\text{depth}}{\text{depth} - 2}, \quad (11.6)$$

where *width*, *height* and *depth* are the dimensions of a block. If there is no overlap in a given direction (see later) then that factor can be eliminated in the formula.

We can also utilize the fact that block indices are only two dimensional in CUDA (though blocks themselves are three-dimensional). We cannot assign all the “blocks” of grid points to thread blocks at once, instead, we assign only a thin, one block wide layer, and the kernels iterate though the simulated space in the third dimension. Since the blocks must overlap, the last two *z*-layers of data can be kept in the shared memory instead of reading them again from global memory, as the blocks iterate though the space (Figure 3). We call this solution the simple “Shared” method because it utilizes the shared memory in a simple way. It is very similar to the 3D finite difference computation example in the CUDA SDK, but in our case the stencil uses off-axis elements, so we need shared memory for all *z*-layers in the block, not only for the central *z*-layer. Moreover, the Shared method fits only the second generation of CUDA devices, because all global memory accesses are uncoalesced according to the strict rules of the first generation of CUDA devices.

For first generation devices the thread blocks must iterate on the first dimension, and they must read and write global memory starting at an address multiple of 64 bytes, therefore the block width must be 16 (using 4-byte floats), to achieve coalesced access. Each block must use a wide tile of shared memory for $(1 + 2 \times 16) \times \text{height} \times \text{depth}$ elements. The extra shared memory is used as a streaming buffer for the global memory. In an iteration step data from the global memory is read to the second 16-element wide part of the shared memory. Then Laplacian can be computed on all elements of the first 16-element wide part, because the extra layer of data required on the left edge is provided from the previous step in the 1-element wide part, and the right edge is provided by the newly read data in the second 16-element wide part. After computing and writing the results back to global memory, the tile is moved to the right by 16 elements, and the iteration continues. The Moving Tiles method achieves coalesced memory access and it can be implemented without shared memory bank conflicts, because the block width is 16, which is equal to the number of shared memory banks. However, because of the high shared memory requirement less blocks can be allocated on a multiprocessor at once, limiting the performance for more complicated reaction-diffusion systems.

On the edge of the simulated space, the outermost grid points cannot be updated (the Laplacian cannot be computed), because they have no outer neighbours. Instead, these points are boundary points, their values are set according to the boundary conditions of the PDE before each time step. We use three separate kernels for updating these values on the left and right, top and bottom, and front and back sides of the simulated space, because the space is not necessarily cube shaped. Three additional kernels are updating the edges of the space parallel to the *x*, *y*, and *z* axes. Corners do not need values because the stencil does not use them. These kernels are not optimized because their job is very small compared to the Laplacian computation, they contribute approximately 2% to the computational time.

Our last example is an advection-diffusion problem, which has a great relevance in air pollution modelling. Solving diffusion-advection equations to describe the spread and/or transformation of air pollutants is a very important computational and environmental task. The numerical simulations must be obviously achieved faster than in real time in order to use them in decision support.

From the computational point of view this simulation is very similar to the simple diffusion problem, however, an extra advection term is added. Data read into the shared memory for Laplacian computation can be used to approximate first derivatives for advection. An upwind approximation was used to provide a stable solution. The parallel implementations achieve typical acceleration values in the order of 5–40 times compared to CPU using a single-threaded implementation on a 2.8 GHz desktop computer depending on the problem and parallelization strategy used.

Most of the models used in environmental protection and air quality management fall into Lagrangian and Eulerian types. Therefore, it is important to know the real advantage and drawback of the applied models (Figure 11.19). From results presented in this study, it is clearly seen that if we estimate the dispersion of pollutants from a strong point source in local scale a Lagrangian particle model should inevitably be used. This model has a main advantage that the positions of each particle are continuous functions in space. This can overcome the problem of steep concentration gradients arises near a point source, and the Lagrangian particle model can be used even in case of extremely low wind speed, where other models (Gaussian, Eulerian) simple fail and they cannot provide a stable and/or realistic solution. On the other hand, the main problem with this approach is that the each particle represents a given mass or activity (in case of radionuclides), therefore, it is very hard to obtain continuous physical quantity like concentration with small number of particles, increasing this number results in an increase in computational time. Using Lagrangian particle model to simulate the transport of air pollutants from multi-emission sources is practically impossible because of huge computational task. However, this task is really suitable for Eulerian models, and they can easily provide and calculate continuous quantities. Eulerian models can be predominantly used to calculate the transport of chemical species from multi-emission sources. In this framework the chemical reactions occurring between chemical species can be easily handled, because the chemical rate can be calculated from concentrations, which are prognostic variables in Eulerian models. Modelling of the chemical interactions between particles in Lagrangian models is very challenging task, and it involves consideration of the stochastic nature of chemical reactions. In conclusion, the model should be always chosen to a given air pollution problem to provide the accurate and cost efficient solution. Development of such cost efficient strategies requires very accurate calculations, and numerical simulations need a huge computational effort.

There are numerous solutions to address this issue. Parallelization of the models and using supercomputers, clusters, or grid systems to solve problems are a common technique. These systems are built by connecting numerous processors, either by some sort of direct link or by a network connection. Several computing centers can be connected to each other by the Internet, thus creating grids. We investigated a new parallel computational framework to solve environmental related problems using graphical processing unit. A stochastic Lagrangian particle model and an Eulerian model were developed on CUDA to estimate the transport and the transformation of the radionuclides from a single point source during hypothetical accidental releases. Our results show that parallel implementation achieves typical acceleration values in the order of a hundred times in case of Lagrangian model and tens of times in case of Eulerian model compared to CPU using a single-threaded implementation on a regular desktop computer (Figure 6). The relatively high speedup with no additional costs to maintain this parallel architecture could result in a wide usage of GPU for diversified environmental applications in the near future.

We should also mention some important aspects of this technology. In the past years, as this technology has developed, many papers have been published (for as review see Lee et al., 2010), and it seems that the “speedup” gained over general CPU solutions has become the measure of CUDA technology. However, one must be very careful to interpret such results correctly. There are numerous parameters that formulate the final performance gain over the CPU, such as the GPU type, clock frequency, number of CUDA cores, amount of memory, speed of memory on the video card, CPU type, CPU clock, host memory amount and speed, and most importantly, the implementation of the algorithm itself. These together make it almost impossible to predict a given computational speedup when ported to CUDA. Some of the published works show speedups of several hundred times. This is never the “magical” power of CUDA, it is always the result of the unoptimized CPU code which serves as the basis of comparison. Paper published by Lee et al., 2010 carries important information: you can achieve great optimizations on CPU if you have enough experience and expertise, bringing down the relative performance gain of GPU solutions. This can be close to what you could expect by looking at the raw hardware performance of CPUs and GPUs. However, the amount of computational and programming knowledge required to do so, is usually so large, that only computer scientists of specific fields can afford to learn them. This is why CUDA has gained much popularity among scientists from different fields: with relatively limited (but still advanced) knowledge of CPU and GPU programming, the CUDA solution is much faster than the CPU solution. This is the main advantage of CUDA (together with its cost-effectiveness).

We believe that using GPU – as a new computational tool – will revolutionize the environmental computing and can provide a new and cost efficient and effective technique in environmental protection. This system can be effectively used, and hence the most profitable would be in simulation of an accidental release of hazardous materials from industrial facilities (e.g., nuclear power plants). The recent accident at the Fukushima Nuclear Power Plant highlights the importance of predicting accidental release of toxic materials. Implementing a model using this easy-to-maintain and cost efficient computational framework in all facilities storing hazardous materials would be realistic and could help to decrease environmental consequences of possible future accidents.

Figure 11.19: Speedup of different applications on first and second generation video cards (GeForce 8800 GTX and GeForce GTX 275, respectively) compared to CPU (2.33 GHz Core 2).

References

- Baklanov A., Mahura A., Jaffé D., Thaning L., Bergman R., and Andres R.. 2002. *Atmospheric transport patterns and possible consequences for the European North after a nuclear accident* In: *Journal of Environmental Radioactivity*. 60. 23-48.
- Brandt J., Mikkelsen T., Thykier-Nielsen S., and Zlatev Z.. 1996. *Using a combination of two models in tracer simulations* In: *Mathematical and Computer Modelling*. 23. 99-115.
- Bryall D.B. and Maryon R.H.. 1998. *Validation of the UK MET office NAME model against the ETEX data set* In: *Atmospheric Environment*. 32. 4265–4276.
- Garcia-Menendez F. and Odman M.T.. 2011. *Adaptive grid use in air quality modelling* In: *Atmosphere*. 2. 484-509.
- Hart G., Tomlin A., Smith J., and Berzins M.. 1998. *Multi-scale atmospheric dispersion modelling by use of adaptive gridding techniques* In: *Environmental Monitoring and Assessment*. 52. 225–238.
- Horányi A., Ihász I., and Radnóti G.. 1996. *ARPEGE/ALADIN: A numerical Weather prediction model for Central-Europe with the participation of the Hungarian Meteorological Service* In: *Időjárás*. 100. 277-301.
- Lagzi I., Tomlin A. S., Turányi T., and Haszpra L.. 2009. *Modelling photochemical air pollutant formation in Hungary using an adaptive grid technique* In: *International Journal of Environment and Pollution*. 36. 44-58.
- Lagzi I., Kármán D., Tomlin A.S., Turányi T., and Haszpra L.. 2004. *Simulation of the dispersion of nuclear contamination using an adaptive Eulerian grid model* In: *Journal of Environmental Radioactivity*. 75. 59-82.
- Molnár F., Szakály T., Mészáros R., and Lagzi I.. 2010. *Air pollution modelling using a Graphics Processing Unit with CUDA* In: *Computer Physics Communication*. 181. 105-112.
- Molnár F., Izsák F., Mészáros R., and Lagzi I.. 2011. *Simulation of reaction-diffusion processes in three dimensions using CUDA* In: *Chemometrics and Intelligent Laboratory Systems*. 108. 76-85.
- Nasstrom J.S. and Pace J.C.. 1998. *Evaluation of the effect of meteorological data resolution on Lagrangian particle dispersion simulations using the ETEX experiment* In: *Atmospheric Environment*. 32. 4187–4194.
- Sorensen J.H.. 1998. *Sensitivity of the DERMA Long-range Gaussian dispersion model to meteorological input and diffusion parameters* In: *Atmospheric Environment*. 32. 4195–4206.

Chapter 12. Deposition of air pollutants

Deposition of air pollutants is an important loss of gases and aerosol particles from the atmosphere. At the same time, deposition processes of different air pollutants can cause various harmful effects both on ecosystems and built environment. Deposition of an air pollutant affects its atmospheric concentration as well as the state of the environment or human health (see Chapter 13). Therefore, it is an important factor in different types of atmospheric chemical-transport models, and surface exchange models.

The removal of gases and particulates from the atmosphere can occur by dry or wet forms (Figure 12.1). The importance of each deposition form varies with species and locations. Dry deposition is a continuous process, while wet removal can be realized only in the presence of precipitation. Therefore, despite of the dry process is slower than wet deposition, the accumulated removal quantity of a pollutant could be more important in case of dry deposition. Both the dry and wet depositions depend on the properties of the gases or particles and removal processes are governed by several environmental factors (Table 12.1).

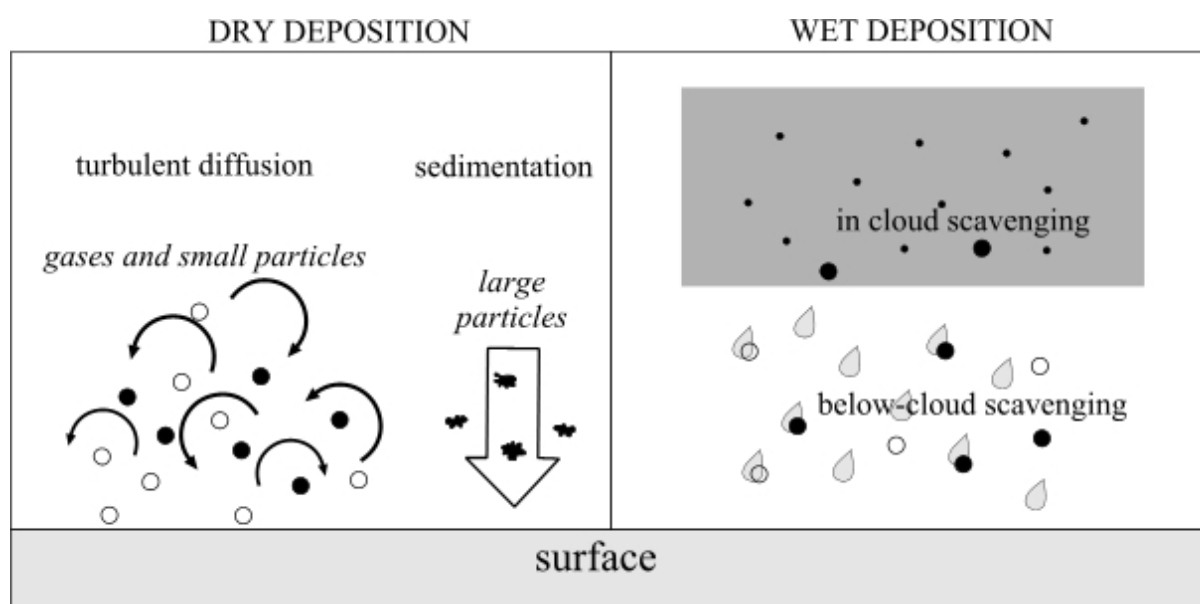


Figure 12.1: Dry and wet deposition processes in the atmosphere

Table 12.1: Factors affecting dry and wet deposition of gases and particles

	dry deposition	wet deposition
gases	near-surface concentration physical and chemical properties of tracer weather condition soil, surface, vegetation properties chemical reactions	gas-specific parameters cloud parameters precipitation
aerosol particles	particle properties near-surface concentration weather condition	particle properties cloud parameters precipitation

12.1. Dry deposition of trace gases

Exchange of trace gases between surface and the atmosphere is mainly governed by the turbulent diffusion. During this process gas transfer can be bi-direction depending on concentration profile of tracer in the near surface layer. If the concentration of a given species increases with height, the turbulent flux of the trace gas is directed from the atmosphere into the surface (deposition). Otherwise, an upward flux is generated (emission). The dry flux of trace gases is generally described by the following form:

$$F = -\overline{w'c'} \quad (12.1)$$

where w' and c' are the fluctuation of vertical wind components and the concentration of pollutant. The minus sign denotes that downward flux is negative. Here we assume stationarity and horizontal homogeneity of wind, air temperature, humidity and concentration of pollutant. Additionally, equation (12.1) is valid only if chemical sources and sinks are negligible. This means that the characteristic transport time (τ_t – the time, while the pollutant is transported from a z_r reference level to the surface) is much shorter than characteristic reaction time of the given pollutant (Foken et al., 1995). The layer, when this condition is satisfied, sometimes called constant flux layer.

Several micrometeorological measuring techniques are available for measuring the flux of tracers in this layer. Next to the flux measurements, detailed deposition models are also widely used to estimate the exchange of gases. In these models, the deposition flux of gases is calculated from the product of the concentration gradient of trace gas and the so-called deposition velocity.

12.1.1. Field measurements

In the last few decades, several micrometeorological methods to quantifying the trace gas exchange (deposition and emission) in the soil-surface-vegetation-atmosphere system have been developed (for example, eddy covariance method, relaxed eddy-accumulation method, aerodynamic profile method). For a review about these measuring methods see e.g. Foken et al. (1995) or Grünhage et al. (2000).

The eddy covariance method is an accurate direct method, which requires sophisticated, fast response sensors to measure simultaneously the fluctuations of wind velocity, air temperature, water vapour and the trace gas concentration. Eddy covariance technique is widely used for the determination of H_2O , CO_2 , SO_2 , O_3 , NO_2 fluxes in the turbulent surface layer. However, for some gases (e.g. NH_3), this technique is not available therefore other micrometeorological measuring methods must be applied. Flux data obtained from eddy covariance measurements by different fast response sensors requires further corrections (e.g. correction of density fluctuation, sensor separation correction, etc.).

The relaxed eddy accumulation method (REA) was proposed by Businger and Oncley (1990). This method based on a conditional sampling of pollutants in the function of vertical wind velocity. The air samples are taken with a constant flow rate into two separate reservoirs for updraft and downdraft air sample, and the flux can be calculated by the measurement of pollutant's concentration in each reservoir. This method is generally used for gases (e.g. for ammonia – NH_3), when fast response sensor is not available (see e.g. Hensen et al., 2009).

The fluxes of gases can also be calculated by the measured vertical profiles of concentration, wind, temperature and humidity. This aerodynamic profile method is based on the Monin–Obukhov similarity theory (see e.g. Foken, 2006), which describe the turbulent transfer of heat, momentum and scalar quantities in the surface layer. Parameters used in this theory can be derived from the measurement of wind speed, temperature, humidity and trace gas concentration at different levels over the surface (Figure 12.2). A simplified version of this measuring technique is the gradient method, when measurements are carried out at only two levels above the surface.

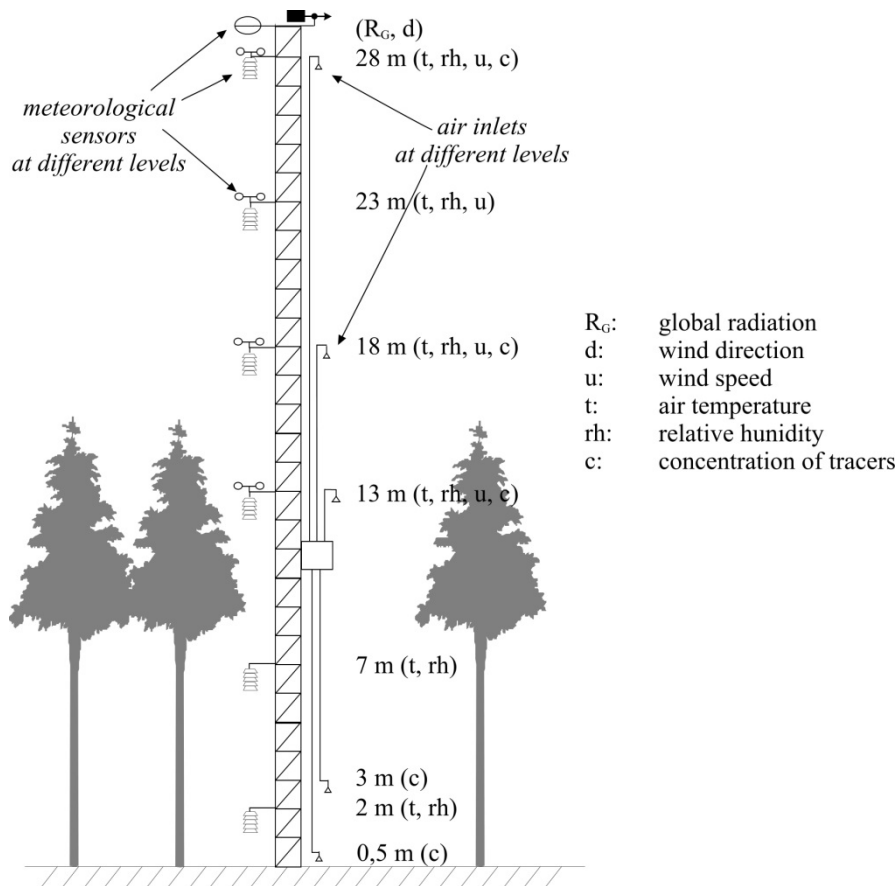


Figure 12.2: A schematic picture of a micrometeorological measuring system in a pine forest, in Mátra Mountain, Hungary, used for the calculation of trace gas fluxes by the aerodynamic profile method.

12.1.2. Deposition/exchange models

Gaseous dry deposition models require various types of input data for the estimation of the dry flux of a trace gas. For flux calculation, the concentration of tracer must be known. Airborne concentration of pollutants a few meters above the ground or over the vegetation can be obtained from both field measurements or from the results of a dispersion model. Other input data depends on the complexity of the model, but generally contain several meteorological elements, physical and chemical properties of pollutant, soil-, surface- and vegetation-specific parameters.

The dry deposition process can be interpreted as an analogy of Ohm's law. Based on this approach, the flux is proportional to the concentration gradients. This proportionality can be expressed by the deposition velocity:

$$F = -v_d [c(z_{ref}) - c(0)] \quad (12.2)$$

where v_d is the deposition velocity, $c(z_{ref})$ and $c(0)$ are the concentration of trace gas at a reference level above the surface and at the surface, respectively. This latter term is zero for a few gases, which have no emission from the surface, such as ozone (O_3), sulphur-dioxide (SO_2) or nitric acid (HNO_3).

The deposition can be estimated by the widely used „big-leaf” model, in which the deposition velocity is defined as the inverse of the sum of the atmospheric and surface resistances:

$$v_d = (R_a + R_b + R_c)^{-1}, \quad (12.3)$$

where R_a , R_b , and R_c are the aerodynamic resistance, the quasi-laminar boundary layer resistance, and the canopy resistance, respectively. Each term are given by less or more detailed parameterization in different models.

The aerodynamic resistance (R_a) describe the turbulent processes over the surface and is independent on the species. The boundary-layer resistance (R_b) affects the deposition in a very thin layer of air contact with the surface elements, where the transfer occurs by molecular diffusivity. These terms can be calculated for example using the Monin–Obukhov similarity theory taking into account atmospheric stability (details can be found e.g. in Nemitz et al., 2009).

In the parameterization of the deposition over vegetated surface, the canopy resistance (R_c) is the most complex part of this resistance network. It is generally contains different resistances, which represent the different pathways of pollutants in the vegetation:

$$R_c = \frac{1}{\{R_{st} + R_m\}^{-1} + \{R_{cut}\}^{-1} + \{R_{ac} + R_{soil}\}^{-1}}, \quad (12.4)$$

where R_{st} , R_m , R_{cut} , R_{ac} and R_{soil} are the stomatal, mesophyll, cuticular, in-canopy aerodynamic and soil resistances, respectively. The stomatal resistance is a key parameter in deposition modelling, which is affected in different degree by both the weather conditions and several plant and soil characteristics. The scheme of this simple resistance network can be seen in Figure 12.3.

Considering, that the flux is constant between the reference height and the top of the canopy, the total ozone flux can be written as follows:

$$F_t = -C_r (R_a + R_b + R_c)^{-1} = -C_c R_c^{-1}, \quad (12.5)$$

where C_r is the concentration at the measuring height, and C_c is the concentration at the top of the canopy, defined as a level, where the flux divides into stomatal (F_{st}) and non-stomatal (F_{ns}) part (Cieslik, 2004):

$$F_t = F_{st} + F_{ns} = -C_c R_{st}^{-1} - C_c R_{ns}^{-1}, \quad (12.6)$$

where R_{st} is the stomatal resistance and R_{ns} is the non-stomatal resistance covering all deposition pathways but stomatal. According to Equations (12.5) and (12.6), the stomatal flux is calculated separately:

$$F_{st} = -C_c R_{st}^{-1} = -\frac{R_c}{(R_a + R_b + R_c) R_{st}} C_r, \quad (12.7)$$

therefore:

$$F_{st} = F_t R_c R_{st}^{-1}. \quad (12.8)$$

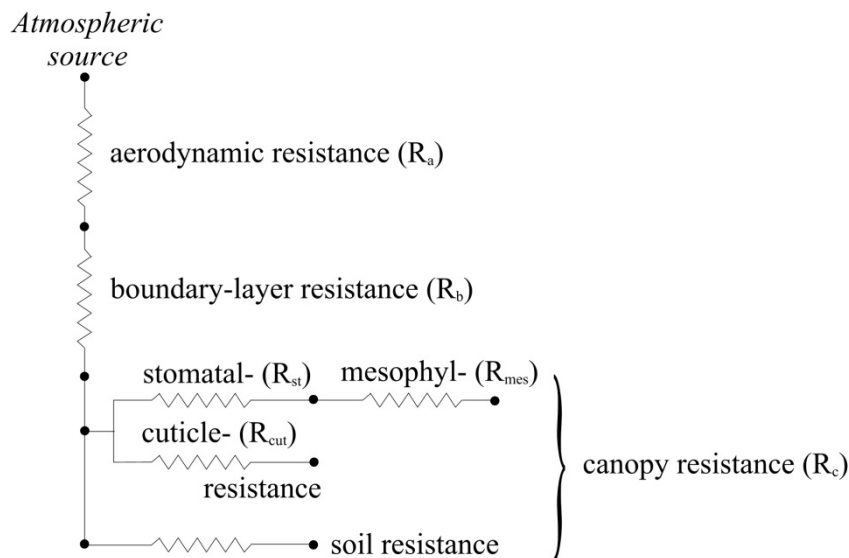


Figure 12.3: A widely used simple resistance network in dry deposition models

The main limitation of these deposition models lies in the uncertainty and variability of the model input data, such as the time- and species-dependent parameters. Therefore, these parameters may give rise to significant uncertainties in the simulation results, and it is very important to know the effect of the individual input parameters on model output. Nonlinear models, such as most of the deposition models, can magnify the uncertainties of some parameters and damp others. In many cases, the models may over- or underestimate the fluxes through the calculation of deposition velocity (Mészáros et al., 2009a).

12.1.3. Some results

A typical diurnal course of surface ozone flux obtained from eddy covariance measurements over grassland can be seen in Figure 12.4. (the negative flux means deposition). A pronounced difference appears between night-time and daytime fluxes. At night-time, due to the stable stratification in the near surface layer, the turbulence is weak, therefore no large flux can be observed. Night-time flux is generally no change significantly in time. After sunrise, the stratification becomes unstable, resulting increased flux. Over vegetated surfaces, daytime flux can be more explicit, when environmental conditions are optimal for exchange processes through the plants. At the same time, several environmental factors (e.g. high water stress, low turbulence etc.) can reduce the daytime deposition flux.

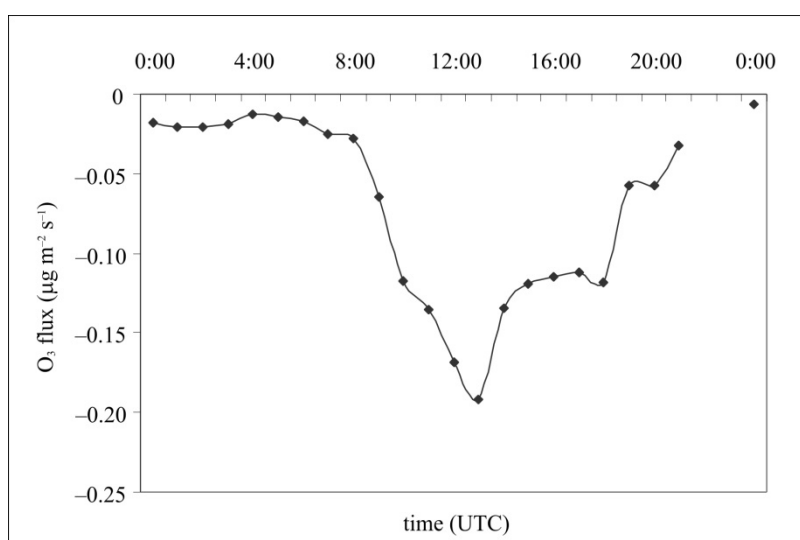


Figure 12.4: Typical daily course of the dry deposition flux of ozone (O₃). Results are obtained from eddy covariance measurements over managed grassland (Braunschweig, Germany), on 7 June, 2000.

Beside weather conditions, the agricultural activities (e.g. cut, fertilization) can also significantly influenced the O₃ fluxes. During a measuring campaign over grassland (Mészáros et al., 2009b), three different phases of vegetation were covered to describe the ozone flux under different conditions: tall grass canopy before cut, short grass after cut, and re-growing vegetation after fertilization. Results of ozone flux measurements indicated that daytime ozone flux decreased after cut, but to a smaller extent than would be expected due to the drastic reduction of *Leaf area index (LAI)*, which decreased both stomatal and cuticular uptake of the ozone. However, at the same time, with decreasing vegetation height and *LAI*, the importance of ground flux and chemical reactions are increased. After fertilization, nitric oxide (NO) emissions are assumed to have increased (inferred by greatly increased soil nitrate levels) providing a further (chemical) sink for ozone thereby affecting the deposition. These complex, highly nonlinear effects reveal the importance of canopy structure and non-stomatal pathways on ozone fluxes.

Similar diurnal pattern of ozone flux was found over pine forest (Figure 12.5). The dry flux of the ozone was measured during a field campaign by eddy covariance method in May, 1998 at Nyírjes station (Mátra Mountain) and the dry deposition velocity of ozone (Figure 12.6) was derived from these measurements. Based on the measurements the average values of deposition velocity for ozone ranges between 0.1 and 0.3 cm s⁻¹ in daytime, and was lower than 0.1 cm s⁻¹ at night-time.

Next to the micrometeorological measurements, detailed model simulations were also performed for the estimation of the dry deposition of ozone. Based on the big-leaf models a one-dimensional ozone dry deposition model was developed for continental climate area. In this model, analogously to Ohm's law, the deposition flux is inferred by multiplying the concentration and the deposition velocity of ozone. The deposition velocity is related to different resistances in the soil-plant-atmosphere system (see Chapter 12.1.2). First investigations were performed for a pine forest (Figure 12.5 and 12.6) in May, 1998.

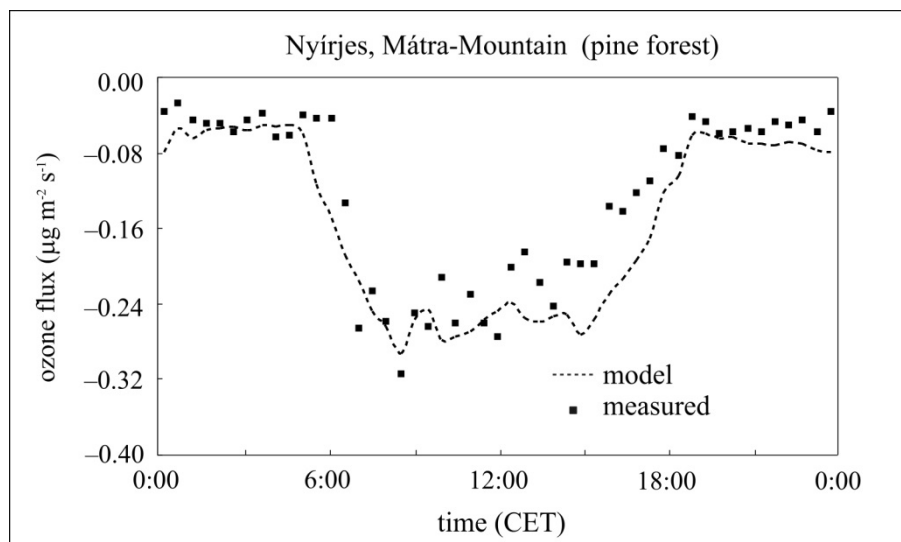


Figure 12.5. Average daily courses of measured and modelled dry deposition flux of ozone (O_3). Results are obtained from eddy covariance measurements over pine forest (Nyírjes, Hungary) and model simulations.

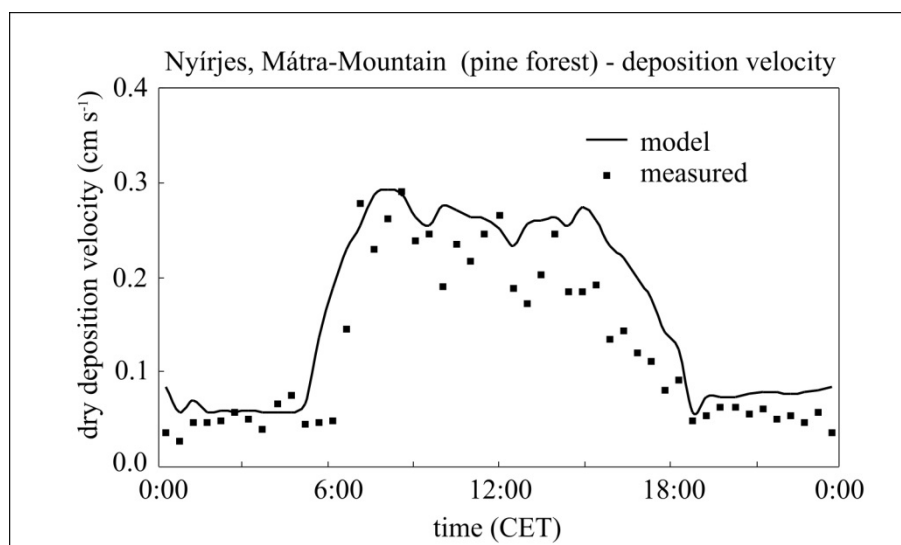


Figure 12.6: Average daily courses of measured and modelled dry deposition velocity of ozone (O_3). Results are obtained from eddy covariance measurements over pine forest (Nyírjes, Hungary) and model simulations.

The dry deposition is strongly depending on the season and the type of the surface. Therefore, model simulations were extended to a longer period and for grassland, too. Figure 12.7 and 12.8 show monthly averages of daytime and night-time deposition velocity for ozone over pine forest and grassland, respectively. Average daytime values are higher (between about 0.25 and 0.35 cm s^{-1}) over forest during the vegetation period. In winter, under mainly stable stratification the typical daytime deposition velocities are between 0.1 to 0.2 cm s^{-1} . Above grassland, during the vegetation period, the daytime dry deposition velocities vary between 0.05 and 0.15 cm s^{-1} . Night-time deposition is lower, than daytime values in all cases.

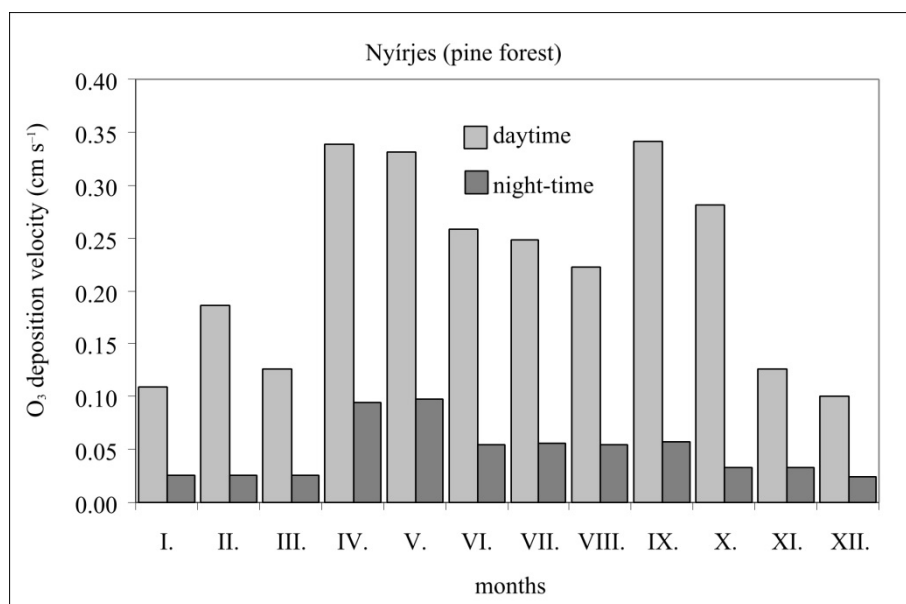


Figure 12.7: Monthly averages of daytime and night-time deposition velocity for ozone (O₃) in 1998 over pine forest (Nyirjes, Mátra Mountain). Results are obtained from model simulations.

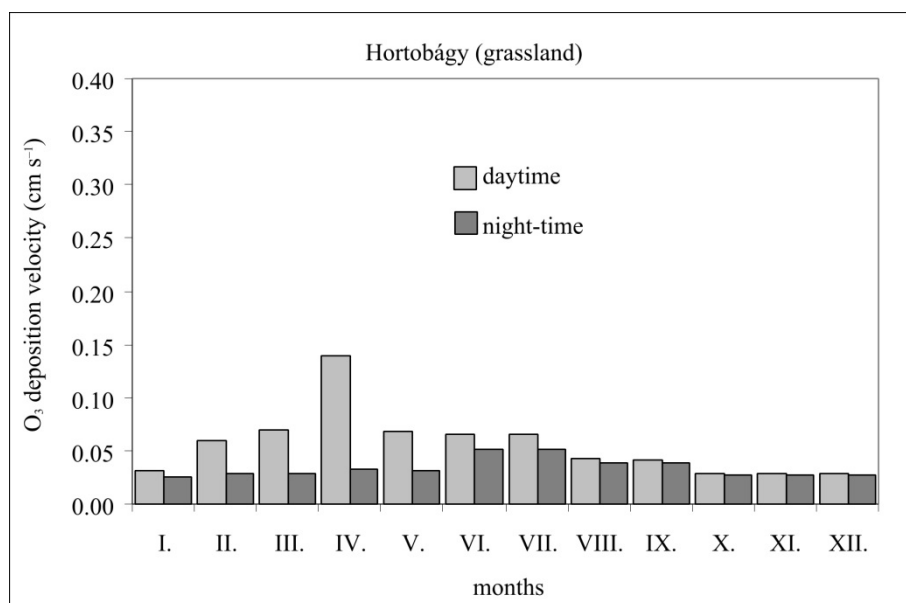


Figure 12.8: Monthly averages of daytime and night-time deposition velocity for ozone (O₃) in 2000 over grassland (Hortobágy). Results are obtained from model simulations.

Due to the higher leaf area index of the vegetation, as well as the stronger turbulence over the canopy, the deposition velocity generally higher in case of forest than for grass.

Dry deposition of ozone shows a typical temporal pattern. Both daily and yearly time series experienced a dual maximum. During the year, the greater values generally appear in late spring and in the beginning of autumn, while during the day in the morning, and afternoon. In winter and in night-time too, the stable stratification blocks the deposition. In summer-time period in the year, and in noon-time period in the day the higher water vapour deficit can also decrease the fluxes.

Deposition velocity of ozone has also been estimated by a deposition model using a regular grid (0.025 × 0.0375 degree resolution) over Hungary. The input meteorological datasets (air temperature, relative humidity, cloudiness, wind speed and air pressure) were taken from the ALADIN meso-scale limited area numerical weather prediction model used by the Hungarian Meteorological Service. Spatial distribution of deposition velocity and total dry flux

of the ozone can be seen in Figure 12.9 and 12.10, respectively for July, 1998. The land surface was categorised into 11 land uses, and 5 soil types. Each land use category was associated with a seasonal pattern of vegetation parameters, stomatal response characteristics and other resistance parameters. In Hungary, in case of vegetation-covered surface, the ozone fluxes mainly depend on soil water content (Mészáros, 2009a). This impact prevails in day-time, when ozone transferred through the stomata, and it is negligible in night-time.

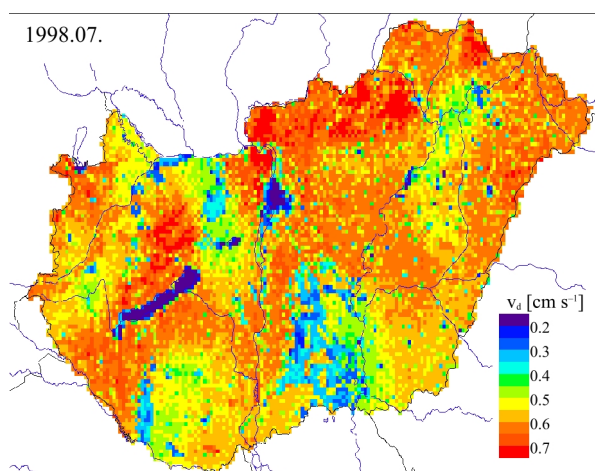


Figure 12.9: Average daytime deposition velocity for ozone (O_3) in July 1998 over Hungary. Results are obtained from model simulations.

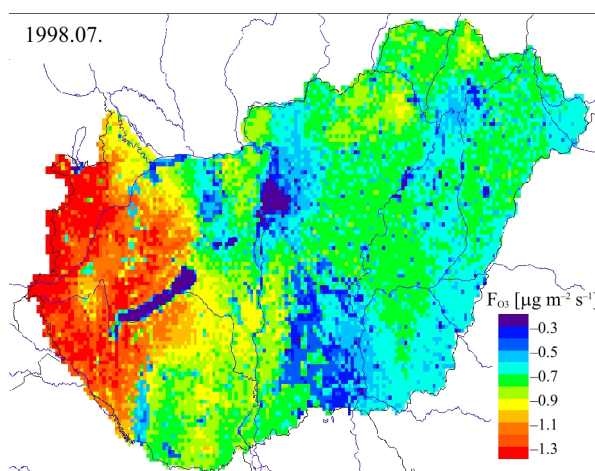


Figure 12.10: Average daytime deposition flux of the ozone (O_3) in July 1998 over Hungary. Results are obtained from model simulations. (Negative sign denotes that the flux is downward.)

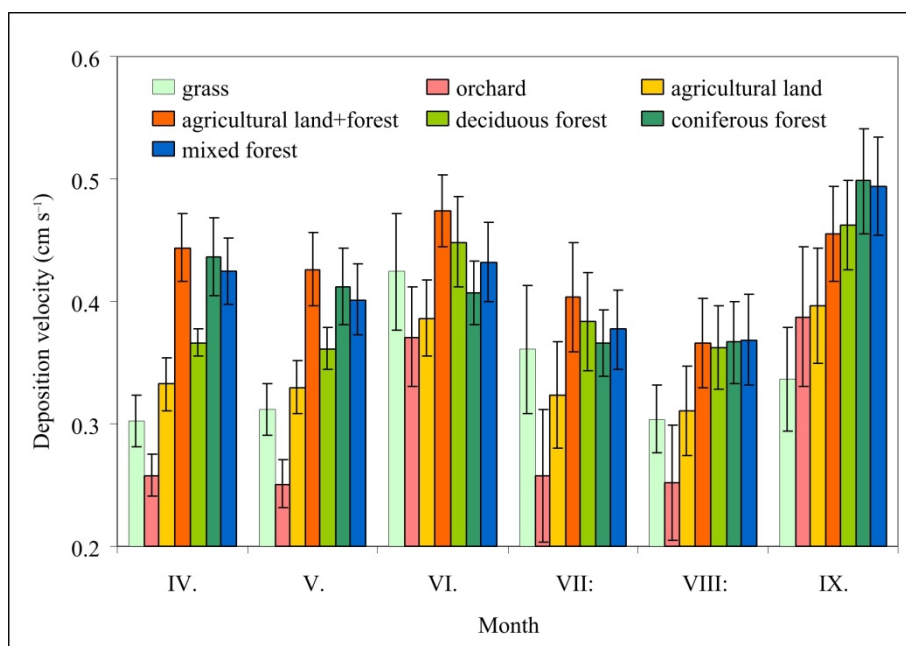


Figure 12.11: Monthly averaged deposition velocities with standard deviations at 12 UTC over different vegetation types (grass, orchard, agricultural land, agricultural land+forest, deciduous forest, coniferous forest, mixed forest) over the model grid.

Temporal variability of daytime ozone deposition velocity during vegetation period is presented in Figure 12.11 for different vegetation types (grass, orchard, agricultural land, agricultural land+forest, deciduous forest, coniferous forest, mixed forest). According to different plant physiology, and characteristics, there are significant differences among deposition velocities in each month even as over each surface type. Due to the plant growth (higher leaf area index), and the optimal environmental conditions for vegetation (higher temperature together with sufficient soil water content), generally higher values occur in June. However, for coniferous forest, higher deposition velocity values were detected in spring than in summer. In this case no significant changes in leaf area index between each period, at the same time the lower temperature in April and in May is more favourable for the stomatal uptake of this type of vegetation. These physiological effects can also be observable less in case of mixed forest, and mixed agricultural land and forest. Decreasing soil water content (due to the warmer period of the year without precipitation) in July and August in 2007 decreased the deposition velocities in all cases. In contrast of this, in September, the values were raised because the soil water content was increased again (for more details see Czender et al., 2009).

12.2. Dry deposition of aerosol particles

12.2.1. Field measurements

Particle dry deposition measurements are usually performed by micrometeorological methods (gradient method, eddy covariance method) and throughfall method (Garland, 2001). Applied micrometeorological methods are similar as in case of gases (12.1.1). The throughfall method is generally used in case of forest canopy for quantification of soil load (Draaijers et al., 1996).

12.2.2. Modelling the dry deposition of particles

Dry deposition of particles is highly depends on their characteristic size. Smaller particles deposited similarly as gases, while removal of larger ones is mainly governed by gravitational settling (sedimentation). Dry deposition processes for particles with a size between 10^{-1} and $1 \mu\text{m}$ are less efficient.

The dry deposition velocity after can be written as (see e.g. Sportisse, 2007):

$$v_d = v_g + \frac{1}{R_a + R_b + v_g R_a R_b}, \quad (12.9)$$

where v_g is the gravitational settling velocity (or terminal settling velocity), and the resistance terms R_a , and R_b are the same term as for gases (see above). As we assume that all deposited particles stick to the surface, the surface resistance (R_c) is zero for particles.

The settling velocity (v_g) can be derived as:

$$v_g = \frac{\rho_p d_p^2 g C}{18\eta}, \quad (12.10)$$

where ρ_p is the density of the particle, d_p is the particle diameter (assuming a spherical particle), g is the acceleration of gravity, C is a correction factor and η is the viscosity coefficient of air.

12.3. Modelling of wet deposition

Precipitation cleanses the air by capturing pollutants and depositing them onto the surface. The efficiency of this process can be expressed by the fractional depletion rate of pollutant concentrations in the air. This rate is generally characterized by the so-called scavenging coefficient. During the parameterization of wet deposition (or wet scavenging) in-cloud scavenging (rainout) and below-cloud scavenging (washout) are usually distinguished. However, for a correct estimation of wet deposition, explicit information about cloud and precipitation water at all model levels would be required. Instead of these complex parameterization schemes (see e.g. Sportisse, 2007), the wet deposition is often estimated by a simple method in chemical transport models. The species dependent scavenging coefficient (Λ in s^{-1}) can take the simple form:

$$\Lambda = AP^B, \quad (12.11)$$

where P is the rate of rainfall (in $mm\ h^{-1}$) and A and B are constants for a specific gas or aerosol particles. In some models A and B vary also in the function of scavenging type (rainout, washout), or in case of aerosol particles in the function of particle radius (Baklanov and Sørensen, 2001).

As the rain intensity is usually a very uncertain parameter, a very simple rain-out type method was proposed by Pudykiewitz (1989) is based on a statistical parameterization using relative humidity data. In this approach, the wet removal is described by the following relation:

$$W = \begin{cases} 0 & \text{for } RH < RH_0 \\ \Lambda \frac{RH - RH_0}{RH_s - RH_0} & \text{for } RH \geq RH_0 \end{cases}, \quad (12.12)$$

where RH , RH_0 and RH_s are the actual, the threshold and the saturated values of relative humidity, respectively and Λ is the scavenging coefficient. A suggested value for RH_0 is 80%, which means, that wet deposition is only considered in the model, if the relative humidity is larger than 80%.

Wet deposition is the major sink process of aerosol particles (see also Chapter 9.). Particles are incorporated into cloud droplets and precipitation elements by several mechanisms. Some paper separates these processes into two main groups, which are the nucleation scavenging and impactation scavenging (e.g. Tost et al., 2006). In the initial phase of hydrometeor formation the nucleation scavenging of aerosol particles serve as cloud condensation nuclei (CCN) or ice nuclei (IN). In contrast to these mechanisms, impactation scavenging is a process, when aerosol particles collide with and stick to existing cloud droplets, or precipitation elements (e.g. raindrops, snow crystals).

The scavenging of atmospheric gases contains several processes. After their diffusion to the surface of hydrometeors, the gas molecules become dissolved in liquid drops or in a quasi-liquid layer at the surface of ice crystals. In the final step of scavenging mechanism, gases diffuse inside the hydrometeors. Detailed models of gas scavenging can be found for example in Sportisse and du Bois (2002) and Sportisse and Djouad (2003).

12.3.1. Wet deposition in Europe

One of the main objectives of EMEP (European Monitoring and Evaluation Programme) is to provide information about deposition of different air pollutants, like acidifying pollutants, heavy metals (HM) or persistence organic compounds (POPs) (www.emep.int). Results of the European scale harmonized monitoring network and model simulations show large reductions in deposition of sulphur species during the last decades. However, orographic effects can lead to form local maxima in wet deposition. Due to high annual precipitation amounts, the wet deposition is typically high in southern Norway and the region around the Alps. Wet deposition of nitrogen ranges from less than $1 \text{ kg N ha}^{-1} \text{ yr}^{-1}$ to more than $20 \text{ kg N ha}^{-1} \text{ yr}^{-1}$. Deposition of oxidized nitrogen is generally somewhat higher than reduced nitrogen in Scandinavia and the Mediterranean, except for a few sites influenced by nearby agriculture. However, in the Benelux area and in Ireland, the contribution of ammonium deposition exceeds that of nitrate, reflecting regional agricultural sources of ammonia (Tørseth et al., 2012)

The wet deposition of calcium in Europe is significantly influenced by Saharan dust. Wet deposition rates exceeding $10 \text{ kg Ca ha}^{-1} \text{ yr}^{-1}$ are observed at sites in Spain, Portugal, Italy, Serbia and Croatia. Sites with high precipitation amounts located close to the sea also experience high rates of wet deposition due to sea salt calcium. (Hjellbrekke and Fjæraa, 2011).

Change of heavy metal deposition varied over the European countries. However, both modelling results and observations showed that wet deposition fluxes of both lead, cadmium and mercury are decreased between 1990 and 2010 (EMEP, 2012).

References

- Baklanov A. and Sørensen J.H.. 2001. *Parameterisation of Radionuclide Deposition in Atmospheric Long-Range Transport Modelling In: Physics and Chemistry of the Earth B.* No. 26.. 10. 787-799.
- Businger J.A. and Oncley S.P.. 1990. *Flux measurements with conditional sampling In: Journal of atmospheric and oceanic technology.* 7. 349–352.
- Cieslik S.A.. 2004. *Ozone uptake by various surface types: a comparison between dose and exposure In: Atmospheric Environment.* 38. 2409–2420.
- Czender Cs., Komjáthy E., Mészáros R., and Lagzi I.. 2009. *Spatial and temporal variability of ozone deposition In: Advances in Science and Research.* 3. 5-7.
- Draaijers G.P.J., Erisman J.W., Spranger T., and Wyers G.P.. 1996. *The application of throughfall measurements for atmospheric deposition modelling In: Atmospheric Environment.* No. 30.. 19. 3349-3361.
- Foken T., Dlugi R., and Kramm G.. 1995. *On the determination of dry deposition and emission of gaseous compounds at the biosphere-atmosphere interface In: Meteorologische Zeitschrift.* 30. 346-360.
- Foken T.. 2006. *50 years of the Monin-Obukhov similarity theory In: Boundary-Layer Meteorology.* 119. 431–447.
- Garland J.A.. 2001. *On the size dependence of particle deposition. Water, Air, and Soil Pollution: Focus.* 1. 323–332.
- Grünhage L., Haenel H-D., and Jäger H-J.. 2000. *The exchange of ozone between vegetation and atmosphere: micrometeorological measurement techniques and models In: Environmental Pollution.* 109. 373–392.
- Hensen A., Nemitz E., Flynn M.J., Blatter A., Jones S.K., Sørensen L.L., Hensen B., Pryor S.C., Jensen B., Otjes R.P., Cobussen J., Loubet B., Erisman J.W., Gallagher M.W., Neftel A., and Sutton M.A.. 2009. *Inter-comparison of ammonia fluxes obtained using the Relaxed Eddy Accumulation technique In: Biogeosciences.* 6. 2575–2588.
- Hjellbrekke A.-G. and Fjæraa A.M.. 2011. *Data Report 2009, Acidifying and eutrophying compounds and particulate matter. EMEP/CCC-Report.* Norwegian Institute for Air Research, Kjeller. 1.

- Mészáros R., Zsély I.Gy., Szinyei D., Vincze Cs., and Lagzi I.. 2009a. *Sensitivity analysis of an ozone deposition model In: Atmospheric Environment*. 43. 663-672.
- Mészáros R., Horváth L., Weidinger T., Neftel A., Nemitz E., Dämmgen U., Cellier P., and Loubet B.. 2009. *Measurement and modelling ozone fluxes over a cut and fertilized grassland In: Biogeosciences*. 6. 1987–1999.
- Nemitz E., Hargreaves K. J., Neftel A., Loubet B., Cellier P., Dorsey J. R., Flynn M., Hensen A., Weidinger T., Mészáros R., Horváth L., Dämmgen U., Frühauf C., Löpmeier, F.J., Gallagher M.W., and Sutton M.A.. 2009. *Intercomparison and assessment of turbulent and physiological exchange parameters of grassland In: Biogeosciences*. 6. 1445–1466.
- J. Pudykiewicz. 1989. *Simulation of the Chernobyl dispersion with a 3-D hemispheric tracer model*. Tellus. 41B. 391–412.
- Sportisse B. and Du Bois L.. 2002. *Numerical and theoretical investigation of a simplified model for the parameterization of below-cloud scavenging by falling raindrops*. Atmospheric Environment. 36. 5719–5727.
- Sportisse B. and Djouad R.. 2003. *Mathematical investigation of mass transfer for atmospheric pollutants into a fixed droplet with aqueous chemistry*. Journal of Geophysical Research. 108 (D2). 4073.
- Sportisse B.. 2007. *A review of parameterizations for modelling dry deposition and scavenging of radionuclides*. Atmospheric Environment. 41. 2683–2698.
- Tørseth K., Aas W., Breivik K., Fjæraa A.M., Fiebig M., Hjellbrekke A. G., Lund Myhre C., Solberg S., and Yttri K. E.. 2012. *Introduction to the European Monitoring and Evaluation Programme (EMEP) and observed atmospheric composition change during 1972–2009*. Atmospheric Chemistry and Physics. 12. 5447–5481.
- Tost H., Jöckel P., Kerkweg A., Sander R., and Lelieveld J.. 2006. *Technical note: a new comprehensive SCAVenging submodel for global atmospheric chemistry modelling*. Atmospheric Chemistry and Physics. 6. 565–574.
- Travnikov O., Ilyin I., Rozovskaya O., Varygina M., Aas W., Uggerud H.T., Mareckova K., and Wankmueller R.. 2012. *Long-term Changes of Heavy Metal Transboundary Pollution of the Environment (1990-2010)*. EMEP Status Report. 2/2012.

<http://www.emep.int>.

Chapter 13. Environmental effects of air pollution

During the first part of the 20th century, due to the dramatically increasing emission of air pollutants at the same time, in the absence of environmental protection technologies, several acute air pollution episodes were formed in some countries. One of the first air pollution disasters is occurred in a heavily industrialised area of Belgium. In December 1930, during the Meuse Valley fog event, the stable atmospheric conditions and industrial pollution from steel mills, coke ovens, foundries, and smelters contributed to the significant accumulation of air pollutants including sulphur dioxide (SO₂) sulphuric acid, and fluoride gases. Due to this extremely polluted air, more than 60 people died (Nemery et al., 2001). Similarly, the stable atmospheric stratification and the strong pollution from intensive industrial activity and coal-fired home led to extreme air pollution episode in Donora (United States) between 27 October and 30 October 1948. Due to this event, in the town with a population of 14000, 20 deaths, 400 hospitalizations and about 6000 respiratory symptoms were reported (Helfand et al., 2001). The London “Great Killer Fog” event in December 1952 was a consequence of the combination of coal burning during residential heating and industrial production and the unfavourable weather situation. This lethal fog in London resulted in about 3000 more deaths than normal during the first 3 weeks of December 1952, and based on the estimations, about 12000 excess deaths occurred from December 1952 and February 1953 (Bell and Davis, 2001).

Another harmful effect of increased emission of air pollutants was also recognized in the 20th century. The term “acid rain” was already introduced in 1872 by Robert Angus Smith, an English scientist, who experienced that acidic precipitation could damage plants and materials. However, acid rain was considered as a serious environmental problem only in the 1970s, when scientists observed the increase in acidity of some lakes and streams. At the same time, it became clear that the effects of air pollutants could be occurred far from the emission sources due to their long-range transport in the atmosphere.

In the last few decades, due to the emission reduction strategies and legislation, and at the same time the decline in industrial production, air quality has improved in several countries. Even so, air pollution and its effects on the environment are still severe environmental problems, particularly as some pollutants may even have long-term effects. Moreover, in some other parts of the world (especially in rapidly developing Asian countries), the situation becomes more severe due the dramatic increases in emission (Figure 13.1). Therefore, continuous monitoring of air quality by measurements and model simulations are essential.

In this chapter, we present some aspects about the effect of air pollution on the environment and the human health.

13.1. The role of each pollutant

Each pollutants emitted to the atmosphere can affect directly or indirectly the human health. Along with harming human health, air pollution can cause a variety of environmental effects, such as acid rain, eutrophication¹, effects on wildlife, ozone depletion, crop and forest damages, global climate change.

Some pollutants can also play important role in weather situations (e.g. reduction of visibility, forming of clouds and precipitation, modification of radiation budget etc.). At the same time, the state of the atmosphere is also affects the degree of air pollution through several processes (e.g. photochemical activity, transport and deposition processes etc.). Table 13.1 summarizes the possible effects of some important pollutants on the human health and on the environment.

¹ Explosive algae growth due to high concentration of nitrogen and phosphorus, which can deplete oxygen in water.

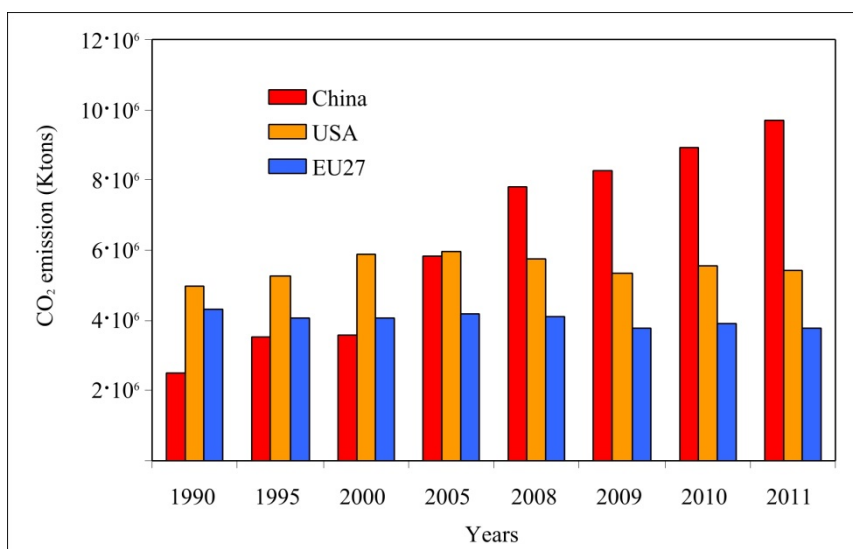


Figure 13.1: Yearly CO₂ emission between 1990 and 2011 in China, USA and EU27. Source of data: <http://edgar.jrc.ec.europa.eu>

Table 13.1: Effects of some air pollutants on human health and on environment

Air pollutants	Effects on human health	Effects on environment
Carbon monoxide (CO)	headache, reduced mental alertness, heart attack, cardiovascular diseases, impaired foetal development, death	contribute to the formation of photo-chemical smog
Sulphur dioxide (SO ₂)	eye irritation, breathing problems, cardiovascular diseases	formation of acid rain, visibility reduction, plant damages
Nitrogen dioxide (NO ₂)	irritation of the lung, respiratory symptoms, susceptibility to respiratory infections, stroke	contribute to the formation of photo-chemical smog, formation of acid rain, visibility reduction, water quality deterioration,
Ozone (O ₃)	respiratory symptoms, eye irritation, asthma	plant and ecosystem damage, visible injury, decreased productivity, crop yield, indirect effect on global warming
Particulate matter	asthma, cardiovascular effects,	visibility impairment, impacts on trace gas cycles,

	lung damage, allergic disease	cloud and fog formation, absorption and scattering radiation
--	----------------------------------	-----------------------------------------------------------------

13.1.1. Carbon monoxide (CO)

Carbon monoxide forms, when carbon in fuel is not burned completely (see more about CO emission in Chapter 2). CO is a colourless, tasteless, odourless and non-irritating gas. It can enter the bloodstream through the lungs and forms carboxyhemoglobin. High concentration of carboxyhemoglobin could be poisonous. CO poisoning cover a wide range of symptoms, depending on severity of exposure, such as headache, dizziness, weakness, nausea, vomiting, disorientation, confusion, collapse and coma (Raub and Benignus, 2002).

Due to the seasonal variation of CO emission and the weather conditions, CO concentration generally higher in winter, and lower in summer period (Figure 13.2). Based on the measurements carried out in Budapest downtown, in 2010, the concentration of carbon monoxide did not reach the occupational exposure limit.

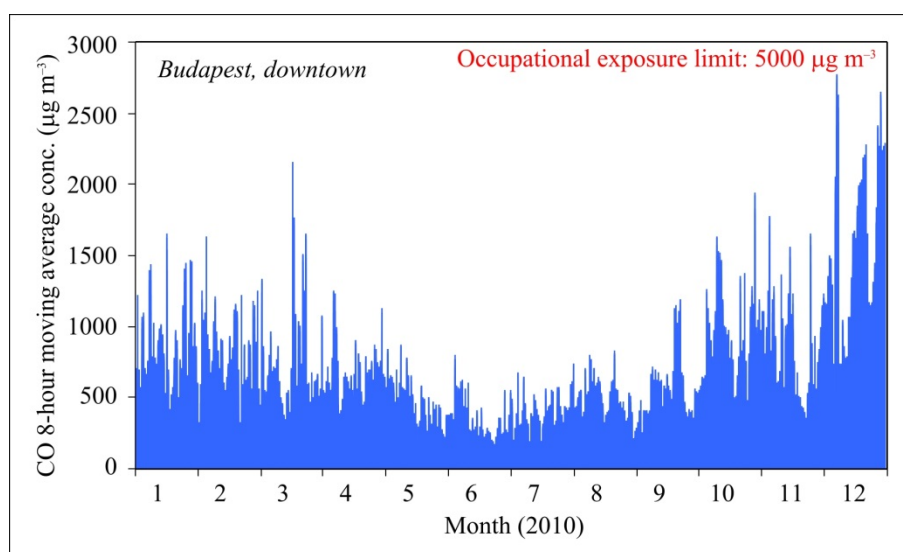


Figure 13.2: 8-hour moving average concentrations of carbon monoxide in Budapest, downtown, in 2010 (at station “Kosztolányi Dezső tér”), based on hourly measurements by Hungarian Air Quality Network. Source of data: <http://www.kvvm.hu/olm/>

However, carbon monoxide can also influence indirectly the air quality. Carbon monoxide in the atmosphere as a precursor compound in tropospheric ozone formation, can contribute to the photochemical smog episodes.

13.1.2. Sulphur dioxide (SO₂)

Sulphur can be found as a trace element in coal and oil. During combustion processes, sulphur combines with oxygen to form sulphur dioxide (SO₂). As SO₂ is relatively inert compound, it can travel long distances from its emission sources. High concentrations of sulphur dioxide can result in breathing problems. Long-term exposure of SO₂ can also causes cardiovascular diseases.

Sulphur dioxide can react with ozone or hydrogen peroxide in the atmosphere, produced sulphur trioxide, which can dissolve in water, forming a dilute solution of sulphuric acid. When this strong acid reaches the surface by precipitation or dry deposition (“acid rain”), it can be damaging to organisms and objects. Due to the rigid emission reduction strategies in Europe, and in Hungary too, the SO₂ emission has decreased significantly in the last decades. Figure 13.3 shows a yearly course of sulphur dioxide concentration in Budapest.

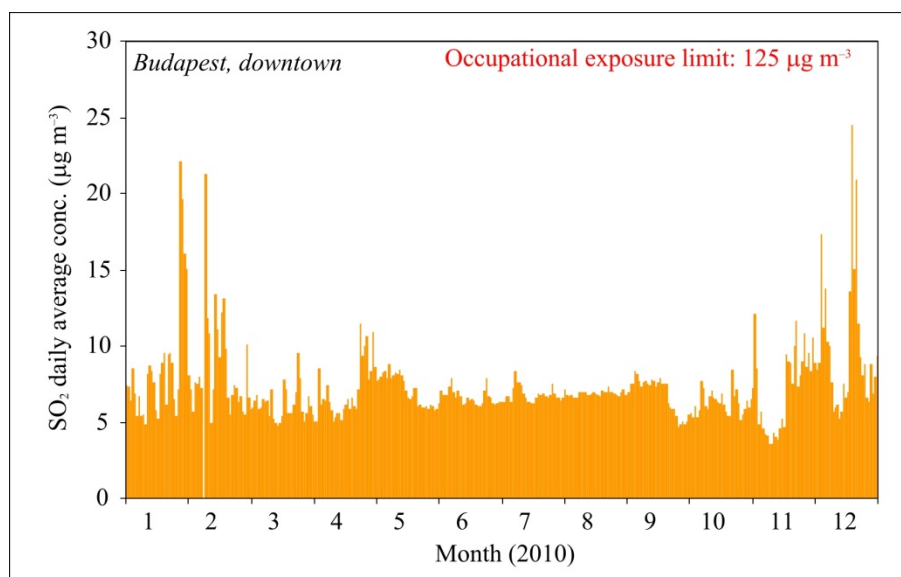


Figure 13.3: Daily average concentrations of sulphur dioxide in Budapest downtown in 2010 (at station “Kosztolányi Dezső tér”), based on hourly measurements by Hungarian Air Quality Network. Source of data: <http://www.kvvm.hu/olm/>

13.1.3. Nitrogen dioxide (NO₂)

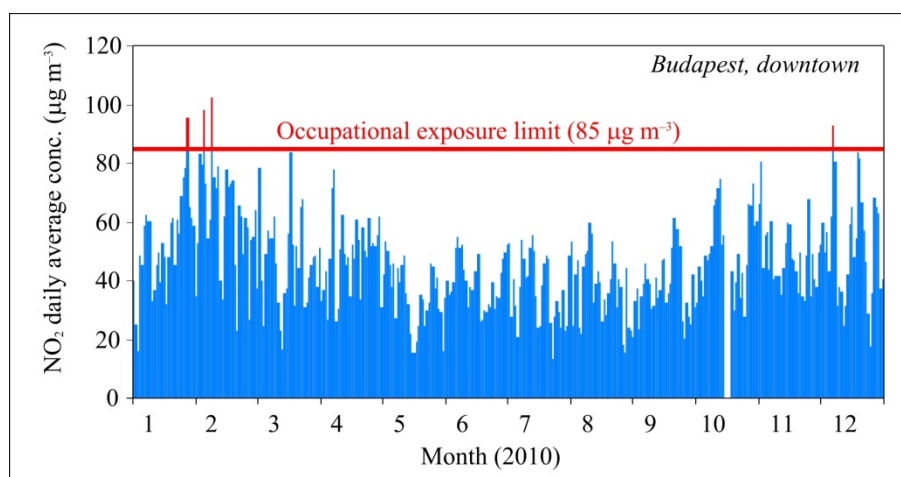


Figure 13.4: Daily average concentrations of nitrogen dioxide in Budapest, downtown in 2010 (at station “Kosztolányi Dezső tér”), based on hourly measurements by Hungarian Air Quality Network. Source of data: <http://www.kvvm.hu/olm/>

Nitrogen dioxide emitted to the atmosphere from transport and from power plants (more details about emission can be found in Chapter 2). The short-term exposure may cause increased respiratory symptoms, while long-term exposure can lead to irritation of the lung, susceptibility to respiratory infections, or even stroke (Andersen et al., 2012).

Nitrogen dioxide and nitric oxide (NO) too, next to the sulphur dioxide are other precursor compounds of acid rain. NO and NO₂ can dissolve in water forming weak solutions of nitric and nitrous acids. Additionally, nitrogen oxides can cause several other environmental problems, such as the decrease of the visibility or eutrophication.

Urban concentration of nitrogen dioxide is still high in Hungary. A yearly course of NO₂ concentration in Budapest downtown can be seen in Figure 13.4. Higher concentration was generally observed in winter season, while lower values were occurred in summer. In 2010, the concentration of nitrogen dioxide exceeds the occupational exposure limit in a few winter days at the given site.

13.1.4. Ozone (O₃)

Ozone in the troposphere forms from its precursor compounds during photochemical reactions (see Chapter 8). Near-surface ozone plays an important role in the formation of photochemical air pollution. Ozone has several injurious effects both on human health (Weschler, 2006), and plant functioning (Emberson, 2003). Human exposure to ozone is associated with respiratory and cardiovascular symptoms.

Elevated ozone concentrations can be potentially harmful to agricultural and natural vegetation. Occasional extreme concentrations may cause visible injury to the vegetation while the long-term, growing-season averaged exposure can result in decreased productivity and crop yield. Recently it has also been shown that the indirect radiative forcing of climate change through ozone effecting on the land carbon sink could be an important factor and can induce a positive feedback for global warming.

Figure 13.5 and Figure 13.6 show the annual cycle of ozone concentration in a downtown and a suburb measuring stations, respectively. In contrast to other pollutants, higher ozone values appear in summer and lower ones in winter. It seems also, that in the suburb, generally larger values can be observable than in the centre of the city.

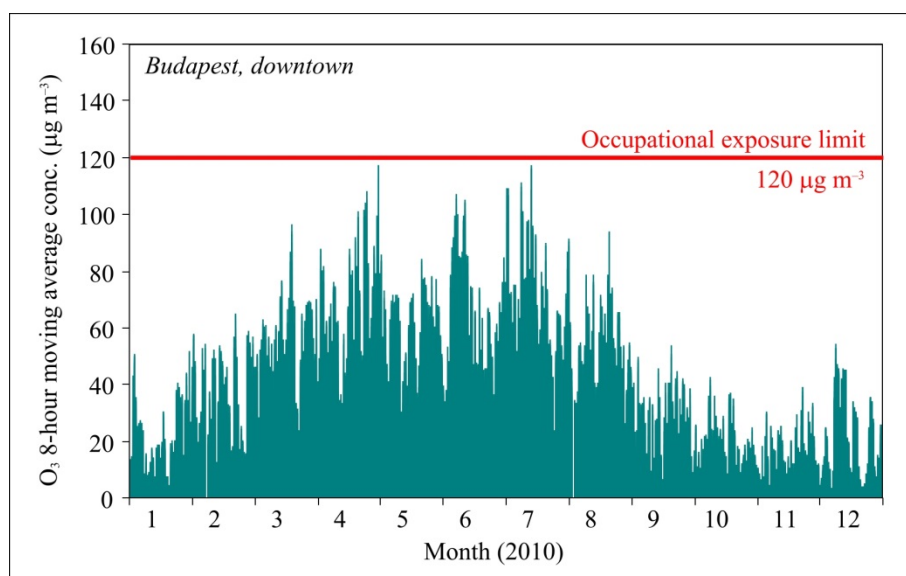


Figure 13.5: Daily average concentrations of ozone in Budapest, downtown in 2010 (at station “Kosztolányi Dezső tér”), based on hourly measurements by Hungarian Air Quality Network. Source of data: <http://www.kvvm.hu/olm/>

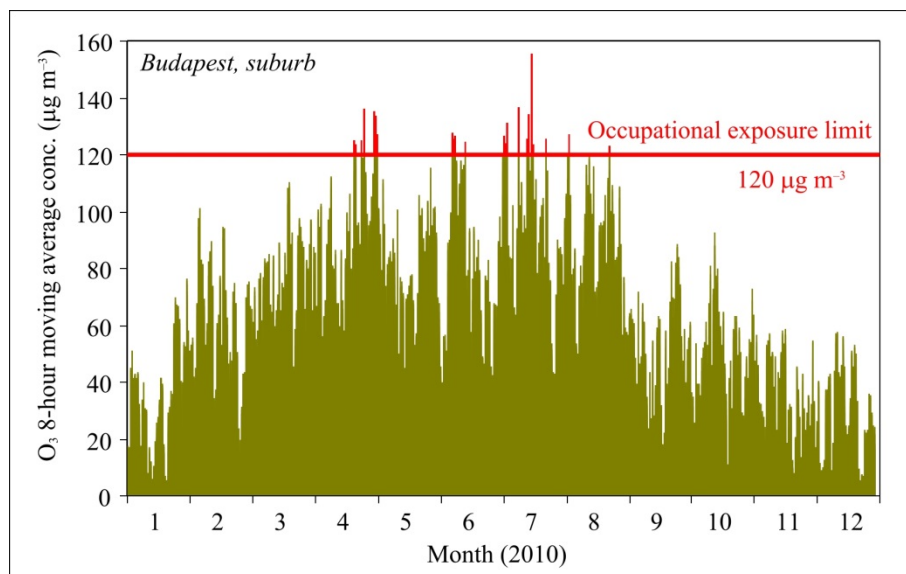


Figure 13.6: Daily average concentrations of ozone in Budapest, suburb in 2010 (at station “Gillice tér”), based on hourly measurements by Hungarian Air Quality Network. Source of data: <http://www.kvvm.hu/olm/>

13.1.5. Particulate matter

Aerosol particles have various natural and anthropogenic sources (for more details see Chapter 2 and Chapter 9). Aerosol particles have important role in lower tropospheric air quality. Aerosols, especially ultra-fine particles can cause several severe health effects, including enhanced mortality, respiratory, cardiovascular and allergic diseases (see. e.g. Pöschl, 2005).

Aerosol particles can also affect significantly the cycles of atmospheric contaminants including nitrogen, sulphur, and atmospheric oxidants. Additionally they can reduce the visibility.

Higher PM_{10} concentrations typically occur in winter (Figure 13.7). Based on the measurements carried out in Budapest downtown station (“Kosztolányi Dezső tér”) in 2010, the PM_{10} concentration exceeded the occupational exposure limit in several days in winter season.

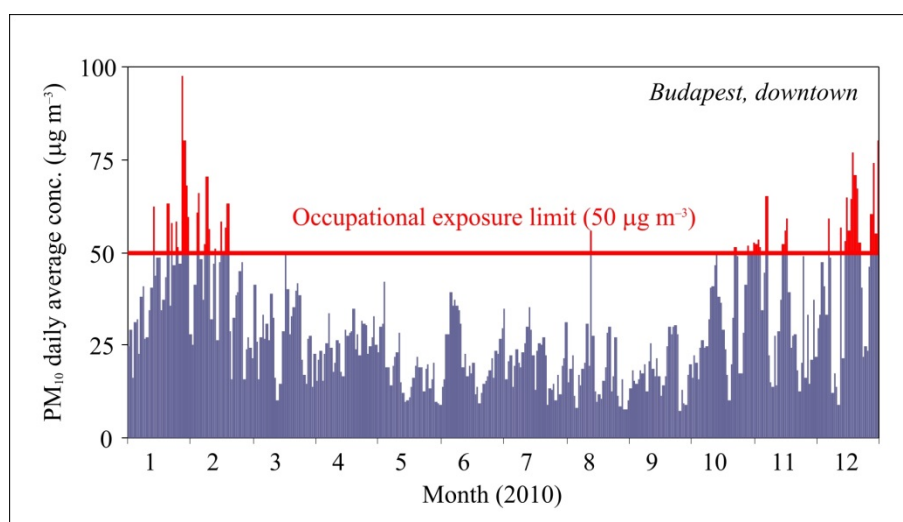


Figure 13.7: Daily average concentrations of PM_{10} in Budapest, downtown in 2010 (at station “Kosztolányi Dezső tér”), based on hourly measurements by Hungarian Air Quality Network. Source of data: <http://www.kvvm.hu/olm/>

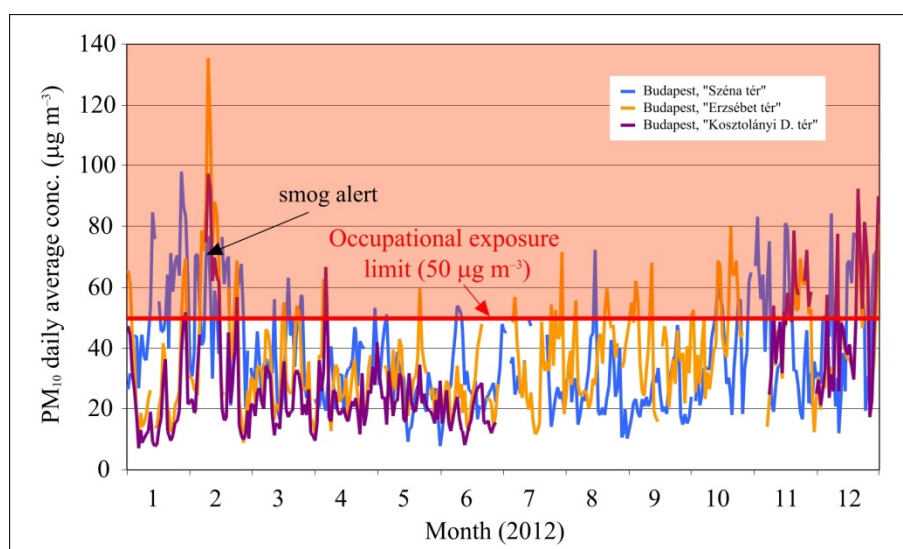


Figure 13.8: Daily average concentrations of PM₁₀ in three different stations (“Széna tér”, “Erzsébet tér” and “Kosztolányi Dezső tér”) in Budapest, downtown in 2010, based on hourly measurements by Hungarian Air Quality Network. Source of data: <http://www.kvvm.hu/olm/>

At the same time, elevated concentration can also be formed in a few days in summer period (Figure 13.8). However, the most severe, long-term events can be realized in winter, when weather conditions favour the formation of London-type smog (as it happened for example in February 2012, in Budapest).

13.2. Some effects on the environment

13.2.1. Smog

The word “smog” was originally generated by the combination of words “smoke” and “fog” to describe a type of air pollution that refers to a mixture of natural fog and several air pollutants. Today, it is a common term applied to different air pollution events mainly formed in large cities.

“London type smog” or sulphurous smog was frequently formed from the 19th century to the mid 20th century in industrialized regions. One of the most disastrous smog events happened in 1952, in London, when thousands of deaths were associated with air pollution. This type of smog is a consequence of large amounts of coal burning in cities or industrial areas. Under stable atmospheric stratification, sulphur dioxide, sulphuric acid, soot particles and other pollutants produced from fossil fuel sources can be piled up. Cold, damp, foggy weather favours the formation of smog. London type smog was largely eliminated during the 20th century, by sulphur dioxide and smoke emission reduction strategies. However, similar air pollution events can occur nowadays in winter season (see Figure 13.8) due to the large emission of particulate matter, nitrogen oxides and other pollutants from traffic and residential heating combined with a long-lasting high-pressure system.

Another type of smog is the “Los Angeles type smog” or photochemical smog. This type of air pollution was first identified in 1954 in Los Angeles (Haagen-Smit and Fox, 1954). The photochemical smog consists of ozone and other closely related secondary pollutants that are produced by photochemical reactions from precursor compounds, which are emitted to the atmosphere mainly by transport. However, the photochemical smog formation is also influenced by the weather conditions. Ozone formation is driven by sunlight. Severe ozone events are often associated with persistent high-pressure systems (anticyclones), light wind and subsidence inversions, which limit vertical dispersion of pollutants. The chemistry of ozone formation also depends on the temperature. Higher temperature accelerates the ozone formation. The elevated ozone levels are always associated with temperatures in excess of 20°C (Sillman, 2003). Ozone formation typically requires a few hours and during this time, the air mass from the city can be transported away. Therefore, high ozone values generally are found downwind of major cities rather than in the downtown. However, occasionally, most severe photochemical smog can be formed in city centre in case of very light wind. Geographical location of the city (if the city is situated for example in a valley) can facilitate the formation of elevated ozone concentrations.

13.2.2. Acid rain

Acid rain is a commonly used term of acidic deposition. During this process, high amounts of strong acids (such as nitric and sulfuric acids) and other acid-forming substances (ions, gases and particles) are removed from the atmosphere to the surface by both dry and wet deposition.

Compounds of acidic deposition are formed from the gaseous emission of sulphur dioxide (SO₂), nitrogen oxides (NO_x) and ammonia (NH₃) and particulate emission of acidifying and neutralizing compounds. Due to the long range transport of these acidic compounds, the harmful effects of acid deposition could be observable even hundreds of kilometers from the emission sources. Acidic deposition caused a critical environmental stress that affects soils, forested landscapes (Figure 13.9) and aquatic ecosystems in the last quarter of 20th century in North America, Europe, and Asia (Driscoll et al., 2001). However, due to the pronounced decrease in sulphur dioxide emission, and based on the continuous pH measurements of precipitation, the acidity of precipitation had decreased significantly in North America and Europe from the 1970s. At the same time, because of losses in soil buffering, the forest ecosystem is currently much more sensitive to acid rain inputs than previously predicted (Likens, 2013).



Figure 13.9: Harmful effect of acid deposition on forest trees

13.3.3. Crop and forest damage by ozone

The background surface ozone concentration increased steadily worldwide in the last decades of 20th century (Vingarzan, 2004). This explicit trend may slow in previous years, but measured values are still high in Europe (EEA, 2011). Moreover, based on air quality model simulations, significant rise of surface ozone concentration is predicted for the future (see e.g. Meleux et al., 2007) causing several environmental damages. Ozone in the near surface layer is one of the most important phytotoxic air pollutants that can cause injury to plant tissues, reduction in plant growth and productivity via ozone uptake, especially through the stomata. Ozone can also affect the mechanism of CO₂ exchange between vegetation and the atmosphere (Sitch et al. 2007). Several studies have reported that ozone can cause the most damage to forest vegetation. Impaired trees biomass growth caused by the elevated ozone concentration.

To estimate the effects of ozone on vegetation, concentration based metrics (e.g. AOTX – accumulated O₃ exposure over a threshold X value) have been proposed at the end of 20th century. However, from the biological aspect, the response of vegetation to ozone is more closely related to the absorbed dose through the stomata than to external ozone exposure (e.g. Musselmann et al. 2006). To characterize the vegetation damage caused by the ozone, in the past decade, flux-based ozone exposure metrics have been favoured as opposed to concentration-based indices. The differences between AOTX and O₃ flux indices are more considerable under dry climatic conditions where vapour pressure deficit and soil moisture deficit limit the stomatal conductance.

The ozone exposure can be estimated by more or less sophisticated deposition models for several types of vegetation or for a region (see. e.g. Mészáros et al., 2009). In such models, the ozone flux is controlled by ozone concentration and by deposition velocity via parameterization of the canopy and stomatal conductances. In general, in the models a multiplicative algorithm of stomatal conductance is applied (see Chapter 12). This method includes functions for the effects of photosynthetically active radiation, air temperature, soil water content, and other parameters affecting the stomatal conductance. Plant stomatal conductance and calculation of the deposition velocity play a key role in most deposition models applied for risk assessment and for estimation climatic effects of tropospheric ozone.

The total ozone flux is the product of the deposition velocity and ozone concentration. Therefore, on the distribution of the flux, the effects of both concentration and deposition fields are apparent. In case of high concentration, generally high flux can be observable. However, the predicted total ozone flux can be relatively low due to low deposition velocities or relatively high in case of high deposition velocity in some regions, demonstrating possible flaws in the assumption that damage can be directly related to ozone concentrations (See Figure 13.10). The plant response and therefore the effective ozone load are more closely related to the ozone flux than to the atmospheric concentrations. The weather situation and soil properties through the stress effects on plants can retard the deposition.

Therefore, in some cases lower amounts of ozone can be settled from the atmosphere, even if the ozone concentration is elevated.

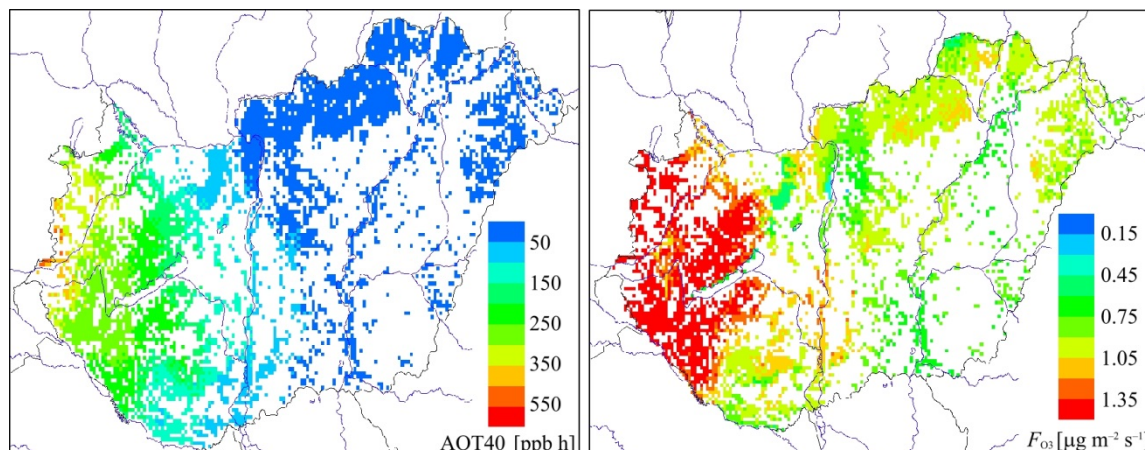


Figure 13.10: Estimated AOT40 and total flux of ozone over deciduous forest in Hungary in July 1998. Model simulations were carried out by TREX transport-deposition model (Eötvös Loránd University). Meteorological data were obtained from ALADIN numerical weather prediction model used at Hungarian Meteorological Service.

References

- Andersen Z.J., Kristiansen L.C., Andersen K.K., Olsen T.S., Hvidberg M., Jensen S.S., Ketzel M., Loft S., Sørensen M., Tjønneland A., Overvad K., and Raaschou-Nielsen O.. 2012. *Stroke and Long-Term Exposure to Outdoor Air Pollution From Nitrogen Dioxide : Cohort Study*. *Stroke*. Vo. 43. 320-325.
- Bell M.L. and Davis D.L.. 2001. *Reassessment of the Lethal London Fog of 1952: Novel Indicators of Acute and Chronic Consequences of Acute Exposure to Air Pollution*. *Environmental Health Perspectives*. Vo. 109. 389–394.
- Driscoll C.T., Lawrence G.B., Bulger A.J., Butler T.J., Cronan C.S., Eagar C., Lambert K.F., Likens G.E., Stoddard J.L., and Weathers K.C.. 2001. *Acidic deposition in the Northeastern United States: sources and inputs, ecosystem effects, and management strategies*. *BioScience*. Vo. 51. No. 3.. 180-198.
- EEA Technical Report, 2011: *Air pollution by ozone across Europe during summer 2010*. EEA Report. No 6/2011. ISBN 978-92-9213-210-1.
- Emberson L.. 2003. *Air pollution impacts on crops and forests: An introduction*. In: *Emberson, L., Ashmore, M., Murray, F., eds, Air pollution impacts on crops and forests. A global assessment*. Imperial College Press, London. Vo. 4. 3-29 pp.
- Haagen-Smit A. J. and Fox M.M.. 1954. *Photochemical ozone formation with hydrocarbons and automobile exhaust*. *Air Repair*. Vo. 4. 105–109.
- Helfand W.H., Lazarus J., and Theerman P.. 2001. *Donora, Pennsylvania: An environmental disaster of the 20th century*. *American Journal of Public Health*. Vo. 91. No. 4. 553.
- Likens G.E.. 2013. *Acid rain*. In: *Weathers, K.C., Strayer, D.L. Likens, G.E. (eds): Fundamentals of Ecosystem Science*. Academic Press. Section V., Chapter 15. 259–264. ISBN: 978-0-12-088774-3.
- Meleux F., Solmon F., and Giorgi F.. 2007. *Increase in summer European ozone amounts due to climate change*. *Atmospheric Environment*. Vo. 41. 7577–7587.
- Mészáros R., Zsély I.Gy., Szinyei D., Vincze Cs., and Lagzi I.. 2009. *Sensitivity analysis of an ozone deposition model*. *Atmospheric Environment*. Vo. 43. 663–672.

- Musselman R.C., Leföhn A.S., Massman W.J., and Heath R.L.. 2006. *A critical review and analysis of the use of exposure- and flux-based ozone indices for predicting vegetation effects*. Atmospheric Environment. Vo. 40. 1869–1888.
- Nemery B., Hoet P.H.M., and Nemmar A.. 2001. *The Meuse Valley fog of 1930: an air pollution disaster*. Lancet. Vo. 357. No. 9257. 704–708.
- Pöschl U.. 2005. *Atmospheric Aerosols: Composition, Transformation, Climate and Health Effects*. Angewandte Chemie International Edition. Vo. 44. 7520–7540.
- Raub J.A. and Benignus V.A.. 2002. *Carbon dioxide and the nervous system. Review*. Neuroscience and Biobehavioral Reviews. Vo. 26. 925–940.
- Sillman S.. 2003. *Tropospheric Ozone and Photochemical Smog*. in: Holland, H.D., Turekian, K.K., eds: *Treatise on Geochemistry*. Environmental Geochemistry, Elsevier. Volume 9. 407–431. ISBN: 978-0-08-043751-4.
- Sitch S., Cox P.M., Collins W.J., and Huntingford C.. 2007. *Indirect radiative forcing of climate change through ozone effects on the land-carbon sink*. Nature. Vo. 448. 791–794.
- Vingarzan R.. 2004. *A review of surface ozone background levels and trends*. Atmospheric Environment. Vo. 38. 3431–3442.
- Weschler C.J.. 2006. *Ozone's Impact on Public Health: Contributions from Indoor Exposures to Ozone and Products of Ozone-Initiated Chemistry*. Environmental Health Perspectives. Vo. 114. 1489–1496.

<http://edgar.jrc.ec.europa.eu>

Chapter 14. The role of air pollution in the global climate change

Since the beginning of the Industrial Revolution in the mid-18th century, growing anthropogenic emission of air pollutants cause increasing trends in their atmospheric concentration levels. During combustion of fossil fuels for industrial and domestic usage and biomass burning, large amount of greenhouse gases and aerosol particles are produced which affect the atmospheric composition. Air pollution has become an increasingly serious problem causing several harmful effects on the environment (see Chapter 13). At the end of the 19th century, Swedish chemist, Svante Arrhenius first quantified the contribution of carbon dioxide to the greenhouse effect and assumed that the variation of atmospheric concentration of carbon dioxide can contribute to the variation of Earth's climate (Arrhenius, 1896). Since then it has become clear that anthropogenic perturbation of the atmospheric composition and enhanced greenhouse effect change the the radiative forcing and have a potential impact on regional and global climate (see e.g. IPCC, 2007).

14.1. Effects of atmospheric composition on the radiation budget

Atmospheric contaminants play important role in the radiation budget of the Earth-atmosphere system through the modification of the intensity of both incoming solar radiation and outgoing terrestrial radiation. One of the main results of these processes is the greenhouse effect (Figure 14.1).

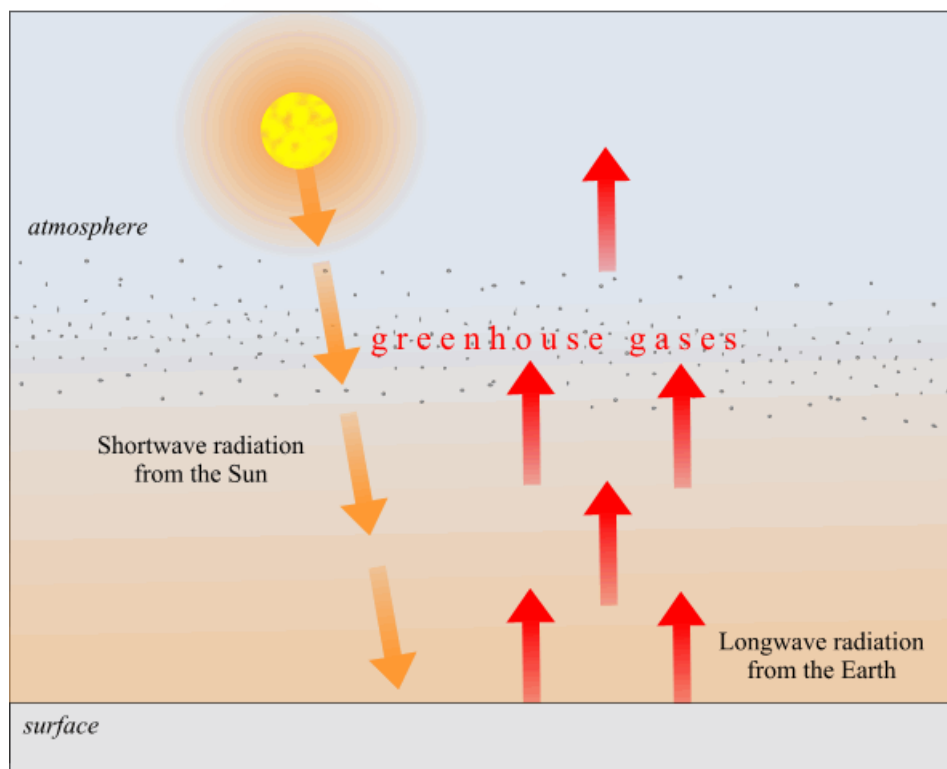


Figure 14.1: The greenhouse effect: the absorption and re-emission of a part of long wave radiation from the Earth by greenhouse gases heating the atmosphere.

The greenhouse effect is a natural process in the atmosphere, by which a part of long wave radiation from Earth's surface is absorbed by atmospheric greenhouse gases (GHGs), and is re-emitted in all directions, thereby heating the atmosphere. Due to this process, the Earth's atmosphere is more than 33 °C warmer that it would be without

it (see table 14.1). However, human activities can modify this greenhouse effect by the increased emission of greenhouse gases, which is the most important factor in recent climate change. Most abundant greenhouse gases are water vapour (H₂O), carbon-dioxide (CO₂), methane (NH₃), nitrous-oxide (N₂O), tropospheric ozone (O₃) and chlorofluorocarbons (CFCs).

Table 14.1: The most important greenhouse gases and their contribution to the atmospheric greenhouse effect

Name	Formula	Effect
Water vapour	H ₂ O	+ 20.6 °C
Carbon-dioxide	CO ₂	+ 7.2 °C
Tropospheric ozone	O ₃	+ 2.4 °C
Nitrous oxide	N ₂ O	+ 1.4 °C
Methane	CH ₄	+ 0.8 °C
Others		+ 0.6 °C
	<i>Sum:</i>	+ 33 °C

Aerosol particles have also significant effects on the radiation budget. These effects can be direct radiative forcing due the scattering absorption radiation or indirect radiative forcing through cloud formation effects (see details in Chapter 7).

14.2. Anthropogenic perturbation of the greenhouse gases

Ice core records show that atmospheric CO₂ concentration varied in the range of 180 to 300 ppm over the glacial-interglacial cycles of the last 650 000 years. The ice core records also indicate that greenhouse gases co-varied with Antarctic temperature over glacial-interglacial cycles, suggesting a close link between natural atmospheric greenhouse gas variations and atmospheric temperature (IPCC, 2007).

For about a thousand years before the Industrial Revolution, the amount of most important long-lived greenhouse gases (CO₂, CH₄ and N₂O) in the atmosphere remained relatively constant. However, since the Industrial Revolution, combustion of fossil fuels, agricultural activities and land use have caused continuous increases in greenhouse gases over about the last 250 years. The rates of increase in levels of these gases are dramatic about from 1850.

Yearly average background concentration of carbon dioxide (CO₂) has increased by almost 40% since pre-industrial times from about 280 ppm to about 390 ppm (in 2010), and is still increasing at an unprecedented rate of on average 0.4% per year (Figure 14.2). However, atmospheric CO₂ concentration increased by only 20 ppm over the 8000 years prior to industrialisation (IPCC, 2007).

The nitrous oxide (N₂O) background concentration in 2010 was 324 ppb, almost 20% higher than its pre-industrial value. Based on ice core data the atmospheric concentration of N₂O varied by less than about 10 ppb for 11 500 years before the beginning of the industrial era (IPCC, 2007). Since then, N₂O concentration has continuously increased due to the increasing anthropogenic emission from agricultural activities and land use change. Over the past few decades, the N₂O concentration has increased approximately linearly by about 0.8 ppb year⁻¹ (Figure 14.3).

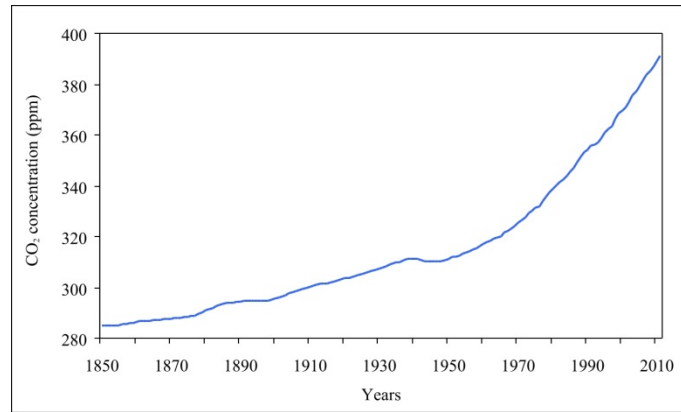


Figure 14.2: Global atmospheric carbon dioxide (CO₂) concentration from 1850. Source of data: <http://data.giss.nasa.gov/modelforce/ghgases/>

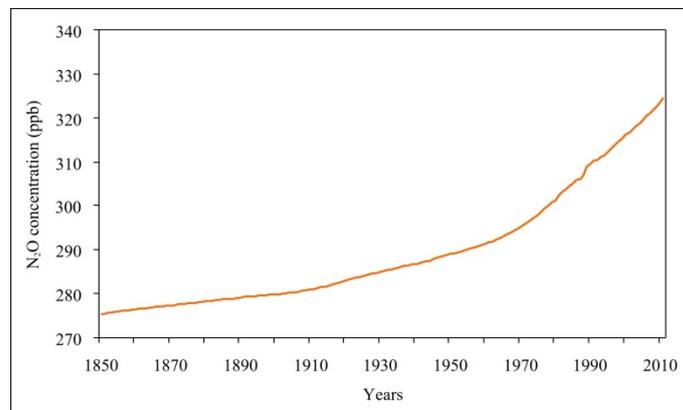


Figure 14.3: Global atmospheric nitrous oxide (N₂O) concentration from 1850 Source of data: <http://data.giss.nasa.gov/modelforce/ghgases/>

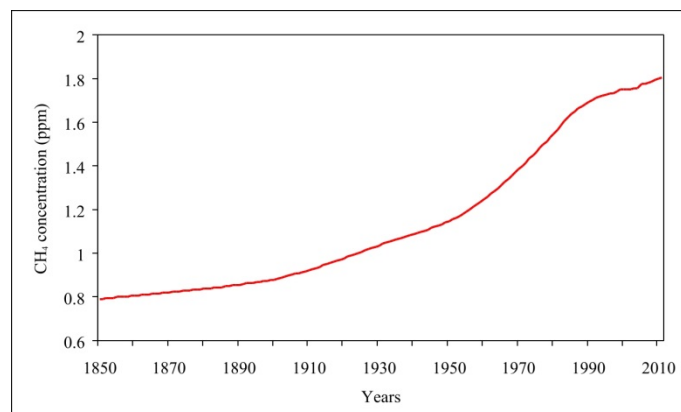


Figure 14.4: Global atmospheric methane (CH₄) concentration from 1850 Source of data: <http://data.giss.nasa.gov/modelforce/ghgases/>

Atmospheric methane (CH₄) concentration has increased dramatically since 1750 due to the increasing anthropogenic emissions. Methane concentrations varied slowly between 580 and 730 ppb over the last 10 000 years, but increased by more than 1 000 ppb in the last two centuries, representing its fastest change over at least the last 80 000 years (IPCC, 2007). Current atmospheric level of methane is about 1800 ppb. However, in the last few decades, the rate of increase has slowed (Figure 14.4). This recent decline in growth rate implies that CH₄ emissions have become comparable to removals due primarily to oxidation by the hydroxyl radical (OH).

Chlorofluorocarbons (CFCs) and hydrochlorofluorocarbons (HCFCs) are emitted into the atmosphere only during anthropogenic emissions from industrial sources. Their atmospheric concentrations have only been detected since 1950s. However, as these gases play important role in stratospheric ozone depletion, their emission reduction strategies were declared in the Montreal Protocol (signed in 1987) for the protection of the ozone layer. Due to the effective reduction of their emissions, atmospheric concentrations are now decreasing by natural removal processes (Figure 14.5).

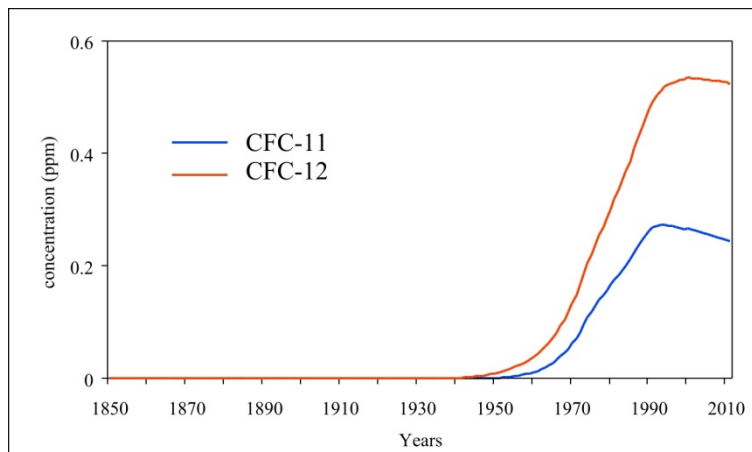


Figure 14.5: Global atmospheric concentration of chlorofluorocarbons (CFC-11 and CFC-12) from 1850. Source of data: <http://data.giss.nasa.gov/modelforce/ghgases/>

Tropospheric ozone (O_3) is a short-lived greenhouse gas produced by chemical reactions of its precursor species (see Chapter 8). The background atmospheric concentration of ozone increased continuously in the last decades of 20th century (Vingarzan, 2004). Spatial and temporal distributions of ozone concentrations, however, show large variability and related to the concentration of the nitrogen oxides (NO and NO_2), carbon monoxide (CO) and other precursor compounds.

14.3. Radiative forcing of atmospheric components

Increased anthropogenic activities since the onset of Industrial Revolution have caused a positive total net anthropogenic radiative forcing (Figure 14.6) due primarily to the modification of atmospheric composition. The increase in the amounts of greenhouse gases causes positive radiation forcing (IPCC 2007). Increases in atmospheric carbon dioxide contribute to the radiative forcing in the greatest extent. CO_2 is responsible for a radiative forcing of $+1.66 \pm 0.17 \text{ W m}^{-2}$. Contribution to radiative forcing of other long-lived greenhouse gases, such as methane, nitrous oxide and halocarbons were $+0.48 \pm 0.05 \text{ W m}^{-2}$, $+0.16 \pm 0.02 \text{ W m}^{-2}$ and $+0.32 \pm 0.03 \text{ W m}^{-2}$, respectively, between 1750 and 2005. Radiative forcing of other industrial fluorinated gases, like hydrofluorocarbons (HFCs), perfluorocarbons (PFCs) or sulphur hexafluoride (SF_6) are relatively small ($+0.017 \text{ W m}^{-2}$) but are increasing rapidly. Estimated radiative forcing caused by tropospheric ozone is $+0.35 [+0.25 \text{ to } +0.65] \text{ W m}^{-2}$. However, changes in stratospheric ozone have caused a small negative radiative forcing ($-0.05 \pm 0.10 \text{ W m}^{-2}$).

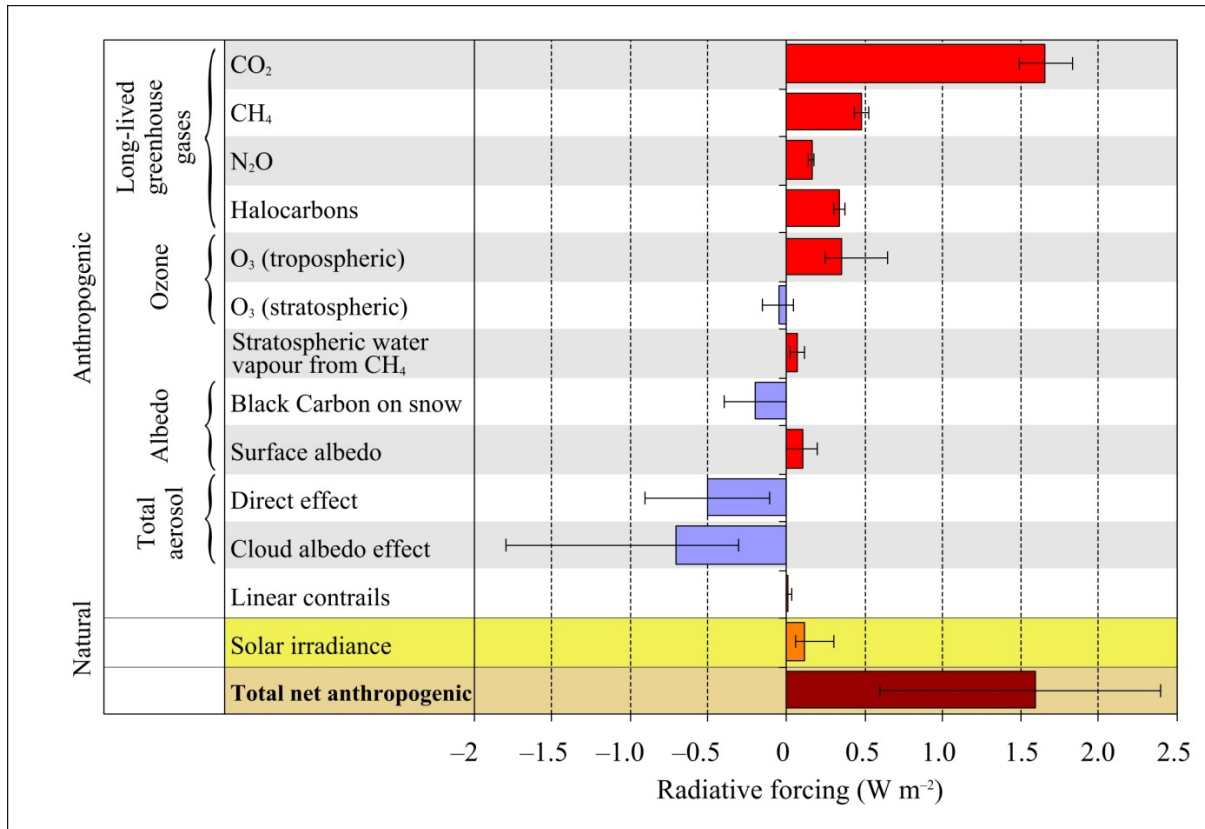


Figure 14.6: Radiative forcing of climate between 1750 and 2005. Estimated global averages and ranging for most important factors. Source of data: IPCC, 2007.

Direct emission of water vapour by human activities has a negligible contribution to radiative forcing. However, increasing methane concentration could increase stratospheric water vapour due to oxidation of CH₄, which can cause an estimated positive radiative forcing ($+0.07 \pm 0.05 \text{ W m}^{-2}$)

The effect of the increasing amount of aerosol particles on the radiative forcing is very complex and not yet fully known. The direct effect of aerosols is the scattering of a part of the incoming solar radiation back into space. This effect causes a negative radiative forcing, which that may partly, and locally even completely, compensates the enhanced greenhouse effect. However, due to their short atmospheric lifetime, the radiative forcing of aerosols is very inhomogeneous in space and in time. On the other hand, some aerosols, such as soot particles, absorb the solar radiation directly, leading to local heating of the atmosphere, or absorb and emit infrared radiation, adding to the enhanced greenhouse effect. Aerosols may also affect the number, density and size of cloud droplets. This may change the amount and optical properties of clouds, and hence their reflection and absorption.

Against the greenhouse gases, increasing amount of anthropogenic aerosols, in total, have led to a net negative radiative forcing, with a greater magnitude in the Northern Hemisphere than in the Southern Hemisphere. A total direct aerosol radiative forcing considering all aerosol types is estimated as $-0.5 \pm 0.4 \text{ W m}^{-2}$. Anthropogenic aerosols effects on water clouds cause an indirect cloud albedo effect causing a radiative forcing of $-0.7 [-0.3 \text{ to } -1.8] \text{ W m}^{-2}$.

Net radiative forcing is also affected by some other anthropogenic factors, such as persistent linear contrails from global aviation, or human-induced changes in surface albedo (Figure 14.6)

The estimated direct natural radiation forcing due to the changes in solar irradiance between 1750 and 2005 is $+0.12 [+0.06 \text{ to } +0.3] \text{ W m}^{-2}$, which is much smaller than the net anthropogenic contribution to the global average radiative forcing over the industrial period.

Total net anthropogenic radiation forcing has a potential impact on regional and global climate. Based on direct measurements from 1880, the global average surface temperature has increased, especially since about 1950 (Figure 14.7). Observations and model simulations also indicate that positive radiative forcing affect the surface

moisture budget. Some forcing agents (particularly aerosols) may have more strongly influenced the hydrological cycle, than other compounds.

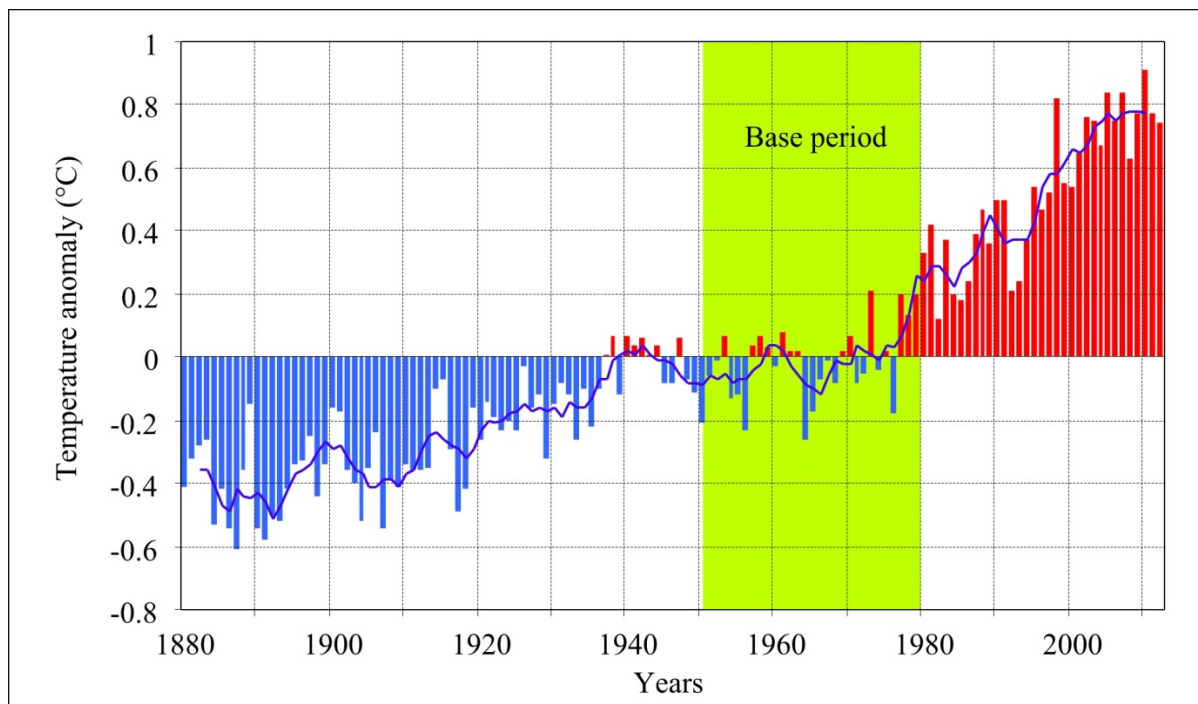


Figure:14.7: Global annual mean temperature anomaly and 5-years running-mean relative to the average of base period between 1951 and 1980. Source of data: <http://data.giss.nasa.gov/gistemp/>

14.4. Future scenarios

To predict the expected changes in climate, global circulation model (GCM) simulations are driven by different emission scenarios. First emission scenarios were produced by IPCC (Intergovernmental Panel on Climate Change) in 1990 (IPCC, 1990). In 1992, IPCC released a new emission scenario set, the so-called IS92 scenario family, which contained 6 different scenarios (Leggett et al., 1992). Due the continuous development of our understanding of possible future greenhouse gas emissions and climate change, IPCC have developed a new scenario set, called SRES (Special Report on Emissions Scenarios – Nakicenovic and Swart, 2000). The next generation of emission scenarios for climate change research and assessment, known as Representative Concentration Pathways (RCPs) (Moss et al, 2010).

14.4.1. SRES scenarios

The SRES scenarios cover a wide range of the main driving forces of future emissions, from demographic to technological and economic developments. Each of four different storyline (namely A1, A2, B1 and B2) assumes a distinctly different direction for future developments (Figure 14.8) and therefore different rates of the expected emissions of greenhouse gases, aerosol particles and other air pollutants.

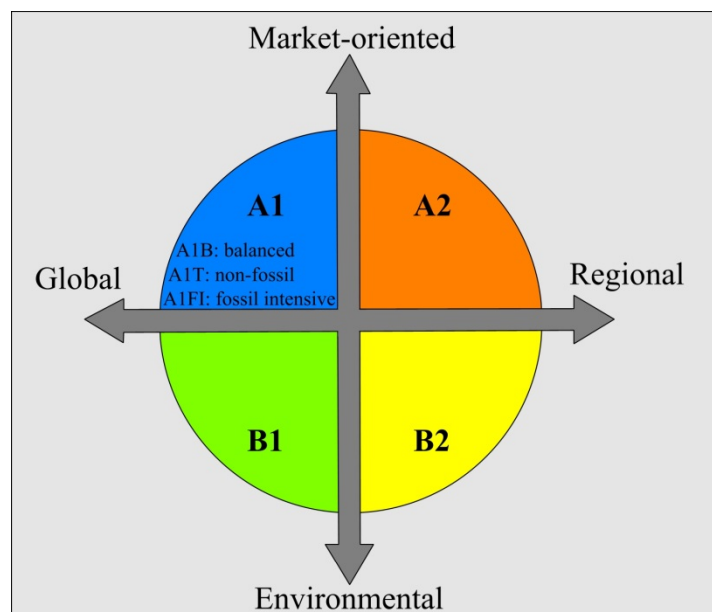


Figure 14.8: Four different storylines (A1, A2 B1 and B2) of SRES scenarios

The four SRES storylines are the following (after IPCC, 2007):

A1 storyline and scenario family: This storyline describes a future world of very rapid economic growth. World population increases until mid-century and declines thereafter. New and more efficient technologies are introduced rapidly. Regional differences in cultural and social fields are decreased. The A1 scenario family develops into three groups that describe alternative directions of technological change in the energy system, which are the following:

- A1FI: fossil intensive,
- A1T: non-fossil energy sources,
- A1B: balance among all sources.

A2 storyline and scenario family: This storyline describes a very heterogeneous world represented by self-reliance and preservation of local identities. Demographics of each region converge very slowly, resulted a continuously increasing global population in 21th century. Economic development is primarily regionally oriented. The economic growth and technological change are more fragmented and slower than in other storylines.

B1 storyline and scenario family: This storyline describes a convergent world as in the A1 storyline, with the same global population that peaks in mid-century and declines thereafter. At the same time, economy changes rapidly toward a service- and information-based direction, introduced clean and resource-efficient technologies. The emphasis is on global solutions to economic, social, and environmental sustainability, including improved equity, but without additional climate initiatives.

B2 storyline and scenario family: This storyline represents a world in which the emphasis is on local solutions to economic, social, and environmental sustainability. It is a world with continuously increasing global population at a rate lower than A2, intermediate levels of economic development, and less rapid and more diverse technological change than in the B1 and A1 storylines. While the scenario is also oriented toward environmental protection and social equity, it focuses on local and regional levels.

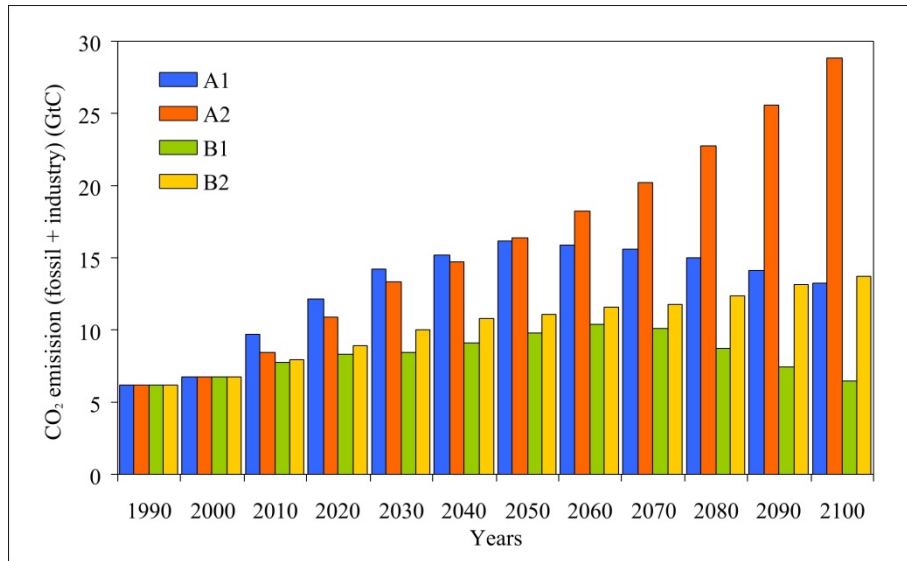


Figure 14.9: SRES scenarios for carbon dioxide (CO₂) emissions from fossil fuels and industry between 1990 and 2100 for each (A1, A2, B1 and B2) storylines. Source of data: Nakicenovic and Swart, 2000).

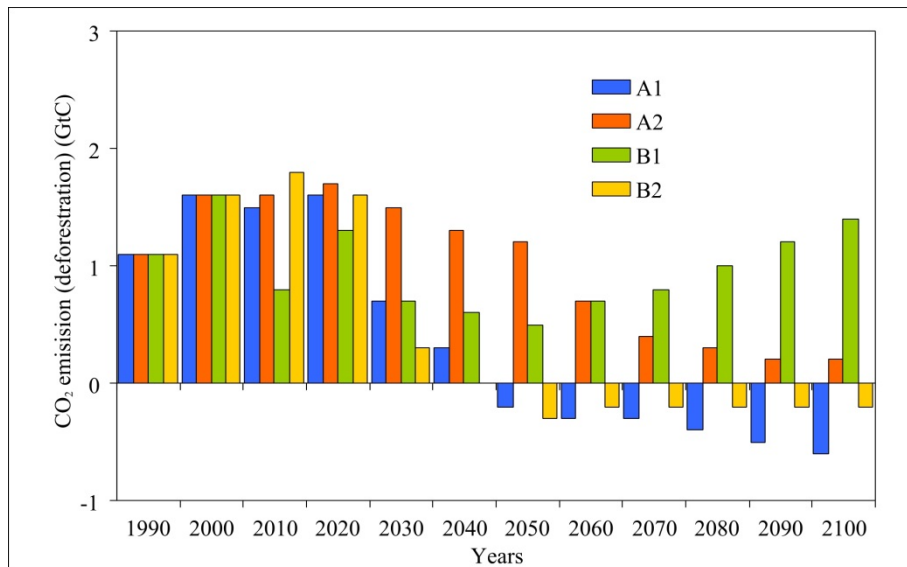


Figure 14.10: SRES scenarios for carbon dioxide (CO₂) emissions from deforestation between 1990 and 2100 for each (A1, A2, B1 and B2) storylines. Source of data: Nakicenovic and Swart, 2000).

Expected global emissions of the most important greenhouse gases in each storyline are presented in Figure 14.9 – 14.12. Figure 14.9 and Figure 14.10 show the expected CO₂ emissions from fossil fuels and industry, and deforestations, respectively. Figure 14.11 and Figure 14.12 presents the predicted global emissions of methane and nitrous oxide, respectively.

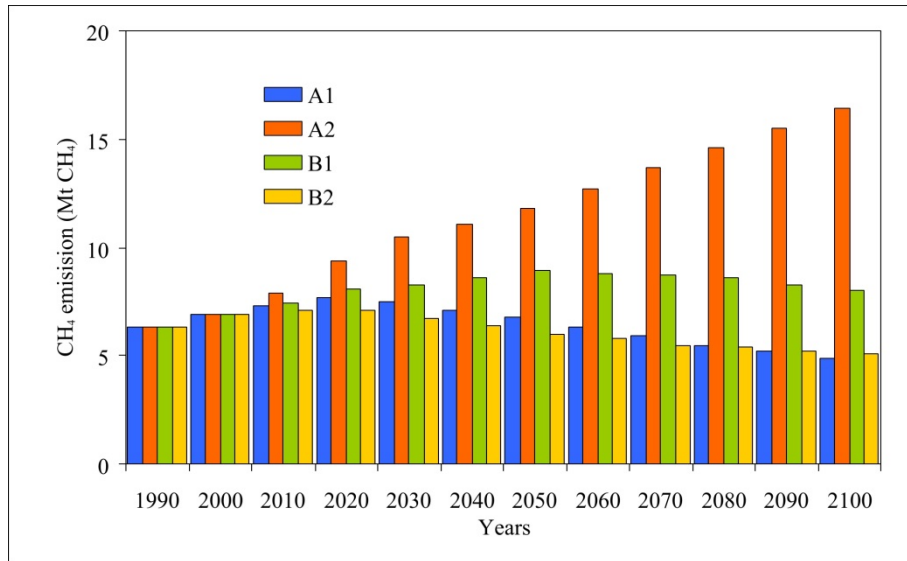


Figure 14.11: SRES scenarios for methane (CH₄) emissions between 1990 and 2100 for each (A1, A2, B1 and B2) storylines. Source of data: Nakicenovic and Swart, 2000).

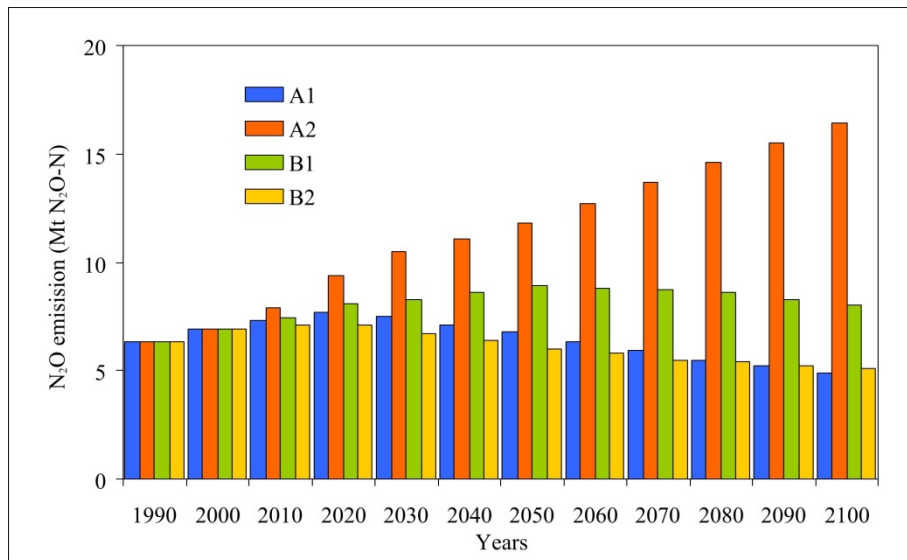


Figure 14.12: SRES scenarios for nitrous oxide (N₂O) emissions between 1990 and 2100 for each (A1, A2, B1 and B2) storylines. Source of data: Nakicenovic and Swart, 2000).

14.4.2. Representative Concentration Pathways (RCPs)

Former scenarios have been used in a linear process, when climate change projections have been carried out based on socioeconomic and emission scenarios (Figure 14.13). In contrast to this sequential form, a parallel process for scenario development (Figure 14.14) were decided by IPCC (Moss et al., 2008). These new generation scenarios have been started to develop in 2007. The parallel approach is initiated with the identification of the so-called RCPs (Representative Concentration Pathways), which should provide better integration, consistency, and consideration of feedbacks, and more time to assess impacts and responses.

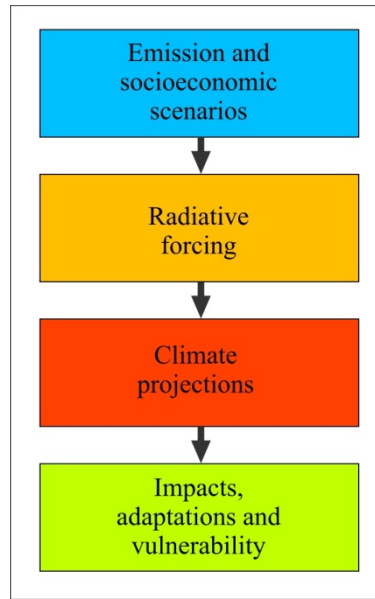


Figure 14.13: Sequential approach to development of global scenarios

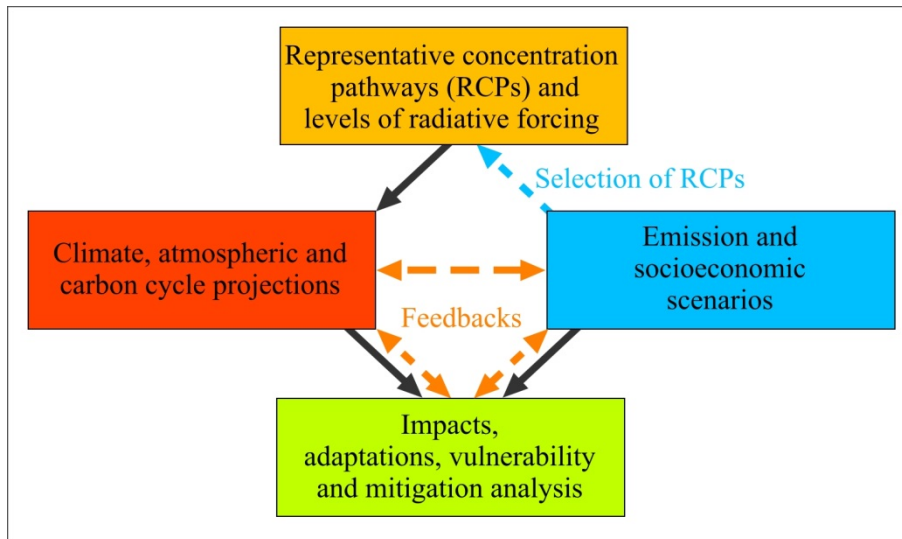


Figure 14.14: Parallel approach to development of global scenarios

RCPs are referred to as pathways to provide time-dependent projections of atmospheric greenhouse gas (GHG) concentrations based on the projections of radiative forcing. They are representative in that they are one of several different scenarios that have similar radiative forcing and emissions characteristics.

Four RCPs (Table 14.2) are produced from available emission and socioeconomic scenarios:

the highest pathway for which radiative forcing reaches $>8.5 \text{ W m}^{-2}$ by 2100 and continues to rise for some amount of time; two intermediate “stabilization pathways” in which radiative forcing is stabilized at approximately 6 W m^{-2} and 4.5 W m^{-2} after 2100; and one pathway where radiative forcing peaks at approximately 3 W m^{-2} before 2100 and then declines (Figure 14.15). All these scenarios include time paths for emissions and concentrations of the full suite of greenhouse gases, aerosols and chemically active gases, as well as land use and land cover.

Table 14.2: Representative Concentration Pathways (RCPs), as emission scenarios for IPCC Fifth Assessment Report, AR5 (Moss et al., 2008).

Name	Radiative forcing	CO ₂ equivalent concentration	Pathways
RCP8.5	>8.5 W m ⁻²	> 1370 ppm (2100)	rising concentration
RCP6.0	~6 W m ⁻²	~ 850 ppm (2100)	at stabilization after 2100
RCP4.5	~4.5 W m ⁻²	~ 650 ppm (2100)	at stabilization after 2100
RCP2.6	~3 W m ⁻²	~ 490 ppm (peak before 2100)	peak before 2100 then decline

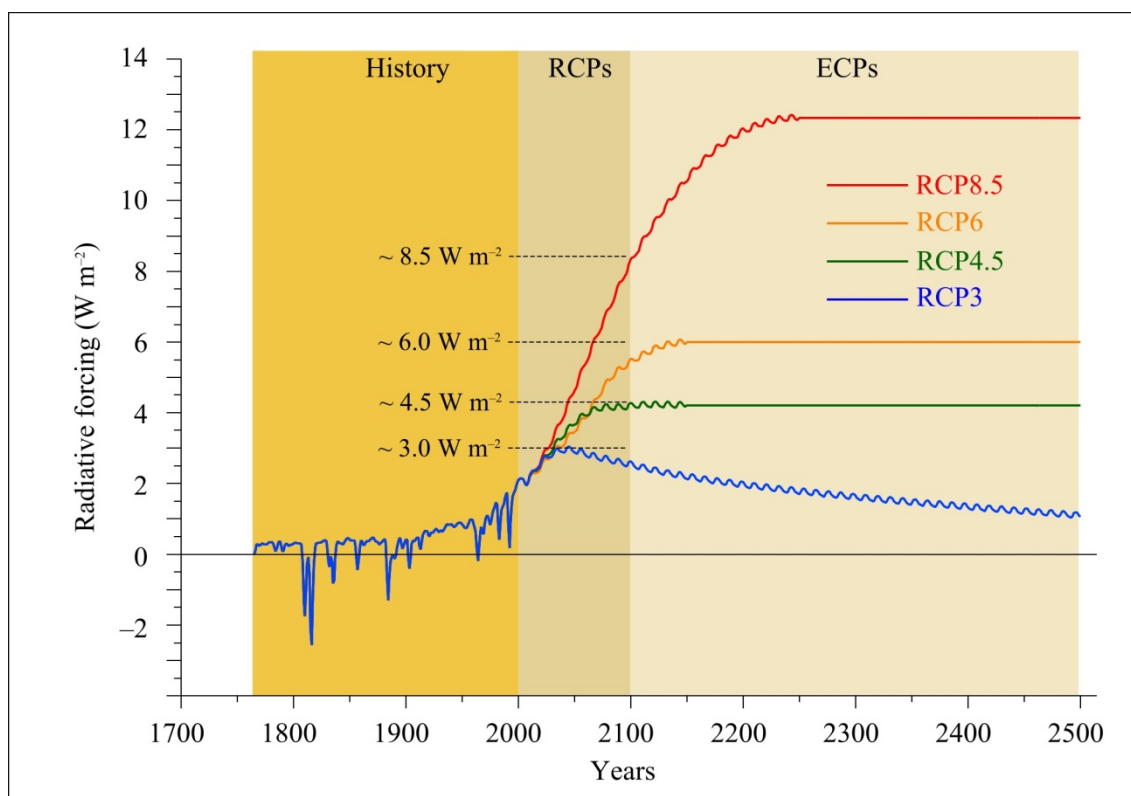


Figure 14.5: Total radiative forcing (anthropogenic + natural) for different RCPs (RCP8.5, RCP6, RCP4.5 and RCP3PD) including short term variations due to volcanic forcing in the past and cyclical solar forcing (except at times of stabilization). RCPs: Representative Concentration Pathways; ECPs: Extended Concentration Pathways. Based on Meinhausen et al., 2011. Source of data: <http://www.pik-potsdam.de/~mmalte/rcps/>

References

Arrhenius S.. 1896. *On the influence of carbonic acid in the air upon the temperature of the ground*. Lond. Edinb. Dublin Phil. Mag. J. Sci. (5th ser.). Vo. 41. 237–275.

IPCC, 1990: *Climate Change. The IPCC response strategies*. WMO/UNEP. 330p.

IPCC, 2007: *Climate Change 2007: The Physical Science Basis. Contribution of Working Group I to the Fourth Assessment Report of the Intergovernmental Panel on Climate Change*. Solomon S., Qin D., Manning M., Chen Z., Marquis M., Averyt K.B., Tignor M., and Miller H.L.. (eds.). Cambridge University Press, Cambridge, United Kingdom and New York, NY, USA. . 996 pp. ISBN 978 0521 88009-1.

Leggett J., Pepper W.J., and Swart R.J.. 1992. *Emission scenarios for IPCC: An update*. In: Houghtonm J.T., Callander, B.A., Varney, S.K. (eds): *Climate Change 1992. Supplementary Report to the IPCC Scientific Assesment*. Cambridge University Press, Cambridge. 69–95 pp. ISBN 0-521-43829-2.

- Meinshausen M., Smith S.J., Calvin K.V., Daniel J.S., Kainuma M.L.T., Lamarque J.-F., Matsumoto K., Montzka S.A., Raper S.C.B., Riahi K., Thomson A.M., Velders G.J.M., and van Vuuren D.. 2011. *The RCP Greenhouse Gas Concentrations and their Extension from 1765 to 2300*. Climatic Change. Vo. 109. 213–241.
- Moss R., Babiker M., Brinkman S., Calvo E., Carter T., Edmonds J., Elgizouli I., Emori S., Erda L., Hibbard K., Jones R., Kainuma M., Kelleher J., Lamarque J.F., Manning M., Matthews B., Meehl J., Meyer L., Mitchell J., Nakicenovic N., O’Neill B., Pichs R., Riahi K., Rose S., Runci P., Stouffer R., van Vuuren D., Weyant J., Wilbanks T., van Ypersele P., and Zurek M.. 2008. *Towards New Scenarios for Analysis of Emissions, Climate Change, Impacts, and Response Strategies. Technical Summary*. Intergovernmental Panel on Climate Change, Geneva. . 25 pp. ISBN: 978-92-9169-124-1.
- Moss R.H., Edmonds J.A., Hibbard K.A., Manning M.R., Rose S.K., van Vuuren D.P., Carter T.R., Emori S., Kainuma M., Kram T., Meehl G.A., Mitchell J.F.B., Nakicenovic N., Riahi K., Smith S.J., Stouffer R.J., Thomson A.M., Weyant J.P., and Wilbanks T.J.. 2010. *The next generation of scenarios for climate change research and assessment*. Nature. Vo. 463. 747–756.
- 2000: *Emission scenarios. A Special Report of IPCC Working Group III*. Nakicenovic N. and Swart R.. (eds.). Cambridge University Press, Cambridge, UK. . 599p. ISBN 0 521 80081 1.
- Vingarzan R.. 2004. *A review of surface ozone background levels and trends*. Atmospheric Environment. Vo. 38. 3431–3442.
- <http://data.giss.nasa.gov/modelforce/ghgases/>.
- <http://data.giss.nasa.gov/gistemp/>.
- <http://www.pik-potsdam.de/~mmalte/rcps/>.

Chapter 15. Monitoring of Air Pollution

Atmospheric environmental protection, including air quality management, response scenarios, health effect and risk estimates as well as atmospheric dispersion modeling would be impossible without the quantitative description of air quality with representative and measurable quantities. Air pollution is a complex process with numerous materials that have very different atmospheric lifetime, environmental and/or health effect; therefore air quality description could not be carried out using one simple quantity. In fact, the correct measurement method and location depends largely on the material and also on the aim of the study. In this chapter, we give an overview of the most common measurement techniques for the typical requirements of scientific and authoritative air quality management.

15.1. Measurement locations

15.1.1. Classification of measurement sites

Air pollution involves emission (release), transmission (dispersion) and immission (deposition/reaction) processes (see Chapter 2), which have to be treated and measured separately.

Emission processes can be categorized as anthropogenic and natural emissions. In many countries, industrial organizations are obliged to perform on-release measurement of their emission, which led to large public databases of emission data from certain facilities (see e.g. <http://edgar.jrc.ec.europa.eu>). However, a large part of anthropogenic emission is not measured directly; such as pollution from traffic, households/heating and agriculture. The effect of these sources are estimated through sample data measured at selected representative points, such as a traffic emission measurement site near a busy road or a micrometeorological station on an agricultural field. Based on these datasets, the magnitude and the temporal and spatial variability of the emission can be estimated.

Natural sources of pollutants are hard to measure because of their large spatial extent and complexity. There are measurement sites to sample emission data from representative points, which, together with the long-term concentration time series of worldwide stations can be used to obtain global- and regional-averaged net emission data of natural sources/receptors.

The optimal measurement location depends largely on the atmospheric lifetime and environmental impact of the material. Materials with long (1–120 years) lifetime are well mixed throughout the atmosphere, thus their annual average concentration can be regarded as spatially constant except in the vicinity of their source regions. This approach is valid for most of the greenhouse gases, like CO₂ and N₂O, which affect environment globally. It means that we require measurements that are representative for the large-scale concentration field, which is not the case close to the source regions. Thus greenhouse gases are measured in background (i.e. far from significant release points) sites.

The most representative greenhouse gas concentration time series have been measured at locations far from any human activities, like the Mauna Loa Observatory in Hawaii or the Amundsen–Scott Station in the Antarctic (Figure. 15.1). These and other *global background* measurement sites provide valuable information of the average concentrations, while *regional background* measurements in rural areas are used to estimate regional variability and transport processes (Table 15.1).

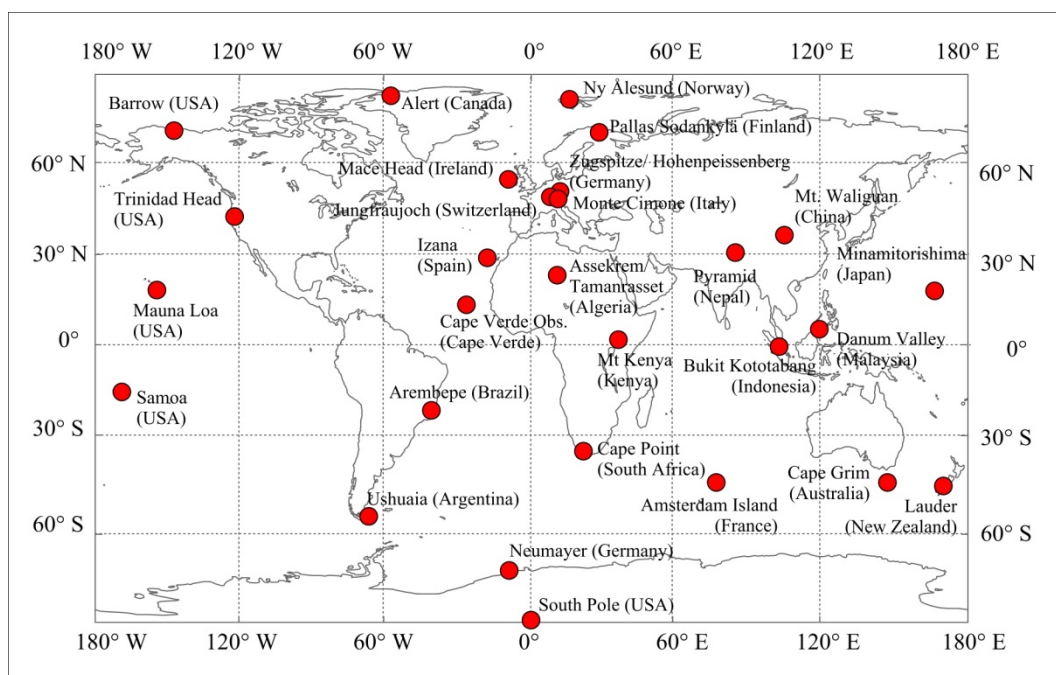


Figure 15.1: Global background measurement sites of the WMO GAW (World Meteorological Organization – Global Atmosphere Watch) project

Table 15.1: Categorization of surface air quality measurement sites

Measurement site	Location	Aim of measurement	Measured quantities	Example
Global background	Far from any human activities	Greenhouse gas global average concentrations	Long-term average concentrations	Mauna Loa Observatory, Hawaii
Regional background / regional emission	Agricultural and rural areas	Greenhouse gas regional average concentrations, regional transport	Long-term average concentrations, fluxes	Hegyhátsál, Hungary
		Toxic/irritating material average deposition, regional transport		
		Sample data to estimate large-scale emission		
Residential background	Suburbs, residential areas	Toxic/irritating material concentrations, health effects	High temporal resolution concentrations	Gilice tér, Budapest
Urban emission	Busy roads, industrial areas	Emission estimation, local scale health effects	High temporal resolution concentrations	Kosztolányi Dezső tér, Budapest
In-situ emission	Release points (stacks)	Accurate emission data to fulfill law obligations	Released mass of pollutant	Paks Nuclear Power Plant, Hungary

Air pollutants with short lifetime have several effects on local or regional scale. Their concentrations can vary with magnitudes between source and background locations, both of which are important to estimate. While close to the source, high concentrations have a significant impact on health and environment (e.g. in an urban area), further

distances can suffer long-term effects through deposition. Therefore within a local environment such as a residential area (often referred to as *residential background* sites), concentration measurement with high temporal and spatial resolution is required. Meanwhile in rural areas, long-term average concentrations and calculated or directly measured depositions are important (Table 15.2).

Table 15.2: Categorization of surface air quality measurement sites for environmental / health effect estimation

	Typical pollutants	Atmospheric life-time	Scale of impact	Representative quantity	Measurement location
Greenhouse gases	CO ₂ , N ₂ O, CH ₄	> 1 year	Global	Concentration	Global background
Toxic / irritating air pollutants	NO _x , O ₃ , SO ₂	< 1 month	100 – 1000 km	Deposition	Regional background
			0 – 100 km	Concentration	Residential background

While surface measurements are representative for a given location, and provide wealthy information about air quality of different regions, more accurate large scale simulations of transport-exchange processes require concentration data on a much finer grid. Remote sensing techniques, especially satellite observations have become a uniquely efficient tool of large scale air quality measurement, and are able to measure vertically integrated total pollutant mass as well as vertical concentration profile for any location with a fine spatial and temporal resolution.

15.1.2. Measurement network in Europe and Hungary

The European Monitoring and Evaluation Programme (EMEP) was funded in 1979 to organize an international co-operation in order to provide public large scale emission and immission data and solve transboundary air pollution problems (<http://www.emep.int>). EMEP consists of five suborganizations:

- Centre on Emission Inventories and Projections (CEIP), Vienna, Austria
- Chemical Coordinating Centre (CCC), Kjeller, Norway
- Meteorological Synthesizing Centre – West (MSC-W), Oslo, Norway
- Meteorological Synthesizing Centre – East (MSC-E), Moscow, Russia
- Centre for Integrated Assessment Modelling (CIAM), Vienna, Austria

CEIP maintains an emission inventory of the most important air pollutants (CO, NH₃, VOC, NO_x, SO₂, PMs, heavy metals and POPs) on a 0.1 degree resolution grid based on emission reports of member countries. The detailed and long-term time series of emission data is publicly available from CEIP's website (<http://www.ceip.at/>) and is widely used in air quality studies of different European regions.

While CEIP holds the emission database, CCC is responsible for immission measurement. EMEP measurement network consists of hundreds of regional background monitoring and/or precipitation analyzer sites. These sites perform a measurement programme defined by EMEP guidelines to provide reliable and comparable results for the whole continent. The measurements mostly focus on acidic components and ozone, but heavy metals and PMs are also measured at numerous sites. Both the archive and actual database of European air quality are available from the CCC website (<http://www.nilu.no/projects/ccc/index.html>). In Hungary, the K-Pusztá station in the Kiskunság region is part of the EMEP monitoring network.

The two MSC centers are responsible for high quality atmospheric dispersion modeling and software development. MSC's Eulerian dispersion model provides reliable analyses fields and forecasts of the continent's air quality as well as a mapping of source-receptor relationships to point out the contribution of each country to the total transboundary air pollution. The model uses CEIP and CCC measurements as input data. Besides the dispersion model's results, its source code is also freely available.

CIAM focuses on climate change and air pollution relationships, with an attached treatment of greenhouse gas and pollutant emission. Based on the more decades long EMEP time series, CIAM provides emission projections, dispersion and health effect modeling using attached multidisciplinary simulation performed by the GAINS model.

In Hungary, air quality measurement sites are operated by the Hungarian Meteorological Service (OMSZ) and the Ministry of Rural Development's Air Quality Network (OLM). Five regional background stations (Fig. 15.2) are maintained by the Hungarian Meteorological Service to measure concentrations and soil-atmosphere fluxes of acidic components, ozone, VOC and greenhouse gases. In addition, a precipitation analyzer station is located in Siófok.

Two additional regional background stations in Kisszentmárton and Sarród are operated by OLM to estimate pollution suffered by environmental protection areas. However, OLM mostly focuses on urban air quality monitoring, and its measurement sites are present in almost all larger towns of the country, including both residential background and urban emission sites (Fig. 15.3–15.4).

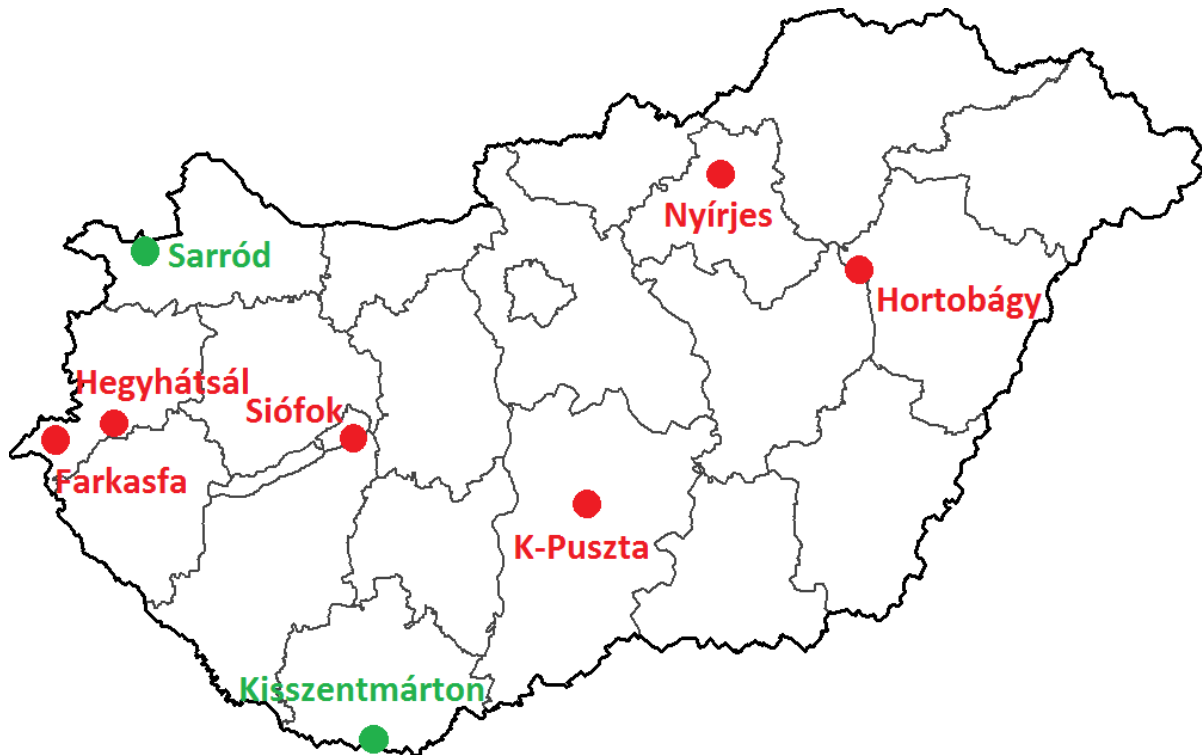


Figure 15.2: Regional background measurement sites in Hungary operated by the Hungarian Meteorological Service (red) and the Hungarian Air Quality Network (green)

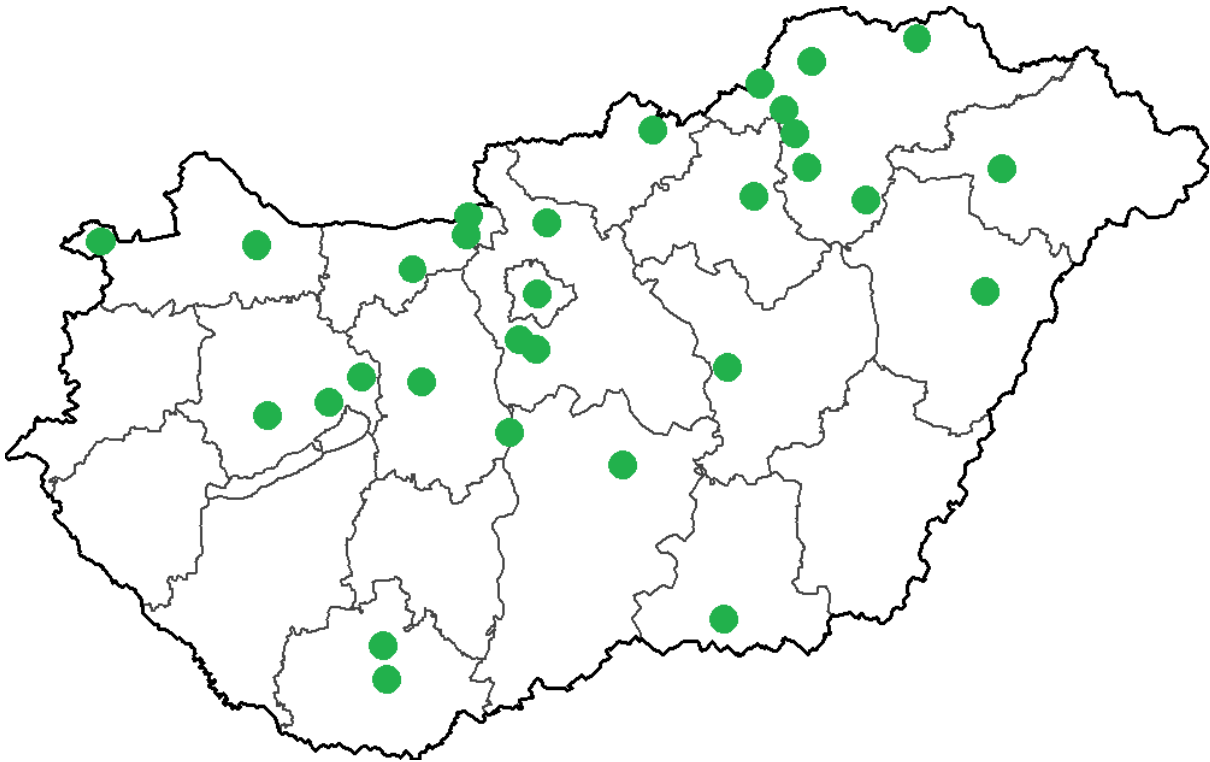


Figure 15.3: Urban measurement sites operated by the Hungarian Air Quality Network (OLM)



Figure 15.4: Urban background measurement site in Budapest, Hungary (source: Hungarian Air Quality Network).

15.2. Measurement techniques

15.2.1. Sampling methods

In order to analyze air quality, we need to take samples of the ambient air without modifying its chemical composition. In order to avoid microscale effects, free air movement around the measurement site has to be provided. On the other hand, the sample inlet must be protected against rainfall and dust that can largely influence measurement data. A sampling system thus has to fulfill the following criterias (Air Quality Sampling Manual, 1997):

- built from materials that do not react with the pollutants to be observed,
- located in a place where free air movement is provided,
- protect the sample from rainwater, dust and insects,
- reliable with low maintenance requirements,
- resistant against elements and wildlife.

Sampling time interval depends largely on the aim of the measurement. Long-term average concentration studies require samples collected during a certain time period, mostly on a daily or longer basis. This *batch sampling* method provides accurate results of average concentration for a period equal or longer than the sampling interval, however, cannot estimate concentration fluctuations on a finer temporal resolution. To obtain hourly or even finer

concentration data, a *continuous monitoring* is needed where sampling is either continuous in time or performed with a very fine (1–10 s) time interval. Continuous monitoring is usually carried out in air quality investigations for public protection purposes, especially in urban areas.

Depending on the measured quantity, either passive or active sampling can be used. *Passive sampling* does not involve any pumping, thus the pollutants only reach the container through their own movement and diffusion. Passive sampling is an efficient tool to estimate deposition; however, concentration measurement requires a well-defined volume flux of air pumped through the measurement device, often referred to as *active sampling*.

15.2.2. Measurement of gas concentrations

15.2.2.1. Spectrophotometry

Spectrophotometry is based on the absorption of radiation by gases at different wavelengths. When a light with a known intensity spectrum passes the sample, the exiting radiation's intensity spectrum can be used to determine the composition of the gas. The absorption wavelengths where intensity significantly drops are a footprint of each material, while the exact values of wavelength-dependent extinction gives information of the concentration, following the Beer–Bouguer–Lambert-law:

$$I = I_0 \exp\{-cL\varepsilon\} \quad (15.1)$$

where I is intensity of the radiation, c is the concentration, ε is the extinction coefficient and L is the optical path-length. Spectrophotometry consists of two main parts: *infrared spectrophotometry* at wavelengths larger than 800 nm, which relies on molecular rotation and vibration excitement; and *ultraviolet-visible spectrophotometry* in the wavelength range of 200–800 nm that is based on electron excitement and atomic absorption.

Infrared spectrophotometry is primarily used for emission measurements of most pollutant gases, like CO, CO₂, NO, SO₂ and hydrocarbons. It is also widely used for CO and CO₂ measurement for ambient and indoor air quality investigations (Ionel and Popescu, 2010). Ultraviolet spectrophotometry is applied for the investigation of gases that have a significant absorption in the UV range, mostly NO and O₃.

In a complex system containing several components like the polluted air, the absorption lines often overlap and cannot be clearly separated. One way to deal with this issue is to extend the wavelength range of the radiation and detect other absorption lines from which the components can be separately identified. Another approach is to use a chemical separation, either with a chemical filter, or with splitting the sample and entering a reactant that neutralizes one of the colliding components.

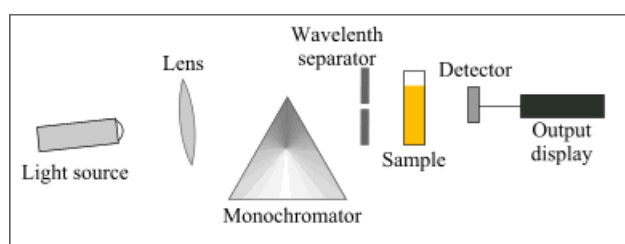


Figure 15.5: Main parts of a single beam spectrophotometer

15.2.2.2. UV fluorescence

UV fluorescence is similar to UV spectrophotometry in a way that ultraviolet radiation is emitted into the sample; however, instead of investigating the whole absorption spectrum, only intensity at the wavelength of the component's fluorescence is measured. In order to avoid interference with the exciting radiation, measurement is carried out in a large angle from the radiation direction. The measured light intensity in this case is directly and only emitted by the investigated gas, thus it provides an exact estimation of the concentration. UV fluorescence is mostly used for SO₂-measurements, which absorbs 215 nm UV radiation and then emits fluorescent radiation between 240–420 nm with a peak of 320 nm (Ionel and Popescu, 2010). As fluorescence emits light with small intensity, the measured signal is usually amplified using photomultiplier tubes.

15.2.2.3. Chemiluminescence

Chemiluminescence is the most common way to measure the photochemical NO, NO₂ and NO_x concentrations. The method is based on the fact that during the reaction of NO with ozone, the resulting NO₂ molecule is excited and releases radiation at 1100 nm wavelength:



The released radiation is amplified by photomultiplier tubes and gives direct information about the NO concentration. The measurement is carried out in two steps: at the beginning, the sample is split and the first part passes through a converter which reduces all NO₂ to NO. Then it gets into the measurement chamber where ozone is added at a constant rate. Measuring the emitted radiation intensity, the concentration of the total NO_x components can be obtained. To receive information about each component, the same measurement is carried out without the converter, thus only the original NO concentration is measured. NO₂ concentration is derived as a difference of measured NO_x and NO levels. A similar method is available for ozone measurement using either NO or ethane (C₂H₄) reactant, however, due to cost and safety reasons, UV-spectrophotometry is more widely used for ozone concentration measurement (Ionel and Popescu, 2010).

15.2.2.4. Gas chromatography

Gas chromatography is a measurement technique for most greenhouse gases like CO₂, CH₄, SF₆ and N₂O as well as for CO. A gas chromatograph has two inlets: an inert carrier flow (usually nitrogen) and a sample injector (Figure 15.6).

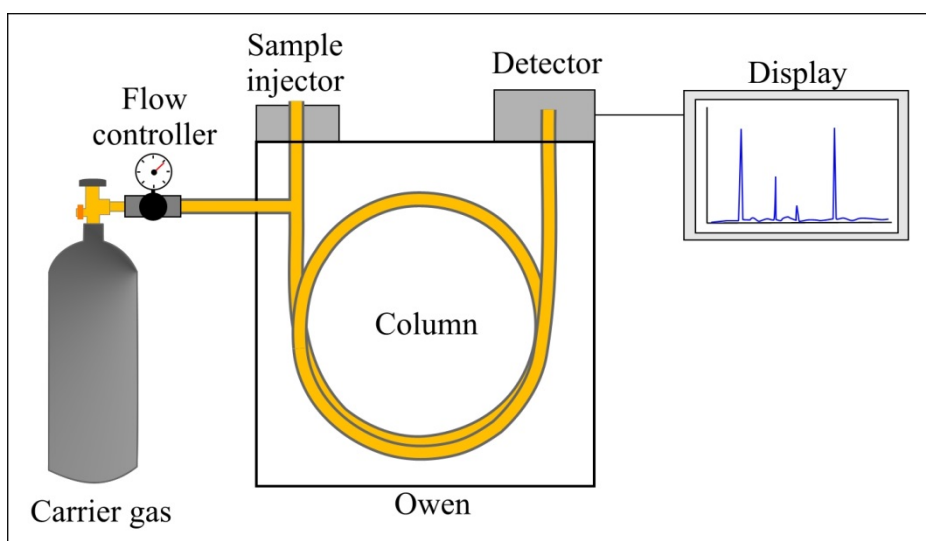


Figure 15.6: Schematic diagram of a gas chromatograph

The sample is driven through the *column* by the carrier flow. The walls of the column are covered with the *stationary phase*, a material which interacts with the gas components to be analyzed. Interaction between the sample and the stationary phase inside the column leads to different arrival time of each component at the detector, which enables their separated measurement.

There are different detectors available for gas chromatographs. A universal detector is based on the difference of thermal conductivity of the materials (*TCD*, *Thermal Conductivity Detector*). A more specific way to measure organic and hydrocarbon compounds is the *Flame Ionization Detector* (FID), which is a hydrogen flame located in an electric field. When carbons enter the flame, ionization occurs and a current starts between the electrodes that provide a direct electrical signal representing the concentration. Gas chromatographs with FID are the most common tools to measure CO₂ and other greenhouse gas concentration (see e.g. Haszpra, et al., 2008) at worldwide stations (Figure 15.7).



Figure 15.7: Gas chromatograph for greenhouse gas measurement at Hegyhátsál station, Hungary

15.2.3. Measurement of aerosol concentrations

Describing the pollution caused by aerosol particles require three parameters to measure:

- total mass concentration of aerosols,
- size distribution,
- chemical composition.

While the former one is measured at almost all air quality observation sites, on-site analysis of aerosol chemical composition is very rare as it requires advanced analytical chemical methods and laboratories. The exact size distribution is usually not known, but the total mass of particles smaller than a given size is measured, referred to as PM10 and PM2.5 (total mass of particulate matter smaller than 10 and 2.5 microns). Size selection is performed at the inlet using a cascade impactor (Figure 15.8). As air is accelerated through multiple narrowing nozzles, small particles remain in the flow, while large particles gain enough momentum to hit the wall where they get trapped in a collection shim.

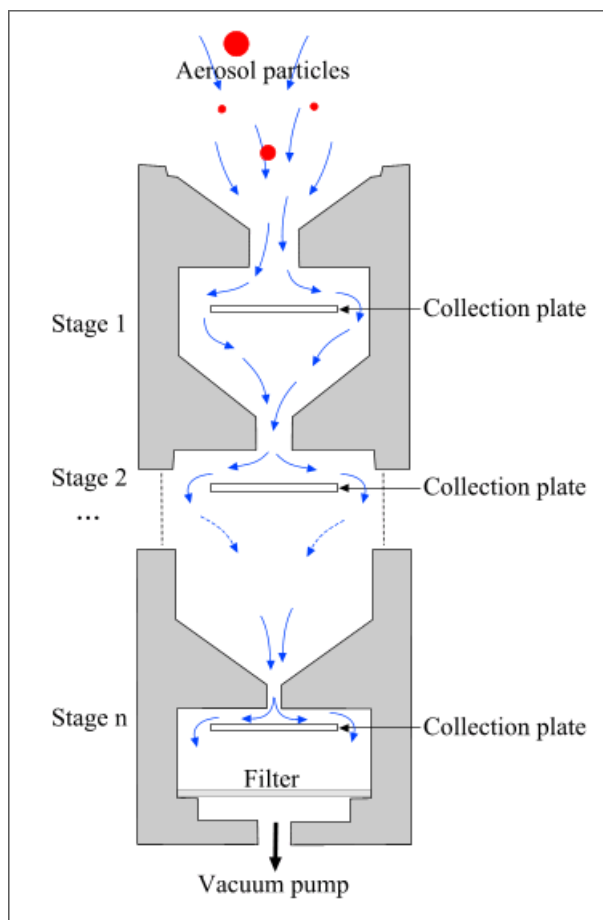


Figure 15.8: Schematic picture of a cascade impactor

Total mass concentration of particles is measured using a Teflon-coated filter and a sensitive scale that measures the mass of the filter. For monitoring purposes, high frequency (1–10 s) mass measurement is required, while batch sampling sites use *high-volume samplers* (HVS) that contain and protect collected aerosols over a long period to estimate average concentrations and perform advanced chemical composition analysis.

15.2.4. Remote sensing

In the recent decades, the extremely fast development of remote sensing methods led to a wide range of both ground- and space-based tools to observe weather and air quality. In atmospheric chemistry, remote sensing measurements are used to satisfy the following needs:

- high spatial resolution air quality data to provide initial fields for transport-exchange models,
- high spatial and temporal resolution air quality data to estimate fluxes,
- air quality information of hardly accessible areas,
- vertical profile measurements,
- measurement of airborne pollutants,
- estimation of ozone concentration in the stratosphere.

15.2.4.1. LIDAR

Light Detection and Ranging (LIDAR) is a ground-based remote sensing tool to obtain high temporal and spatial resolution concentration fields. It is based on the same idea as spectrophotometry: if a radiation is emitted, the materials absorb this radiation at a specific wavelength and scatter it back as an isotropic radiation (Figure 15.9).

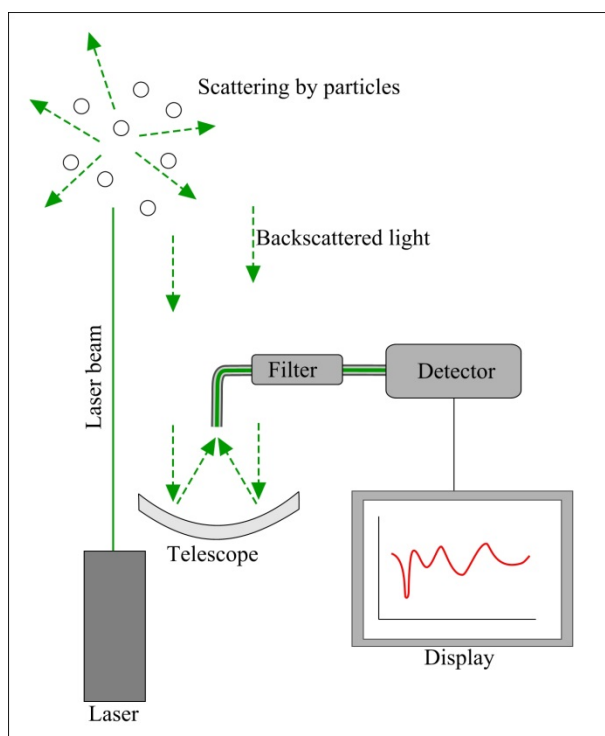


Figure 15.9: Schematic diagram of a LIDAR system

LIDAR emits a monochromatic laser beam at the absorption wavelength of the investigated component, and measures backscatter from the atmosphere. Its high measurement frequency enables measurements in several directions within a short period (like weather radars), which can be analyzed as a continuous concentration field. In order to avoid measurement errors due to global radiation entering the detector, a *differential absorption LIDAR* (DIAL) is often used that emits two laser beams, one tuned to the absorption wavelength, and the other one tuned just below or over it, being the reference beam. The beams are emitted alternately, and the difference between the two backscatter values can be regarded as the backscatter of the investigated gas.

15.2.4.2. Differential optical absorption spectroscopy (DOAS)

DOAS consists of a continuous light source with known emission spectrum, usually a Xe-arc lamp, and a detector in a certain range from the source. DOAS is also based on spectrophotometry with the difference that the sample in which the emitted light suffers extinction is the atmosphere itself. The distance between the lamp and the detector ranges from several hundred meters to many kilometers. DOAS is often used to obtain average concentrations within an urban street canyon or over an industrial area.

15.2.4.3. Satellite observations

Total mass of pollutants in a vertical column can be obtained using spectrophotometers on satellites that calculate concentrations based on wavelength-dependent radiation extinction throughout the whole atmosphere from the infrared to the ultraviolet range. As forecast-oriented meteorological satellites measure radiation intensities at a wide range of wavelengths, air quality data can be obtained using their multi-channel sensors, like the ones on the METEOSAT, GOES, MetOp or MODIS satellites. Most satellite data post-processing tools provide methods to create aerosol or carbon monoxide (CO) concentration maps using the satellite intensity data at the absorption wavelengths of the selected material. In addition, air quality oriented sensors have also been developed to perform more detailed observation, especially in the UV range, which is poorly measured for forecast purposes, but gets a high importance in atmospheric photochemistry.

A polar orbiter satellite designated primarily for atmospheric chemistry purposes was ESA's *Envisat* launched in 2002. Its data was used in a wide range of projects including climate change, atmospheric dispersion, hydrology, cartography and agricultural research. *Envisat* finished its mission in 2012. Based on its success, the POES (*Polar Operational Environmental Satellites*) project was created, including both NOAA and MetOp satellites launched

between 2002–2012. They host numerous sensors for weather and air quality monitoring, vegetation analysis and several other environmental research purposes.

Satellite spectrophotometers are able to measure vertical total concentration of different pollutants. Most pollutants only occur in the low levels, thus the vertical total mass is usually representative for the near-ground concentrations. However, vertical concentration profile becomes extremely important in the case of ozone measurement because of the significant difference between stratospheric and tropospheric ozone.

The total vertical ozone concentration, measured by space-based UV-spectrophotometers is described with a single value, the Dobson Unit (DU). 1 DU refers to a vertical total mass of gas that would occupy a 10 micron thick layer on the surface under standard temperature and pressure. As the stratosphere contains significantly more ozone than the troposphere, the vertical total ozone concentration expressed in DU is representative for the stratospheric ozone (Figure 15.10).

EP/TOMS Version 8 Monthly Average Total Ozone June 2000

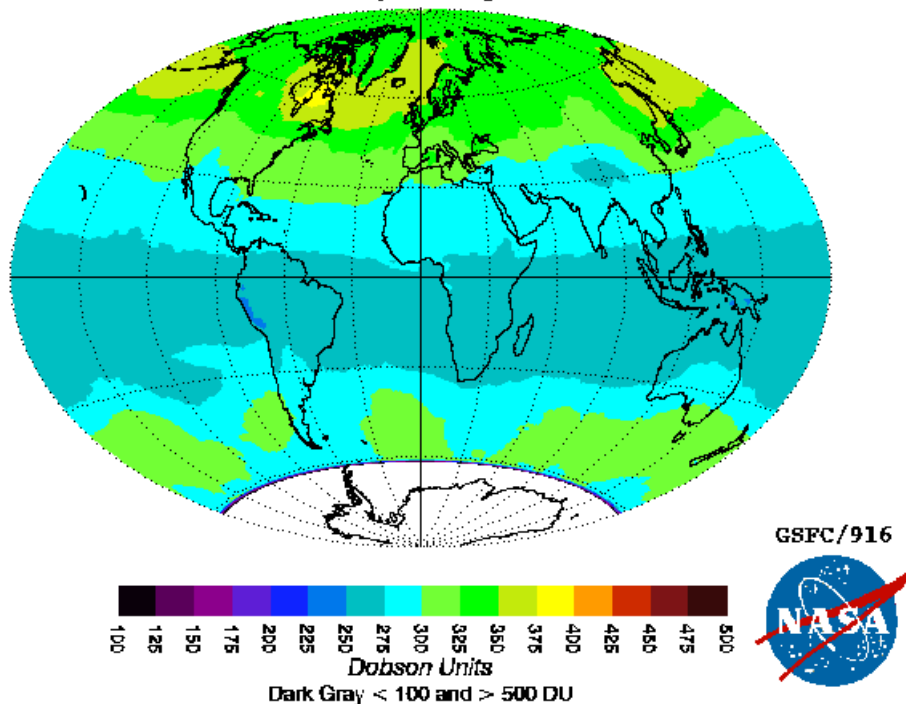


Figure 15.10: Average total vertical ozone concentration of June 2000, measured by space-based UV-spectrophotometer (source: NASA)

However, there is a way to obtain tropospheric ozone concentrations from satellite measurement based on the *Doppler broadening* effect: if the radiation is absorbed by particles that move at relatively high speed due to their thermal motion, the Doppler effect shifts the wavelength of the absorbed radiation. In the stratosphere, where density is low and thermal motion is significant, Doppler broadening results in wider absorption bands. Thus, with measuring the shape of the absorption line, the ratio of low-level and high-level ozone can be estimated.

While geostationary satellites perform continuous monitoring of the observed area's air quality, low-level polar orbiters are able to perform much more sophisticated measurements at a designated area. Equipped with space-based LIDAR-s, they are able to measure detailed 3D concentration profiles, and their fast movement enables them to collect data from thousands of kilometers within a few minutes of time. It leads to high resolution vertical cross-sections along the satellite path that provide wealthy information about air quality patterns (Figure 15.11.). During measurement campaigns, even more detailed 3D concentration data is obtained using airplanes equipped with LIDAR-s, which is used in critical air pollution situations, or to validate satellite results.

15.2.5. Rainwater analysis

Measuring the atmospheric concentrations and surface fluxes of different materials usually gives a good estimation about the health and environmental impact of the pollution. However, wet deposition has to be also taken into account for soluble pollutants, especially for acidic components, that produce their effect mainly through wet deposition.

Rainwater analysis consists of two main parts: pH measurement to estimate acidic wet deposition often referred to as acidic rain; and composition measurement including water hardness to estimate wet deposition of soluble gases and minerals. Rainwater pH is measured using electronic pH-meters that rely on the electric conductivity of the water and provide a direct electronic signal that enables automatic monitoring.

Rainwater composition is measured using spectrophotometric and analytical chemical tools to analyze the solution. The most important ions that have a significant wet deposition are Cl^- , SO_4^{2-} , NO_3^- , NH_4^+ , Na^+ , K^+ , Mg^{2+} and Ca^{2+} . Measurement of the heavy metal, especially lead content of rainwater is also important to estimate their deposition and environmental accumulation.

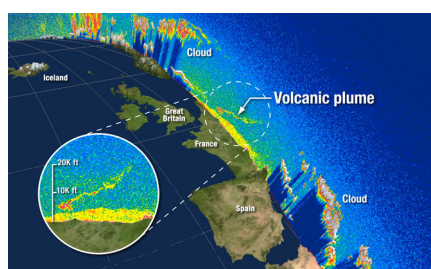


Figure 15.11: Vertical cross-section of aerosol concentrations on April 17, 2010; based on LIDAR measurements performed by the CALIPSO satellite. Besides high-level clouds in northern Europe and the Mediterranean, the air pollution over France and the volcanic plume of the Eyjafjallajökull eruption is also visible. (source: NASA)

Vertical cross-section of aerosol concentrations on April 17, 2010

15.3. Conclusion

Air quality management and research relies on accurate measurement data that gives information about emission, concentration and immission (deposition) processes. The location of measurement sites has to be selected based on the atmospheric lifetime and the impact scale of the investigated material; thus the air quality measurement points range from global background sites far from any human activities to emission measurement in the vicinity of the source areas.

To measure concentrations, there are various methods available. Most of them are based on wavelength-selective radiation detectors and spectrum analyses, using absorption spectrophotometry, fluorescence or chemiluminescence. Greenhouse gas concentrations are often measured with gas chromatography, a tool where a column interacts with the sample in a selective way that each material reaches the detector separately. Dry deposition can be measured through high temporal resolution concentration measurement to estimate fluxes, or using passive sampling to directly measure fallout of a pollutant over a certain period. Wet deposition is estimated from rainwater pH monitoring and chemical composition analysis.

Remote sensing tools have gone through a fast development in the past decade. Ground-based LIDAR and DOAS instruments are able to measure detailed 3D profiles of concentration and wind, while space-based spectrophotometers provide high temporal and spatial resolution data of vertical total concentrations, and they are able to estimate vertical profiles based on Doppler broadening of absorption bands. Polar orbiter satellites are often equipped with LIDAR-s to obtain high resolution vertical profiles along the satellite path. Satellite measurements have now become the most effective tools to monitor air pollution as well as atmospheric trace gas fluxes and transport.

References

Air Quality Sampling Manual. The State of Queensland Department of Environment. 1997. ISBN 0 7242 6998 3.

Ionel I. and Popescu F.. 2010. *Methods for Online Monitoring of Air Pollution Concentration*. Air Quality, Ashok Kumar (Ed.). ISBN: 978-953-307-131-2.

Haszpra L., Barcza Z., Hidy D., Szilágyi I., Dlugokencky E., and Tans P.. 2008. *Trends and temporal variations of major greenhouse gases at a rural site in Central Europe*. Atmospheric Environment. 42. 8707–8716.

<http://www.ceip.at/>.

<http://edgar.jrc.ec.europa.eu/>.

<http://www.ceip.at/>.

<http://www.nilu.no/projects/ccc/index.html>.

Chapter 16. Questions:

- 1.1: Describe the composition of the Earth's atmosphere.
- 1.2: How temperature changes vertically in each atmospheric layers and why?
- 2.1: Which are the main natural and anthropogenic sources of air pollution?
- 2.2: How emissions of main air pollutants have changed in Europe in the recent years?
- 3.1: What is the quasi steady state approximation (QSSA)?
- 3.2: What is the difference between the differential rate and integrated rate law?
- 4.1: Describe the main chemical reactions of oxygen in the atmosphere.
- 4.2: Describe the main stages of evolution on the Earth.
- 5.1: Describe the importance of terrestrial processes in carbon cycle.
- 5.2: Group the most important carbon species in the atmosphere.
- 6.1: Describe the nitrogen cycle.
- 6.2: Describe the similarity and differences between nitrification and denitrification.
- 7.1: Describe the sulphur cycle.
- 7.2: Group the most important sulphur species in the atmosphere.
- 8.1: Which are the main differences between chemistry of tropospheric and stratospheric ozone?
- 8.2: Describe the typical vertical profile of the ozone.
- 8.3: Describe the typical temporal and spatial variations of tropospheric ozone.
- 9.1: Which are the main sources of aerosol particles?
- 9.2: Which are the main sinks of aerosol particles?
- 9.3: Describe the main properties of different aerosol particles.
- 10.1: What are the most used models for dispersion of air pollutants in the atmosphere?
- 10.2: Derive the atmospheric transport equation.
- 11.1: Describe the advantage of the adaptive gridding.
- 11.2: What are the main strategies for parallel computing?
- 12.1: Which factors affect the dry and wet deposition of gases and particles?
- 12.2: Which methods can be used to determine the dry and wet deposition of atmospheric gases and aerosol particles?
- 13.1: Describe the effects of main air pollutants on human health.
- 13.2: What kind of environmental problems can be formed due to the effects of main air pollutants?
- 14.1: How do the atmospheric composition and its changes affect the radiation budget of the Earths-atmosphere system?

Questions:

14.1: How can we estimate the future greenhouse gas emissions?

15.1: Which types of surface air quality measurement sites exist?

15.2: How can the atmospheric gas and aerosol concentrations be measured?